University of Fort Hare
Together in Excellence

Synthesis and characterization of metal sulfide nanoparticles/polymer nanocomposites

By

Johannes Zanoxolo Mbese

Student Number: 200604458

Being a dissertation submitted to the Faculty of Science and Agriculture in fulfillment of the requirements for the award of the degree of

MASTER OF SCIENCE IN CHEMISTRY

of the

University of Fort Hare

Supervisor: Prof. P. A. Ajibade

Department of Chemistry

University of Fort Hare

Private Bag X 1314

Alice

5700

South Africa

December 2013

TABLE OF CONTENTS

TITLE PAGE i
TABLE OF CONTENTS ii
ACKNOWLEDGEMENTS xii
DECLARATION BY CANDIDATE xiv
CERTIFICATION xv
DEDICATION xvi
ABSTRACT xvii
CHAPTER ONE 1
1.0 INTRODUCTION AND LITERATURE REVIEW 1
1.1 Metal sulfide nanoparticles 1
1.2 Particle size 3
1.3 Metal sulfide nanoparticles and nanocomposites synthetic techniques 4
1.3.1 Sol-Gel method 4
1.3.2 Microemulsions 6
1.3.3 Hydrothermal or solvothermal synthesis 9
1.3.4 Single source precursors method 10
1.4 Properties of metal sulfide nanoparticles 13
1.5 Potential applications of nanomaterials 15
1.5.1 Sensors 15
1.5.2 Solar cell 16
1.5.3 Catalysis 16
1.5.4 Lasers 17
1.5.5 Light emitting diodes 17
1.5.6 Biological labeling 18
1.5.7 Other applications 19
1.6 Chemistry of some selected dithiocarbamate compounds 22
1.6.1 Zn(II), Cd(II) and Hg(II) complexes 23
1.7 Aims and objectives of this project 24
1.8 References 25
CHAPTER TWO 36
2.0 EXPERIMENTAL 36
2.1 Chemicals and solvents 36

2.2. Physical measurements 36
2.2.1 Melting point 37
2.2.2 Solubility 37
2.2.3 Elemental analysis 37
2.2.4 UV-Visible spectroscopy 37
2.2.5 Photoluminescence spectroscopy 37
2.2.6 Infrared spectroscopy 37
2.2.7 Nuclear magnetic resonance spectroscopy 38
2.2.8 X-ray diffraction 38
2.2.9 Thermogravimetric analysis 38
2.2.10 Scanning Electron Microscopy 39
2.2.11 Energy Dispersive X-ray analysis 39
2.2.12 Transmission Electron Microscopy 39
2.3. Synthesis of dithiocarbamate ligands 39
2.3.1 Synthesis of ammonium N-phenyldithiocarbamate, $NH_4[C_6H_5(H)NCS_2]$, L^1 40
2.3.2 Synthesis of ammonium N-methyl-N-phenyldithiocarbamate, $NH_4[C_6H_5(CH_3)NCS_2]$, L^2 41
2.3.3 Synthesis of ammonium N-ethyl-N-phenyldithiocarbamate, $NH_4[C_6H_5(C_2H_5)NCS_2]$, L^3 41
2.4. Synthesis of metal dithiocarbamate complexes 42
2.4.1 Synthesis of $[(C_6H_5N(H)CS_2)Zn(S_2C(CH_3)NH_5C_6)]$, ZnL^1L^2 44
2.4.2 Synthesis of $[(C_6H_5N(H)CS_2)Cd(S_2C(CH_3)NH_5C_6)]$, CdL^1L^2 45
2.4.3 Synthesis of $[(C_6H_5N(H)CS_2)Hg(S_2C(CH_3)NH_5C_6)]$, HgL^1L^2 45
2.4.4 Synthesis of $[(C_6H_5N(H)CS_2)Zn(S_2C(C_2H_5)NH_5C_6)]$, ZnL^1L^3 45
2.4.5 Synthesis of $[(C_6H_5N(H)CS_2)Cd(S_2C(C_2H_5)NH_5C_6)]$, CdL^1L^3 46
2.4.6 Synthesis of $[(C_6H_5N(H)CS_2)Hg(S_2C(C_2H_5)NH_5C_6)]$, HgL^1L^3 46
2.5 Experimental procedure for synthesis of HDA-capped ZnS, CdS and HgS nanoparticles 46
2.6 Single crystal X-ray crystallography 47
2.7 Experimental procedure for synthesis of metal sulfide nanoparticles / poly (methyl methacrylate) nanocomposites 48
2.7 References 49
CHAPTER THREE 50
3.0 CHARACTERIZATION OF THE METAL DITHIOCARBAMATE COMPLEXES 50
3.1 Introduction 50
3.2. Characterization of (N- phenyl-N, N-methyl phenyl dithiocarbamato)M(II) complexes, $[ML^1L^2]$, where M = Zn, Cd, and Hg, ... 53
3.2.1 UV-Vis spectroscopy 53
3.2.2 Infrared spectra 54

3.2.3 NMR spectra of the ligands, (L^1 and L^2) 56
3.2.4 NMR spectra of metal complexes, ML^1L^2 57
3.2.5 Thermal decomposition of metal complexes, ML^1L^2 58
3.2.6 Scanning Electron Microscopy and EDX of CdL^1L^2 62
3.2.7 Scanning Electron Microscopy and EDX of ZnL^1L^2 64
3.3 Characterization of (N- phenyl-N, N-ethyl phenyl dithiocarbamato)M(II) complexes, [ML^1L^3], where M = Zn, Cd and Hg 66
3.3.1 Electronic spectra 66
3.3.2 Infrared spectra 66
3.3.3 NMR spectra of ammonium N-ethyl-N-phenyl dithiocarbamate ligand 69
3.3.4 NMR spectra of the metal complexes, ML^1L^3 69
3.3.5 Thermal decomposition patterns 70
3.4.0 Molecular structure of Zn and Hg Complexes. 73
3.5 References 80
CHAPTER FOUR 88
4.0 CHARACTERIZATION OF METAL SULFIDE NANOPARTICLES 88
4.1 Introduction 88
4.2 Characterization of ZnS, CdS and HgS nanoparticles from (N-phenyl-N, N-methyl phenyl dithiocarbamate)M(II) complexes 89
4.2.1 Optical properties of HDA-capped ZnS, CdS and HgS nanoparticles 89
4.2.2 Photoluminescence spectra of HDA-capped ZnS, CdS and HgS nanoparticles 91
4.2.3 XRD spectra of HDA-capped ZnS2, CdS2 and HgS2 nanoparticles 93
4.2.4 TEM image of HDA-capped ZnS2, CdS2 and HgS2 nanoparticles 95
4.2.5 SEM and EDX of HDA-capped ZnS2, CdS2 and HgS2 nanoparticles 99
4.3 Characterization of ZnS, CdS and HgS nanoparticles from (N- phenyl-N,N-ethyl phenyl dithiocarbamate)M(II) complexes 104
4.3.1 Optical properties of HDA-capped ZnS, CdS and HgS nanoparticles 104
4.3.2 XRD spectra of HDA-capped ZnS3, CdS3 and HgS3 nanoparticles 106
4.3.3 TEM image of HDA-capped ZnS3, CdS3 and HgS3 nanoparticles 108
4.3.4 SEM and EDX of HDA-capped ZnS3, CdS3 and HgS3 nanoparticles 112
4.4 References 117
CHAPTER FIVE 125
5.0 CHARACTERIZATION OF METAL SULFIDE NANOPARTICLES / POLY METHYL METHACRYLATE NANOCOMPOSITES 125
5.1 Introduction 125
5.2 Characterization of metal sulfide nanoparticles/ poly (methyl methacrylate) nanocomposites synthesized form ZnS2, CdS2 and HgS2 129

5.2.1 Infrared spectra of ZnS2/PMMA, CdS2/PMMA and HgS2/PMMA nanocomposites 129
5.2.2 X-ray diffraction patterns 130
5.2.3 Thermogravimetric analyses of MS2/PMMA nanocomposites 132
5.2.4 SEM and EDX of ZnS2/PMMA, CdS2/PMMA and HgS2/PMMA nanocomposites 135
5.2.5 TEM images of ZnS2/PMMA, CdS2/PMMA and HgS2/PMMA nanocomposites 139
5.3 Characterization of metal sulfide nanoparticles/ poly (methyl methacrylate) nanocomposites synthesized form ZnS3, CdS3 and HgS3 144
5.3.1 Infrared spectra of ZnS3/PMMA, CdS3/PMMA and HgS3/PMMA nanocomposites 144
5.3.2 X-ray diffraction patterns 145
5.3.3 TGA of ZnS3/PMMA, CdS3/PMMA and HgS3/PMMA nanocomposites 147
5.3.4 SEM and EDX studies of ZnS3/PMMA, CdS3/PMMA and HgS3/PMMA nanocomposites... 149
5.3.5 TEM of ZnS3/PMMA, CdS3/PMMA and HgS3/PMMA nanocomposites 154
5.4 References 159
CHAPTER SIX 166
6.0 CONCLUSIONS AND RECOMMENDATIONS 166
6.1 Summary of results 166
6.2 Conclusions 167
6.3 Recommendations and suggestions for future studies 169
6.4 References 170
6.5 Appendix .....**Error! Bookmark not defined.**

LIST OF FIGURES

Figure 1.1: Length scale showing size of nanomaterials in comparison to various biological components ……... 2
Figure 1.2: Numerous routes in the sol-gel process to control the morphology of the product…… 5
Figure 1.3: Demonstrations (a) Schematic of size selective displacement from interface. (b) Confocal Microscopy images of 2.8 nm CdSe stabilized droplets (c) Droplets after addition of 4.6 nm CdSe NPs. Scale Bar, 20 µm…… ...7
Figure1.4: Triangular diagram for a water/surfactant/oil system showing various amphiphilic aggregates are shown……. 8
Figure 1.5: Schematic energy diagrams illustrating the situation for a nanoparticle, in between a molecule and a bulk semiconductor…….. 14
Figure 1.6: Schematic of filtration system where a nanofiber membrane is allowed to separate the containment from the fluid…… 19
Figure 1.7: A schematic of electrospinning process…….. 21
Figure 3.1: Resonance structures for dithiocarbamate anions…….. 50
Figure 3.2: Infrared spectra of dithiocarbamate ligands and their corresponding metal complexes… 56
Figure 3.3: Superimposed TG profiles of ML^1L^2 complexes……... 59
Figure 3.4: TG/DTG profiles of ZnL^1L^2, CdL^1L^2 and HgL^1L^2 complexes……... 60
Figure 3.5: SEM micrograph of the complex CdL^1L^2 residues after thermal degradations (A) low magnification, (B) high magnification (C) EDX spectrum of the sample…… 63
Figure 3.6: SEM micrograph of ZnL^1L^2 residues after thermal degradations (A) low magnification, (B) high magnification (C) EDX spectrum of the sample…… 65
Figure 3.7: Infrared dithiocarbamate ligands and their corresponding mixed dithiocarbamate ligand complexes……. 67
Figure 3.8: Superimposed TG profiles of ML^1L^3 complexes……... 71
Figure 3.9: TG/DTG profiles of ZnL^1L^3, CdL^1L^3 and HgL^1L^3 complexes…….. 72
Figure 3.10: Molecular structure of the mercury complex…….. 74
Figure 3.11: Packing diagram of the mercury complex……... 74
Figure 3.12: Molecular structure of the zinc complex……. 76
Figure 3.13: Packing diagram of the zinc complex…….. 76
Figure 3.14: The root mean square deviation overlay picture of the two Hg(II) molecules in the asymmetric unit of Complex Hg…….. 77
Figure 4.1: Absorption and emission spectra of HDA-capped ZnS, CdS and HgS nanoparticles prepared from (N- phenyl-N,N-methyl phenyl dithiocarbamate)M(II) complexes at 180 ^oC …… 92
Figure 4.2: XRD studies of HDA-capped ZnS2, CdS2 and HgS2 nanoparticles…… 94
Figure 4.3: TEM image of HDA-capped ZnS2 nanoparticles prepared from (N- phenyl-N,N-methyl phenyl dithiocarbamate)Zn(II) complex…… …….. 95
Figure 4.4: TEM image of HDA-capped CdS2 nanoparticles prepared from (N- phenyl-N,N-methyl phenyl dithiocarbamate)Cd(II) complex……. 97
Figure 4.5: TEM image of HDA-capped HgS2 nanoparticles prepared from (N- phenyl-N,N-methyl phenyl dithiocarbamate)Hg(II) complex……. 98
Figure 4.6: SEM micrograph of the ZnS (labeled as ZnS2) from ZnL^1L^2 complex (A) low magnification, (B) high magnification (C) EDX spectrum of the sample…….. 101
Figure 4.7: SEM micrograph of the CdS (labeled as CdS2) from CdL^1L^2 complex (A) low magnification, (B) high magnification (C) EDX spectrum of the sample…….. 102
Figure 4.8: SEM micrograph of the HgS (labeled as HgS2) from HgL^1L^2 complex (A) low magnification, (B) high magnification (C) EDX spectrum of the sample…….. 103

Figure 4.9: Absorption and emission spectra of HDA-capped ZnS, CdS and HgS nanoparticles prepared from (N- phenyl-N,N-ethyl phenyl dithiocarbamate)M(II) complexes at 180 ^{o}C……105
Figure 4.10: XRD studies of HDA-capped ZnS3, CdS3 and HgS3 nanoparticles……. 107
Figure 4.11: TEM image of HDA-capped ZnS3 nanoparticles prepared from (N- phenyl-N,N-ethyl phenyl dithiocarbamate)Zn(II) complexes at 180 ^{o}C for 60 min…… 109
Figure 4.12: TEM image of HDA-capped CdS3 nanoparticles prepared from (N- phenyl-N,N-ethyl phenyl dithiocarbamate)Cd(II) complexes at 180 ^{o}C for 60 min……..... 110
Figure 4.13: TEM image of HDA-capped HgS3 nanoparticles prepared from (*N*- phenyl-*N*,*N*-ethyl phenyl dithiocarbamate)Hg(II) complexes at 180 ^{o}C for 60 min…… 111
Figure 4.14: SEM micrograph of the ZnS (labeled as ZnS3) from ZnL^1L^3 complex (A) low magnification, (B) high magnification (C) EDX spectrum of the sample…….. 113
Figure 4.15: SEM micrograph of the CdS (labeled as CdS3) from CdL^1L^3 complex (A) low magnification, (B) high magnification (C) EDX spectrum of the sample…….. 114
Figure 4.16: SEM micrograph of the HgS (labeled as HgS3) from HgL^1L^3 complex (A) low magnification, (B) high magnification (C) EDX spectrum of the sample…….. 116
Figure 5.1: Repeating units of poly(methyl methacrylate)……. 126
Figure 5.2: The FTIR spectra of PMMA and its MS2/PMMA nanocomposites……..…….. 129
Figure 5.3: XRD patterns of pure PMMA, ZnS2/PMMA, CdS2/PMMA and HgS2/PMMA nanocomposites…….. 130
Figure 5.4: TGA curves for ML^1L^2 precursor complex, pure PMMA and their MS2/PMMA nanocomposites. M = Zn, Cd and Hg…… 133
Figure 5.5: (A) and (B) are SEM micrograph of ZnS^2/PMMA nanocomposites at low and high magnification prepared from 3wt. % ZnS2 nanoparticles dispersed in PMMA matrix. (C) EDX spectrum of the sample…….……. 136
Figure 5.6: (A) and (B) are SEM micrograph of CdS^2/PMMA nanocomposites at low and high magnification prepared from 3wt. % CdS2 nanoparticles dispersed in PMMA matrix. (C) EDX spectrum of the sample…….. 137
Figure 5.7: (A) and (B) are SEM micrograph of HgS^2/PMMA nanocomposites at low and high magnification prepared from 3wt. % HgS2 nanoparticles dispersed in PMMA matrix. (C) EDX spectrum of the sample…….. 138
Figure 5.8: TEM image of ZnS2/PMMA nanocomposites prepared from 3wt. % ZnS2 nanoparticles dispersed in PMMA matrix……... 140
Figure 5.9: TEM image of CdS2/PMMA nanocomposites prepared from 3wt. % CdS2 nanoparticles dispersed in PMMA matrix…… 141
Figure 5.10: TEM image of HgS2/PMMA nanocomposites prepared from 3wt. % HgS2 nanoparticles dispersed in PMMA matrix…… 142
Figure 5.11: The FTIR spectra of PMMA and its MS3/PMMA nanocomposites…….... 145
Figure 5.12: XRD patterns PMMA, ZnS3/PMMA, CdS3/PMMA and HgS3/PMMA nanocomposites……... 146
Figure 5.13: TGA curves for ML^1L^3 precursor complexes, pure PMMA and their MS3/PMMA nanocomposites. M = Zn, Cd and Hg……. 148
Figure 5.14: (A) and (B) are SEM micrograph of ZnS3/PMMA nanocomposites at different magnification prepared from 3wt. % ZnS3 nanoparticles dispersed in PMMA matrix. (C) EDX spectrum of the sample……... 151
Figure 5.15: (A) and (B) are SEM micrograph of CdS3/PMMA nanocomposites at low and high magnification prepared from 3wt. % CdS3 nanoparticles dispersed in PMMA matrix. (C) EDX spectrum of the sample…….. 152
Figure 5.16: ((A) and (B) are SEM micrograph of HgS3/PMMA nanocomposites at different

magnification prepared from 3wt. % HgS3 nanoparticles dispersed in PMMA matrix. (C) EDX spectrum of the sample……... 153
Figure 5.17: TEM image of ZnS3/PMMA nanocomposites prepared from 3wt. % ZnS3 nanoparticles dispersed in PMMA matrix……. 156
Figure 5.18: TEM image of CdS3/PMMA nanocomposites prepared from 3wt. % CdS3 nanoparticles dispersed in PMMA matrix……. 157
Figure 5.19: TEM image of HgS3/PMMA nanocomposites prepared from 3wt. % HgS3 nanoparticles dispersed in PMMA matrix……. 158

LIST OF TABLES

Table 1.1: Comparisons of properties between gold as bulk and gold as nanoparticles……..... 3

Table 1.2: Major types of 1, 1-dithiolates……...…….. 22

Table 2.1: showing the proposed structures and their corresponding codes……. 44

Table 3.1: Solubility of ligands and complexes in different solvents……... 52

Table 3.2: Elemental analysis and physical properties of the prepared complexes…….. 53

Table 3.3: Selected IR spectra data for the ligands and complexes of ML^1L^2…….. 55

Table 3.4: Selected IR spectra data for the ligands and complexes of ML^1L^3…….. 68

Table 3.5: Crystal data and structure refinement for Complexes 1 and 2 (polymorphs I and II)…... 77

Table 3.6: Bond distances and angles (Å / °)…… 79

Table 3.**7:** Bond distances and angles (Å / °)…… 79

Table 4.1: Energy band gaps of ZnS2, CdS2 and HgS2 nanoparticles……. 90

Table 4.2: Energy band gaps of ZnS2, CdS2 and HgS2 nanoparticles……... 104

Table 5.1: Characteristic frequencies of PMMA in FTIR …….…… 125

LIST OF SCHEMES

Scheme 2.1: General synthetic routes for dithiocarbamate ligands…….. 40

Scheme 2.2: Synthesis of ammonium N-phenyldithiocarbamate……. 41

Scheme 2.3: Synthesis of ammonium N-methyl-N-phenyldithiocarbamate…… 41

Scheme 2.4: Synthesis of ammonium N-ethyl-N-phenyldithiocarbamate……... 42

Scheme 2.5: Proposed reaction for the synthesis of monomeric dithiocarbamate metal complexes, where R = CH_3 or C_2H_5 and M = Zn, Cd, or Hg…….. 43

Scheme 5.1: Preparative scheme showing reaction steps from dithiocarbamates ligands, metal complexes, HDA-capped nanoparticles and then MS/PMMA nanocomposites…… 128

ABBREVIATIONS

MS	Metal sulfide
SAFP	Science and Agriculture Foundation Programme
TEM	Transmission electron microscopy
et al	Et alia
LED	Light emitting diodes
Eg	Band gap
SSP	Single Source precursor
NMR	Nuclear magnetic resonance
SEM	Scanning electron microscopy
p-XRD	Powder X-ray diffraction
NPs	Nanoparticles
MMA	Methyl methacrylate
PMMA	Poly (methyl methacrylate)
QD	Quantum dot
HDA	Hexadecylamine
PL	Photoluminescence
ATR	Attenuated total reflectance
UV-Vis	Ultra violet-visible
FWHM	Full width half maxima
TOP	Trioctyl phosphine
etc.	Et cetera
i.e.	Id est.
PL	Photoluminescence
FTIR	Fourier transform infrared
XRD	X-ray diffraction
EDX	Energy dispersion X-ray
EMU	Electron Microscopy Unit
M.pt	Melting point
GMRDC	Govan Mbeki Research and Development Center
PVA	Polyvinyl alcohol
DMSO	Dimethylsulphoxide
DTG	Differential thermal gravimetric

ACKNOWLEDGEMENTS

Praise be to God the Almighty, master of times and circumstances for being God yesterday, today and forever in my life, without Him, all this would be impossible.

I am so grateful to my supervisor, Prof. P. A. Ajibade, for his guidance, patience and many good things he is doing in support of my educational progress and career such as allowing me to work under him in his resourceful inorganic research laboratory and giving a clear background and understanding about inorganic materials chemistry. I also appreciate his advices, motivation and suggestions he gave me during my hard and challenging times of this M.Sc Chemistry research study. I am still looking forward to work with him under his supervision.

I am grateful to Dr. Benjamin C. Ejelonu (former Post-Doc in our Inorganic Laboratory at the University of Fort Hare) for his helpful discussions, technical advices and support during my research experiments. Your laboratory skills are highly appreciated. A special thanks to academic and non-academic staff in the department of chemistry, University of Fort Hare for their general help and showing interest in my research work. In particular, special thanks to Mr. K. Tshapu and Mr. T. Mcako at the chemistry department for their assistance with analysis of samples using the FT-IR, XRD, DSC and TGA. Thanks to Miss N. C. Matyumza, Technical Officer at Electron Microscopy Unit (EMU) University of Fort Hare for capturing the SEM images and for EDX analysis of samples. I also acknowledge the support from my family, their endless love, carriage and passion for me to be somebody someday.

I wish to thank my manager at Science and Agriculture Foundation Programme (SAFP), University of Fort Hare Mr. P. M. Kwinana for allowing me to study while working for SAFP and I also appreciate his interest in my research work progress.

I highly appreciate the financial support by the NRF and DST Innovation Masters Scholarship and Govan Mbeki Research and Development Center (GMRDC), University of Fort Hare. Finally, I thank the University of Fort Hare for making available the materials and facilities for the completion of this work.

DECLARATION BY CANDIDATE

"I hereby declare that the dissertation submitted for M.Sc in Chemistry, at the University of Fort Hare, is my own original work and has not previously been submitted to any other institution of higher learning. I further declare that all sources cited or quoted are indicated and acknowledged by means of a comprehensive list of references".

04 November 2013_____ _____

Date J. Z. Mbese

CERTIFICATION

This is to certify that this dissertation is a record of original research carried out by Johannes Zanoxolo MBESE under my supervision at the Department of Chemistry, Faculty of Science and Agriculture, University of Fort Hare, South Africa.

_____ _____

Date Supervisor: Prof. P. A. Ajibade

B.Sc (Hons), MSc (Ibadan), PhD (UniZul), MRSC (UK)

DEDICATION

This study is dedicated to:

To my lovely family

For their endless

Love and support

ABSTRACT

The focus of this project was to synthesize and characterize metal sulfide nanoparticles /polymer nanocomposites. The work involved the synthesis of dithiocarbamato ligands and complexes derived from aniline. Zn(II), Cd(II) and Hg(II) dithiocarbamato complexes were used as single-molecule precursors for the synthesis of the ZnS, CdS and HgS nanoparticles and their optical and structural properties studied. The other focus of this work was to synthesize a combined functionality metal sulfide nanoparticles/polymer nanocomposites by dispersing as-synthesized ZnS, CdS and HgS nanoparticles in polymethyl methacrylate (PMMA) matrix.

The characterization of the ligands, complexes, nanoparticles and nanocomposites were investigated using relevant instrumental tools like UV-Vis, photoluminescence (PL), Fourier transform infrared (FTIR), X-ray diffraction (XRD), energy dispersion X-ray (EDX), nuclear magnetic resonance (NMR), scanning electron microscopy (SEM) and transmission electron microscopy (TEM).

CHAPTER ONE

1.0 INTRODUCTION AND LITERATURE REVIEW

1.1 Metal sulfide nanoparticles

The advancement of the methods of synthesis and tools of characterization of metal sulfide nanoparticles has promoted an intense growth in the study of nanoscience and nanotechnology in the fields of materials science and engineering [1-5]. In relation to these studies, the fundamental properties and their potential use in nanotechnological applications has stimulated interest and understanding of metal sulfide nanoparticles. Nanotechnology is the science and technology of materials having one of the dimensions less than 100 nm (1 nm = $1x10^{-9}$ m). Nanotechnology involves the control and manipulation of matter at the manometer scale to produce new class of materials with novel structural properties and creating new devices. Nanoscience is the study of phenomena and manipulation of materials at atomic, molecular and micromolecular scales, where properties differ significantly from those at a larger scale [6-11]. Nanomaterials and nanostructures with dimensions that range from 1 to 100 nm, often exhibit novel and significantly changed physical, chemical and biological properties [12]. Figure 1.1, below shows micro-nano length scale of nanomaterials in comparison to various biological components ranging from 1mm to 0.1 nm.

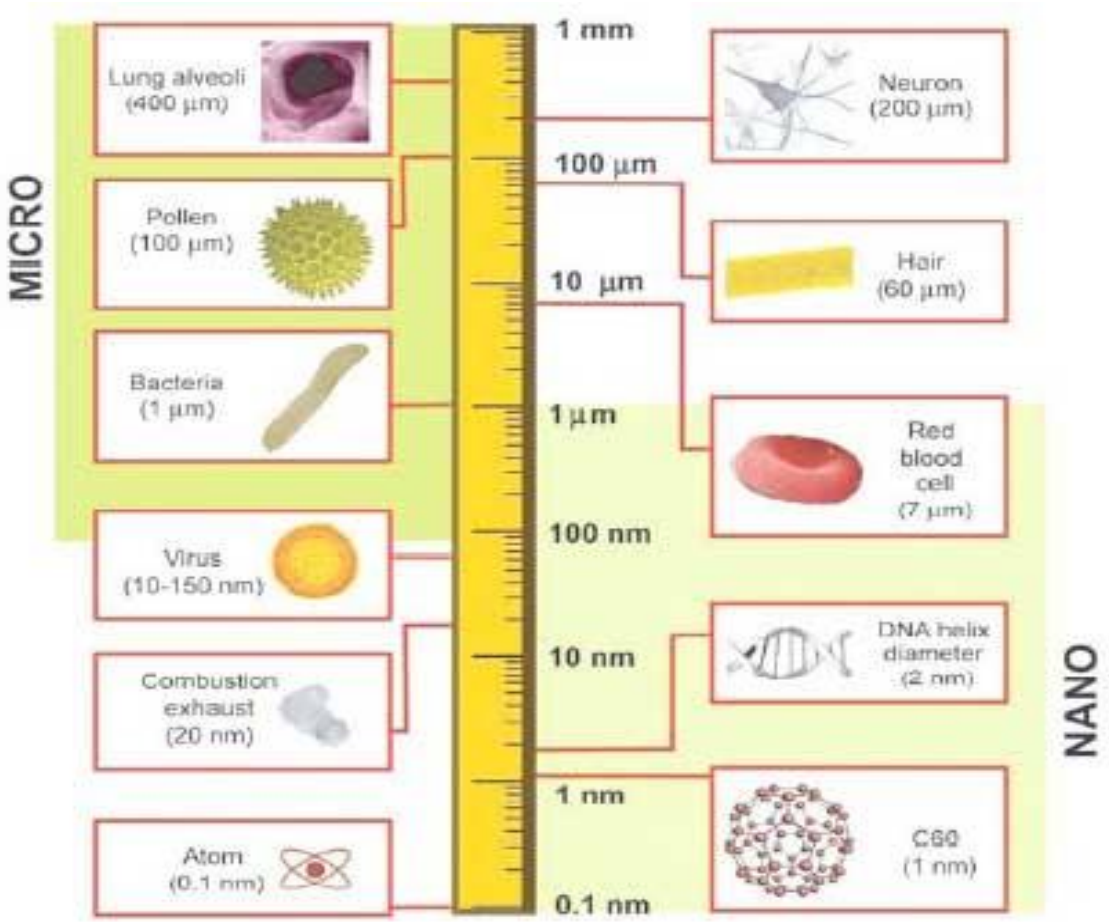

Figure 1.1: Length scale showing size of nanomaterials in comparison to various biological components [12]

The size of these particles varies between 1 nm to several microns, and they can therefore be classified as either nanoparticles (any dimension smaller than 1 micron) or microparticles (all dimensions larger than one micron). The term nanoparticles typically refer to materials in which all three dimensions are in the nanoscale range of 1-100 nm and is a basic unit of nanoworld. The production of high quality semiconductor nanoparticles of dimension ranging from 1-20 nm becomes so important because of their unusual properties. In this study, the term nanoparticles or nanomaterials will refer to purposefully created, engineered particles with at least one dimension between 1 and 100 nanometers.

1.2 Particle size

Size is the most general characteristics of nanomaterials, as evidenced from the name itself. All existing definitions of nanomaterials include size, requiring at least one of the dimensions of nanomaterials to be on the order of 1-100 nm. Roduner [13], discussed surface effects and quantum size effects as the main reasons why nanomaterials show properties so different from those of the bulk. The example in Table 1.1 below compares gold as bulk and gold as nanoparticles. This example depicts that physical, chemical, electronic and optical property of materials at nano-scale deviate substantially from those of bulk materials. The control of size of nanomaterials to improve their properties has been a challenge to the field of materials chemistry [14].

Table 1.1: Comparisons of properties between gold as bulk and gold as nanoparticles [15]

Bulk Gold	**Gold as nanoparticles**
	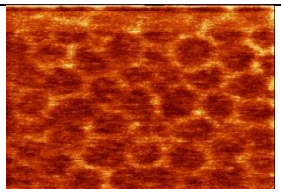
Shiny	Varies in appearance depending on size and shape of cluster
Always gold in colour	Never gold in colour, found in range of colours
Inert	A very good catalyst
Conducts electricity	Not a conductor but a semiconductor

Since the colour of gold nanoparticles differs from that of bulk gold, as indicated in the Table above, there was some confusion about the nature of the nanoparticles for a long time, until Faradays in 1774 found that bulk gold contained extremely small gold particles [16].

1.3 Metal sulfide nanoparticles and nanocomposites synthetic techniques

Numerous synthetic routes have been designed and employed for the synthesis of metal sulfide nanoparticles (ZnS, CdS, CuS, ZnSe, CdSe, HgS, etc) over a range of composition, size and shapes [17]. The systematic manipulations of shapes and sizes of inorganic compounds greatly benefit the various application fields including optics, magnetic, electronics, catalysis and medicine.

However, shape control has been much more difficult to achieve. Hence, exploration of novel method for the preparation of differently shaped nanoparticles is challenging research area [18]. Regardless of the technique, the goal of nanoparticle synthesis generally focuses on:

- minimizing and controlling particle size,
- maintaining a narrow size distribution,
- control of particle morphology, and
- Control of crystallinity.

The ability to control size enables the variation of particle properties, while the narrow size distribution allows greater precision and is required for studies of size-dependent effects. Particle shape and crystal structure can also influence material properties. Sol-gel method, microemulsion, hydrothermal or solvothermal synthesis, polymer matrix and single source molecular precursor method are among the synthetic techniques for nanoparticles. These synthetic techniques are discussed below:

1.3.1 Sol-Gel method

The sol-gel process is a wet-chemical technique also known as chemical solution deposition, widely used recently in the fields of materials science and ceramic engineering. Such

methods are used primarily for the synthesis of materials starting from a chemical solution (*sol*, short for solution) which acts as the precursor for an integrated network (or *gel*) of either discrete particles or network polymers [19]. The sol-gel method is a useful and attractive technique for the preparation of nanosized particles because of its advantages such as good stoichiometric control and the production of ultrafine particles with a narrow size distribution in a relatively short processing time at lower temperatures [20]. The size of particles depends on several parameters in sol-gel method. Those parameters include dilution of the solutions, concentration of the solution and annealing temperature of the dried gel [21]. Figure 1.2 shows the numerous methods employed in sol-gel process.

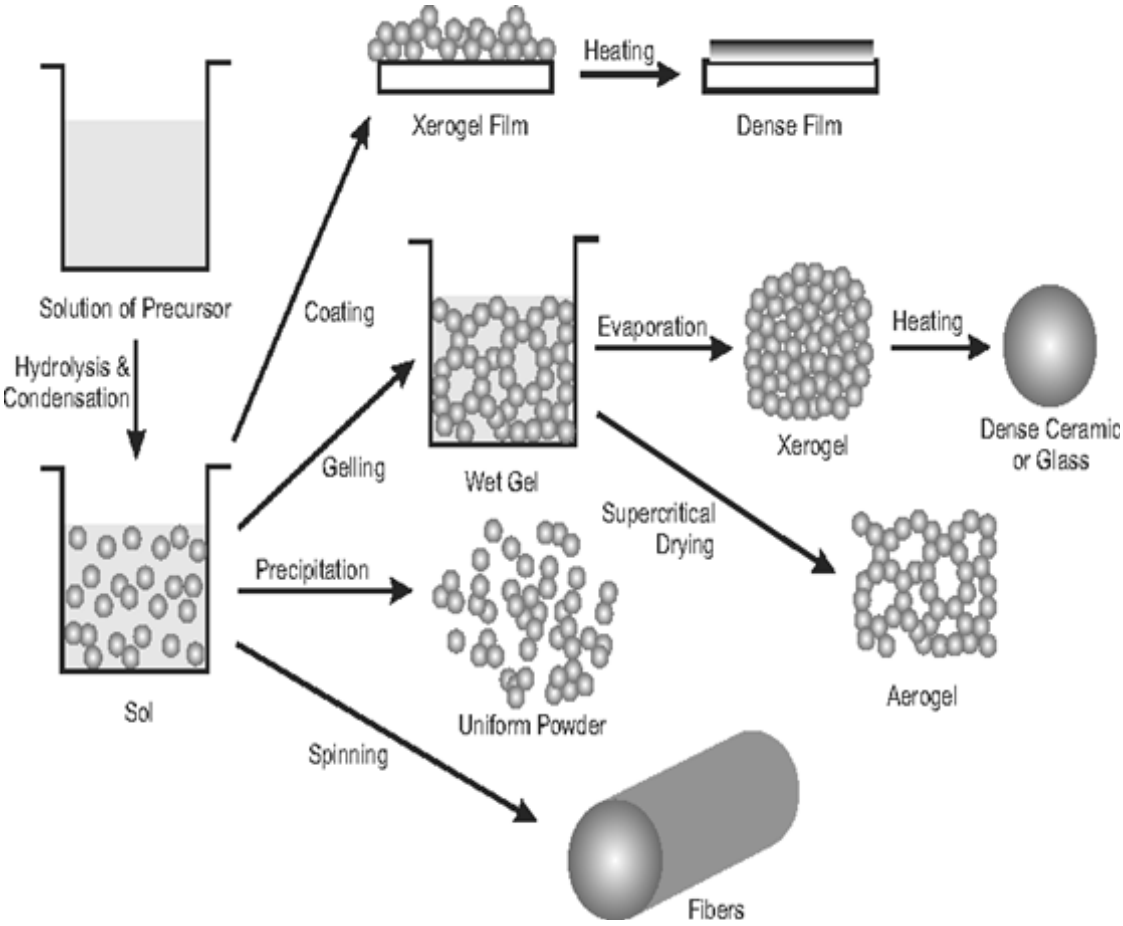

Figure 1.2: Numerous routes in the sol-gel process to control the morphology of the product [22]

In general, the precursor or starting compound is either an inorganic (no carbon) metal salt (chloride, nitrate and sulfate) or a metal organic compound such as an alkoxide. Metal alkoxides are the most widely used precursors, because they react readily with water and are known for many metals. Although sol-gel process is used mainly for the synthesis of composite in matrix that forms a gel like silica, some semiconductor nanoparticles have also been synthesized by this method [23, 24]. This method has been employed for the synthesis of copper/copper oxide in silica matrix [25-27]. There is some reference to synthesis of polypyyrole/iron oxide nanoparticles [28] and CdSe/CdS core shell nanoparticles by this method [29]. Recently, more attention has been paid on the sol-gel process due to the very low temperature involved in the synthesis. The sol-gel process is simple, cost-effective and suitable for scale-up. Sol-gel technique gives particles with broad size distribution and high concentration of defects that its usage [30].

1.3.2 Microemulsions

A microemulsion is a thermodynamically stable dispersion of two immiscible fluids that could be oil, water and surfactant. Recently, group II-IV semiconductor nanostructure materials of ZnS nanoparticles and ZnS/PMMA nanocomposites have been synthesized by this method to produce ultrafine and monodisperse nanoparticles [31]. Russell *et al* studied the size selective adsorption of nanoparticles at the oil-water interface by varying fluorescent CdSe quantum dots [32]. Initially smaller size CdSe nanoparticles (~2.8 nm, green fluorescence) were used to stabilize water-in-oil type emulsion. Later, they introduced larger size CdSe nanoparticles (~4.6 nm, red fluorescence) to the toluene phase. As a result, larger CdSe nanoparticles assembled on the surface of existing stabilized droplets, displacing the smaller 2.8 nm NPs (Figure 1.3). Some advantages of this process are easy control of the quantum dot size by changing the molar ratio of water to surfactant, a narrow distribution of

size as compared to the sol gel process, and ease of dispersion of the quantum dots. Some disadvantages include low yield and incorporation of impurities and defects.

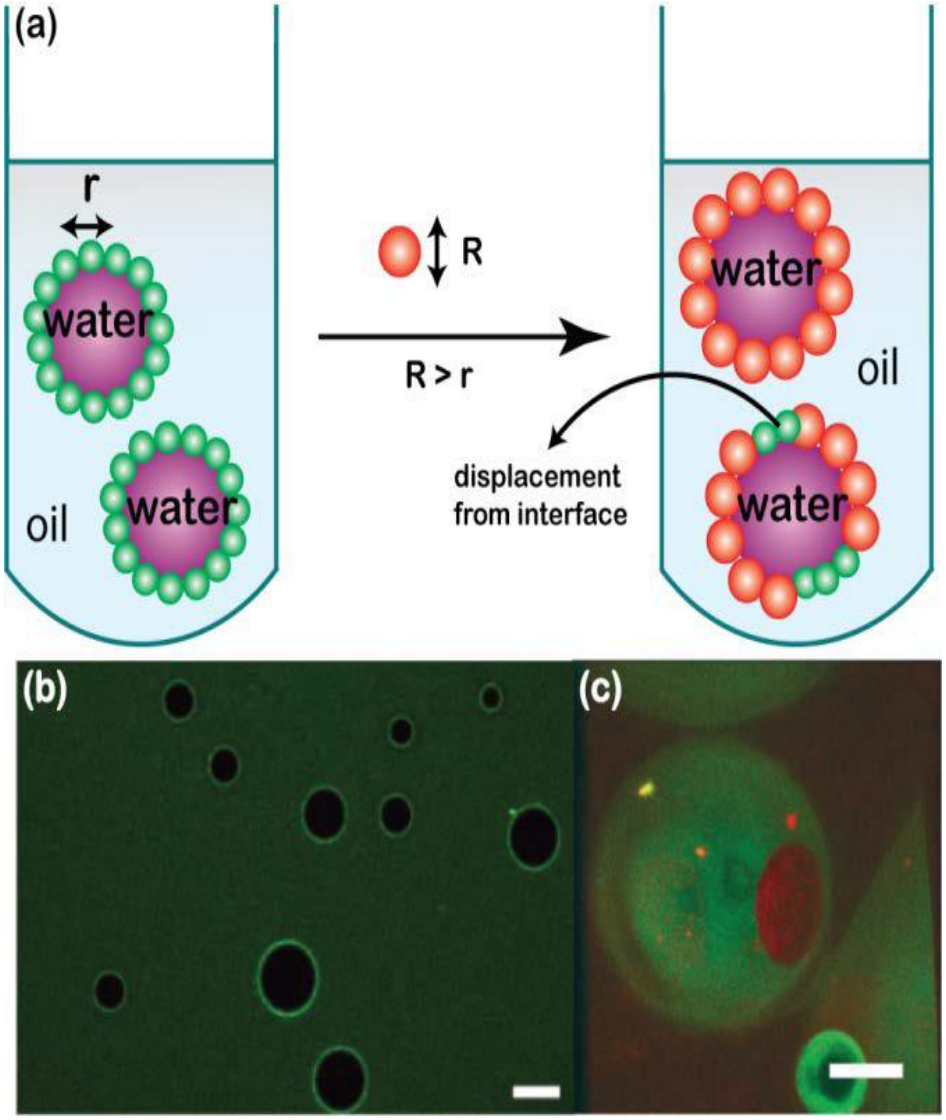

Figure 1.3: Demonstrations (a) Schematic of size selective displacement from interface. (b) Confocal microscopy images of 2.8 nm CdSe stabilized droplets (c) Droplets after addition of 4.6 nm CdSe NPs. Scale Bar, 20 µm [32]

The composition of a ternary water/surfactant/oil microemulsion is completely defined by two parameters: The surfactant molar concentration and the molar ratio between water and

surfactant (W_0). A three component system is usually represented by a triangular phase diagram if the temperature is kept constant (Figure 1.4).

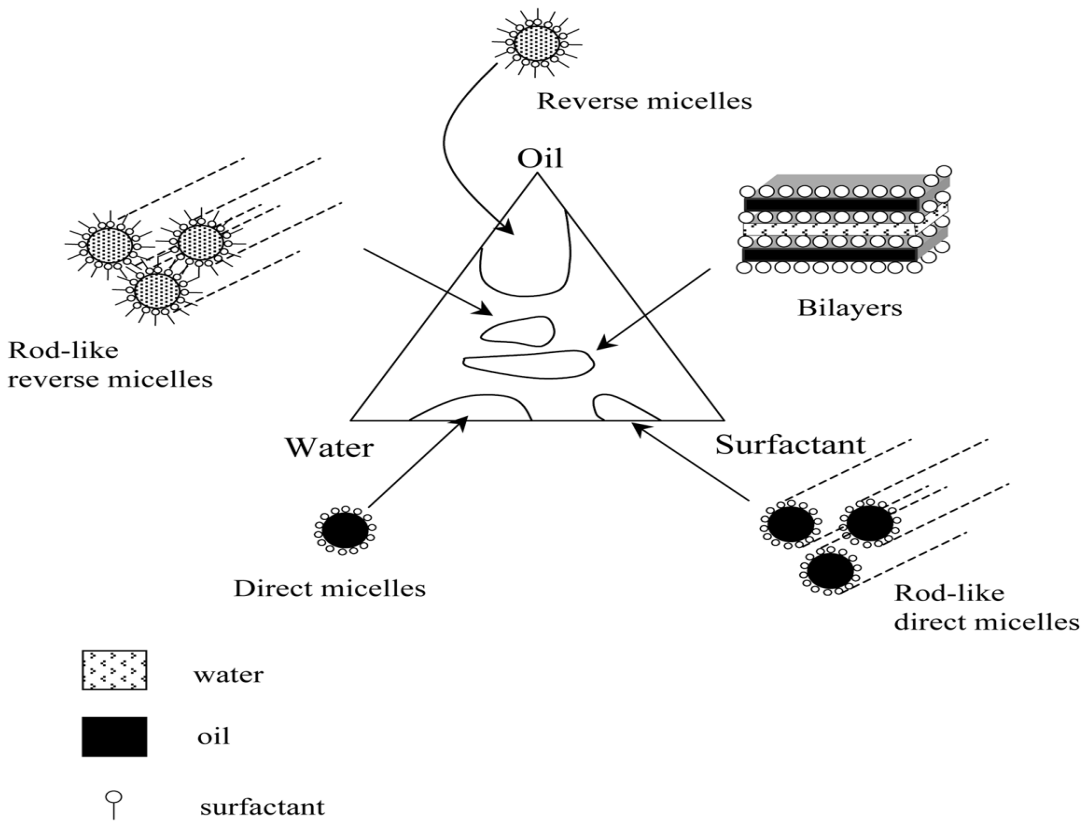

Figure1.4: Triangular diagram for a water/surfactant/oil system showing various amphiphilic aggregates are shown [33]

If the concentration of the surfactant is high enough, at every water/oil ratio the system forms a single phase. On the water-rich region of the phase diagram, direct micelles are formed: Oil droplets are dispersed in the water medium and stabilized by a surfactant film (L_1, or 'oil-in-water microemulsion'). On the oil-rich side of the phase diagram, reverse micelles are formed: In this case, water droplets are dispersed in the oil medium and again are stabilized by a surfactant film (L_2, or 'water-in-oil microemulsion'). In the intermediate region, bicontinuous structures are possible: In certain cases, at these conditions a liquid crystalline phase can form (lamellar phase, L_α) [33].

1.3.3 Hydrothermal or solvothermal synthesis

Hydrothermal technique is used when preparing nanoparticles with hollow structure in which temperature and pH has significant role. ZnO nanoparticles which has many important applications in photelectrode, solar cells, and nanolasers, because of its wide band gap and large excitation binding energy of 60 meV has been synthesized in this method [34]. Different nanostructures including nanowires, nanorods, nanotubes, nanoribbons, nanoneedles, nanocables, tetrapods, comb-like structures can be prepared from ZnO and these new structures have wide application in different areas [34]. For example, Aditya and Mallick [35] synthesized ZnO nanostructures using hydrothermal route, in a typical experiment zinc acetate was slowly added to an aqueous solution of triethanolamine to reach the desirable pH referred to as the initial pH 9. Then, potassium hydroxide was added to the solution pH to a certain value referred to as the final pH 10. The resultant solution was heated at certain temperature (100 °C), from which ZnO hollow particles are prepared. Conventional stirring results in the formation of highly agglomerated nanoparticles, while uniform nanospheres are formed during hydrothermal synthesis.

They found that the formation of ZnO nanostructures is due to the decomposition of amine-based zinc complex in basic media, the solution pH during the formation and decomposition of the zinc complex has an important influence on the morphology of ZnO nanostructures. For typical zinc complex formed at pH 8, decomposition at pH 10 results in the formation of ZnO nanoparticles consisted of tinier nanocrystals. Since the decomposition pH controls the rate of ZnO formation, it affects the size but not the shape of nanostructures. For higher pH just the nucleation rate increases to avoid continuous growth of the particles to achieve larger sizes. Whereas the initial pH affects the nature of the zinc complex generated, generation of zinc complex at pH 9 leads to the formation of hollow nanospheres.

Solvothermal route is very simple method that can be used to fabricate hollow spheres, without using toxic reagents such as H_2S, or special device and significant energy input. The first solvothermal syntheses were carried out by Robert Wilhelm Bunsen (1811-1899) in 1839 at the University of Marburg. Bunsen grew barium carbonate and strontium carbonate at temperatures above 200 ^{o}C and pressures above 100 bar [36]. In this method, a solution is prepared by using required reactants, and then the product is heated and dried to get hollow particles. The present process also provides a mild and effective route for the production of CdS nanowires/polymer composite films, which might be used in the fabrication of novel optical and electronic devices. This method has been reported elsewhere [36], where a polymer-controlled growth strategy was used to prepare CdS nanowires/polymer composite films based by using ethylenediamine as the reaction medium and polyvinyl alcohol (PVA) as the polymer-controller matrix. The CdS nanowires dispersed in the PVA matrix show larger aspect ratios compared with the sample prepared without PVA.

1.3.4 Single source precursors method

Single-source precursor method has been demonstrated as a versatile, relatively simple and efficient route for the synthesis of crystalline semiconductor nanoparticles [37]. Various chalcogenides metal complexes of dithio/diselenocarbamates, xanthates, thioureas, and thiosemicarbazides have been successfully used as single-source precursors for the synthesis of II/VI semiconductor nanoparticles. The literature that reported the initial work on the use of metal complexes has been known since 1815 when Zeise prepared xanthates of potassium, barium, lead and copper [38]. A number of studies have been reported on the use of metal complexes as a single source precursor. For example, Ajibade and Onwudiwe [39] synthesized group 12 complexes of mixed alkyl-phenyl dithiocarbamate to prepare ZnS, CdS,

and HgS semiconductor nanoparticles. Thermogravimetric analysis showed that the complexes decomposed sharply to form their respective metal sulfides.

However, the general synthetic scheme remains the same: A solution containing molecular precursors (metal complexes) is injected into a flask where a coordinating solvent is heated at high temperatures (up to 300 ^{o}C or higher). The reaction is carried out under a moderate flow of an inert gas (nitrogen or argon). By coordinating solvent or surfactant, we mean a species that can coordinate the surface of the nanocrystals during their growth. These molecules must be stable at the high temperatures required for the growth. They are usually compounds containing phosphorus or nitrogen based coordinating groups. Some examples are long alkyl chains phosphines, phosphine oxides, phosphates, phosphonates, amides or amines, nitrogen-containing aromatics, but also carboxylic acids, and so on. The choice of the surfactant (or the mixture of surfactants) depends on the particular reaction.

Surfactants that coordinate too strongly to one or more of the atoms that will be part of the crystal are not suitable, as they would not allow particles to grow. On the other hand, a weak coordinating surfactant would produce large particles, as well as aggregation effects. In addition, bulky surfactants limit growth, to produce small particles, whereas less bulky surfactants lead to bigger particles. The precursors are introduced either in elemental form (i.e. Se) or as metal-organic compounds. They are usually dissolved in a high boiling point solvent, like an alkyl phosphine.

Shen and co-workers [40] used metal diethyldithiocarbamate complex as single source precursor and oleic acid and oleyamine as surfactants, for the synthesis of metal sulfides of zero-dimensional (0-D) Ag_2S, ZnS and CdS QDs, one-dimentional (1-D) CdS nanorods and

ZnS ultrathin nanowires, two-dimensional (2-D) SnS nanosheets, Bi_2S3 and Fe_7S_8 nanoplates. These metal sulfide nanocrystals had well-defined morphology and their chemical composition exhibited excellent optical, electronic and magnetic properties, showing a potential for a wide range applications. Metal dialkyldithiophosphates has been reported as excellent single source precursors to synthesize several kinds of high-quality metal sulfide nanomaterials such as CdS, CuS, Bi_2S_3 and Sb_2S_3 [41]. High-quality PbS and CdS nanowires have been synthesized by this method [42]. In a typical synthesis of PbS nanowires, $[Pb(S_2CNEt_2)_2]$ was first dissolved in phenyl ether with warming, and combined with a tri-n-octylphosphine (TOP) solution of Bi catalyst nanoparticles. The mixture was then rapidly injected into a pre-heated tri-n-octylphosphine oxide (TOPO) solvent or TOPO/TOP mixed solvent at a desired temperature (in the range of 210-300 ^{o}C), held at this temperature for 5 min, and allowed to cool.

Many semiconductor/polymer nanocomposites like CdS/polyvinyl alcohol, CdS/N-polyvinylcarbazole and CdS/polystyrene have been synthesized using various methods [43]. However, there are no reports in the literature where a single source precursor method is used to synthesize its semiconductor nanoparticles in polymer matrix. Incorporation of semiconductor nanocrystals into polymer matrix has recently attracted considerable interest because polymer matrix provides processability, flexibility and transparency, the semiconductor nanocrystals contribute to the desired optical properties [44]. The interplay between polymer chemistry and quantum dot synthesis has become more important. Biryukov and co-workers [45] presented the results of investigations into the optical properties of semiconductor quantum dots (including absorption, fluorescence, and nonlinear scattering) in CdS/MMA dispersions and CdS/PMMA composites prepared by one-step in a monomer medium. It was demonstrated that selective optical excitation during synthesis of

CdS nanoparticles in the monomer medium allows the particle sizes to be controlled. It was also demonstrated that changes of the sulfur/cadmium ratio in the reaction mixture influence significantly the fluorescent properties of particles. Nonlinear scattering of the synthesized media was investigated, and revealed that scattering in optically homogeneous composites was much weaker than in dispersions where agglomerates with sizes up to 100 nm were presented.

He *et al* [46] reported the synthesis of CdS/poly(vinyl-carbazole) (PVK) nanocomposites via an in situ microwave irradiation method. In this system, pyridine was used as reaction solvent. Evidence was presented that the formation of semiconductor and the polymerization of the monomer were simultaneous. The product was characterized by FT-IR, X-ray diffraction (XRD) and transmission electron microscopy (TEM). The photoluminescence property of the product was also studied. There is a report on the use of electrospinning technique to fabricate poly(methyl methacrylate) (PMMA) fibres incorporating CdS and CdSe nanoparticles [47]. In this report different nanoparticle loadings (0, 1, 3, 5, 7 and 10 wt% with respect to PMMA) were used and the effect of the quantum dots on the properties of the fibres were reported.

1.4 Properties of metal sulfide nanoparticles

The optical properties is one of the most fascinating and useful aspects of nanomaterials and depend on parameters such as size, shape, surface characteristics, and other variables including doping and interaction with the surrounding environment or other nanostructures [48-50]. The study of nonlinear optical properties of semiconductor quantum dots, or nanoparticles with dimensions close to the Bohr radius of the electron-hole pair are of recent interest, due to their possible application in future high-capacity communication networks, optoelectronics and photonic devices [51,52]. This interest is stimulated by remarkably

different optical properties when semiconductor sizes are decreased from bulk to a few nanometers as predicted by quantum confinement theory. It has been demonstrated (Figure 1.5) that the linear optical properties of semiconductor nanoparticles depend strongly upon particle size, for example, the blue shift of excitonic absorption and emission peaks with decreasing particle size [39, 53].

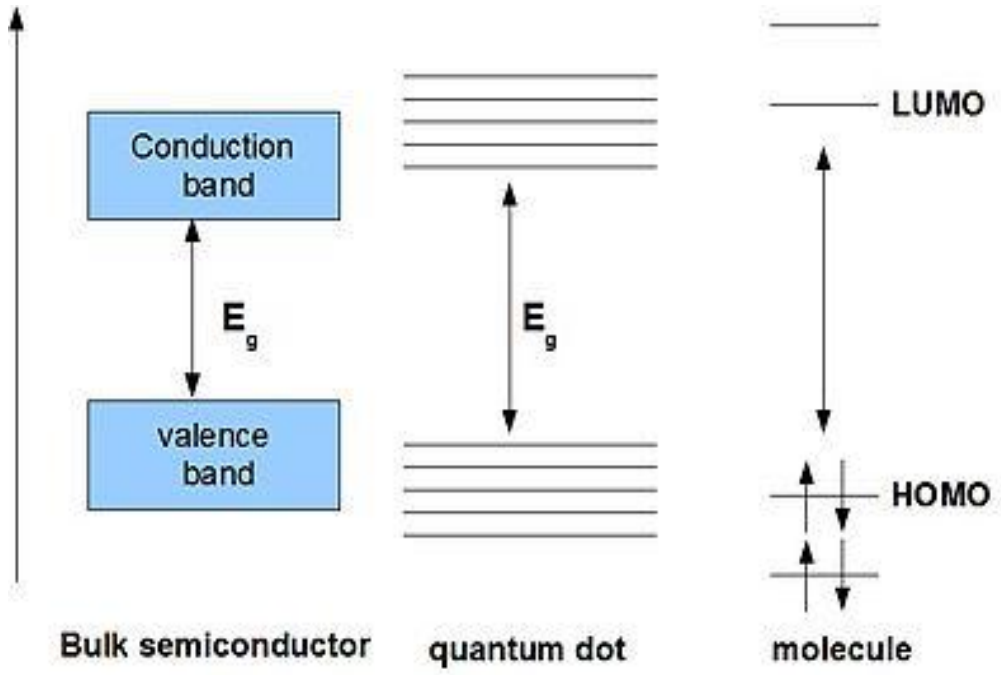

Figure 1.5: Schematic energy diagrams illustrating the situation for a nanoparticle, in between a molecule and a bulk semiconductor

The simplest example is the well-known blue-shift of absorption and photoluminescence spectra of semiconductor nanoparticles with decreasing particle size, particularly when the size is small enough. At smaller nanoparticle sizes, the energy band gap increases and the optical spectrum is shifted toward the short wavelength region. Photoluminescence in solids is a process in which luminescence is stimulated by the interaction of photons (electromagnetic radiation) with a material. The process is divided into two major types,

namely intrinsic and extrinsic photoluminescence. Intrinsic photoluminescence is observed in materials which contain no impurity atoms. Extrinsic photoluminescence is caused by intentionally incorporated impurities and in most cases metallic impurities or defects [54, 55].

1.5 Potential applications of nanomaterials

Nanomaterials are useful in fields such materials science, technology and engineering. Some applications of nanomaterials are discussed below.

1.5.1 Sensors

Many kinds of materials such as polymers, semiconductors, carbon graphites and organic/inorganic composites have been used as sensing materials to detect the targeted gases based on various sensing techniques and principles [56]. The application of semiconductor nanocrystals, or quantum dots, as biochemical sensors has been reviewed [57]. It was found that optical fiber technology can introduce some interesting features in optical sensing applications and some of the most important are real-time remote detection, miniaturization, immunity to electromagnetic interference and multiplexing ability. Zinc oxide (ZnO) is a versatile material with wide band-gap that found application in chemical sensors [58]. CdS has been studied due to its potential technological applications in environmental and biological sensors [59, 60]. Due to their luminescence and nonlinear optical properties, quantum size effect, and other excellent physical and chemical properties, nanocrystalline semiconductors of group II-VI, are useful in gas and UV sensors [61]. The doped ZnS semiconductor materials have a wide range of applications in optical sensors [50]. Alexandrescu and co-workers [30] prepared metal-based nanocomposites containing $Fe(CO)_5$ and methyl methacrylate (MMA) by applying the one-step laser pyrolysis to gas mixtures. The nanocomposite was tested for acting as gas sensor by variation of the electrical resistance in the presence of NO_2, CO, and CO_2. Preliminary results show that at higher laser power

density they exhibit rather high sensitivity towards NO_2 detection and NO_2 selectivity relative to CO and CO_2.

1.5.2 Solar cell

CdS is used as window material for hetero junction solar cells to avoid the recombination of photogenerated carriers which improves the solar cells efficiency [59]. CdS is used in solar cell systems as an important semiconductor and CdS films have demonstrated to be effective in most applications [60]. Polymer/nanoparticle composite films are used in different fields of technology such as solar cell device [62, 63]. Most recently, Yu *et al* [1] prepared $SnSe_2$ quantum dot sensitized solar cells by employing molecular metal chalcogenide as precursors. The $SnSe_2$ sensitized TiO_2 solar cells was found to have powerful conversion efficiency. Nanocrystal based solar cells have been demonstrated as a possible next generation lower-cost alternative to traditional silicon based solar cells [64]. Polycrystalline thin-film solar cells such as CdTe/CdS require p-type absorber layer (CdTe) of optimum optoelectronic properties and n-type wide-band gap partner layers to form the p-n junction [65]. Currently, CdTe/CdS thin film solar cells hold a record of 16.5 % energy conversion efficiency compared to the maximum theoretical efficiency reported for CdTe solar cells is 29% and the reported band offsets at CdTe/CdS heterojunctions fall into a wide range of 0.58-119 eV [66].

1.5.3 Catalysis

The use of chalcogenides as organocatalysts was resently reviewed by McGarrigle *et al* [67]. Nanostructured TiO_2 and ZnO have been prepared and tested as effective catalysts in the degradation of organic targets activated by light showing higher photocatalytic efficiency than their commercial counterpart. The synthesis of CdS nanocrystals with tailored optical properties has been reported [68] and may find use in heterogeneous photocatalysis. Mercury sulfide (HgS) is a promising material for catalysts and infrared detectors when coated with

Rh or used alone. Materials with hollow nanostructure have larger surface area compared to other morphologies with the same mass, which make it more applicable for catalysis or infrared absorption. However, compared with other semiconductors, the report of hollow sphere of HgS is relatively limited but, a novel and simple solution approach was developed to fabricate hollow nanospheres of cubic HgS [69].

1.5.4 Lasers

Semiconductor lasers are said to be "the laser of the future" because they are compact, have the potential for mass production, can be easily integrated, their properties can be improved easily, and are becoming more powerful and efficient [70]. The majority of semiconductor materials are based on a combination of elements in group 13 of the periodic table (such as Al, Ga, In) and group 15 (such as N, P, As, Sb) hence referred to as the III-V compounds [71-73].

1.5.5 Light emitting diodes

Incorporation of semiconductor nanocrystals into polymer matrix has recently attracted considerable interest and has wide applications in diverse areas such as light-emitting devices (LEDs), mainly due to the unique properties of semiconductor nanocrystals and polymer [74]. While the polymer matrix provides processability, flexibility and transparency, the semiconductor nanocrystals contribute to the desired optical properties. Interest in conducting polymers has its origins in the possible commercial applications of these materials. The commercial applications are based on the promise of a novel combination of light weight, processibility and electrical conductivity. Some conducting polymer can change their optical properties on applications of current or voltage and therefore may find useful applications as heat shutter and light emitting diodes (LEDs) [75-77]. Other nano materials in light emitting devices which are used in the communication sector are GaN, GaAlAs, GaAs,

InGaAsP, and GaP, AlAs [78, 79]. Liquid Crystals as well as having applications in displays have potential applications for improving switching speeds in telecoms by replacement of silicon. They also have potential as photonic materials leading to improved optical materials with higher resolution. Light emitting diodes continue to develop and underpin many applications-laptops, mobile phones, etc. Constant advances are being made in low power-consumption devices and displays.

Further to this, development of non-display applications is becoming increasingly important in lasing and photonics, telecoms, biology/medicine, control of microwaves. Cyanophenyl materials, fluorinated tolans, biological membranes, phospholipids and the protein solution that is extruded by the spider to generate silk is a liquid crystal phase [80-84]. Song and Lee [85] synthesized (CdSe)ZnS quantum dot QD-PMMA polymer composite and fabricated QD-polymer composite films after producing the CdSe and (CdSe)ZnS QDs by direct colloidal chemical synthesis and the surface-passivation method. Green or red light emitting (CdSe)ZnS QD-PMMA polymer composite film by combining the green or red light emitting (CdSe)ZnS dots with PMMA of high optical transparency in the visible region and spin-coating the composite solution. These studies revealed that a white light emitting device can be fabricated by combining our green/red light emitting QD-polymer composites with a blue LED as an excitation source.

1.5.6 Biological labelling

Highly luminescent II–VI semiconductor nanoparticles have attracted much attention because of their various applications in areas such as biological labelling [86]. Quality of nanoparticles and core-shell particles is quite good and such particles would be useful for biological labelling [87]. Cadmium based nanocrystals, CdS, CdSe, CdTe have also been

explored for a variety of applications including light-emitting diodes, lasers and biological labelling [88]. Their size-dependant narrow emission spectrum paired with a broad absorption allows for multiplexed detection with a single excitation light source, rendering quantum dots an attractive system for simultaneous labelling of different target molecules or cellular structures in biology.

1.5.7 Other applications

The semiconductor nanoparticles or nanofiber templates when used as sensors in environmental applications are also gaining prominence [55-59]. Most pollutants in water exist in small concentrations. These trace contaminants, such as pharmaceuticals, cosmetics, hormones are potential carcinogens and can cause other health problems when present in water [89].Their detection is often difficult to achieve, because they occur in parts per billion concentrations. Nanofiber based membranes (Figure 1.6) are now also offering potential means of detecting these compounds in water.

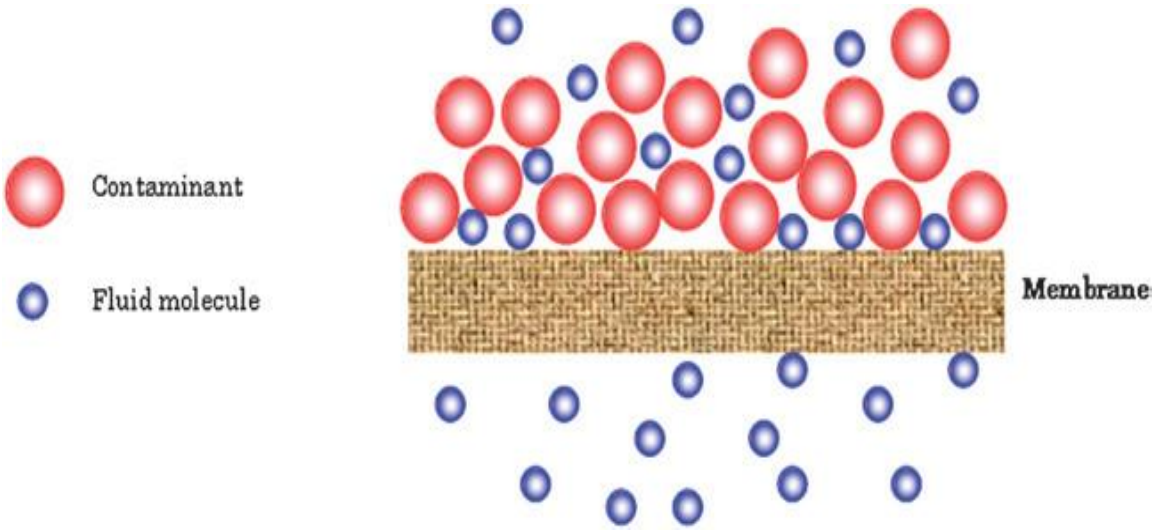

Figure 1.6: Schematic of filtration system where a nanofiber membrane is allowed to separate the containment from the fluid [89]

The membrane technologies still remain as one of the solutions for remediation of environmental problems such as water and air treatment. There are numerous reports on preparation of polymer nanofibers containing metal nanoparticles. The nanosized structure of electrospun fibre web has intrinsic properties which are suitable for various applications. The small fibre diameter, small pore size, and high surface area of the nanofibre web are properties that are advantageous for filtration applications. Electrospun nanofibres can be used as an effective layer in composite filter media. Jin *et al* [88] used electrospinning process (Figure 1.7) to prepare polymer nanofibers containing Ag nanoparticles. In this process poly(N-vinylpyrrolidone) (PVP) and poly(vinyl alcohol) (PVA) polymer solutions were used separately to prepare polymer nanofibers containing Ag nanoparticles. The resulting polymer nanofibers were found to exhibit the distinctive optical, electrical, catalytic, or antimicrobial properties of metal nanoparticles.

Electrospinning of materials involves the application of a strong electric field to a droplet of a fluid, such as a melt or blend solution. The set up mainly consists of a spinneret, collector and high voltage power supply. A potential (in kV) is applied between the spinneret and a collector; both are electrically conducting and separated at an optimum distance between the two. The interactions of the electrical charges in the polymer fluid with the external electric field causes the pendant droplet to deform into a conical structure called the Taylor cone and a critical voltage is attained.

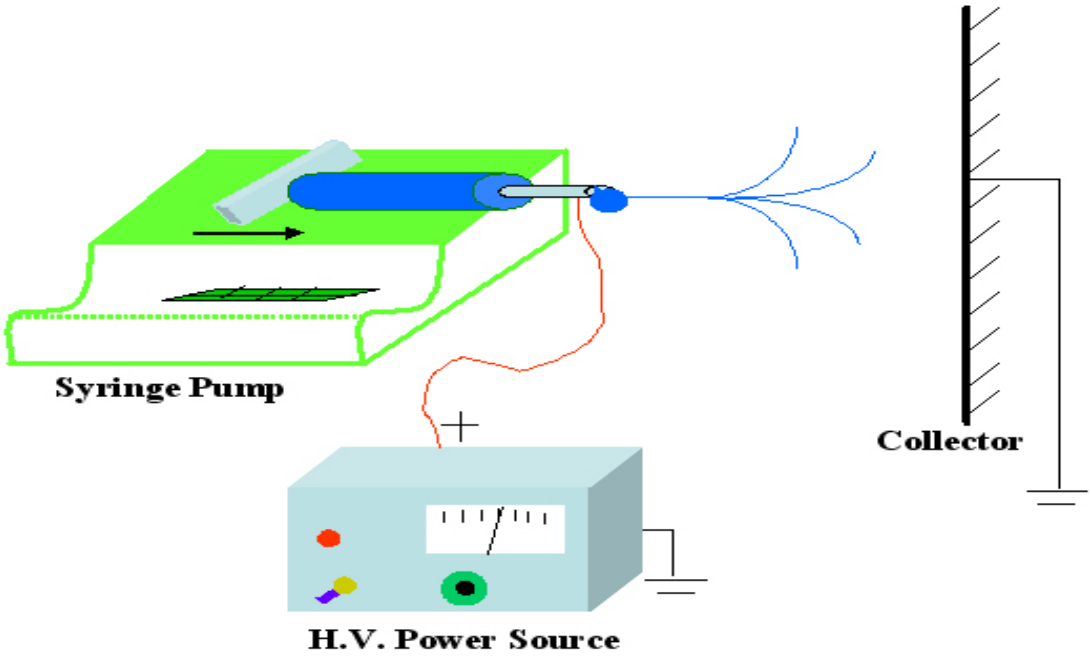

Figure 1.7: A schematic of electrospinning process [56]

When the applied voltage surpasses the critical value at which repulsive electrostatic forces overcome the surface tension, a fine charged jet is ejected from the tip of the Taylor cone [56]. These charged jets undergo a whipping motion and elongate continuously *via* electrostatic repulsion until they are deposited onto a grounded collector; resulting in the formation of fine fibers. Instability can occur if the applied external electrostatic field is not above the critical value, which would cause the jet to break up into droplets. Such phenomenon is called Rayleigh instability. Therefore, the formation of nanofibers is a function of operating parameters such as applied voltage, solution feeding rate and solution properties, mainly conductivity, viscosity and surface tension. Consequently, these electrospinning process parameters can be tuned to produce a wide range of fiber diameters. Fibres produced by electrospinning have high surface area and have found application in nanocatalysis, tissue scaffolds, filtration and optical electronics [47]. The small fibre diameters that enable the slip-flow effect advantageous for filtration are easily achievable with the electrospinning method [89].

1.6 Chemistry of some selected dithiocarbamate compounds

The chemistry of dithiocarbamate ligands has received much attention due to its ability to stabilize transition metals in a variety of oxidation states [90]. Apart from its technological applications such as accelerators in vulcanization, high pressure lubricants, pesticides and fungicides in agriculture [91, 92] , its use in the preparation of dithiocarbamate metal complexes and then semiconducting nanoparticles has drawn more attention to the field of material sciences, technology and engineering [93, 94]. Dithiocarbamates belong to a class of compounds called 1,1-dithiolates. This group of compounds also includes the dithiophosphates, dithiosphinates, dithiocarbamates and other related compounds (Table 1.2).

Table 1.2: Major types of 1,1-dithiolates [95]

Composition	**Structure**	**Name**
$R_2NCS_2^-$	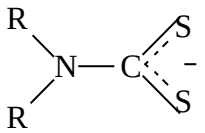	dithiocarbamates
OCS_2^{2-}	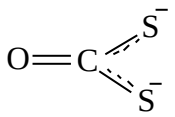	dithiocarbonate
CS_3^{2-}	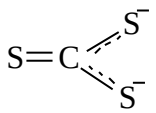	trithiocarbonate
RCS_2^-	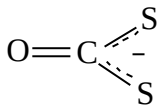	dithiocarboxylate
$ROCS_2^-$	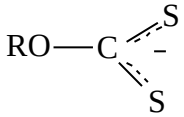	xanthate
$(RO)_2PS_2^-$	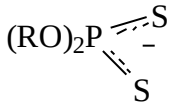	dithiophosphate

$R_2PS_2^-$	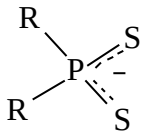	dithiophosphinate
RCS_3^-	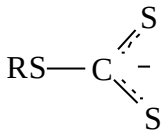	thioxanthate
$RNCS_2^{2-}$	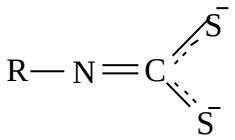	dithiocarbimate

The dithiocarbamate ligands tend to form complexes with metal ions having partly filled d orbitals, or ions with d orbitals. They form complexes with the elements from Ti to Se (except Ge), Nb to Te and W to Bi [96]. The dithiocarbamate ligands generally form insoluble complexes in water but soluble in organic solvents such as toluene or chloroform. A number of dithiocarbamate ligands have been synthesized and used in the preparation of dithiocarbamate metal complexes single molecular precursors for metal sulfide nanoparticles synthesis [97-102].

1.6.1 Zn(II), Cd(II) and Hg(II) complexes

Zn(II), Cd(II) and Hg(II) complexes have d^{10} electronic configuration meaning that they are not dependent on specific coordination geometry, the geometry can instead accommodate the charge and size of the ligands. Tetrahedral coordination preferred over octahedral (Oh) because tetrahedral (Td) Zn, Cd and Hg are a stronger Lewis acid than octahedral (Oh) would be. The d^{10} Electronic configuration like Zn^{2+}, Cd^{2+} and Hg^{2+} absorb strongly in the ultraviolet region and yield broad emission bands mainly in the ultraviolet and blue-green spectra area depending on matrix composition [103-106]. Dithiocarbamates and their complexes with transition metals have been used as common pesticides, vulcanizing or

analytical agents for decades [107]. Dithiocarbamate complexes are also interesting from a structural viewpoint. They exhibit a wide range of coordination geometries and modes of bonding. Dialkyl-dithiocarbamate is found as a unidentate ligand, a bridging ligand, and as a bidentate in both symmetrical and unsymmetrical environments [108].

1.7 Aims and objectives of this project

This work has two major aims:

Aim 1: To use metal chalcogenides as single source precursor to synthesize ZnS, CdS and HgS nanoparticles.

In order to achieve aim 1, objectives are:

- To synthesize and characterize dithiocarbamate ligands derived from aniline.
- To synthesize and characterize dithiocarbamate complexes of Zn(II), Cd(II) and Hg(II).
- To synthesize metal sulfide (MS) nanoparticles derived from as-synthesized dithiocarbamate complexes by using single source precursor (SSP).
- To study the optical and structural properties of the nanoparticles.

Aim 2: To synthesize and characterize ZnS, CdS and HgS nanoparticles in PMMA matrix.

To achieve aim 2, the objectives are as follows:

- To synthesize metal sulfides nanoparticles/PMMA nanocomposites.
- To characterize the nanocomposites using FTIR, XRD, TGA, SEM and TEM.

1.8 References

1. Yu, X.; Zhu, J.; Zhang, Y.; Weng, J.; Hu, L.; Dai, S. $SnSe_2$ quantum dot sensitized solar cells prepared employing molecular metal chalcogenide as precursors. *Chem. Commun*. **2012**, *48*, 3324-3326.
2. Jacoby, M. New tools for tiny jobs. *Chem. Eng. News* **2000**, *78*, 33-35.
3. Jorge, P.; Martins, M.A.; Trindade, T.; Santos, J.S.; Farahi, F. Optical fiber sensing using quantum dots, *Sensors* **2007**, *7*, 3489-3534.
4. Gubin, S.P.; Kataeva, N.A.; Khomutov, G.B. Promising avenues of research in nanoscience: Chemistry of semiconductor nanoparticles. *Rus. Chem. Bull. Int. Ed.* **2005**, *54*, 827-852.
5. Bacherikov1, Y.; Davydenko, M.O.; Dmytruk, A.M.; Dmitruk, I.M.; Lytvyn, P.M.; Prokopenko, I.V.; Romanyuk, V.R. CdSe nanoparticles grown with different chelates. *Semicond. Phys. Quant. Electro. Optoelectro.* **2006**, *9*, 75-79.
6. Zhang, B.; Yan, B. Analytical strategies for characterizing nanoparticle's surface chemistry. *Anal. Bioanal. Chem*. **2010**, *3*, 1-21.
7. Ramsden, J.J. What is nanotechnology? *Nanotech. Percept.* **2005**, *1*, 3-17.
8. Weiss, J.; Takhistov, P.; Mcclements, D.J. Functional materials in food nanotechnology. *J. food sci.* **2006**, *71*, R 107-116.
9. Mehta, M.D. Nanoscience and nanotechnology: Assessing the nature of innovation in these fields. *Bull. Sci. Tech. Soc.* **2002**, *22*, 269-273.
10. Huang, C.; Notten, A.; Rasters, N. Nanoscience and technology publications and patents: a review of social science studies and search strategies. *J. Tech. Transf.* **2011**, *36*, 145-172.
11. Corr, S.A.; Rakovich, Y.P.; Gun'ko, Y.K. Multifunctional magnetic-fluorescent nanocomposites for biomedical applications. *Nanoscale. Res. Lett.* **2008**, *3*, 87-104.

12. Buzea, C.; Blandino, I.I.P.; Robbie, K. Nanomaterials and nanoparticles: Sources and toxicity. *Biointerphases* **2007**, *2*, MR 17-172.
13. Roduner, E. Size matters: Why nanomaterials are different. *Chem. Soc. Rev*. **2006**, *35*, 583-592.
14. Heitmann, J.; Muller, F.; Zacharias, M.; Gosele, U. Silicon nanocrystals: Size matters. *Adv. Mater.* **2005**, *17*, 795-803.
15. Eustis, S.; El-Sayed, M.A. Why gold nanoparticles are more precious than pretty gold: Noble metal surface plasmon resonance and its enhancement of the radiative and nonradiative properties of nanocrystals of different shapes. *Chem. Soc. Rev.* **2006,** *35*, 209-217.
16. Nalwa, H.S. Nanocomposites of polymers and inorganic particles. *Encyclop. Nanosci. Nanotech.* **2004**, *6*, 235-247.
17. Liao, X.-H.; Zhu, J.-J.; Chen, H.-Y. Microwave synthesis of nanocrystalline metal sulfides in formaldehyde solution. *Mater. Sci. and Eng.* **2001**, B85, 85–89.
18. Sabah, A.; Siddiqi, S.A.; Ali, S. Fabrication and characterization of CdS nanoparticles annealed by using different radiations. *World Ac. Sci. Eng. Tech.* **2010**, 82-89.
19. Kovtyukhova, N.I.; Buzaneva, E.V.; Waraksa, C.C.; Martin, B.R.; Mallouk, T.E. Surface sol-gel synthesis of ultrathin semiconductor films. *Chem. Mater.* **2000**, *12*, 383-389.
20. Chen, D.-H.; He, X.-R. Synthesis of nickel ferrite nanoparticles by sol-gel method. *Mater. Res. Bull.* **2001**, *36*, 1369-1377.
21. Dang, M.-Z.; Rancourt, D.G.; Dutrizac, J.E.; Lamarche, G.; Provencher, R. Interplay of surface conditions, particle size, stoichiometry, cell parameters, and magnetism in synthetic hematite-like materials. *Hyperfine Interact.* **1998**, *117*, 271-319.
22. Livage, J.; Henry, M.; Sanchez, C. Sol-gel chemistry of transition metal oxides. *Prog. Solid State Chem*. **1988**, *18*, 259-341.

23. Boissiere, M.; Meadows, P.J.; Brayner, R.; He´lary, C.; Livage, J.; Coradin, T. Turning biopolymer particles into hybrid capsules: The example of silica/alginate nanocomposites. *J. Mater. Chem.* **2006,** *16***,** 1178-1182.

24. Caruso, R.A.; Antonietti, M. Sol-gel nanocoating: An approach to the preparation of structured materials. *Chem. Mater*. **2001**, 13, 3272-3280.

25. Pal, B.N.; Chakravorty, D. Electrical properties of composites with tin-tin oxide core-shell nanostructure and their sensing behaviour. *J. Phys. D Appl. Phys.* **2005**, *38*, 3537-3542.

26. Basu, S.; Chakravorty, D. Optical properties of nanocomposites with iron core-iron oxide shell structure. *J. Non-Crys. Solids* **2006**, *352*, 380-385.

27. Chatterjee, K.; Das, D.; Chakravorty, D. Optical absorption in composites containing copper core-copper-oxide shell nanostructure in a silica gel. *J. Phys. D Appl. Phys*. **2005**, *38*: 451-455.

28. Chipara, M.; Skomski, R.; Sellmyer, D.J. Electrodeposition and magnetic properties of polypyrrole-Fe nanocomposites. *Mater. Lett*. **2007**, *61*, 2412-2415.

29. Lu S-Y, Lin I-H: Characterization of polypyrrole-CdSe/CdTe nanocomposite films prepared with an all electrochemical deposition process. *J. phys. Chem. B.* **2003**, *107*, 6974-6978.

30. Alexandrescu, R.; Morjan, I.; Tomescu, A.; Simion, C.E.; Scarisoreanu, M.; Birjega, R.; Fleaca, C.; Gavrila, L.; Soare, I.; Dumitrache, F.; Prodan, G. Direct production of a novel iron-based nanocomposite from the laser pyrolysis of $Fe(CO)_5$/MMA mixtures: Structural and sensing properties. *J. Nanomater.* **2010**, 1-12.

31. Wangno, K.; Supothina, S.; Ratismith, W.; T. Charinpanitkul, T. Synthesis of nano-sized zinc sulfide via micro-emulsion route. *In TIChE International Conference, Hatyai, Songkhlam*, Thailand, **2011**, 1-4.

32. Russell, J. T.; Lin, Y.; Böker, A.; Su, L.; Carl, P.; Zettl, H.; He, J.; Sill, K.; Tangirala, R.; Emrick, T.; Littrell, K.; Thiyagarajan, P.; Cookson, D.; Fery, A.; Wang, Q.; Russell, T. P. Self-assemble and cross-linking of bionanoparticles at liquid-liquid interfaces. *Angew. Chem. Int. Ed.* **2005**, *44*, 2420.
33. Manna, L. Dynamic organic templating as a means of controlling sizes and shapes of colloidal semiconductor nanocrystals. Thesis, Universita' degli studi di bari, **2000**.
34. Eftekhari, A. Flower like bundles of ZnO nanosheeets as an intermediate between hollow nanoshpere and nanoparticles. *Mater. Sci. Eng.* A. **2006**, 437 446-450.
35. Aditya, V.G.; Mallick, B.R. Preparation of silica nanoparticles using microemulsion techniques. B.Tech Thesis, National Institute of Technology, Rourkela, **2008**.
36. Yao, J.; Zhao, G.; Wang, D.; Han, G. Solvothermal synthesis and characterization of CdS nanowires/PVA composite films. *Mater. Lett.* **2005**, 59, 3652-3655.
37. O'Brien, P.; Park, J.H.; Waters, J. A single source approach to deposition of nickel sulfide thin films by LP-MOCVD. *Thin Solid Films* **2003**, 431, 502-505.
38. Nair, P.S.; Radhakrishnan, T.; Revaprasadu, N.; Kolawole, G.; O'Brien, P. Cadmium ethylxanthate: A novel single-source precursor for the preparation of CdS nanoparticles. *J. Mater. Chem*. **2002**, *12*, 2722-2725.
39. Onwudiwe, D.C.; Ajibade, P.A. ZnS, CdS and HgS nanoparticles via alkyl-phenyl dithiocarbamate complexes as single source precursors. *Int. J. Mol. Sci.* **2011**, *12*, 5538-5551.
40. Shen, S.; Zhang, Y.; Peng, L.; Xu, B.; Du, Y.; Deng, M.; Xu, H.; Wang, Q. Generalized synthesis of metal sulfide nanocrystals from single-source precursors: size, shape and chemical composition control and their properties. *Cryst. Eng. Comm*. **2011**, *13*, 4572-4579.

41. Lou, W.; Wang, X.; Chen, M.; Liu, W.; Hao, J. A simple route to synthesize size-controlled Ag_2S core-shell nanocrystals, and their self-assembly. *Nanotech*. **2008**, *19*, 1-8.
42. Sun, J.; Buhro, W.E. The use of single-source precursors for the solution–liquid–solid growth of metal sulfide semiconductor nanowires. *Angew. Chem*. **2008**, *120*, 3259-3262.
43. Lee, H.L.; Mohammed, I.A.; Belmahi, M.; Assouar, M.B.; Rinnert, H.; Alnot, M. Thermal and optical properties of CdS nanoparticles in thermotropic liquid crystal monomers. *Mater.* **2010**, *3*, 2069-2086.
44. Zhang, L.; Li, F.; Chen, Y.; Wang, X. Synthesis of transparent ZnO/PMMA nanocomposite films through free-radical copolymerization of asymmetric zinc methacrylate acetate and in-situ thermal decomposition. *J. Luminesc.* **2011**, *131*, 1701-1706.
45. Biryukov, A.A.; Izaak, T.I.; Gotovtseva, E.Y.; Lapin, I.N.; Potekaev, A.I.; Svetlichnyi, V.A. Optical properties of CdS/MMA dispersions and CdS/PMMA nanocomposites prepared by one-step, size controlled synthesis. *Rus. Phys. J.* **2011**, *53*, 849-856.
46. He, R.; Qian, X.; Yin, J.; Bian, L.; Xi, H.; Zhu, Z. In situ synthesis of CdS/PVK nanocomposites and their optical properties. *Mater. Lett.* **2003**, *57*, 1351- 1354.
47. Mthethwa, T.P.; Moloto, M.J.; De Vries, A.; Matabola, K.P. Properties of electrospun CdS and CdSe filled poly(methyl methacrylate) (PMMA) nanofibres. *Mater. Res. Bull.* **2011**, 46, 569-575.
48. Ramamurthy. N.; Rajesh K.M.; Murugadoss. G. Synthesis and study of optical properties of CdS nanoparticles using effective surfactants. *Nanosci. Nanotech*: *An Int. J.* **2011**, *1*, 12-16.
49. Pattabi, M.; Uchil, J. Synthesis of cadmium sulfide nanoparticles. *Sol. Energy Mater. Sol. Cells* **2000**, *63*, 309-314.

50. Jayanthi, K.; Chawla, S.; Chander, H.; Haranath, D. Structural, optical and photoluminescence properties of ZnS: Cu nanoparticle thin films as a function of dopant concentration and quantum confinement effect. *Cryst. Res. Technol*. **2007**, *42*, 976-982.

51. O'Brien, P.; Peakett, N.L. Nanocrystalline semiconductors: Synthesis, properties, and perspectives. *Chem. Mater.* **2001**, *13*, 3843-3858.

52. Singh, C.P.; Bindra, K.S.; Oak, S.M. Non linear optical studies in semiconductor-doped glasses under femtosecond pulse excitation. *Pramana-J. Phys.* **2010**, 75, 1169-1173.

53. Gubin, S.P.; Kataeva, N.A.; Khomutov, G. B. Promising avenues of research in nanoscience: Chemistry of semiconductor nanoparticles. *Rus. Chem. Bull. Int. Ed.* **2005**, *54*, 827-852.

54. Dhlamini, M.S. Luminescent properties of synthesized PbS nanoparticle phosphors. Ph.D. Thesis, University of the Free State, RSA, **2008**.

55. Lalena, J.N.; Cleary, D.A.; Carpenter, E.E.; Dean, N.F. Inorganic materials synthesis and fabrication. John Wiley & Sons, Inc. **2008**, pp171-172.

56. Ding, B.; Wang, M.; Yu, J.; Sun, G. Gas sensors based on electrospun nanofibers. *Sensors* **2009**, *9*, 1609-1624.

57. Jorge, P.; Martins, M.A.; Trindade, T.; Santos, J.L.; Farahi, F. Optical fiber sensing using quantum dots. *Sensors* **2007**, *7*, 3489-3534.

58. Joshi, P.; Chakraborti, S.; Chakrabarti, P.; Singh, S.P.; Ansari, Z.A.; Husain, M.; Shanker, V. ZnO nanoparticles as an antibacterial agent against *E.coli*. *Sci. Adv. Mater.* **2012**, 4,173-178.

59. Rao, B.S.; Kumar, B.R.; Reddy, V.R.; Rao, T.S. Preparation and characterization of CdS nanoparticles by chemical co-precipitation technique. *Chalco. Lett.* **2011**, *8*, 177-185.

60. Singh, V.; Chauhan, P. Synthesis and structural properties of wurtzite type CdS nanoparticles. *Chalco. Lett.* **2009**, *6*, 421-426.

61. Zhang, Y.C.; Chen, W.W.; Hu, X.Y. Controllable synthesis and optical properties of Zn-doped CdS nanorods from single-source molecular precursors. *Cryst. Growth Design* **2007**, *7*, 580-586.

62. Sashchiuk, A.; Lifshitz, E.; Reisfeld, R.; Saraidarov, T.; Zelner, M.; Willenz, A. Optical and conductivity properties of PbS nanocrystals in amorphous zirconia sol-gel films. *J. Sol-Gel Sci. Technol.* **2002**, *24*, 31-38.

63. Dixit, M.; Gupta, S.; Mathur, V.; Rathore, K.S.; Sharma, K.; Saxena, N.S. Study of glass transition temperature of PMMA and CdS-PMMA composite. *Chalco. Lett.* **2009**, *6*,131-136.

64. Plante, I.J.-L.; Zeid, T.W.; Yang, P.; Mokari, T. Synthesis of metal sulfide nanomaterials via thermal decomposition of single-source precursors. *J. Mater. Chem.* **2010**, *20*, 6612-6617.

65. Romeo, A.; Terheggen, M.; Abou-Ras, D.; Bätzner, D.L.; Haug, F.-J.; Kälin, M.; Rudmann, D.; Tiwari, A.N. Development of Thin-film Cu(In,Ga)Se_2 and CdTe Solar Cells. *Prog. Photovolt: Res. Appl.* **2004**, *12*, 93-111.

66. Khan, Z.R.; Zulfequar, M.; Khan, M.S. Structural, optical, photoluminescence, dielectric and electrical studies of vacuum-evaporated CdTe thin films. *Bull. Mater. Sci*. **2012**, *35*, 169-174.

67. McGarrigle, E.M.; Myers, E.L.; Illa, O.; Shaw, M.A.; Riches, S.L.; Aggarwal, V.K. Chalcogenides as organocatalysts. *Chem. Rev*. **2007**, 107, 5841-5883.

68. Prabhu, R.R.; Khadar, M. Characterization of chemically synthesized CdS nanoparticles. *J. Phys.* **2005**, 65, 801-807.

69. Lv, J.; Feng, Y.; Zhang, S.; Guo, J. Simple solution approach to hollow nanospheres of cubic HgS. *Mater. Lett.* **2005**, 59, 3109-3111.

70. Barrelet, C.J.; Wu, Y.; Bell, D.C.; Lieber, C.M. Synthesis of CdS and ZnS nanowires using single-source molecular precursors. *J. Am. Chem. Soc.* **2003**, *125*, 11498-11499.

71. Rockenberger, J.; Troger, L.; Kornowski, A.; Vossmeyer, T.; Eychmuller, A.; Feldhaus, J.; Weller, H. EXAFS studies on the size dependence of structural and dynamic properties of CdS nanoparticles. *J. Phys. Chem. B* **1997**, *101*, 2691-2701.

72. Baset, S.; Akbari, H.; Zeynali, H.; Shafie, M. Size measurement of metal and semiconductor nanoparticles via UV-Vis absorption spectra. *Dig. J. Nanomater. Biostruct.* **2011**, 6, 709-716.

73. Prabhu, R.R.; Khadar, M. Characterization of chemically synthesized CdS nanoparticles. *J. Phys.* **2005**, 65, 801-807.

74. Zhang, L.; Li, F.; Chen, Y.; Wang, X. Synthesis of transparent ZnO/PMMA nanocomposite films through free-radical copolymerization of asymmetric zinc methacrylate acetate and in-situ thermal decomposition. *J. Luminesc.* **2011**, *131*, 1701-1706.

75. Asharaf, S.M.; Ahmad, S.; Riaz, U. Pseudothermoset blends of poly (methyl methacrylate) and polypyrrole morphological, thermal, and conductivity studies. *J. Appl. Polym. Sci.* **2004**, *93***,** 82-91

76. Dutta, P.; De, S.K. Electrical properties of polypyrrole doped with β-naphthalene sulfonic acid and polypyrrole-polymethyl methacrylate blends *Synthetic Metals*. **2003**, *139*, 201-206.

77. Sharma, R. Optical studies of CdS:Mn nanoparticles. *Luminesc.* **2012**, *27*, 501-504.

78. Leonard, D.; Krishnamurthy, M.; Reaves, C.M.; Denbaars, S.P.; Petroff, P.M. *Direct* formation of quantum-sized dots from uniform coherent islands of InGaAs on GaAs surfaces. *Appl. Phys. Lett.* **1993**, *63*, 3203-3205.

79. Altieri, P.; Gurioli, M.; Sanguinetti, S.; Grilli, E.; Guzzi, M.; Frigeri, P.; Franchi, S.Competition in the carrier capture between InGaAs/AlGaAs quantum dots and deep point defects. *Eur. Phys. J. B.* **2002**, 28,157-161.

80. Xiao. M.; Wang, L.; Wu, Y.; Huang, X.; Dang, Z. Preparation and characterization of CdS nanoparticles decorated into titanate nanotubes and their photocatalytic properties. *Nanotech.* **2008**, 19, 1-7.

81. Revaprasadu, N.; Mlondo, S.N. Use of metal complexes to synthesize semiconductor nanoparticles. *Pure Appl. Chem.* **2006**, 78, 1691-1701.

82. Sounderya, N.; Zhang, Y. Use of core/shell structured nanoparticles for biomedical applications. *Recent Pat. Biomed. Eng.* **2008**, *1*, 34-42.

83. Song, H.; Lee, S. Photoluminescent (CdSe)ZnS quantum dot-polymethylmethacrylate polymer composite thin films in the visible spectra range. *Nanotech.* **2007**, 18, 1-6.

84. Jang, J.; Kim, S.; Lee, K.J. Fabrication of CdS/PMMA core/shell nanoparticles by dispersion mediated interfacial polymerization. *Chem. Commun.* **2007**, 2689-2691.

85. Bangal, M.; Ashtaputre, S.; Marathe, S.; Ethiraj, A.; Hebalkar, N.; Gosavi, S.W.; Urban, J.; Kulkarni, S.K. Semiconductor nanoparticles. *Hyperf. Interact.* **2005**, *160*, 81-94.

86. Smith, A.M.; Duan, H.; Mohs, A.M.; Nie, S. Bioconjugated quantum dots for *in vivo* molecular and cellular imaging. *Adv. Drug Deliv. Rev.* **2008**, *60*, 1226-1240.

87. Thavasi, V.; Singh, G.; Ramakrishna, S. Electrospun nanofibers in energy and environmental applications. *Energy Environ. Sci.* **2008**, *1*, 205-221.

88. Jin, W.J.; Lee, H.K.; Jeong,E.H.; Park, W.H.; Youk, J.H. Preparation of polymer nanofibers containing silver nanoparticles by using poly(n-vinylpyrrolidone). *Macromol. Rapid Commun.* **2005**, *26*, 1903-1907.

89. Heikkilä, P. Nanostructured fibre composites, and materials for air filtration. Ph.D. Theses, Tampere University of Technology, **2008**.

90. Ajibade, P.A.; Onwudiwe, D.C. Synthesis and characterization of group 12 complexes of N,N-methyl phenyl-N,N-butyl phenyl dithiocarbamate. *J. Coord. Chem.* **2011**, *64*, 2963-2973.

91. Fabretti, A.C.; Franchini, G.C.; Preti, C.; Tosi, G.; Zannini, P. Transition metal complexes with 2-methyl-, 3-methy-, and 4-methyl-piperidine dithiocarbamate as ligands. *Transition Met. Chem*. **1985**, 10, 284-287.

92. Regulacio, M.D.; Tomson, N.; Stoll, S.L. Dithiocarbamate precursors for rare-earth sulfides. *Chem. Mater.* **2005**, *17*, 3114-3121.

93. Valarmathi, P.; Thirumaran, S.; Ragi, P.; Ciattini, S. Synthesis and spectra studies on nitrogen donor adducts of bis(4-ethylpiperazinecarbodithioato-S,S')M(II) (M = Zn, Cd) and use of adducts of cadmium dithiocarbamate for the preparation of cadmium sulfide. *J. Coord. Chem*. **2011**, 64, 4157-4167.

94. Alfassi, Z.B. Instrumental multi-element chemical analysis Kluwer Academic Publishers, Netherlands, **1998**.

95. Mamba, S.M. Synthesis, characterization and applications of dithiocarbamate transition metal complexes. M.Sc. Thesis, University of Johannesburg, RSA, **2009.**

96. Peakett, N.L.; O'Brien, P. Syntheses of semiconductor nanoparticles using single-molecular precursors. *Chem. Rec.* **2001**, 1, 467-479.

97. Nair, P.S.; Radhakrishnan, T.; Revaprasadu, N.; Kolawole, G.A.; O'Brien, P. $Cd(NH_2CSNHNHCSNH_2)Cl_2$: A new single-source precursor for the preparation of CdS nanoparticles. *Polyhedron* **2003**, 22, 3129-3135.

98. Maeda, K.; Domen, K. New non-oxide photocatalysts designed for overall water splitting under visible light. *J. Phys. Chem. C.* **2007**, *111*, 7851-7861.

99. Singh, N.; Bhattacharya, S. Synthesis and characterization of some triorgano, diorgano, monoorganotin and a triorganolead heteroaromatic dithiocarbamate complexes. *J. Organomet. Chem.* **2012**, 700, 69-77.

100. Jain, V.K. Chemistry of molecular precursors for compound semiconductor nanoparticles. *J. Indian Chem. Soc.* **2008**, 85, 123-129.

101. Ajibade, P.A.Synthesis and Use of $[Cd(Detu)_2(OOCCH_3)_2]\cdot H_2O$ as single molecule precursor for CdS nanoparticles. *Scient. W.J.* **2013**, 1-6.

102. Marimuthu, G.; Ramalingam, K.; Rizzoli, C.; Arivanandhan, M. Solvothermal preparation of nano-b-HgS from a precursor, bis(dibenzyldithiocarbamato)mercury(II). *J. Nanopart. Res.* **2012**, 14, 1-11.

103. Ehrt, D. Photoluminescence in glasses and glass ceramics. *Mater. Sci. and Eng.* **2009**, *2*, 1-8.

104. Chen, J.; Cao, S.; Wang, D.; Wu, S.; Wang, X. A phenol-based compartmental ligand as a potential chemosensor for zinc(II) cations. *J. Braz. Chem. Soc.* **2009**, 20, 13-18.

105. Xu, Z.; Yoon, J.; Spring, D.R. Fluorescent chemosensors for Zn^{2+}. *Chem. Soc. Rev.* **2010**, *39*, 1996-2006.

106. Cvek, B.; Dvorak, Z. Targeting of nuclear factor-*k*B and proteasome by dithiocarbamate complexes with metals. *Cur. Pharmaceut. Des.* **2007**, *13*, 000-000.

107. Cotton, F. A.; Wilkinson, G; Murillo, C.A.; Bochmann, M. Advanced inorganic chemistry, 6th Ed.; Wiley and Sons: New York, **1999**.

108. Onwudiwe, D.C.; Ajibade, P.A. Synthesis and crystal structure of bis(N-alkyl-N-phenyl dithiocarbamato)mercury(II). *J. Chem. Crystallogr*. **2011**, *41*, 980-985.

CHAPTER TWO

2.0 EXPERIMENTAL

2.1 Chemicals and solvents

The chemicals and solvents used in this work were of analytical grade and used as purchased from Sigma-Aldrich and Merck without further purification.

Chemicals:

Aniline, N-methyl aniline, N-ethyl aniline, concentrated aqueous ammonia, sodium hydroxide, carbon disulfide, anhydrous cadmium chloride, zinc chloride, mercury chloride, hexadecylamine and poly (methyl methacrylate).

Solvents:

Absolute ethanol, methanol, distilled water, toluene, chloroform, dimethysulfoxide, N,N'-dimethyformamide, acetone, diethylether and tri^{n}octylphosphine

2.2. Physical measurements

The instrumental techniques for sample characterization such as ultraviolet-visible (UV-Vis), photoluminescence (PL), fourier transform infra-red (FTIR) and nuclear magnetic resonance spectroscopy (NMR), powder X-ray diffraction (XRD), transmission electron microscopy (TEM), scanning electron microscopy **(**SEM), energy dispersive X-ray analysis (EDX) and thermogravimetric analysis (TGA) were used. The carefully selected instruments were employed for the characterization of dithiocarbamate ligands, metal dithiocarbamate complexes, metal sulfide nanoparticles and nanocomposites.

2.2.1 Melting point

Samples of complexes in capillary tubes were introduced into a Stuart melting point apparatus model SMP 11 for melting point determinination.

2.2.2 Solubility

Solvents of different dielectric constant and polarities at hot and cold temperatures such as water, toluene, dimethylsulfoxide etc, were used to determine the solubility of complexes.

2.2.3 Elemental analysis

Elemental analyses for C, H, N and S were carried out on a Fison elemental analyzer.

2.2.4 UV-Visible spectroscopy

Electronic spectra of metal sulfide nanoparticles in toluene were run in the range 200-900 nm on Perkin Elmer λ25 UV-Vis spectrophotometer. The samples were prepared using toluene as a solvent and placed in glass cuvettes of 1 cm path length. All nanoparticles were soluble in toluene.

2.2.5 Photoluminescence spectroscopy

The photoluminescence of the nanoparticles were measured using Perkin Elmer LS 45 Fluorimeter. The samples were dissolved in toluene and placed in glass cuvettes of 1 cm path length.

2.2.6 Infrared spectroscopy

Infrared spectra of dithiocarbamate ligands were recorded on Perkin Elmer 2000 FTIR spectrophotometer as KBr discs in the range 4000-370 cm^{-1} region. The spectra of metal dithiocarbamate complexes and metal sulfide nanoparticles / poly (methyl methacrylate)

nanocomposites were recorded on Bruker Tensor 27 attenuated total reflectance (ATR)-FTIR equipped with narrow band MCT detector, dedicated flow-through cell, made from a Teflon piece, a fused silica plate (45 x 35 x 3 mm) with holes for in- and outlet (36 mm apart), and a flat (1mm) viton seal. The cell was mounted on an attachment for ATR measurements in the region of 4000-600 cm^{-1}.

2.2.7 Nuclear magnetic resonance spectroscopy

The NMR spectra of ligands and complexes were recorded on a Bruker ultrashield 400 NMR spectrometer operating at frequencies of 400.1 MHz for ^{1}H and 100.6 MHz for ^{13}C nuclei. The temperature of the measurements was 303 K. NMR samples were prepared by dissolving the complexes in dimethylsulphoxide (DMSO) as solvent and placed in a magnetic field.

2.2.8 X-ray diffraction

The powder XRD spectra of metal sulfide nanoparticles and metal sulfide nanoparticles / poly (methyl methacrylate) nanocomposites were carried out on a Bruker-D8 advance powder X-Ray diffractometer instrument operating at a voltage of 40 kV and a current of 30 mA with Cu kα radiation. The XRD samples were made by drop coating the sample on a glass plate.

2.2.9 Thermogravimetric analysis

Thermogravimetric analyses experiments of complexes and metal sulfide nanoparticles / poly (methyl methacrylate) nanocomposites were carried out on a Perkin Elmer thermogravimetric analyzer (TGA 7) fitted with a thermal analysis controller (TAC 7/ DX). Samples of 10-20 mg of each complex was loaded into an alumina pan and weight changes was recorded as a function of temperature for a 10 °C min^{-1} temperature gradient between 20-900 °C. A purge gas of flowing nitrogen at a rate of 20 mL min^{-1} was used.

2.2.10 Scanning Electron Microscopy

The SEM has been used to study the microstructure of the metal dithiocarbamate complexes, metal sulfide nanoparticles and nanocomposites. SEM images were obtained in a Jeol, JSM-6390 LV apparatus, using an accelerating voltage between 15-20 kV at different magnifications, as indicated on the SEM images.

2.2.11 Energy Dispersive X-ray analysis

Energy dispersive spectra were processed using energy dispersive X-ray analysis (EDX) attached to a Jeol, JSM-6390 LV SEM with Noran System Six software.

2.2.12 Transmission Electron Microscopy

The TEM images were obtained using a ZEISS Libra 120 electron microscope operated at 120 kV. The samples were prepared by placing a drop of a solution of the sample in toluene on a carbon coated copper grid (300 mesh, agar). The excess solvent was wicked away with a paper tip and the samples were allowed to dry completely over night at room temperature. Images were recorded on a megaview G2 camera using iTEM Olympus software.

2.3. Synthesis of dithiocarbamate ligands

In this work, the following dithiocarbamate ligands were synthesized and characterized:

(i) Ammonium N-phenyldithiocarbamate, $NH_4[C_6H_5(H)NCS_2]$, L^1

(ii) Ammonium N-methyl-N-phenyldithiocarbamate, $NH_4[C_6H_5(CH_3)NCS_2]$, L^2

(iii) Ammonium N-ethyl-N-phenyldithiocarbamate, $NH_4[C_6H_5(C_2H_5)NCS_2]$, L^3

Where L^1, L^2 and L^3 denote ligand1, ligand2 and ligand3 respectively. Generally, dithiocarbamate ligands are prepared by simply reacting carbon disulfide with primary or secondary amine in the presence of a strong base (Scheme 2.1). It has been found that the

dithiocarbamates obtained from secondary amine are more stable than those synthesized from primary amine [1].

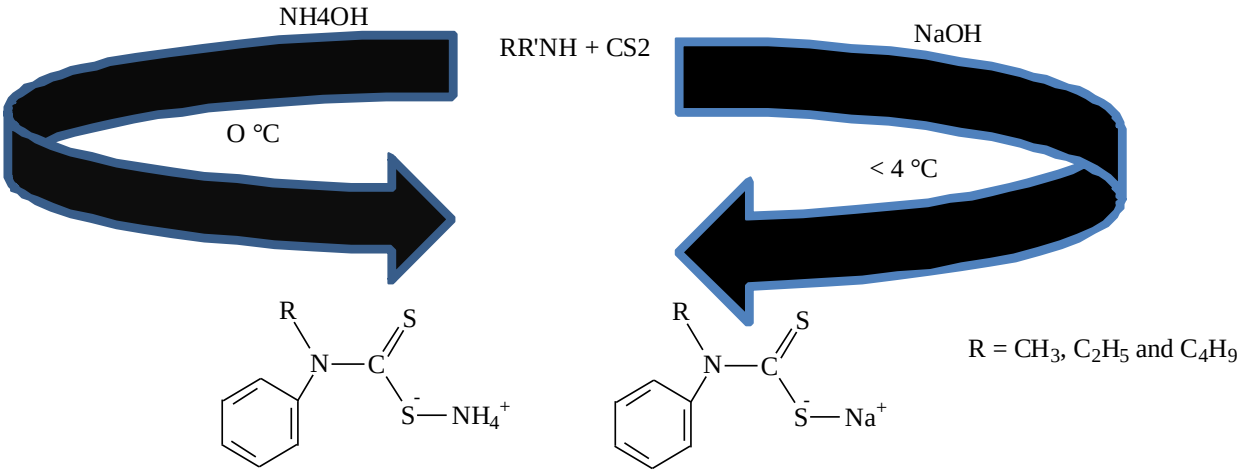

Scheme 2.1: General synthetic routes for dithiocarbamate ligands

2.3.1 Synthesis of ammonium N-phenyldithiocarbamate, $NH_4[C_6H_5(H)NCS_2]$, L^1

This compound was prepared by a modified literature method [2]. In a typical experiment, 30 mL of concentrated ammonium hydroxide was added slowly to 9.13 mL (0.1 mol) aniline in an ice cold mixture at 0-4 °C. To this mixture, 6.04 mL (0.1 mol) of carbon disulfide was added drop-wise with constant stirring for 1 h in an ice bath and refluxed for a further 1 h at room temperature. The resulting yellowish solid obtained was filtered by suction and rinsed three times with cold ethanol. The product obtained is air and thermally unstable. The scheme 2.2 show the synthesis of the ligand derived from aniline, used a main ligand in a mixed ligand method when preparing metal complexes.

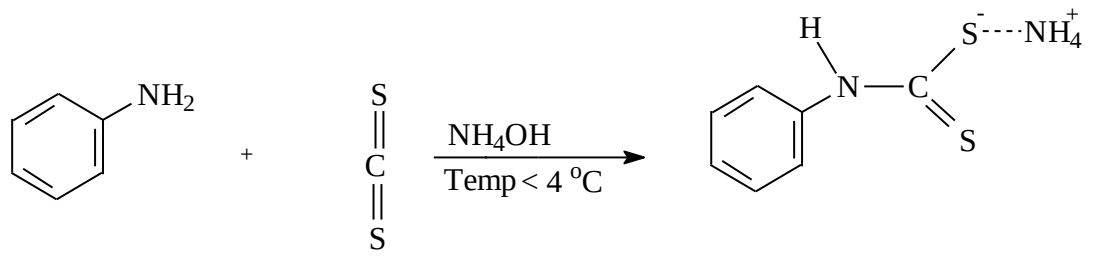

Scheme 2.2: Synthesis of ammonium N-phenyldithiocarbamate

2.3.2 Synthesis of ammonium N-methyl-N-phenyldithiocarbamate, $NH_4[C_6H_5(CH_3)NCS_2]$, L^2

The ligand was synthesized as described in the literature [3, 4]. In a typical experiment, 12.1 mL (0.2 mol) of carbon disulfide (density 1.2) was added into 30 mL concentrated aqueous ammonia in ice. To this solution, 21.80 mL (0.2 mol) of N-methyl aniline was added and the mixture was stirred for about 6-7 h while ensuring the temperature is less than 4 °C. A yellowish white solid product was separated out by filtration and then washed with cold ethanol three times. Analytically pure $NH_4[C_6H_5(CH_3)NCS_2)]$ was obtained and stored in the refrigerator since the product is air and thermally unstable. The scheme 2.3 show the synthesis of L^2.

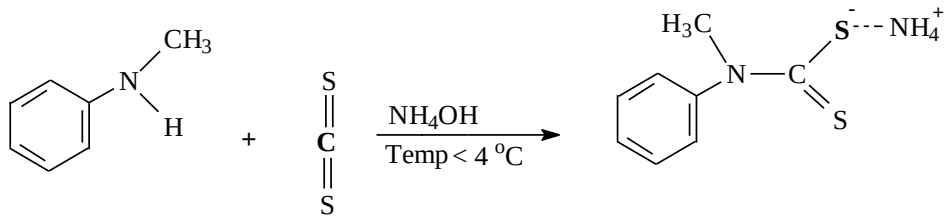

Scheme 2.3: Synthesis of ammonium N-methyl-N-phenyldithiocarbamate

2.3.3 Synthesis of ammonium N-ethyl-N-phenyldithiocarbamate, $NH_4[C_6H_5(C_2H_5)NCS_2]$, L^3

The L^3 was prepared according to a reported procedure [3]. To a mixture of 12.88 mL (0.1mol) of N-ethyl aniline and concentrated aqueous ammonia (30 mL) in ice, was added

6.00 mL (0.1 mol) of ice cold carbon disulfide. The yellowish green liquid mixture was stirred for 6-7 h given yellowish white solid product which was filtered by suction and rinsed three times with cold ethanol given thermally unstable, moisture and air-sensitive, ammonium salt of N-ethyl-N-phenyldithiocarbamate which was stored in the refrigerator. The scheme for the synthesis of L^3 is shown below.

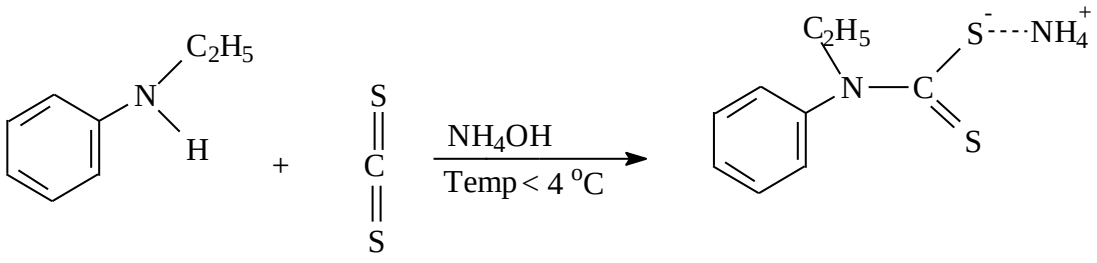

Scheme 2.4: Synthesis of ammonium N-ethyl-N-phenyldithiocarbamate

2.4. Synthesis of metal dithiocarbamate complexes

Below is the list of six precursor complexes prepared:

(I) (N-phenyl-N, N-methyl phenyl dithiocarbamato)Zn(II), $[(C_6H_5N(H)CS_2)Zn(S_2C(CH_3)NH_5C_6)]$, $[ZnL^1L^2]$;

(II) (N-phenyl-N,N-methyl phenyl dithiocarbamato)Cd(II), $[(C_6H_5N(H)CS_2)Cd(S_2C(CH_3)NH_5C_6)]$, $[CdL^1L^2]$;

(III) (N-phenyl-N,N-methyl phenyl dithiocarbamato)Hg(II), $[(C_6H_5N(H)CS_2)Hg(S_2C(CH_3)NH_5C_6)]$, $[HgL^1L^2]$;

(IV) (N-phenyl-N, N-ethyl phenyl dithiocarbamato)Zn(II), $[(C_6H_5N(H)CS_2)Zn(S_2C(C_2H_5)NH_5C_6)]$, $[ZnL^1L^3]$;

(V) (N-phenyl-N,N-ethyl phenyl dithiocarbamato)Cd(II), $[(C_6H_5N(H)CS_2)Cd(S_2C(C_2H_5)NH_5C_6)]$, $[CdL^1L^3]$ and

(VI) (N-phenyl-N,N-ethyl phenyl dithiocarbamato)Hg(II), $[(C_6H_5N(H)CS_2)Hg(S_2C(C_2H_5)NH_5C_6)]$, $[HgL^1L^3]$.

They were prepared at room temperature by mixing the aquous solutions of the ligands (L^1, L^2 or L^3) with aquous solution of the respective metal salts according to the literature methods [3, 4]. The products obtained were in powder form. The detailed scheme of synthesis for these complexes is presented below. The method used is called mixed ligands method and is preferable over simple ligand method [4]. Other proposed structures are shown in Table 2.1 below.

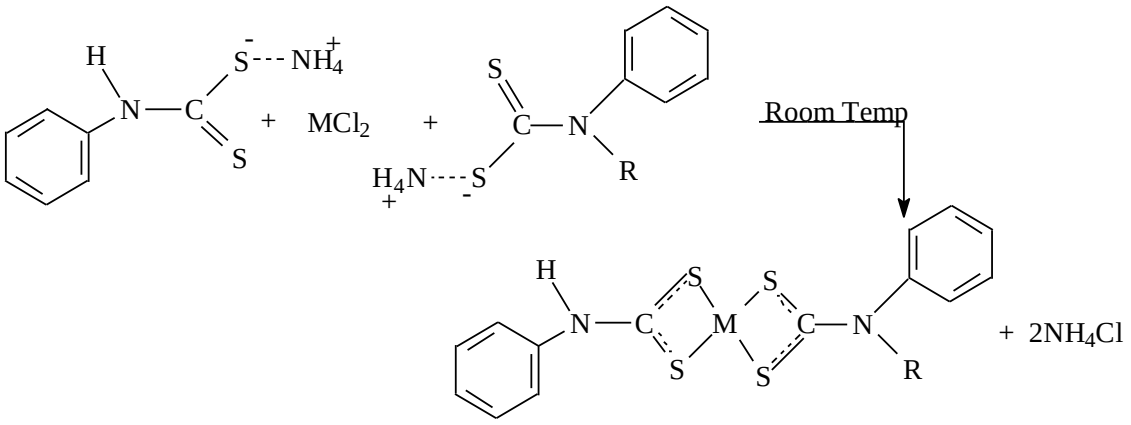

Scheme 2.5: Proposed reaction for the synthesis of monomeric dithiocarbamate metal complexes, where R = CH_3 or C_2H_5 and M = Zn, Cd, or Hg

Table 2.1: showing the proposed structures and their corresponding codes

Structure code	**Proposed structure**
$ML^{1}L^{2,3}$	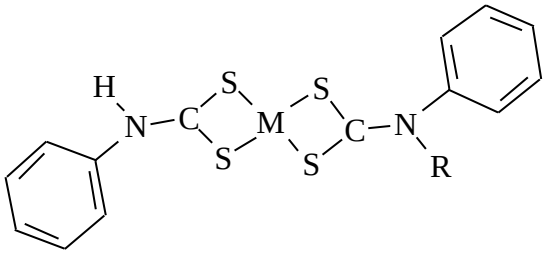
$ML^{2,3}L^{2,3}$	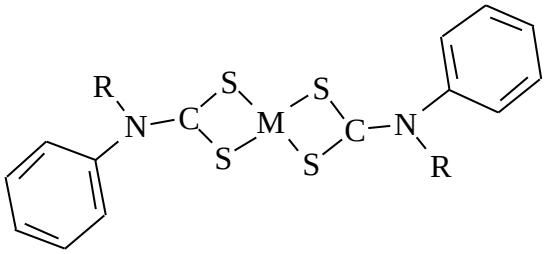
$ML^{2,3}L^{3,2}$	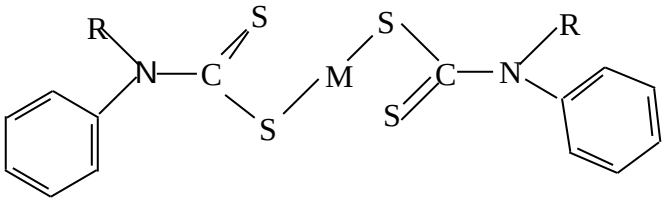
$(ML^{2,3}L^{2,3})^{2}$	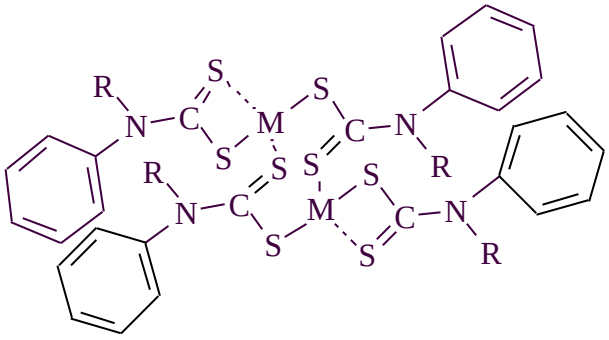

2.4.1 Synthesis of $[(C_6H_5N(H)CS_2)Zn(S_2C(CH_3)NH_5C_6)]$, ZnL^1L^2

Equimolar solutions containing 1.25 mmol of L^1 (0.2316 g) and L^2 (0.2504 g) dissolved in 40 mL of water were added simultaneously to solution of $ZnCl_2$ (1.25 mmol, 0.1704 g) dissolved in 20 mL of water. A yellowish white precipitate was observed immediately. The reaction

mixture was stirred for 1 h at room temperature. The product was filtered and washed with distilled water. The precursor obtained was dried under vacuum over $CaCl_2$.

2.4.2 Synthesis of $[(C_6H_5N(H)CS_2)Cd(S_2C(CH_3)NH_5C_6)]$, CdL^1L^2

A thoroughly stirred aqueous solutions of L^1 (1.25 mmol, 0.2316 g) and L^2 (1.25 mmol, 0.2510 g) were added simultaneously into a solution of $CdCl_2$ (0.2291 g, 1.25 mmol). A yellow precipitate was observed immediately. The reaction mixture was stirred for 1 h at room temperature. The product was filtered and washed with distilled water. The precursor obtained was dried under vacuum over $CaCl_2$.

2.4.3 Synthesis of $[(C_6H_5N(H)CS_2)Hg(S_2C(CH_3)NH_5C_6)]$, HgL^1L^2

This complex was prepared by using similar procedure as described in 2.4.1 and 2.4.2 using $HgCl_2$ (1.25 mmol, 0.3394 g). A pale green precipitate began to form after five minutes. The mixture was stirred at room temperature for a further 1 h and the product, a pale green precipitate, was collected by filtration. The crude product was washed three times with distilled water (3 x 10 mL).

2.4.4 Synthesis of $[(C_6H_5N(H)CS_2)Zn(S_2C(C_2H_5)NH_5C_6)]$, ZnL^1L^3

To a well stirred solution of an equimolar (1.25 mmol) concentration of ligands L^1 (0.2316 g) and L^3 (0.2679 g) in 40 mL of water was added $ZnCl_2$ (1.25 mmol, 0.1704 g) in 20 mL of the same solvent to obtain an immediate precipitation. The reaction mixture was then stirred for 1 h at room temperature. The white product was filtered, washed with water and dried in vacuum.

2.4.5 Synthesis of $[(C_6H_5N(H)CS_2)Cd(S_2C(C_2H_5)NH_5C_6)]$, CdL^1L^3

This complex was prepared by the similar procedure as described in 2.4.4 using $CdCl_2$ (1.25 mmol, 0.2291 g). A white yellow precipitate began to form immediately. The mixture was stirred at room temperature for a further 1 hour. A yellow precipitate was collected by filtration. The yellow product was washed three times with distilled water (3 x 10 mL).

2.4.6 Synthesis of $[(C_6H_5N(H)CS_2)Hg(S_2C(C_2H_5)NH_5C_6)]$, HgL^1L^3

This complex was prepared by the similar procedure as described in 2.4.4 using $HgCl_2$ (1.25 mmol, 0.3394 g). A pale green precipitate began to form immediately. The mixture was stirred at room temperature for a further 1 h and the product, a black precipitate, was collected by filtration. The dark product was washed three times with distilled water (3 x 10 mL).

2.5 Experimental procedure for synthesis of HDA-capped ZnS, CdS and HgS nanoparticles

In a typical experiment, 0.2 g of $[ZnL^1L^2]$ complex was dissolved in 4 mL of tri^{n}octylphosphine (TOP). This solution was then injected into 4 g of hot hexadecylamine (HDA) at a temperature of 180 °C. A subsequent decrease in temperature of about 20-30 °C was observed. The solution was then allowed to stabilize at 180 °C and then heated for a further 60 min. The solution was then allowed to cool to about 70 °C, and large amount of methanol was added to remove the excess HDA. The as-synthesized flocculent precipitate was separated by centrifugation and was redispersed in toluene. The solvent was then removed by evaporation under reduced pressure to give HDA-capped ZnS nanoparticles. The particles were again washed with methanol three times and redispersed in toluene for spectroscopic measurements. The same approach was used for $[CdL^1L^2]$, $[HgL^1L^2]$,

[ZnL^1L^3], [CdL^1L^3] and [HgL^1L^3] complexes to prepare their respective HDA-capped ZnS, CdS and HgS nanoparticles.

2.6 Single crystal X-ray crystallography

A white crystal with approximate dimensions 0.27 x 0.19 x 0.17 mm^3 was selected under oil under ambient conditions and attached to the tip of a MiTeGen MicroMount©. The crystal was mounted in a stream of cold nitrogen at 100(2) K and centered in the X-ray beam by using a video camera. The crystal evaluation and data collection were performed on a Bruker SMART APEXII diffractometer with Cu Kα (λ = 1.54178 Å) radiation and the diffractometer to crystal distance of 4.03 cm. The initial cell constants were obtained from three series of w scans at different starting angles. Each series consisted of 35 frames collected at intervals of 0.7^o in a 25° range about w with the exposure time of 3 seconds per frame. The reflections were successfully indexed by an automated indexing routine built in the APEXII program. The final cell constants were calculated from a set of 3206 strong reflections from the actual data collection. The data were collected by using the full sphere data collection routine to survey the reciprocal space to the extent of a full sphere to a resolution of 0.82 Å. A total of 27791 data were harvested by collecting 19 sets of frames with 0.7^o scans in w with an exposure time 4-8 sec per frame. These highly redundant datasets were corrected for Lorentz and polarization effects. The absorption correction was based on fitting a function to the empirical transmission surface as sampled by multiple equivalent measurements [5]. The systematic absences in the diffraction data were uniquely consistent for the space group *P*21/*c* that yielded chemically reasonable and computationally stable results of refinement [6]. A successful solution by the direct methods provided most non-hydrogen atoms atoms from the *E*-map. The remaining non-hydrogen atoms were located in an altering series of least-squares cycles and difference Fourier maps. All non-hydrogen atoms were refined with

anisotropic displacement coefficients. All hydrogen atoms were included in the structure factor calculation at idealized positions and were allowed to ride on the neighbouring atoms with relative isotropic displacement coefficients.

2.7 Experimental procedure for synthesis of metal sulfide nanoparticles / poly (methyl methacrylate) nanocomposites

The nanocomposites were prepared from their respective metal sulfide nanoparticles using a modified methods reported by Prabhu1 *et al* [7] and Agrawal *et al* 8]. In a typical experiment, 1.5 g of PMMA was dissolved in 20 mL toluene solution in a 100 mL glass beaker with the aid of magnetic stirrer for one hour. Another beaker solution containing 3.0 % (0.045 g) weight percent of ZnS nanoparticles dissolved in toluene was slowly added into the beaker containing the PMMA toluene solution with heating and vigorous stirring. The experiment continued for about 30 minutes. The resulting turbid solutions were poured on a Petri dish and allowed to dry in air. The other solution of PMMA with 0.0 % MS was also prepared the same way. The white ZnS2/PMMA nanocomposite was obtained. The similar procedure was used for the synthesis of ZnS3/PMMA, CdS2/PMMA, CdS3/PMMA, HgS2/PMMA and HgS3/PMMA nanocomposites. The yellow to white nanocomposites of CdS/PMMA, ZnS/PMMA and HgS/PMMA were obtained in a good yield of 85-95 % and the thickness of prepared samples was 0.1-0.2 mm.

2.7 References

1. Emayavaramban, M.; Gopi, N.S.; Manivannan, C. Synthesis, characterization and antimicrobial screening of Hg (II), Mn (II), Fe (II), Cd (II) dithiocarbamate complexes. *AJCC.* **2011**, *1*, 25-34.
2. Mahapatra, B.B.; Panda, S.K. Coordination Compounds of Co^{II}, Ni^{II}, Cu^{II}, Zn^{II}, Cd^{II} and Hg^{II} with tridentate ONS donor Azo dye ligands. *Biokemistri. Vol.* **2010**, *22*, 71-75.
3. Onwudiwe, D.C.; Ajibade, P.A. Synthesis and characterization of metal complexes of N-alkyl-N-phenyl dithiocarbamates. *Polyhedron* **2010**, *29*, 1431-1436.
4. Onwudiwe, D.C.; Ajibade, P.A. Synthesis and crystal structure of bis(N-alkyl-N-phenyl dithiocarbamato)mercury(II). *J. Chem. Crystallogr*. **2011**, *41*, 980-985.
5. Bruker-AXS. APEX2, SADABS, and SAINT software reference manuals. Bruker-AXS, Madison, Wisconsin, USA, **2007**.
6. Sheldrick, G.M. A short history of *SHELX*. *Acta Cryst*. **2008**, *A64*, 112-122.
7. Prabhu1, S.G.; Pattabi, B.M. Incorporation of acetoacetanilide crystals in host PMMA polymer matrix and characterizations of the hybrid composite. *J. Mine. Mater. Charact. Eng*. **2012**, *11*, 519-527.
8. Agrawal, S.; Patidar, D.; Saxena, N.S. Glass transition temperature and thermal stability of ZnS/PMMA nanocomposites. *Phase Trans.* **2011**, *84*, 888-900.

CHAPTER THREE

3.0 CHARACTERIZATION OF THE METAL DITHIOCARBAMATE COMPLEXES

3.1 Introduction

A driving force for synthesis and characterization of metal complexes belonging to 1,1-dithiolates family is the fact that these materials display useful properties with wide range of applications [1-4]. A number of dithiocarbamate transition metal complexes have been synthesized using several methods [5, 6]. Dithiocarbamate ligands are known to have different resonant forms of dithiocarbamic moiety (Figure 3.1), thus can act as monodentate, bidentate chelating or bidentate bridging ligands due to binding character.

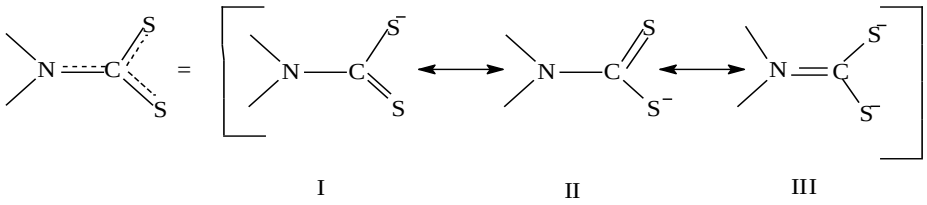

Figure 3.1: Resonance structures for dithiocarbamate anions [7]

The two sulfur atoms of a metal-coordinated dithiocarbamate ligand maintain an additional coordination capability due to the availability of, at least, one pair of potentially bonding electrons [8]. The anion $[S_2CNR_2]^-$ has high affinity compared with other 1,1-dithiolate anions and its high coordinating properties has been attributed to the significant contribution of the resonance form of the anion to the electronic structure of the dithiocarbamate ligand [9]. Dithiocarbamates have strong metal binding properties and can form chelates with all transition elements and the bidentate anion could also form bridge between two transition metal centers [7]. This method was used elsewhere [10] for the synthesis of

bis(dialkyldithiocarbamato)diorganodithiophosphatobismuth(III) complexes which showed good antibacterial effect. The mixed ligands method has been used in the synthesis and characterization these adducts: [Cd(2-mpipdtc)$_2$(1,10-phen)], [Cd(2-mpipdtc)$_2$(bipy)], [Cd(4-mpipdtc)$_2$(1,10-phen)] and [Cd(4mpipdtc)$_2$(bipy)] [11]. Dithiocarbamates are good complexing agents and a large number of interesting complexes with metal ions have been synthesized. The interesting studies of such complexes have been repeatedly reviewed by several researchers. For example, the electrochemical studies on metal chelates of dithiocarbamates were reviewed by Budnikov and Troepol'skaya [12], Singh *et al* [13], and their structural aspects by Victoriano [5]. The recent articles from our research group cover the vast scope on chemistry, synthesis and characterization of dithiocarbamato metal complexes [3, 7, 9]. Other important reviews by Manav *et al* [14, 15] deal with platinum(IV) and palladium(II) dithiocarbamates complexes.

For the synthesis of metal dithiocarbamate complexes, the mixed ligand method was adopted because this method is preferable over the simple ligand method since it forms stable complexes [16-18]. The equimolar concentrations of two different ligands and their respective metal salts solutions were mixed thoroughly in the ratio 1:1:1. All six complexes were characterized using elemental analysis (EA), Fourier transform infrared (FTIR) spectroscopy, nuclear magnetic resonance (NMR) spectroscopy and thermal gravimetric analysis (TGA). The decomposition residues of some Zn(II) and Cd(II) dithiocarbamate complexes were characterized using scanning electron microscopy **(**SEM) attached with energy dispersive X-ray analysis (EDX).

The solubility of all metal complexes were tested using various polar, non polar solvents and mixture of two solvents in known ratios. 8 mg of metal complex was taken and dissolved into

2 mL of corresponding solvent and checked the solubility. The solubility test of three dithiocarbamate ligands and their six metal dithiocarbamate complexes were conducted in different solvents as shown in Table 3.1. It was found that all complexes were not soluble in water and they were all completely soluble in toluene. Toluene was therefore used in most experiments in this work.

Table 3.1: Solubility of ligands and complexes in different solvents

Solvent	ε	L^1	L^2	L^3	ZnL^1L^2	CdL^1L^2	HgL^1L^2	ZnL^1L^3	CdL^1L^3	HgL^1L^3
Water	80.4	Sol	Sol	Sol	Ins	Ins	Ins	Ins	Ins	Ins
DMF	36.7	Sp	Sp	Sp	--	--	--	--	--	--
Toluene	2.4	Sol	Sol	Sol	Sol*	Sol	Sol*	Sol*	Sol	Sol*
$CHCl_3$	4.8	Sol	Sol	Sol	Sol	Sol	Sol	Sol	Sol	Sol
DMF/Et_2O		--	--	--	Sol	Sol	Sol	Sol	Sol	Sol
$Tolu/Et_2O$		--	--	--	Sol*	Sol	Sol	Sol*	Sol	Sol*
$CHCl_3/Et_2O$		--	--	--	Sol	Sol	Sol	Sol	Sol	Sol
$CHCl_3/EtOH$		--	--	--	Sol	Sol	Sol	Sol	Sol	Sol*
DMF/EtOH		Sol	Sol	Sol	Sol	Sol	Sol	Sol	Sol	Sol

Key:

ε = dielectric constant, Sol* = Soluble and crystals formed, Sol = Soluble, Ins = Insoluble, Sp = Sparingly Soluble, -- = not checked

Elemental analysis and physical properties metal dithiocarbamate complexes are presented in Table 3.2. The physical appearance of zinc, cadmium and mercury complexes were found to be white, yellow and pale green respectively.

Table 3.2: Elemental analysis and physical properties of the prepared complexes

Complex	Colour	M.pt.(^oC)	Elemental analysis (%) Calculated (Found)				
			C	H	N	S	Code
$C_6H_5N(H)CS_2ZnS_2C(CH_3)NC_6H_5$	White	210-215	43.32 (43.57)	3.39 (3.35)	6.74 (6.75)	30.83	ZnL^1L^2
$C_6H_5N(H)CS_2CdS_2C(CH_3)NC_6H_5$	Yellow	205-220	38.92 (37.98)	3.05 (3.08)	6.05 (6.10)	27.70	CdL^1L^2
$C_6H_5N(H)CS_2HgS_2C(CH_3)NC_6H_5$	pale green	150-155	32.61 (32.93)	2.56 (2.50)	5.07 (5.04)	23.17	HgL^1L^2
$C_6H_5N(H)CS_2ZnS_2C(C_2H_5)NC_6H_5$	White	190-210	44.87 (44.85)	3.77 (3.76)	6.54 (6.52)	29.88	ZnL^1L^3
$C_6H_5N(H)CS_2CdS_2C(C_2H_5)NC_6H_5$	Yellow	200-210	40.17 (40.24)	3.37 (3.74)	5.86 (5.70)	26.76	CdL^1L^3
$C_6H_5N(H)CS_2HgS_2C(C_2H_5)NC_6H_5$	Pale green	150-160	33.92 (33.90)	2.85 (2.82)	4.95 (4.93)	22.60	HgL^1L^3

3.2. Characterization of (N- phenyl-N, N-methyl phenyl dithiocarbamato)M(II) complexes, [ML^1L^2], where M = Zn, Cd, and Hg,

3.2.1 UV-Vis spectroscopy

The electronic spectra of dithiocarbamates ligands show three prominent absorption bands assigned to the chromophore group NCS_2 [19, 20]. In the spectrum of ammonium N-phenyldithiocarbamate ligand (L^1), the band at 34722 cm^{-1} (288 nm) is due to intraligand $\pi \rightarrow \pi^*$ transitions located on the NCS group. The band at 33557 cm^{-1} (298 nm) also arises

from $\pi \rightarrow \pi^*$ transitions, but within the SCS group. The band at 32467 cm^{-1} (308 nm) is attributed to $n \rightarrow \pi^*$ electronic transitions located on the sulfur atoms. In the spectrum of ammonium N-methyl-N-phenyldithiocarbamate (L^2), the band at 34482 cm^{-1} (290 nm) is due to intraligand $\pi \rightarrow \pi^*$ transitions located on the NCS group. The next band located at 33333 cm^{-1} (300 nm) also arises from $\pi \rightarrow \pi^*$ transitions, but within the SCS group. The band at 31645 cm^{-1} (316 nm) is attributed to $n \rightarrow \pi^*$ electronic transitions located on the sulfur atoms. The intraligand bands were also observed in the electronic spectra of Zn(II), Cd(II) and Hg(II) dithiocarbamate complexes, formulated as ZnL^1L^2, CdL^1L^2 and HgL^1L^2 [21, 22]. The three complexes are diamagnetic with electron configuration of d^{10} [23, 24].

3.2.2 Infrared spectra

The peaks of interest of the dithiocarbamate ligands and their corresponding metal complexes were carefully compared and assigned. The spectra are shown in Figure 3.2 and all the assignments of peaks are compared to those in literatures [25-30]. The bands of interest in the free ligands (L^1 and L^2) were observed in the range 1432-1488 cm^{-1} and 1069-1261 cm^{-1}attributed to the ν(C–N) and $\nu(C_2–N)$ respectively. The ν(C-H) frequencies were observed at 2930 $cm^{-1}$and 2852 cm^{-1}. Infrared spectra of the complexes showed that the thioureide ν(C–N) band is in the regions 1450-1500 cm^{-1} as observed in the ligands. Other ν(CN) vibrations, 1359 and 1261cm^{-1} were somewhat lower in the complexes. Both complexes showed more than two bands in the region 950-1050 cm^{-1} region due to ν(C-S). This is an indication that the dithiocarbamate ligands are bidentately coordinated to the metal ions. The ν(S-N) vibration is observed around 855 cm^{-1} in the complexes as well as the ligands. The bands in the far IR of the complexes attributed to the frequencies of metal(II)-sulfur bond, ν(M–S) were not observed since the bands in the 400-300 cm^{-1} range cannot be observed with a normal FTIR. In general, ν(M–S) frequencies are observed in the 400 and 350 cm^{-1} region.

Table 3.3 shows the infrared spectra data of dithiocarbamates ligands and their metal complexes of ML^1L^2.

Table 3.3: Selected IR spectra data for the ligands and complexes of ML^1L^2

Compound	**Vibrational Modes (cm^{-1})**			
	***v*C=S + *v*C-N**	***π*C=S**	***v*C=S**	***v*C-N**
L^1	757	646	548	1635, 1498, 1401, 1322, 1212, 1163, 1028
L^2	752	625	558	1606, 1492, 1406, 1357, 1268, 1154, 1057
ZnL^1L^2	758	625	555	1593, 1490, 1416, 1378, 1282, 1237, 1129, 1091, 1066
CdL^1L^2	758	623	523	1373, 1063
HgL^1L^2	768	626	557	1592, 1490, 1442, 1372, 1259, 1109, 1068

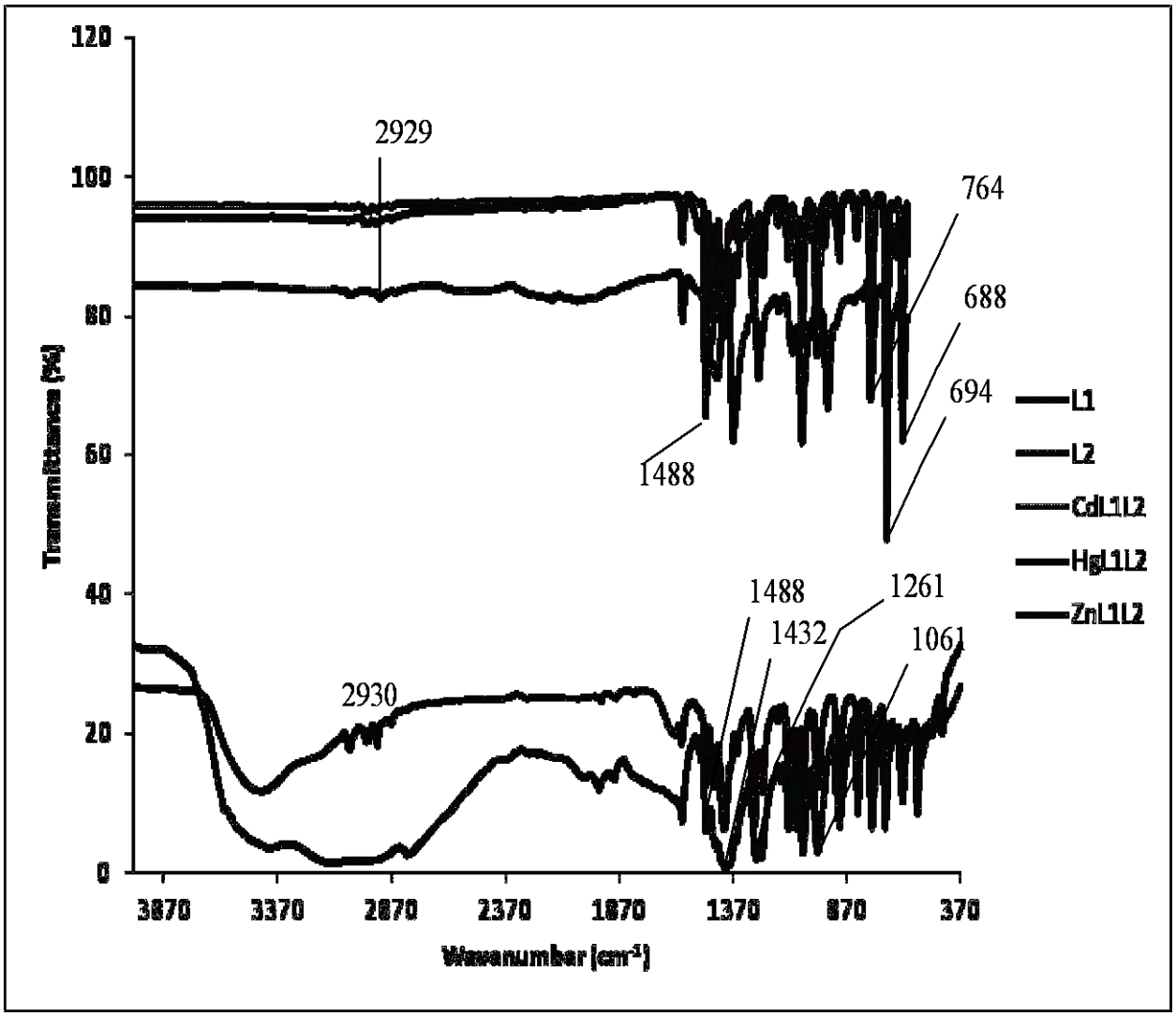

Figure 3.2: Infrared spectra of dithiocarbamate ligands and their corresponding metal complexes

3.2.3 NMR spectra of the ligands, (L^1 and L^2)

The ^{1}H- and ^{13}C-NMR spectra was recorded on a Bruker ultrashield 400 NMR spectrometer (400.1 MHz for ^{1}H, 100.6 MHz for ^{13}C nuclei) using dmso-d_6 solvent. The ^{1}H-NMR ammonium N-phenyldithiocarbamate ligand, (L^1) derived from aniline, display a broad singlet peak of one proton at 3.43 ppm, (1H, s) ascribed to (N-H) proton. The multiplex peaks appearing from 7.52-7.41 (m, 5H, $–C_6H_5$) ppm, was due to the phenyl ring protons [30]. The single peak appearing at 2.49 ppm is due to dimethylsulfoxide (dmso-d_6), the solvent used.

The ^{1}H-NMR of ammonium N-methly-N-phenyldithiocarbamate ligand, L^2 derived from methyl aniline, display a sharp singlet peak of three protons at 3.62 (s, 3H, N-CH_3) ppm. An up-field of 0.19 ppm as compared to L^1 was observed. This change could be attributed to electronegativity difference between N-H and N-C from L^1 and L^2 respectivelty. The multiplex peaks appearing from 7.27-6.49 ppm were due to the phenyl ring protons of L^2 [31]. The peak of the solvent DMSO-d_6 was found at 2.49 ppm, in the same position as L^1.

The ^{13}C-NMR of ammonium N-phenyldithiocarbamate ligand, L^1 revealed six aromatic carbons peaks between 113.89-128.81 ppm. The signal observed at 214.81 ppm is characteristic of carbon atom in -CS_2 of the dithiocarbamate ligand. The absence of the signal corresponding to alkyl group confirmed the structure of L^1. For ammonium N-methyl-N-phenyldithiocarbamate ligand, L^2, the signal due to –CH_3 group was found at 29.71 ppm. The signals for aromatic carbons were found in the region between 111.60-128.83 ppm. The signal due to – CS_2 appeared at 215.46 ppm. The presence of the signal due to –CH_3 group was found at 29.71 ppm confirmed the structure of L^2 [32].

3.2.4 NMR spectra of metal complexes, ML^1L^2

The ^{1}H-NMR signals of the dithiocarbamate complexes formulated as ML^1L^2were carefully assigned. For ZnL^1L^2 complex, there was a sharp singlet peak of one proton at 3.36 ppm (1H, s) ascribed to (N-H) proton of L^1 ligand. A downfield by δ 0.07 ppm as compared to the chemical shift of L^1 ligand was observed. There was a week signal at δ 3.63 ppm that could be assigned to methyl group bonded to N atom of the other ligand, L^2 (N-methly-N-phenyldithiocarbamate ligand). The multiplex peaks appearing from 7.52-7.11 (m, –C_6H_5) ppm, were due to the phenyl rings protons. The complex showed the single peak appearing at 2.49 ppm, due to dimethylsulfoxide solvent. For CdL^1L^2 complex, there was a sharp singlet

peak of one proton at 3.75 ppm (1H, s) ascribed to (N-H) proton of L^1 ligand. A sharp singlet peak at δ 3.54 ppm with shoulder at δ 3.46 ppm could be assigned to methyl group bonded N atom of the other ligand, L^2. The shoulder at δ 3.46 ppm may be due to impurities or contaminated compound. The multiplex peaks appearing from 7.49-7.03 (m, $–C_6H_5$) ppm, were due to the phenyl rings protons [33]. The complex showed single peak appearing at 2.62 ppm, due to dimethylsulfoxide (DMSO) solvent. For HgL^1L^2 complex, there was a sharp peak of one proton at 3.72 ppm (1H, s) ascribed to (N-H) proton of L^1 ligand. There was also a sharp singlet peak at δ 3.54 ppm assigned to methyl group bonded N atom of the other ligand, L^2. That peak at δ 3.54 ppm was also observed in Cd L^1L^2 complex. The multiplex peaks for aromatic rings protons appeared at 7.66-7.12 (m, $–C_6H_5$) ppm. The single peak due to dimethylsulfoxide (DMSO) solvent at 2.49 ppm was observed.

The aromatic ring carbon for the complexes appeared as multiplex in the region 123.42-130.01 ppm. The methyl carbon bonded to N atom appeared at 53.47 ppm in ZnL^1L^2, 48.54 ppm in CdL^1L^2 and HgL^1L^2 complexes respectively. The primary methyl carbon of the ethyl group was assigned to the peak in the region 12.16 ppm. The absence of a peak that is found between 12 and 14 ppm, corresponding to primary methyl carbon (when alkyl group of two or more C atom is present), was interesting since it revealed formation of the ML^1L^2 complexes [30-33].

3.2.5 Thermal decomposition of metal complexes, ML^1L^2

To evaluate whether the N-phenyl-N, N-methyl phenyl dithiocarbamato)M(II) complexes can be used as precursors for metal sulfide nanoparticles, their thermal behaviour was studied using thermogravimetric analysis (TGA). Thermal decomposition profile of the complexes, formulated as ZnL^1L^2, CdL^1L^2 and HgL^1L^2 in shown in Figure 3.3. The thermograms were

obtained using thermogravimetric analyzer operating under nitrogen environment, in order to evaluate the potentials of the complexes as single source precursors.

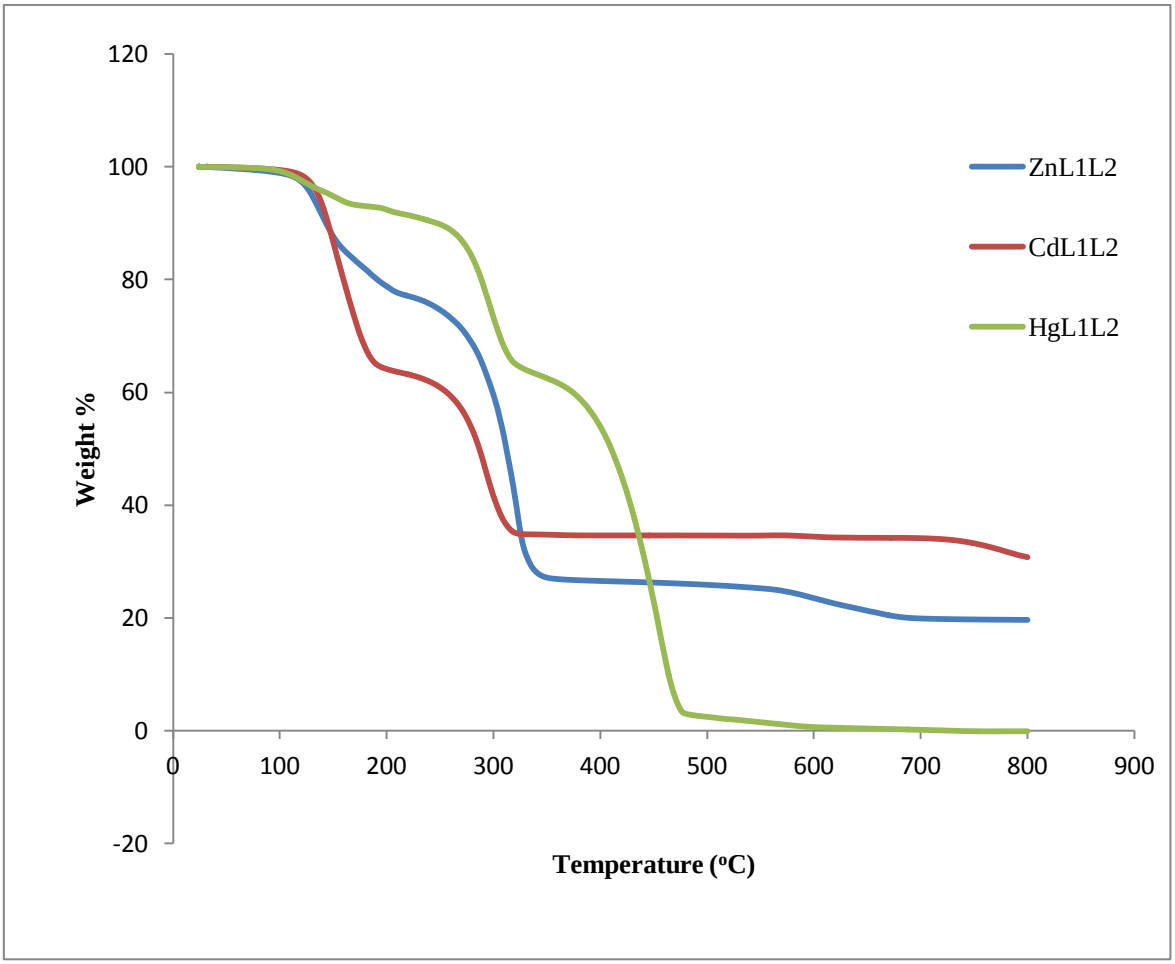

Figure 3.3: Superimposed TG profiles of ML^1L^2 complexes

Some dithiocarbamate complexes have been synthesized using mixed ligands method and thermal decomposition studies on those complexes were reported in the literatures [34-36]. The temperature ranges and percentage mass losses during the decompositions as well as the temperature corresponding to the maximum rate of decomposition, DTG_{max} are deduced from thermal decomposition profile of the complexes. A TG/DTG curves of the complexes formulated as ZnL^1L^2, CdL^1L^2 and HgL^1L^2 are shown in Figure 3.4.

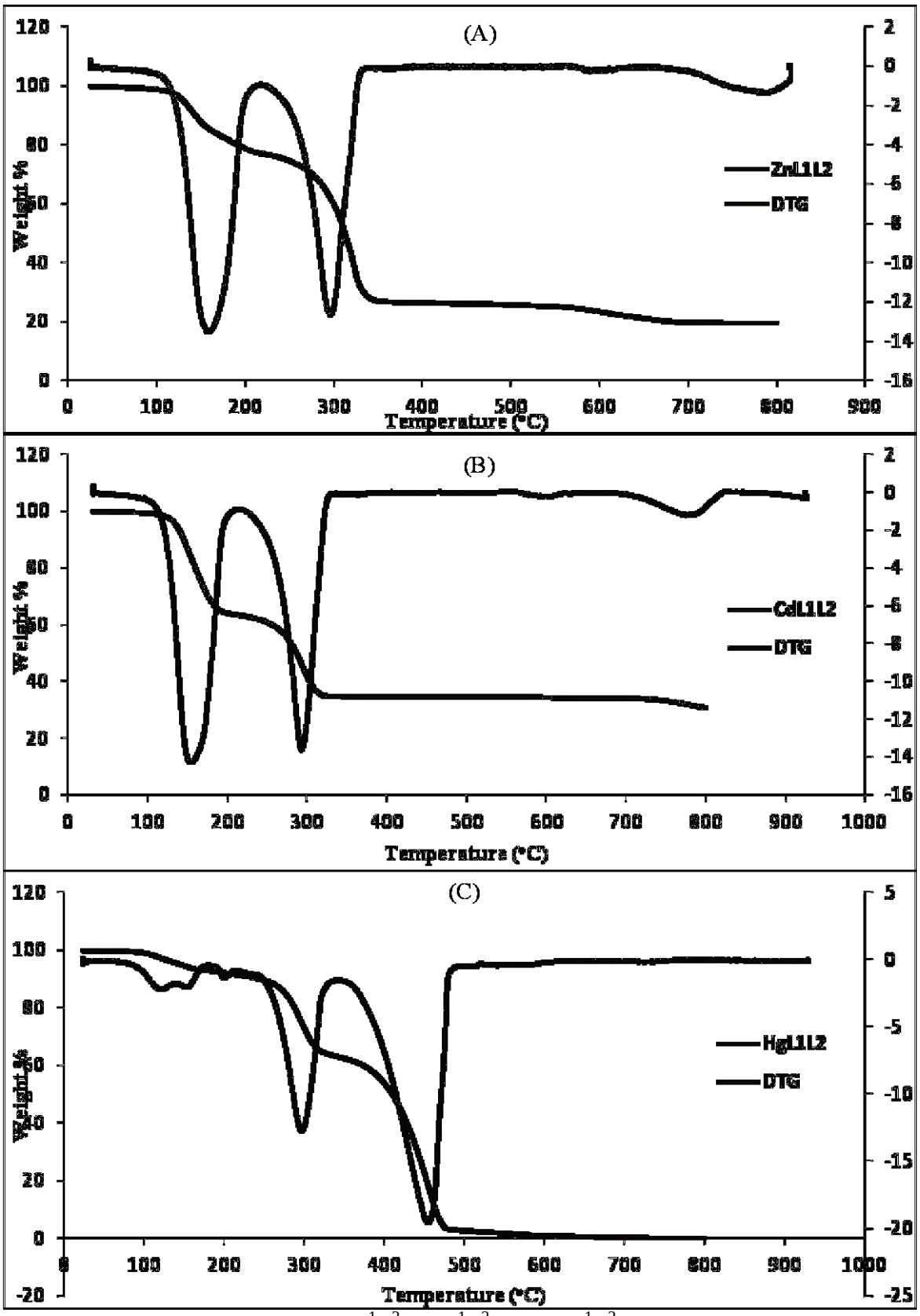

Figure 3.4: TG/DTG profiles of ZnL^1L^2, CdL^1L^2 and HgL^1L^2 complexes

The thermal decomposition of ZnL^1L^2 in Figure 3.3 shows two stage decomposition patterns as confirmed by the TG/DTG profiles of the complex in Figure 3.4 (A). In TGA curve, a weight loss of 76.8 % associated with the release of both N-phenyldithiocarbamate, L^1 and N-methly-N-phenyldithiocarbamate, L^2 ligands was observed. The two individual decomposition steps could not be separated since it is not clear which ligand decomposed first. Thermal decomposition of ZnL^1L^2 complex led to the formation of zinc sulfide (ZnS). The TG/DTG profiles of ZnL^1L^2 shows the two main degradation steps at 152 ^oC and 295 ^oC. The residual weight of 23.2 % is consisted with the calculated value of ZnS (23.4%).

The thermal decomposition of CdL^1L^2 is shown in Figures (3.3 and 3.4 (B)). There is a weight loss of 68.8 % associated with the decomposition of both L^1 and L^2 ligands, leaving the residual weight of about 31.5 %. This residual weight corresponds to the calculated value of CdS (31.2 %). The two main degradation step for the complex occur at 145 ^oC and 290 ^oC [37].

The thermal behaviour for HgL^1L^2 appeared different when compared to $ZnL^1L^2$and CdL^1L^2 complexes. The physical appearance of HgL^1L^2 was like a hydrate meaning that it had water in its crystal lattice. The TGA/DTG curve (Figure 3.4 (C)) displays three stages of decomposition. The first decomposition stage at 99.4 ^oC with the weight loss of about 5.5 % is assign to solvents or other contaminants reacted with complex due to a high reactivity of mercury [38]. The second step at 350 ^oC corresponds to the decomposition of both L^1 and L^2 ligands, leaving a total of residual weight of 35 % [39]. It has also been reported that the product of HgS heated in the air at 350 ^oC changes to mercuric oxide [40], which in turn decomposes to mercury vapour and oxygen at about 500 °C according to the chemical reaction in equation 3.2 [41, 42]:

$$HgS(s) \rightarrow Hg(g) + \frac{1}{2} S_2(g) \qquad 3.2$$

The last step of decomposition at 450 ^{o}C occurred during the volatilization of mercury compound leaving about 2 % of HgO. This residual weight of 35 % corresponds with the calculated value of HgO (39.3%). The superimposed TG profiles (Figure 3.4) of (N-phenyl-N, N-methyl phenyl dithiocarbamato)M(II) complexes suggest that the thermal stability increases in this order: $HgL^1L^2 < ZnL^1L^2 < CdL^1L^2$.

3.2.6 Scanning Electron Microscopy and EDX of CdL^1L^2

The SEM/EDX was employed to study the structural morphology and compositions of the thermal degradations residues obtained from decompositions of the complexes. The structured morphology of the decomposed product of the complex was determined by SEM analysis. Figure 3.5 show the SEM micrographs of complex at different magnification. The shape of the sample showed uniform hexagonal particles. The uniformity and similar dimension of particles indicate good crystallinity of the particles [43, 44]. The EDX elemental analysis (Figure 3.5 (C) showed the presence of cadmium and sulfur in the decomposed sample confirming the suitability of the complexes as single source precursor for the synthesis of cadmium sulfide nanoparticles.

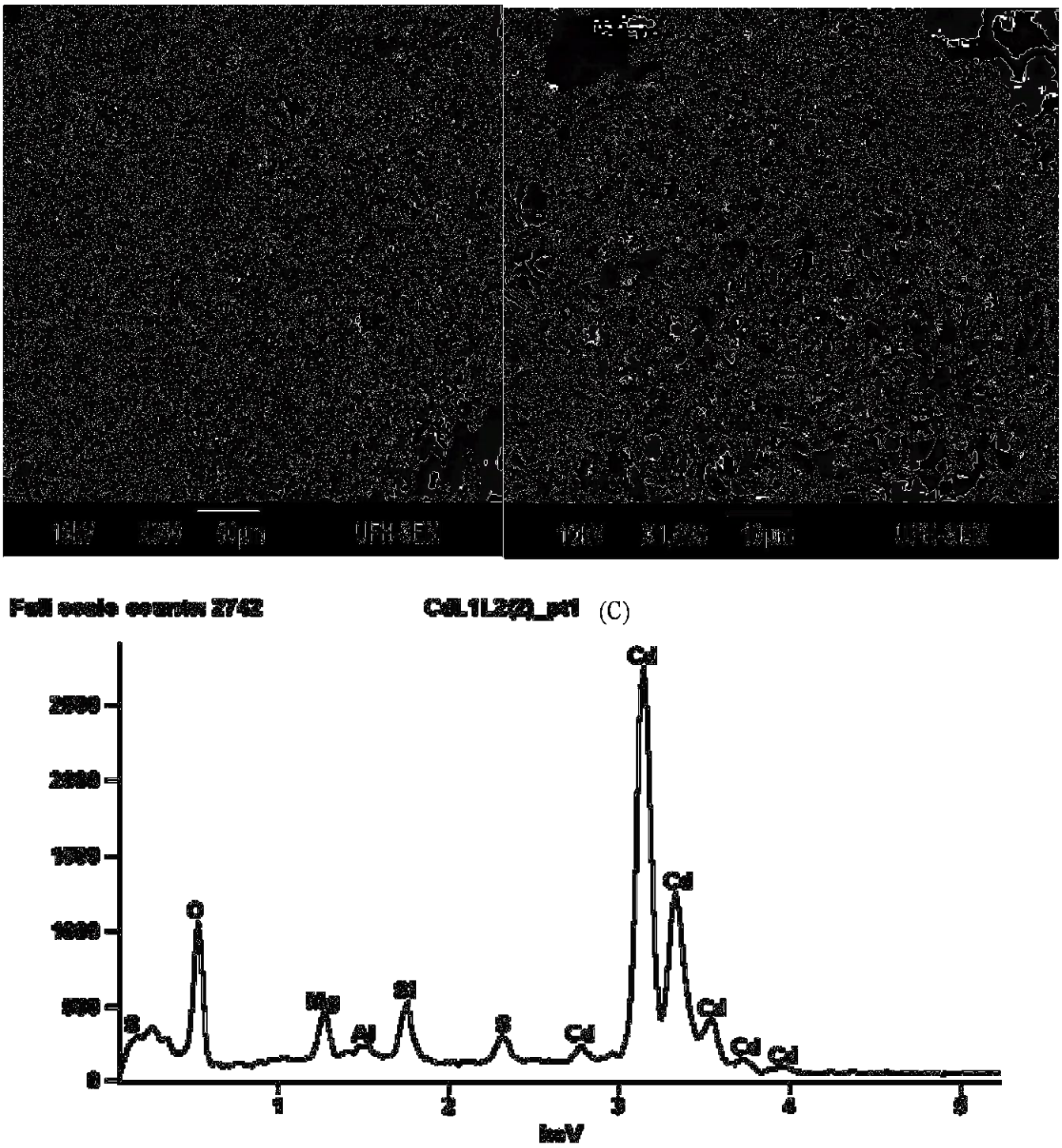

Figure 3.5: SEM micrograph of the complex CdL^1L^2 residues after thermal degradations (A) low magnification, (B) high magnification (C) EDX spectrum of the sample

3.2.7 Scanning Electron Microscopy and EDX of ZnL^1L^2

The SEM micrograph of the decomposed product of (N-phenyl-N, N-methyl phenyl dithiocarbamato)Zn(II**)** complex at different magnification are shown in Figures 3.6(A and B). The EDX elemental analysis in Figure 3.6 (C) show the presence of cadmium and sulfur in the decomposed sample confirming the suitability of the complexes as single source precursor for the synthesis of metal sulfide nanoparticles [45, 46]. The other traces of elements like, aluminium is from the melting aluminium pan used in TGA since the melting point of aluminium is 650 ^{o}C and oxygen reacted with sample during heating. The SEM/EDX of HgL^1L^2 complex could not be obtained because there was no residue at the end of thermogravimetric analysis experiment. This can be confirmed by the TGA/DTG curve of HgL^1L^2 in Figure 3.4 (C).

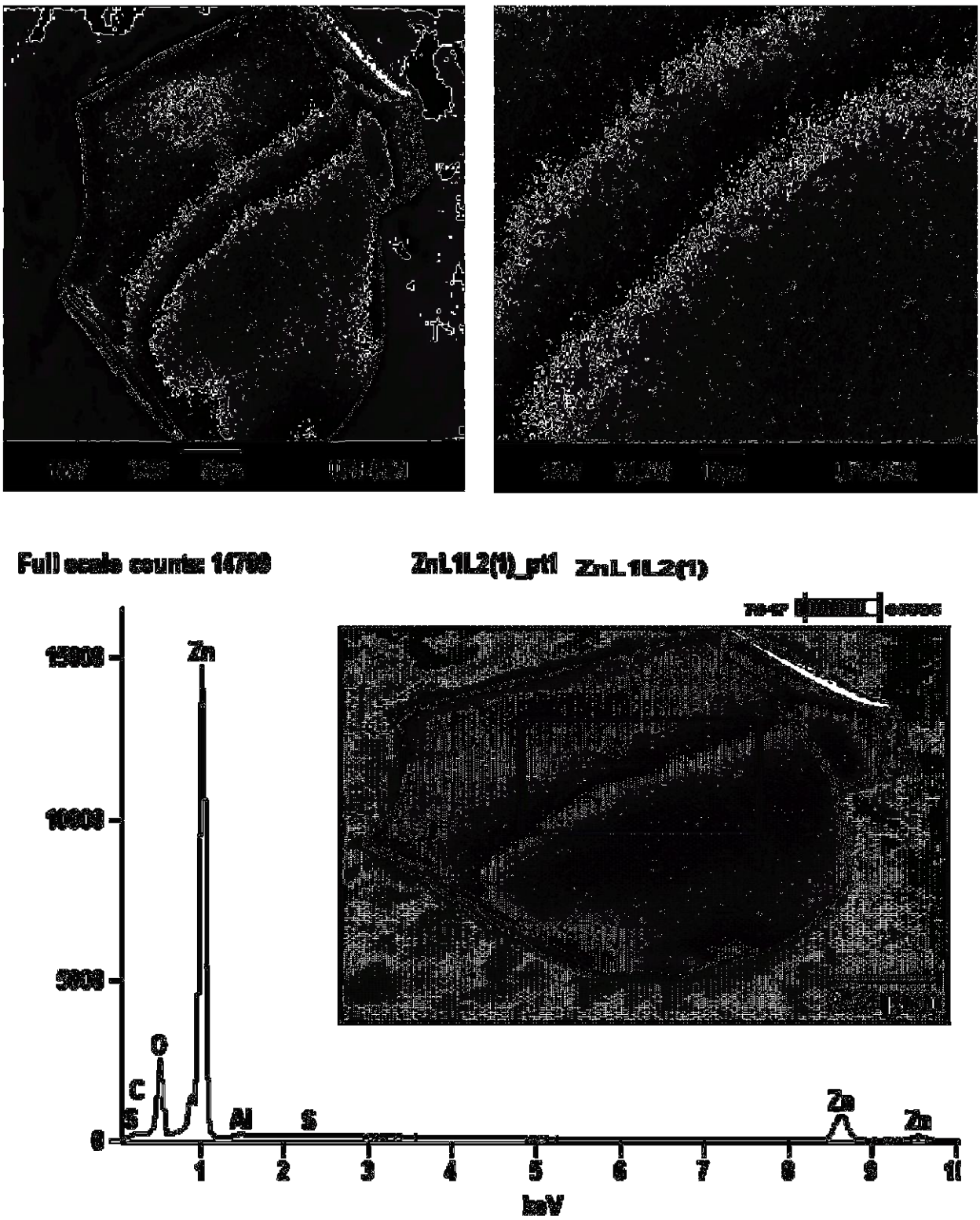

Figure 3.6: SEM micrograph of ZnL^1L^2 residues after thermal degradations (A) low magnification, (B) high magnification (C) EDX spectrum of the sample

3.3 Characterization of (N- phenyl-N, N-ethyl phenyl dithiocarbamato) M (II) complexes, [ML^1L^3], where M = Zn, Cd and Hg

3.3.1 Electronic spectra

In the spectrum of ammonium N-ethyl-N-phenyldithiocarbamate ligand (L^3), the bands at 34965 cm^{-1} (286 nm), 33333 cm^{-1} (300 nm) and 29498 cm^{-1} (339 nm) are due to intraligand $\pi \rightarrow \pi^*$ transitions located on the N-C=S group, $\pi \rightarrow \pi^*$ transitions within the S-C=S group and $n \rightarrow \pi^*$ electronic transitions located on the sulfur atoms respectively [47, 48]. The electronic spectrum of ammonium N-phenyldithiocarbamate ligand (L^1) was discussed earlier in this Chapter. In the electronic spectra of Zn(II), Cd(II) and Hg(II) complexes, the bands are below 350 nm confirming the presence of intra ligand $\pi \rightarrow \pi^*$ transitions, mainly associated with N-C=S and S-C=S groups [49]. The observed magnetic moment value of zero for Zn (II), Cd (II) and Hg (II) complexes, indicating diamagnetic nature of the complex [50, 51].

3.3.2 Infrared spectra

The infrared spectra of the ligands and their respective complexes are shown in Figure 3.7. The dithiocarbamate ligands (L^1 and L^3) show two diagnostic bands in their infrared spectra. First is the band due to ν(C–N) thioureide vibration which is observed in the region 1498-1548 cm^{-1} [52]. The special feature of dithiocarbamate ligands is an additional n-electron flow from nitrogen to sulfur *via* a planar delocalized π-orbital system [23, 50-52]. The high vibrational frequencies of this band in the complexes indicate a partial double bond character of the CN group arising from mesomeric drift of electrons from the dithiocarbamate moiety towards the M(II) ion centre [23] and the contribution of resonance structure in Figure 3.1 of the thioureide form in accordance with [7]. The second single band which appears in the

region 964–973 cm^{-1} corresponds to v(C–S) and indicates bidentate coordination mode of the dithiocarbamate moiety through the two sulfur donor-atoms [3].

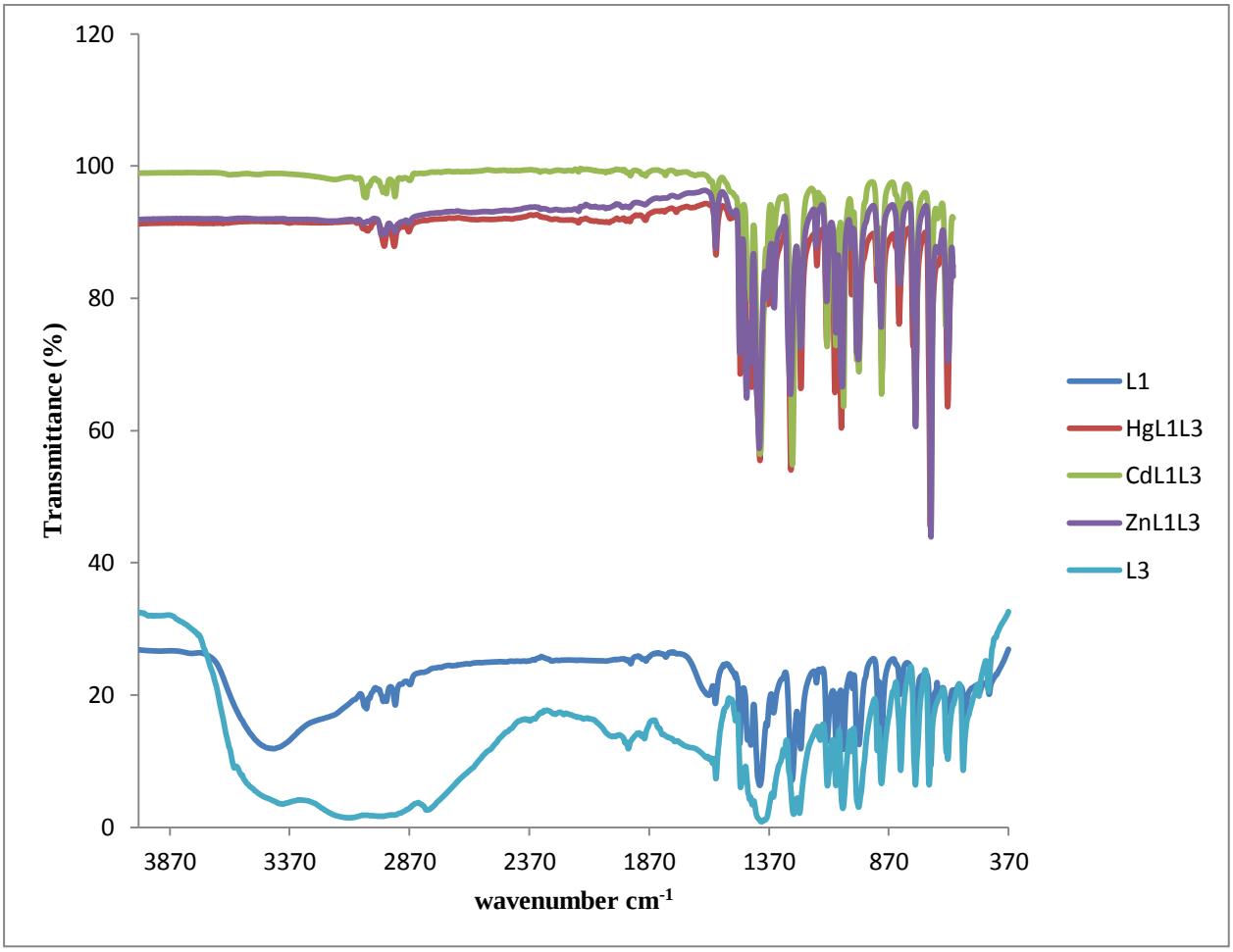

Figure 3.7: Infrared dithiocarbamate ligands and their corresponding mixed dithiocarbamate ligand complexes

Important IR bands for the ligands and complexes are given in Table 3.4. The existence of a single *v*(C=S) band at 755-758 cm^{-1} suggest that the ligands are bound to the metal ions in chelating bidentate modes [53]. The metal-ligand bond in the complexes was not shown since ATR-FTIR has runs from 4000-600 cm^{-1}. The M-S bond usually appeared in the region of 325-384 cm^{-1} indicated the existence of metal-ligand bond [54].

Table 3.4: Selected IR spectra data for the ligands and complexes of ML^1L^3

Compound	**Vibrational Modes (cm^{-1})**			
	***v*C=S + *v*C-N**	***π*C=S**	***v*C=S**	***v*C-N**
L^1	757	646	548	1635, 1498, 1401, 1322, 1212, 1163, 1028
L^3	758	623	559	1591, 1401, 1267, 1125, 1061
ZnL^1L^3	758	622	554	1592, 1492, 1410, 1348, 1280, 1129, 1065
CdL^1L^3	755	619	453	1625, 1595, 1491, 1406, 1350, 1273, 1126, 1058
HgL^1L^3	757	624	555	1408, 1277, 1128, 1067, 1002

The band observed at about 3436 cm^{-1} is undoubtedly assigned to the N-H stretching frequency in all complexes. This simply indicates that the nitrogen to metal bonds are not present and therefore the bonding in this complex is between the sulfur and the metal ions. The bonding of sulfur to metal ion is expected to increase the contribution of the highly polar structure to the dithiocarbamates, resulting in a greater double bond character for the nitrogen to carbon bond and a greater single bond character for the carbon to sulfur bond. In the free ligands, L^1 bands observed in the region 1635-1028 cm^{-1} and in L^3 bands observed in the region 1591-1061 cm^{-1}, are due to *v*(C-N) stretching vibrations. The vibration bands observed at 757 cm^{-1} in $L^1$and at 758 cm^{-1} in L^2, are due *v*(C=S) stretching vibrations. These bands are shifted to lower frequency by 1 cm^{-1} and 6 cm^{-1} in the complexes respectively. This behaviour signify a decrease in the double bond character of the C=S bond which confirms the coordination of sulfur atoms in the dithiocarbamates to the metal ions [55].

3.3.3 NMR spectra of ammonium N-ethyl-N-phenyl dithiocarbamate ligand

The ^{1}H-NMR of L^3 derived from ethyl aniline, reveal the chemical shift values for the methylene carbon bonded directly to N atom of L^3 (N-CH_2) observed in the range of 4.25-4.31 ppm. The primary protons in ethyl had chemical shift value which appeared up-field in the range 2.96-3.01 ppm [53]. The aromatic protons showed multiplex peaks appearing from 7.29-6.46 ppm [56] and the peak due to the DMSO solvent was found at 2.49 ppm.

The ^{13}C-NMR spectrum of L^3 reveal the signal due to α-carbon of the –CH_3 group was observed at 37.28 ppm and the –CH_2- carbon signal at 50.96 ppm. The six signals for aromatic carbons were found in the region 111.92-128.83 ppm. The signal due to –CS_2 appeared at 214.53 ppm. The presence of the signals due to –CH_3 and –CH_2- showing the attachment of ethyl group to N atom confirms the formation of the structure of ammonium N-ethyl-N-phenyldithiocarbamate ligand, (L^3). For all the dithiocarbamate ligands the signal corresponding to the solvent was found at 40 ppm.

3.3.4 NMR spectra of the metal complexes, ML^1L^3

For ZnL^1L^3 complex, it showed a quartet signals at δ 4.09, 4.10, 4.12 and 4.14 ppm, corresponding to ethyl group protons. The multiplex peaks for aromatic rings protons appeared at 7.25-7.45 (8H, m, –C_6H_5) ppm. A sharp peak of one proton at 3.36 ppm (1H, s) ascribed to (N-H) proton of L^1 ligand. The peak at δ 2.49 ppm was assigned to DMSO. For CdL^1L^3 complex, it showed a quartet signals at δ 4.09, 4.10, 4.12 and 4.14 ppm, corresponding to ethyl group protons. The multiplex peaks for aromatic rings protons appeared at 7.23-7.43 (8H, m, –C_6H_5) ppm. A sharp peak of one proton at 3.35 ppm (1H, s) ascribed to (N-H) proton of L^1 ligand. The peak at δ 2.49 ppm was observed for DMSO. The Hg L^1L^3 complex showed a multiplex signals at δ 4.07-4.17 (8H, m, –C_2H_5) ppm assigned to

ethyl group protons. The multiplex peaks for aromatic rings protons appeared at 7.22-7.46 (8H, m, $–C_6H_5$) ppm. A sharp peak of one proton at 3.35 ppm (1H, s) assigned to (N-H) proton of L^1 ligand is not easily seen due to deuterium exchange.

The ^{13}C-NMR spectrum of ZnL^1L^3 showed multiplex peaks for aromatic rings carbon at 126.96-129.22 ppm. The peak corresponding to ethyl group carbons bonded to N atom appeared at 53.46 ppm. The primary methyl carbon in ethyl was assign to the peak at 12.12 ppm. The complex CdL^1L^3 revealed the multiplex peaks for aromatic rings carbon at 126.88-129.15 ppm. A peak was observed for CH_3 carbon bonded to N atom at 54.69 ppm. The primary methyl carbon in ethyl was assign to 12.13 ppm. The HgL^1L^3 complex showed aromatic rings carbon appeared at 125.51-130.52 ppm. The single peak CH_3 carbon bonded to N atom appeared at 49.56 ppm. The primary methyl carbon in ethyl was assigned to 12.16 ppm and the peaks at this region were peaks of interest since they revealed the formation of the ML^1L^3 complexes.

3.3.5 Thermal decomposition patterns

The thermal decomposition of the ML^1L^3 complexes was investigated by the combination of TGA/DTG analysis. Figure 3.8 showed the superimposed TG profiles of the metal complexes formulated as ZnL^1L^3, CdL^1L^3 and HgL^1L^3. The thermogram pattern of ZnL^1L^3 displays two steps corresponding to 70 % weight loss associated with the release of both N-phenyldithiocarbamate, L^1 and N-elthyl-N-phenyldithiocarbamate, L^3 ligands. Thermal decomposition of the complex led to the formation of zinc sulfide (ZnS) with about 30 % residue, which was 7 % more than calculated value of 23 %. The TG/DTG profiles (Figure 3.9) of ZnL^1L^3 show that the two main degradation steps at 150 ^oC and 290 ^oC. The TGA pattern of CdL^1L^3 displays three main decomposition steps with a total weight loss of 80 %.

The first step of decomposition below 100 ^{o}C could be ascribed to the loss of solvents. The last two decomposition steps associated with the decomposition of both L^1 and L^3 ligands. The residue CdS of 20 % was obtained at the end of analysis and was 10% less than expected value of 30 % [57-61]. The TG/DTG profiles in Figure 3.9 confirm the three decomposition steps of the sample.

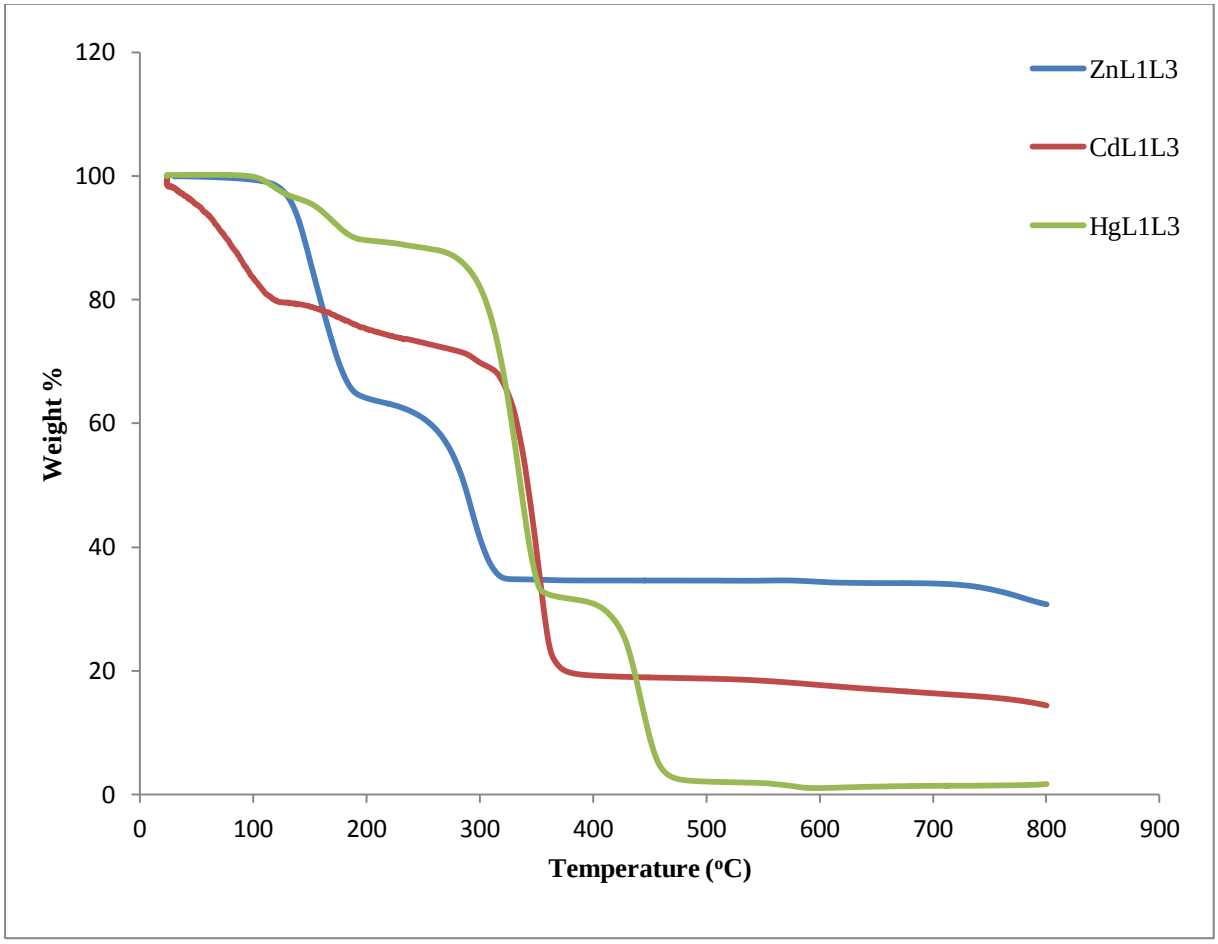

Figure 3.8: Superimposed TG profiles of ML^1L^3 complexes

The TGA pattern of HgL^1L^3 displays three main decomposition steps with a total weight loss of 95 % corresponding to the formation of the HgS. The TG/DTG reveals the high volatility of the sample at the temperature range of 280-460 ^{o}C but the complex can still be used as a precursor for the synthesis of HgS [57, 60, 61].

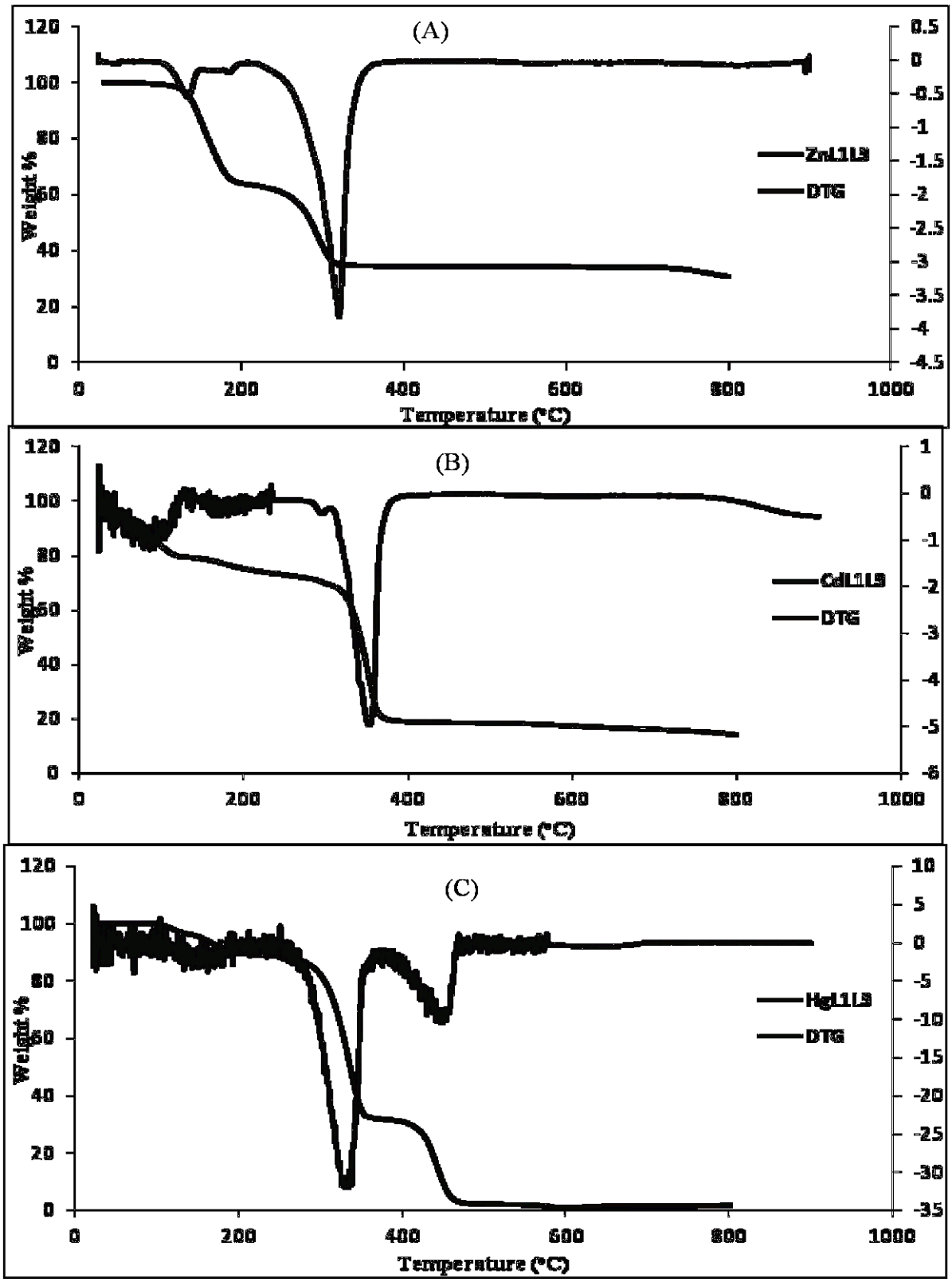

Figure 3.9: TG/DTG profiles of ZnL^1L^3, CdL^1L^3 and HgL^1L^3 complexes

3.4.0 Molecular structure of Zn and Hg Complexes

Crystal data and structure refinement information for complexes **1** and **2** are summarized in table 3.5. Crystal data and structure refinement information for complex **3**, a polymorph of complex **2**, are included for comparison purposes. Selected bond length and bond angles are shown in Tables 3.6 and 3.7.

Compound [Hg] is a pseudo-polymorph of a previously reported bis(μ_2-N-Ethyl-N-phenyldithiocarbamato-S,S')-bis-N-phenyldithiocarbamato-S,S')-di-mercury(II) (4) [62]. Whereas 4 crystallizes in $P2_1/c$ space group as centrosymmetric dimeric structure, complex [Hg] crystallizes in *P*-1 space group with two monomeric molecules of the Hg(II) complex and two molecules of toluene solvent in the asymmetric unit. One of the toluene solvent molecules is located in a general position, while the second one is disordered about an inversion centre. In both [Hg] molecules, the [Hg] centre is strongly coordinated by two S atoms with two short Hg—S bond distances of 2.3834(6) and 2.3985(6) for molecule **1** and 2.3848(6) and 2.4091(6) Å for molecule **2** and interact with the other two S atoms through two long Hg…S interactions 2.8139(6) and 2.8850(6) for molecule 1 and 2.7880(6) and 2.9348(6) Å for molecule **2** showing the tendency of [Hg] to prefer linear coordination geometry. The long Hg…S interactions in both molecules are possibly responsible for the deviation from ideal linear geometry as seen in the S5—Hg1—S8 and S1—Hg2—S4 angles of 166. 58(2) and 165.47(2)° respectively. Comparatively all bond distances and angles are similar to those of previously reported related complexes. Figure 3.14 shows the root mean square deviation overlay of the two cations. The root mean square deviation for the two cations is 0.0678. This value is relatively low and is probably due to the difference in the orientation of mainly the ethyl and phenyl moieties.

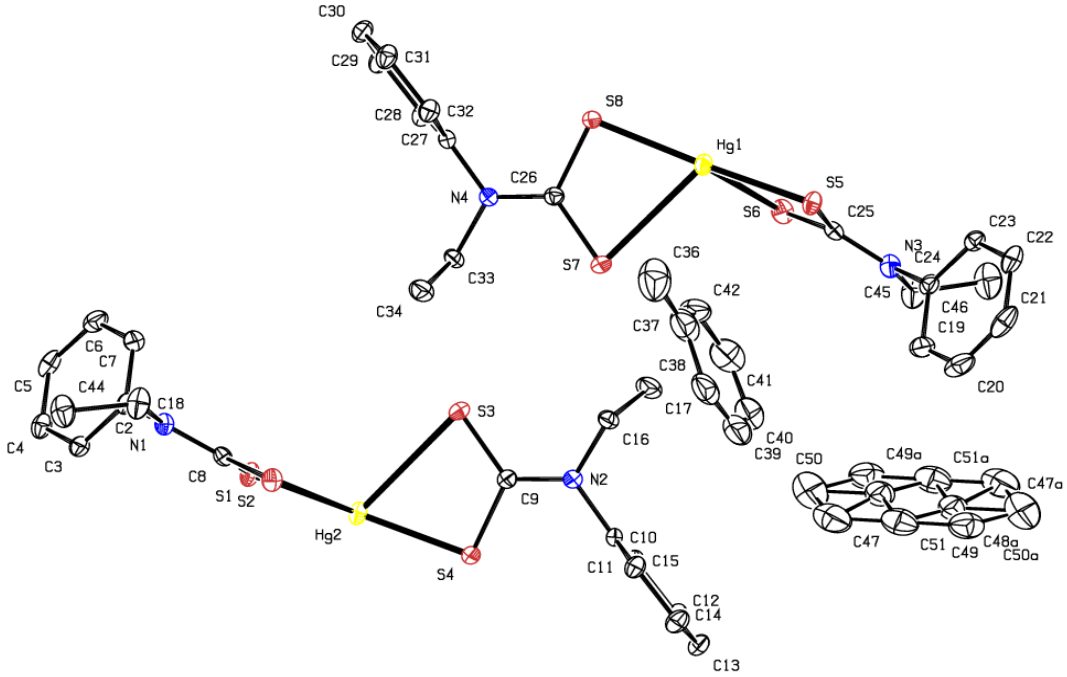

Figure 3.10: Molecular structure of the mercury complex

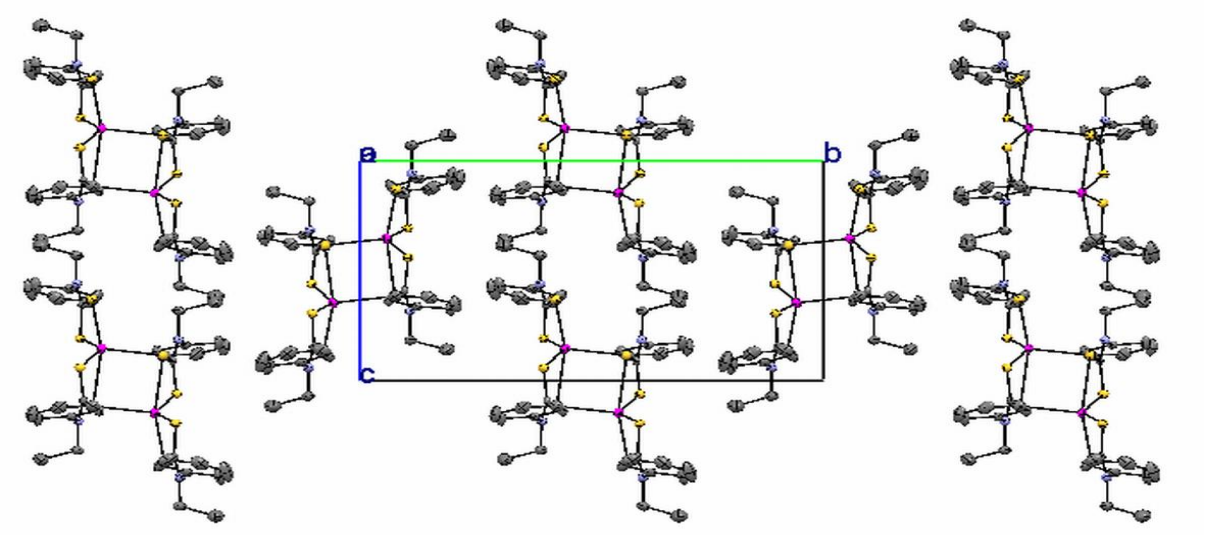

Figure 3.11: Packing diagram of the mercury complex

The [Zn] compound is a polymorph of 3 and is similar to a number of similar dithiocarbamates in literature diisopropyldithiocarbamate zinc [63] and diethyldithiocarbamate zinc [64]. The molecular structure is shown in Fig. 3.12 while important bond distances and angles are shown in Tables 3.6 and 3.7. Compound [Zn] has a

centrosymmetric dimeric structure in which the [Zn] atom symmetrically chelated by one terminal bidentate dithiocarbamate anion and non-symmetrically coordinated by the other dithiocarbamate anion. The coordinated dithiocarbamate uses the second S atom to bridge the two Zn(II) centers resulting in a binuclear dimeric complex. The two Zn—S chelating and the coordinating bond distances are 2.3333(11), 2.4647(11) and 2.3200(10) Å. The chelation and coordination behaviour of these ligands can also be confirmed by Δd and θ which are 0.1 Å and 3.6° respectively for the chelating ligand and 0.5 Å and 17.3° for the monodentate ligand. The bridging S atom interacts with the next [Zn] atom across an inversion center, forming a short Zn—S bond length of 2.3927(11) Å [symmetry code: 1-x, -y, 1-z] and this results in an eight-member symmetric metallacycle containing the two Zn(II) centers and the coordinating dithiocarbamate S and C atoms. Another Zn—S interaction is longer, 2.8539(11) Å and is comparable to corresponding values found in similar zinc dithiocarbamates [3, 64]. The Zn(II) centre shows a strongly distorted tetrahedral geometry, but if the long Zn—S bond distance is taken into account, then the Zn(II) center shows a distorted square pyramidal geometry, in which the square base is made up of CS_2—Zn—S_2C; the dihedral angle between the N—CS_2Zn planes is 39.3(3)°. The analogous Zn—S interaction in **3** is slightly shorter, 2.7513(6) Å while the dihedral angle is 41.8(2)°. Two of the tetrahedral angles deviate significantly (76.02(3)° and 137.33(4)° from the ideal 109°.

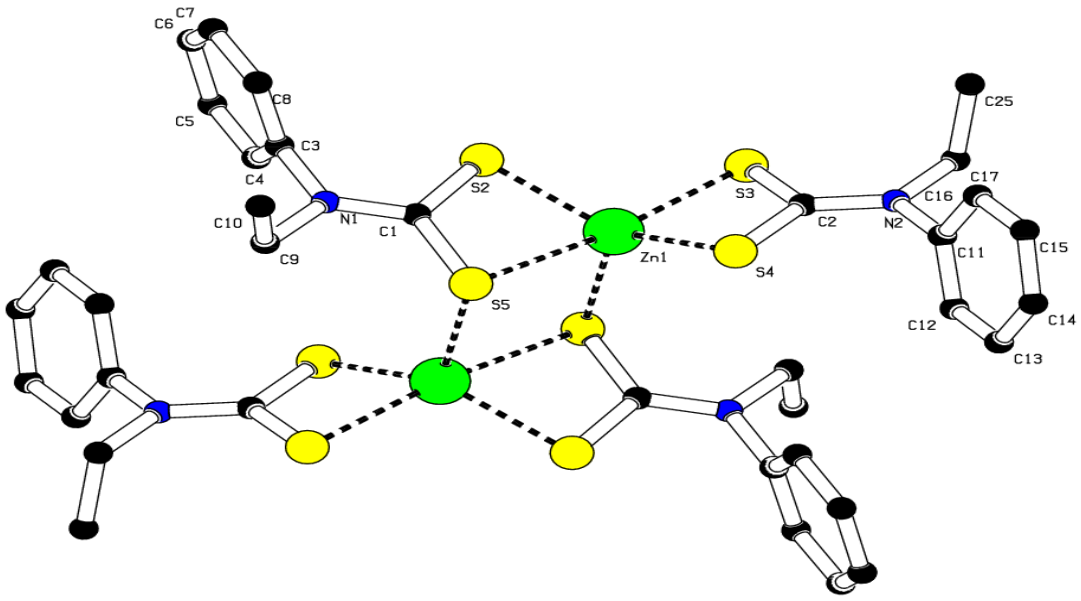

Figure 3.12: Molecular structure of the zinc complex

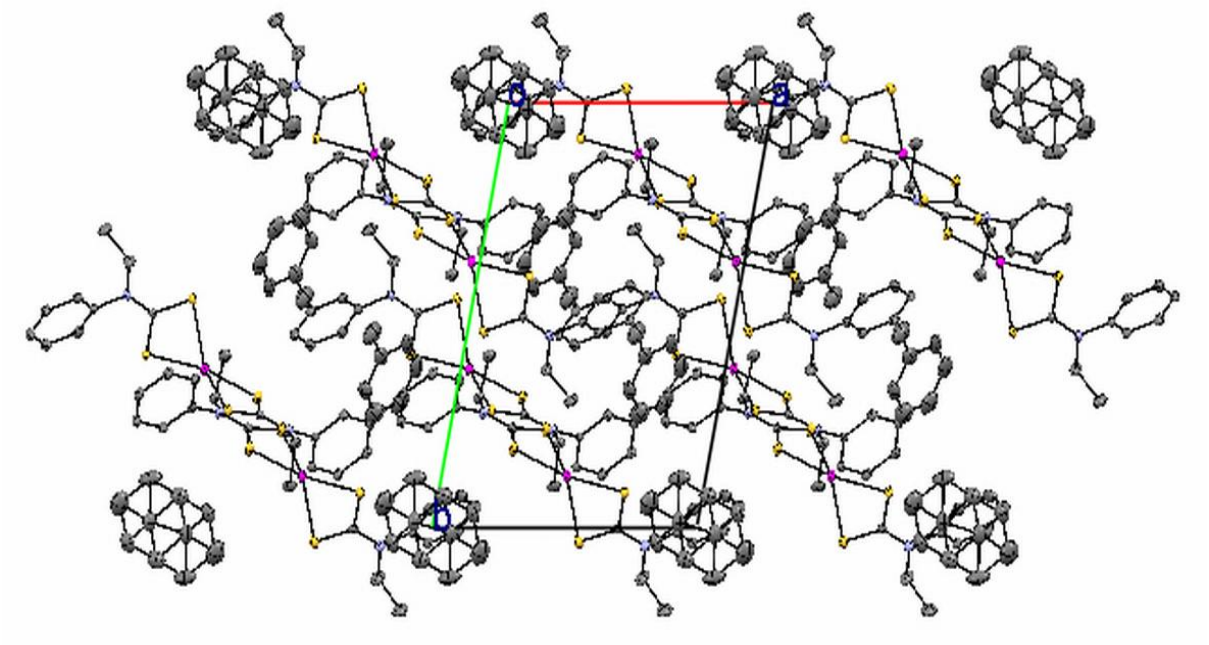

Figure 3.13: Packing diagram of the zinc complex

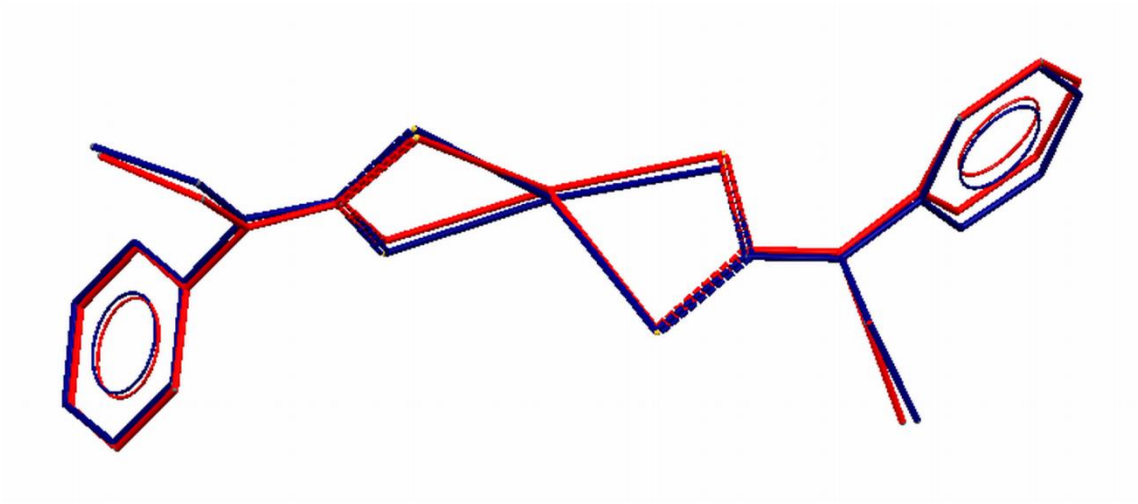

Figure 3.14: The root mean square deviation overlay picture of the two Hg(II) molecules in the asymmetric unit of Complex [Hg]

Table 3.5: Crystal data and structure refinement for Complexes 1 and 2 (polymorphs I and II)

	1	**2**	**3** [63]
Empirical formula	C_{93} H_{96} N_8 S_{16} Hg_4	C_{36} H_{40} N_4 S_8 Zn_2	C_{36} H_{40} N_4 S_8 Zn_2
Formula weight	2641.26	915.94	915.94
Temperature (K)	173(2)	173(2)	173(2)
Wavelength	0.71073	0.71073	0.71073
Crystal system	Triclinic	Monoclinic	Triclinic
Space group	*P*-1	$P2_1$/c	*P*-1
Unit cell dimensions			
a (Å)	10.9135(2)	10.2405(6)	8.7163(3)
b (Å)	15.3173(3)	17.8168(10)	10.5618(3)
c (Å)	15.6160(3)	14.6214(8)	12.0172(3)
α (°)	101.0320(10)		66.341(2)
β(°)	101.4750(10)	132.510(3)	79.577(2)
γ (°)	99.1740(10)		83.156(2)

Volume (Å^3)	2457.50(8)	1956.53(19)	995.26(5)
Z	1	2	1
D_{calc} (Mg m^{-3})	1.785	1.547	1.528
Absorption coefficient (mm^{-1})	6.616	1.677	1.657
F (0 0 0)	1286	944	472
Crystal size (mm)	0.31 x 0.20 x 0.15	0.28 x 0.28 x 0.28	0.20 x 0.18 x 0.16
θ range (°)	1.95 to 28.00	2.21 to 28.00	3.10 to 28.28
Limiting indices	-14<=h<=14,	-13<=h<=13,	-11<=h<=11,
	-20<=k<=20,	-23<=k<=23,	-14<=k<=14,
	-20<=l<=20	-19<=l<=18	-16<=l<=16
Reflections collected	51370	29865	31692
Independent reflections	11661	4679	4931
	[*R*(int) = 0.0283]	[*R*(int) = 0.0462]	[*R*(int) = 0.0341]
Completeness to θ = 28.45° (%)	98.3	98.5	99.8
Max. and min. transmission	0.4369 and 0.2335	0.6509 and 0.6509	0.7022 and 0.3245
Data / restraints / parameters	11661 / 0 / 564	4679 / 2 / 228	4471 / 28 / 235
Goodness-of-fit on F^2	1.075	1.134	1.111
Final *R* indices [$I > 2\sigma(I)$]	R_1 = 0.0187,	R_1 = 0.0511,	R_1 = 0.0127,
	wR_2 = 0.0451	wR_2 = 0.1308	wR_2 = 0.0322
R indices (all data)	R1 = 0.0232,	R1 = 0.0627,	R1 = 0.0135,
	wR2 = 0.0482	wR2 = 0.1367	wR2 = 0.0326
Largest diff. peak & hole (e.Å^3)	1.165 and -1.120	2.171 and -0.621	0.462 and -0.621

Absorption correction - Semi-empirical from equivalents; Refinement method - Full-matrix least-squares on F^2.

Table 3.6: Bond distances and angles (Å / °)

	Molecule 1	**Molecule 2**		**Molecule 1**	**Molecule 2**
Bond distances					
Hg—S	2.3834(6)	2.3848(6)	Hg—S	2.8139(6)	2.7880(6)
Hg—S	2.3985(6)	2.4091(6)	Hg—S	2.8850(6)	2.9348(6)
C—S	1.708(2)	1.710(2)	C—S	1.693(2)	1.689(2)
C—S	1.748(2)	1.746(2)	C—S	1.758(2)	1.755(2)
Bond angles					
S—Zn—S	68.437(17)	67.492(17)	S—Zn—S	114.191(18)	114.297(18)
S—Zn—S	69.348(18)	69.652(18)	S—Zn—S	124.056(19)	124.879(19)
S—Zn—S	93.550(17)	95.875(17)	S—Zn—S	166. 58(2)	165.47(2)
S—C—S	119.42(13)	119.47(14)	S—C—S	120.53(13)	120.17(13)

Table 3.7: Bond distances and angles (Å / °)

	2	**3** [63]		**2**	**3** [63]
Bond distances					
Zn—S	2.3200(10)	2.3501(7)	Zn—S	2.3333(11)	2.4007(5)
Zn—S	2.4647(11)	2.3659(6)	Zn—S	2.3927(11)	2.4431(6)
Zn—S	2.8539(11)	2.7513(6)			
C—S	1.716(4)		C—S	1.718(4)	
C—S	1.737(4)		C—S	1.738(4)	
Bond angles					
S—Zn—S	69.41(3)		S—Zn—S	106.34(4)	
S—Zn—S	76.02(4)		S—Zn—S	108.39(4)	
S—Zn—S	89.03(3)		S—Zn—S	114.74(4)	
S—Zn—S	94.99(4)		S—Zn—S	137.12(4)	
S—Zn—S	104.98(4)		S—Zn—S	164.33(4)	
S—C—S			S—C—S		

3.5 References

1. Valarmathi, P.; Thirumaran, S.; Ragi, P.; Ciattini, S. Synthesis and spectra studies on nitrogen donor adducts of bis(4-ethylpiperazinecarbodithioato-S,S')M(II) (M = Zn, Cd) and use of adducts of cadmium dithiocarbamate for the preparation of cadmium sulfide. *J. Coord. Chem.* **2011**, *64*, 4157-4167.
2. Bang, J.H.; Suslick, K.S. Applications of ultrasound to the synthesis of nanostructured materials. *Adv. Mater.* **2010**, *22*, 1039-1059.
3. Onwudiwe, D.C.; Ajibade, P.A. Synthesis and characterization of metal complexes of N-alkyl-N-phenyl dithiocarbamates. *Polyhedron* **2010**, *29*, 1431-1436.
4. McGarrigle, E.M.; Myers, E.L.; Illa, O.; Shaw, M.A.; Riches, S.L.; Aggarwal, V.K. Chalcogenides as organocatalysts. *Chem. Rev*. **2007**, 107, 5841-5883.
5. Victoriano, L.I. The reactivity of metal species towards thiuram sulfides: An alternative route to the syntheses of metal dithiocarbamates. *Coord. Chem. Rev.* **2000**, *196*, 383-398.
6. Mamba, S.M. Synthesis, characterization and applications of dithiocarbamate transition metal complexes. M.Sc. Thesis, University of Johannesburg, RSA, **2009**.
7. Ajibade, P.A.; Onwudiwe, D.C. Synthesis and characterization of group 12 complexes of N,N-methyl phenyl-N,N-butyl phenyl dithiocarbamate. *J. Coord. Chem.* **2011**, 64, 2963-2973.
8. Elduque, A.; Finestra, C.; Lopez, J.A.; Lahoz, F.J.; Merchan, F.; Oro, L.A.; Pinillos, M.T. Rhodium dithiocarbamate compounds as metalloligands: A controlled way for the construction of binuclear complexes. *Inorg. Chem.* **1998**, *37*, 824-829.
9. Onwudiwe, D.C.; Ajibade, P.A. Synthesis and crystal structure of bis(N-alkyl-N-phenyl dithiocarbamato)mercury(II). *J. Chem. Crystallogr*. **2011**, *41*, 980-985.

10. Chauhan, H.P.S.; Shaik, N.M.; Singh, U.P. Synthetic, spectroscopic and antimicrobial studies of bis(dialkyldithiocarbamato)diorganodithiophosphatobismuth(III) complexes. *Appl. Organometal. Chem.* **2005**, *19*, 1132-1139.
11. Srinivasan, N.; Rani, P.J.; Thirumaran, S. Synthesis and spectra studies on mixed ligand complexes of Cd(II) dithiocarbamates with nitrogen donors: Single crystal X-ray structure of bis(4-methylpiperidinecarbodithioato-S,S')(1,10-phenanthroline)cadmium(II). *J. Coord. Chem.* **2009**, *62*, 1271-1277.
12. Budnikov, G.K.; Troepol'skaya, T.V. Electrochemistry of metal chelates in non-aqueous media. Translated from *Uspekhi Khimii*. **1979**, *48*, 829-853.
13. Singh, N.; Kumar, A.; Prasad, R.; Molloy, K.C.; Mahon, M.F. Syntheses, crystal, photoluminescence and electrochemical investigation of some new phenylmercury(II) dithiocarbamate complexes involving ferrocene. *Dalton Trans.* **2010**, *39*, 2667-2675.
14. Manav, N.; Mishra, A.K.; Kaushik, N.K. Triphenyl phosphine adducts of platinum(IV) and palladium(II) dithiocarbamates complexes: A spectra and *in vitro* study. *Spectrochim. Acta Part A.* **2004**, *60*, 3087-3092.
15. Manav, N.; Mishra, A.K.; Kaushik, N.K. *In vitro* antitumour and antibacterial studies of some Pt(IV) dithiocarbamate complexes. *Spectrochim. Acta Part A.* **2006**, *65*, 32-35.
16. Khan, H.; Badshah, A.; Zia-ur- Rehman, Said, M.; Murtaza, G.; Shah, A.; Butler, I.S.; Ahmed, S.; Fontaine, F.-G. New dimeric and supramolecular mixed ligand palladium(II) dithiocarbamates as potent DNA binders. *Polyhedron* **2012**, *39*, 1-8.
17. Kheiri, F.-N.; Tsipis, C.A.; Tsiamis, C.L.; Manoussakis, G.E. Syntheses and spectroscopic study of a new series of mixed-ligand complexes of As(II1) and Sb(II1) with dithio-ligands. *Can. J. Chem.* **1979**, *57*, 767-772.

18. Pastorek, R.; Kameníček, J.; Březina, F.; Šindelář, Z.; Jehlářová, E.; Duffy, N.V.; Glowiak, C.T. Dithiocarbamate complexes of nickel with triphenylphosphine and isothiocyanate as mixed ligands. *Chem. Papers* **1994**, *48*, 317-323.
19. Mahapatra, B.B.; Panda, S.K. Coordination compounds of Co^{II}, Ni^{II}, Cu^{II}, Zn^{II}, Cd^{II} and Hg^{II} with tridentate ONS Donor Azo dye ligands. *Biokemistri Vol.* **2010**, *22*, 71-75.
20. Leka, Z.; Grujic, S.A.; Tesic, Z.; Lukic, S.; Skuban, S.; Trifunovic,S. The synthesis and characterization of complexes of zinc(II), cadmium(II), platinum(II) and palladium(II) with potassium 3-dithiocarboxy-3-aza-5-aminopentanoate. *J. Serb. Chem. Soc.* **2004**, *69*,137-143.
21. El-Said, A.I.; Aly, A.A.M.; El-Meligy, M.S.; Ibrahim, M.A. Mixed ligand zinc(II) and cadmium(II) complexes containing ceftriaxone or cephradine antibiotics and different donors. *J. Argent. Chem. Soc.* **2009**, *97*, 149-165.
22. Liu, J.-N.; Wu, B.-W.; Zhang, B.; Liu, Y. Synthesis and characterization of metal complexes of Cu(II), Ni(II), Zn(II), Co(II), Mn(II) and Cd(II) with tetradentate schiff bases. *Turk. J. Chem.* **2006**, *30*, 41-48.
23. Moloto, N.; Revaprasadu, N.; Moloto, M.J.; O'Brien, P.; Raftery, J. N, N'-diisopropylthiourea and N,N'-dicyclohexylthiourea zinc(II) complexes as precursors for the synthesis of ZnS nanoparticles. *S. Afr. J. Sci.* **2009**, *105*, 258–263.
24. Osowole, A.A.; Oni, A.A.; Onyegbula, K.; Hassan, A.T. Synthesis, spectra, magnetic and *In vitro* anticancer properties of some metal(II) complexes of 3-[2,4-dihydro-1H-inden-4-ylimino) methyl] napthalene-2-ol. *Inter. Res. J. Chem.* **2012**, *2*, 211-220.
25. Odola, A.J.; Woods, J.A.O. Synthesis, characterization and antimicrobial activity studies of new Nickel(II) mixed ligand complexes of disubstituted dithiocarbamates with ethylsalicylaldiminate. *Arch. Appl. Sci. Res.* **2011**, *3*, 463-470.

26. Raya, I.; Baba, I.; Yamin, B.M. New mixed ligands complexes of samarium(III) with dithiocarbamates and 1,10-phenanthroline. *Malaysia J. Anal. Sci.* **2006**, *10*, 93-98.

27. Regulacio, M.D.; Tomson, N.; Stoll, S.L. Dithiocarbamate precursors for rare-earth sulfides. *Chem. Mater.* **2005**, *17*, 3114-3121.

28. Nabipour, H. Synthesis of a new dithiocarbamate cobalt complex and its nanoparticles with the study of their biological properties. *Int. J. Nano. Dim.* **2011**, *1*, 225-232.

29. Ahmad, S.; Sarwar, M.; Ahmad, S.; Ali, S.; Khurram. Mixed ligand copper (II) complexes of pyrrolidinedithiocarbamate and diamines. *J. Chem. Soc. Pak.* **2010**, *32*, 443-448.

30. Alverdi, V.; Giovagnini, L.; Marzano, C.; Seraglia, R.; Bettio, F.; Sitran, S.; Graziani, R.; Fregona, D. Characterization studies and cytotoxicity assays of Pt(II) and Pd(II) dithiocarbamate complexes by means of FT-IR, NMR spectroscopy and mass spectrometry. *J. Inorg. Biochem.* **2004**, *98*, 1117-1128.

31. Alverdi, V.; Giovagnini, L.; Marzano, C.; Seraglia, R.; Bettio, F.; Sitran, S.; Graziani, R.; Fregona, D. Characterization studies and cytotoxicity assays of Pt(II) and Pd(II) dithiocarbamate complexes by means of FT-IR, NMR spectroscopy and mass spectrometry. *J. Inorg. Biochem.* **2004**, *98*, 1117-1128.

32. Kamaludin, N.F.; Awang, N.; Baba, I.; Hamid, A.; Meng, C.K. Synthesis, characterization and crystal structure of organotin(IV) N-butyl-N-phenyldithiocarbamate compounds and their cytotoxicity in human leukemia cell lines. *Pak. J. Bio. Sci.* **2013**, *16*, 12-21.

33. Coleman, J.N.; Weiss, E.A.; Frederick, M.T. Influence of binding dithiocarbamate ligands on charge transport through solid-state arrays of colloidal CdSe quantum dots. *Nanoscape* **2011**, *8*, 40-44.

34. Awang,N.; Baba, I.; Yamin, B.M.;Halim, A.A. Preparation, characterization and antimicrobial assay of 1,10-phenanthroline and 2,2'-bipyridyl adducts of cadmium(II) N-sec-butyl-N-propyldithiocarbamate: Crystal structure of $Cd[S_2CN(i\text{-}C_4H_9)(C_3H_7)]$ (2,2'-bipyridyl). *World Appl. Sc. J.* **2011**, *12*, 1568-1574.

35. Dawood, Z.F.; Mohammed, T.J.; Sharif, M.R. New nickel (II) complexes with benzilbis (semicarbazone) and dithiocarbamate ligands. In *Proceedings of the 5th Scientific Conference, College of Veterinary Medicine, University of Mosul, Iraqi J. Vet. Sci.* **2009**, *23*, 135-141.

36. Kodina, G.E.; Malysheva, A.O.; Klement'eva, O.E.; Gorshkov, N.I.; Lumpov, A.A.; Suglobov, D.N. Synthesis and *in vitro* evaluation of $Tc(CO)_3^+$ complexes with dithiocarbamate ligands containing morpholine moiety. *J. Nuc. Radiochem. Sci.* **2005**, *6*, 187-188.

37. Memon, A.A.; Afzaal, M.; Malik, M.A.; Nguyen, C.Q.; O'Brien, P.; Raftery, J. The N-alkyldithiocarbamato complexes $[M(S_2CNHR)_2]$ (M = Cd(II) Zn(II); R = C_2H_5, C_4H_9, C_6H_{13}, $C_{12}H_{25}$); their synthesis, thermal decomposition and use to prepare of nanoparticles and nanorods of CdS. *Dalton Trans.* **2006**, 4499-4505.

38. Sabounchei, S.J.; Bagherjeri, F.A.; Boskovic, C.; Gable, R.W.; Karamian, R.; Asadbegy, M. Reactivity of mercury(II) halides with the α-keto stabilized sulfonium ylides: Crystal structures of two new polymer and binuclear complexes and *in vitro* antibacterial study. *Polyhedron* **2013**, *53*, 1-7.

39. Kumar, S.; Kaushik, N.K. Preparation, characterization and thermal studies on bis-[N-(ethyl, m-tolyl)-dithiocarbamato] complexes of zinc(II), cadmium(II) and mercury(II). *J. Therm. Anal.* **1981**, *21*, 3–7.

40. Onwudiwe, D.C.; Ajibade, P.A. Synthesis, characterization and thermal studies of Zn(II), Cd(II) and Hg(II) Complexes of N-methyl-N-phenyldithiocarbamate: The single crystal structure of $[(C_6H_5)(CH_3)NCS_2]_4Hg_2$. *Int. J. Mol. Sci.* **2011**, *12*, 1964-1978.
41. Onwudiwe, D.C.; Ajibade, P.A. Thermal studies of Zn(II), Cd(II) and Hg(II) complexes of some N-alkyl-N-phenyl dithiocarbamates. *Int. J. Mol. Sci.* **2012**, *13*, 9502-9513.
42. Hardy, A.D.; Sutherland, H.H.; Vaishanav, R.; Worthing, M.A. A report on the composition of mercurials used in traditional medicines in Oman. *J. Ethropharmacol*. **1995**, *49*, 17-22.
43. Zhang, Y.C.; Wang, G.Y.; Hu, X.Y. Solvothermal synthesis of hexagonal CdS nano-structures from a single-source molecular precursor. *J. Alloys Compd.* **2007**, *437*, 47-52.
44. Sabah, A.; Siddiqi, S.A.; Ali, S. Fabrication and characterization of CdS nanoparticles annealed by using different radiations. *W.Ac. Sci, Eng. Tech*. **2010**, 82-89.
45. Song, C.; Yang, M.; Wang, D.; Hu, Z. Synthesis and optical properties of ZnS hollow spheres from single source precursor. *Mater. Res. Bull*. **2010**, *45*, 1021-1025.
46. Liu, S.; Zhang, H.; Swihart, M.T. Spray pyrolysis synthesis of ZnS nanoparticles from a single-source precursor. *Nanotech*. **2009**, *20*, 1-8.
47. Al-Sabaawi, S.A. Synthesis and characterization of some mononuclear Mn(II), Fe(II), Co(II), Ni(II), Cu(II) and Zn(II) complexes containing bis-(2-thiophenelidene) thiosemicarbazone ligand. *Col. B. Edu. Res. J*. **2011**, *11*, 765-776.
48. Padmaja, M.; Pragathi, J.; Anupama, B.; Kumari, C.G. Synthesis, spectra characterization, molecular modeling, and mntimicrobial studies of Cu(II), Ni(II), Co(II), Mn(II) and Zn(II) complexes of ONO Schiff base. *E. J. Chem*. **2012**, *9*, 2145-2154.
49. Beck W.; Giunth M.; Castilo M.; Zippel H. N-dithiocarboxy-α-aminosaure-complexes of nickel, palladium and platinum(II). *Chem.Ber*. **1978**, *111*, 1246-1252.

50. Dos Santos, H.F.; De Almeida, W.B.; Zerner, M.C. Theoretical near UV and Visible electronic spectra for the Zn^{II}-anhydrotetracycline complex. *J. Chem. Soc. Perkin Trans.* **1998**, *2*, 2519-2526.

51. Osowole, A.A.; Oni, A.A.; Onyegbula, K.; Hassan, A.T. Synthesis, spectra, magnetic and *in-vitro* anticancer properties of some metal(II) complexes of 3-[2,4-dihydro-1H-inden-4-ylimino) methyl] napthalene-2-ol. *Inter. Res. J. Chem.* **2012**, *2*, 211-220.

52. Ajibade, P.A.; Idemudia, O.G.; Okoh, A.I. Synthesis, characterization and antibacterial studies of metal complexes of sulfadiazine with N-alkyl-N-phenyldithiocarbamate. *Bull. Chem. Soc. Ethiop.* **2013**, 27, 77-84.

53. Muthalib, A.F.A.; Baba, I.; Farina, Y.; Samsudin, M.W. Synthesis and characterization of diphenyltin(IV) dithiocarbamate compounds. *Mal. J. Anal. Sci.* **2011**, *15*, 106-112.

54. Rodarte de Moura, C.V.; de Sousa, A.P.G.; Silva, R.M.; Abras, A.; Horner, M.; Bortoluzzi, A.J.; Filgueiras, C.A.L.; Wardell, J.L. Syntheses and spectra of triphenyltin heteroarenethiolates - crystal structures of triphenyltin 1-methyltetrazole-5-thiolate and triphenyltin benzoxazole-2-thiolate. *Polyhedon* **1999**, 18, 2961-2969.

55. Criado, J.J.; Fernandez, I.; Macias, B. Novel chelates of Pd(II) dithiocarbamates: Spectroscopic studies and thermal behaviour. *Inorg. Chim. Acta.* **1990**, *174*, 67-75.

56. Ahamad, M.M.; Rao, R.M.; Kumar, E.V.S.; Jayaraju, A.; Begum, N.T; Sreeramulu, J. Synthesis, characterization and biological evaluation of novel dithiocarbamate metal complexes. *J. Chem. Pharm. Res.* **2012**, *4*, 1601-1605.

57. Khan, S.; Nami, S.A.A.; Siddiqi, K.S. Piperazine pivoted transition metal dithiocarbamates. *J. Mol. Struct.* **2008**, *875*, 478–485.

58. Bonati F.; Ugo R. Organotin(IV) N,N'-disubstituted dithiocarbamates. *J. Organomet. Chem.* **1967**, *10*, 257- 268.

59. Pandeya, K.B.; Singh R.; P Mathur. K.; Singh R.P. E.S.R. spectra of mixed ligand manganese(II) dithiocarbamates. *Transition Met. Chem.* **1986**, *11*, 340-350.

60. Manohar, A.; Ramalingam, K.; Karpagavel, K.; Kulandaisamy, A. bis(di(2-hydroxyethyl)dithiocarbamato) cadmium(II) with N-donor ligands: Synthesis, spectra, thermal studies and bond valence sum (BVS) analysis. *Int. J. Chem. Tech Res*. **2012**, 4, 1023-1032.

61. Gajanan, P.; Sharma, H.K. A new approach of synthesis of micro/nanoscale HgS spheres. *Synth. React. Inorg. Met.-Org. Nano-Met. Chem*. **2010**, *40*, 312-318.

62. Ondrusova, D; Pajtasova, M; Jona, E; Koman, M. Structural properties of Co(III), Hg(II) and Pb(II) N-ethyl-N-phenyldithiocarbamates and their application in the rubber industry. *Solid State Phenomena* **2003**, *90-91*, 383-388.

63. Miyamae, T; Fujioka, M; Tsubogo, Y; Tonariya, Y; Dohi, Y; Akashi, Y; Watanabe, H. Detection of a large arteriovenous fistula between the internal lliac vessels by radionuclide angiography. *J. Nuc. Med*. **1979**, *20*, 36-38.

64. Tiekink, E.R.T. On the structure of cadmium isopropylxanthate. Corrigendum. *Acta Cryst*. **2000**. *C56*, 1176.

CHAPTER FOUR

4.0 CHARACTERIZATION OF METAL SULFIDE NANOPARTICLES

4.1 Introduction

Group II–VI semiconductor nanoparticles have been of particular interest because of their size-dependent optic, electric, and magnetic properties compared with those of bulk materials [1-5]. ZnS, CdS and HgS nanoparticles are important semiconductor compounds and their wide range properties and potential applications have been explored. For example, ZnS is a group II–VI semiconductor with a wide direct band gap of 3.65 eV (bulk) with two stable crystal structures, the cubic zinc blende at low temperature and the hexagonal wurtzite at high temperature [6, 7]. It has been used in optoelectronic devices application operating in the region from visible to near infrared including optical coatings, solar cells, infrared windows, lasers, displays, electrooptic modulators, photoconductors, field effect transistors, sensors, transductors, light-emitting applications and photonic crystal devices [8-18].

Among group II–VI semiconductor, CdS has been widely studied and has a direct band gap of 2.42 eV [19-22]. It has potential technological applications similar to those of ZnS such as in solar cells, field effect transistors, photovoltaic, light emitting diodes, photocatalysis, photoluminesce, infrared photodetector, environmental sensors and biological sensors [23, 24]. HgS is a technologically important nanocrystal which has pronounced dichorism, photoelectric, acousto-optic properties and electrostatic image properties [25]. Despite these applications of HgS nanoparticles, relatively scarce studies are available due to difficulty in synthesis and toxicity of mercury. Only few detailed studies are available on preparation and characterization of HgS nanoparticles [25].

Our focus in this study was to use group 12 metal complexes as single source precursors to synthesize metal sulfide nanoparticles of II-VI semiconductors such as ZnS, CdS and HgS. This method has been demonstrated as a versatile, relatively simple and efficient route for the synthesis of crystalline semiconductor nanoparticles [4, 25, 26]. The experimental procedure for the synthesis of ZnS, CdS and HgS nanoparticles was described in Chapter Two, Section 2.5. ZnS, CdS and HgS nanoparticles synthesized from the thermolysis of six metal complexes were characterized by UV-Vis, PL, XRD, SEM and TEM.

4.2 Characterization of ZnS, CdS and HgS nanoparticles from (N-phenyl-N, N-methyl phenyl dithiocarbamate)M(II) complexes

4.2.1 Optical properties of HDA-capped ZnS, CdS and HgS nanoparticles

The semiconducting nanoparticles are of interest to many materials scientist and engineers because of their optical properties. The main optical property of semiconductor nanoparticles is the energy band gap [26, 27]. Figure 4.1 shows the absorption and emission spectra of HDA-capped ZnS, CdS and HgS nanoparticles (labeled as ZnS2, CdS2 and HgS2) prepared from (N- phenyl-N, N-methyl phenyl dithiocarbamate)M(II) precursor complexes that were thermolyzed at 180 ^{o}C for 60 min. The UV-Vis absorption spectra were employed to examine the quantum confinement effect of the synthesized nanoparticles. The spectra for ZnS2, CdS2 and HgS2 nanoparticles showed strong cut off where the absorbance is minimum at 319, 316 and 314 nm respectively. The cut off wavelength was then used to determine the energy band gap E_g^* of the ZnS2, CdS2 and HgS2 nanoparticles according to the following equation:

$$E_g^* = \frac{hc}{\lambda_c} \tag{4.1}$$

where h = Planks constant = 6.626 x 10^{-34} Joules sec, C = Speed of light = 3.0 x 108 meter/sec and λ_c = Cut off wavelength. The band gap calculation results are shown in Table 4.1. The conversion factor 1eV = 1.6 X 10^{-19} Joules was used in all calculation.

Table 4.1: Energy band gaps of ZnS2, CdS2 and HgS2 nanoparticles

Nanoparticles	***h***	**C**	λ_c	E_g^*	**eV**
ZnS2	6.63E-34	3.00E+08	3.19E-07	6.331E-19	3.89
CdS2	6.63E-34	3.00E+08	3.16E-07	6.291E-19	3.93
HgS2	6.63E-34	3.00E+08	3.14E-07	6.231E-19	3.96

The UV-Vis spectra exhibited a blue-shift with respect to that of the bulk samples which is attributed to the quantum size effect because the known bulk energy band gaps of ZnS, CdS and HgS absorption peaks are expected at 337.6 nm (Eg = 3.68 eV)[28, 29], 513.4 nm (Eg = 2.42 eV) [30, 31] and 621.2 nm (Eg = 2.03 eV) [32, 33] respectively. Using the estimated band gap values from the optical spectra of nanoparticles, the particle size can be calculated using the Brus equation (Equation 4.2) [34, 35] derived from the effective mass model:

$$E_g^* = E_g^{bulk} + \frac{\bar{h}^2\pi^2}{2r^2}\left(\frac{1}{m_e^*}+\frac{1}{m_h^*}\right) - \frac{1.8e^2}{4\pi\varepsilon\varepsilon_0 r} - \frac{0.124e^4}{\bar{h}^2(4\pi\varepsilon\varepsilon_0)^2}\left(\frac{1}{m_e^*}+\frac{1}{m_h^*}\right)^{-1} \quad (4.2)$$

band gap energy (eV) of the nanoparticle, determined from the UV-Visible absorbance spectrum, band gap energy (eV) of the bulk nanoparticles at room temperature, h = Planck's Constant, 6.625×10^{-34} J·s, r = particle radius (m), m_e = mass of a free electron, 9.11×10^{-31} kg, = $0.19m_e$ (effective mass of a conduction band electron in nanoparticles), = $0.80m_e$ (effective mass of a valence band hole in nanoparticles), e = elementary charge,

1.602×10^{-19}C, ε_0 = $8.854\times10^{-12}C^2N^{-1}m^{-2}$ (permittivity of free space), ε = relative permittivity of nanoparticles)

The particle size for ZnS2 was estimated using Brus equation, where (m_e* = 0.42m_0, m_h* = 0.61m_0), ε = 5.2 and ε_0 = $8.854\times10^{-12}C^2N^{-1}m^{-2}$ [36, 37]. The ZnS2 particle size was found to be 4.3 nm with a band gap of 3.89 eV. For CdS2, m_e* = 0.19 m_0, m_h* = 0.80m_0, ε = 5.7 and ε_0 = $8.854\times10^{-12}C^2N^{-1}m^{-2}$ [38, 39]. The particle size for CdS2 was found to be 3.2 nm with a band gap of 3.93 eV. The estimated particle size for HgS2 was found to be 2.8 nm with the band gap of 3.96 eV and similar results have been reported elsewhere [40, 41].

4.2.2 Photoluminescence spectra of HDA-capped ZnS, CdS and HgS nanoparticles

The photoluminescence spectrum of HDA-capped ZnS, CdS and HgS nanoparticles was recorded at excitation wavelength of 394 nm at room temperature and the resulting spectra are also shown in Figure 4.1. The photoluminescence spectra showed narrow emission curves with the emission maximum at 386, 438 and 392 nm, for ZnS, CdS and HgS nanoparticles respectively confirming the high crystalline nature of the as-synthesized nanoparticles [42]. The positions of these peaks are red shifted in relation to the optical absorption band edges. The observed broadening of the emission peak could be attributed to both the size distribution and the increase of the surface states due to the increase in surface to volume ratio for smaller nanoparticles [43].

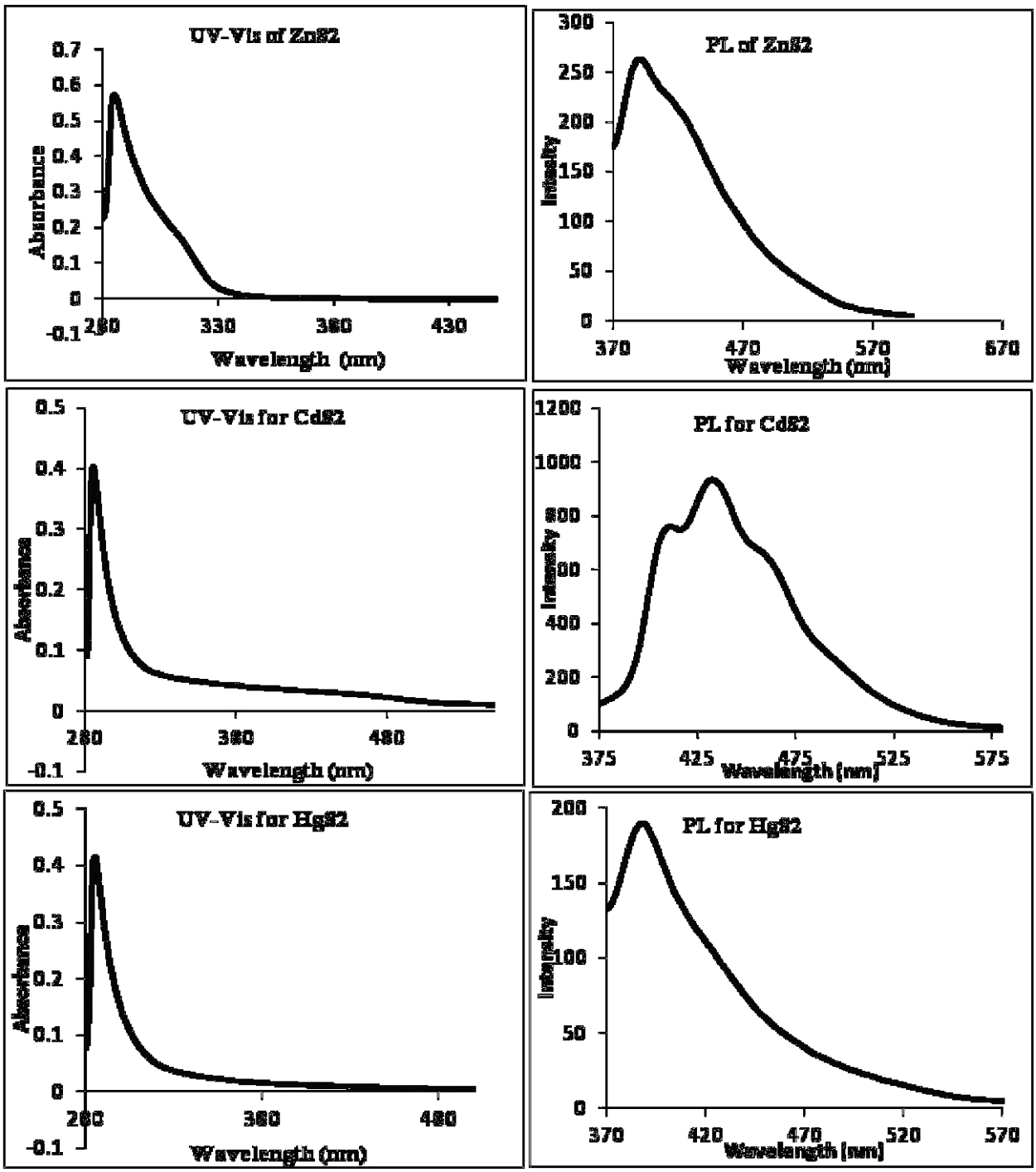

Figure 4.1: Absorption and emission spectra of HDA-capped ZnS, CdS and HgS nanoparticles prepared from (*N*- phenyl-*N*,*N*-methyl phenyl dithiocarbamate)M(II) complexes

4.2.3 XRD spectra of HDA-capped ZnS2, CdS2 and HgS2 nanoparticles

The XRD pattern of synthesized HDA-capped ZnS2, CdS2 and HgS2 nanoparticles is shown in Figure 4.2. HDA-capped ZnS shows three important peaks corresponding to the (111), (220) and (311) planes, indicates the characteristic peaks of cubic crystal structure of ZnS nanoparticles. The peaks observed in the XRD patterns correspond well with those of the β-ZnS (cubic) reported in the JCPDS powder diffraction. Intensities of the three most important peaks of ZnS, namely (111), (220) and (311) reflections corresponding to 26.8º, 45.6º and 52.5º respectively. The crystallite size was calculated using Scherrer's equation,

$$D = k\lambda / \beta\cos\theta \qquad (4.3)$$

Where; D is the crystallite size, λ is the wavelength of the X-ray radiation (CuKα = 0.15406 nm), k is a constant taken as 0.94, θ is the diffraction angle and β is the corrected half width of the diffraction peak. This is the generally accepted method to estimate the mean crystallite size of nanoparticles [44-46]. The calculated average crystallite size of ZnS2 from these peaks using Scherer's formula is 4.1 nm. Broadening of the XRD peaks indicates the formation of ZnS nanocrystals and the elongation of the XRD pattern of nanoparticles also shows the surface passivation [47]. The XRD pattern of CdS2 (Figure 4.2) exhibit two broad peaks at 29.9^{o}and 41.9^o assignable to the (111) and (400) Miller indices respectively. This suggests small crystallite sizes of hexagonal phase (JCPDS card, No. 05-0566). The peaks are broad indicating that the average crystallite size is smaller compared to that of ZnS2. The calculated average crystallite size was found to be 3.6 nm. The hexagonal morphology of CdS was also revealed by SEM image of the decomposition residue of (N-phenyl-N, N-methyl phenyl dithiocarbamato)Cd(II) complex discussed in Chapter three. The XRD pattern of HgS as shown in Figure 4.2 revealed the major peaks centered at 2θ = 27.3^o, 30.1^o, 40.2^o and 52.3^o corresponding to (111), (200), (311) and 411 planes of the cubic phase on the XRD

pattern [48]. The calculated average crystallite size was found to be 2.4 nm. All the peaks with the (*) are due to HDA.

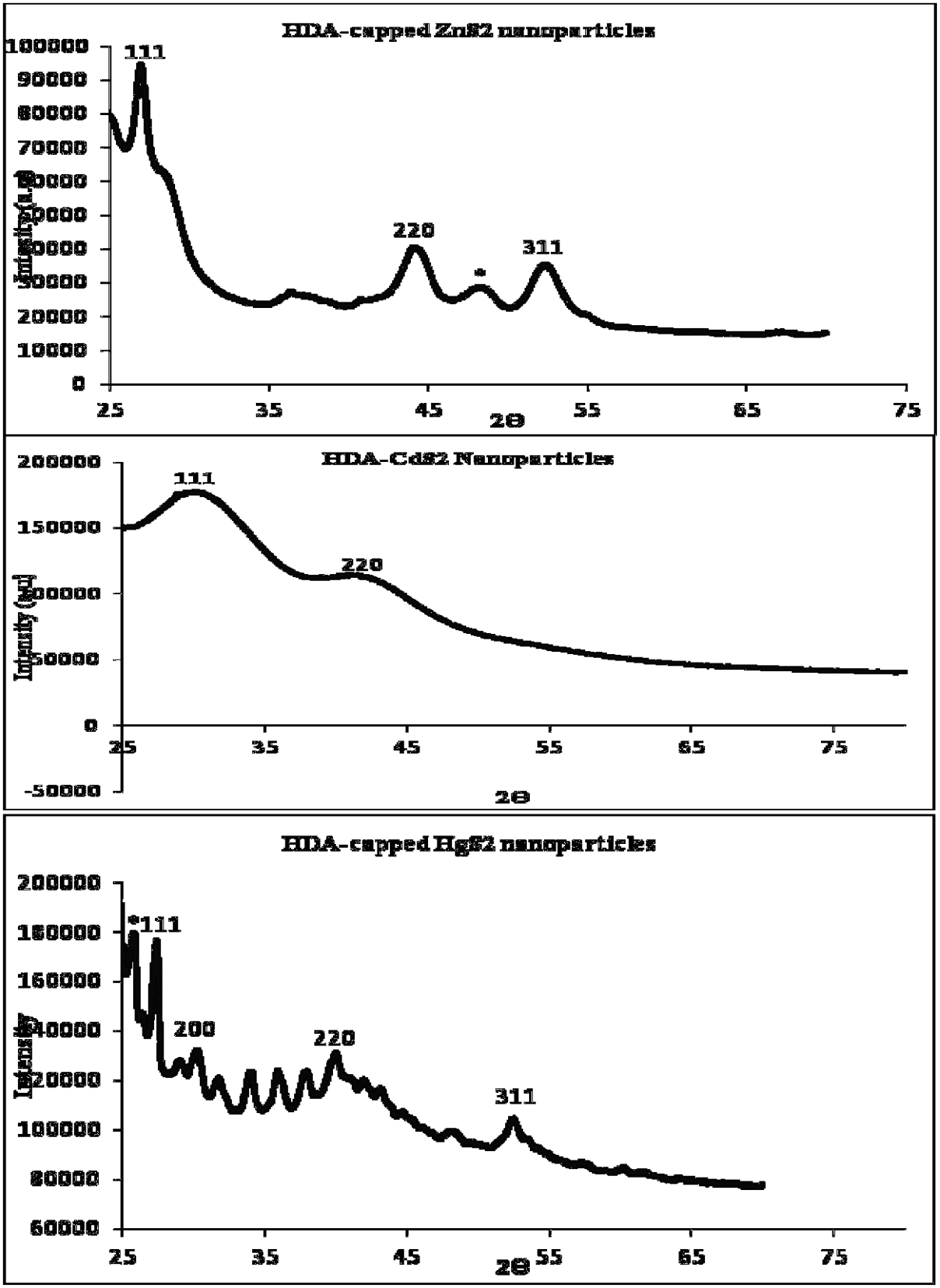

Figure 4.2: XRD studies of HDA-capped ZnS2, CdS2 and HgS2 nanoparticles

4.2.4 TEM image of HDA-capped ZnS2, CdS2 and HgS2 nanoparticles

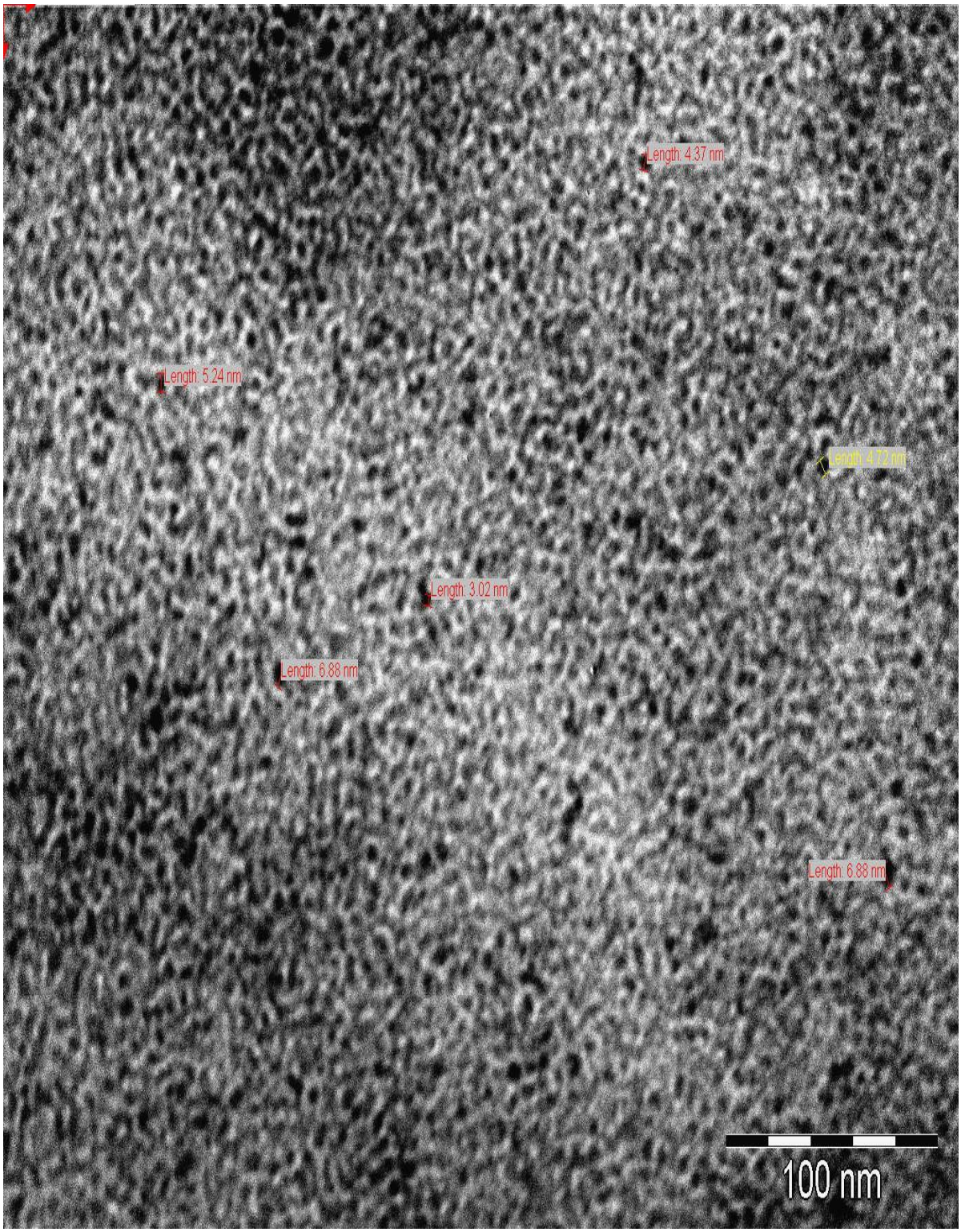

Figure 4.3: TEM image of HDA-capped ZnS2 nanoparticles prepared from (N- phenyl-N,N-methyl phenyl dithiocarbamate)Zn(II) complex

To further study the size of nanoparticles and structural morphology of HDA-capped nanoparticles, transmission electron microscopy (TEM) was employed. Images were obtained using a ZEISS Libra 120 electron microscope operated at 120 kV. The TEM image of HDA-capped ZnS2 nanoparticles revealed nanoparticles mainly close-to-spherical shape with an average diameter of 3-5.2 nm, which indicates that the nanoparticles have smaller ZnS crystal grains as shown in Figure 4.3 [49, 50].

TEM image of HDA-capped CdS2 nanoparticles is shown in Figure 4.4. The nanoparticles showed a mixture of cubic, hexagonal and close-to-spherical morphology with a diameter range of 11 to 22.04 nm. The images reveal good crystallinity of the nanoparticles. The lattice spacing of nanoparticles images was measured at higher magnification which shows the corresponding planes of hexagonal structure of CdS supporting the existence of a crystalline structure. The CdS nanoparticles shows tendency to agglomerates as they settle on the carbon coated copper grid although clearly crystalline nanoparticles are obtained as shown by the TEM image (Figure 4.4). This TEM image show the crystallinity of particles confirmed by the lattice planes observed on the XRD [51].

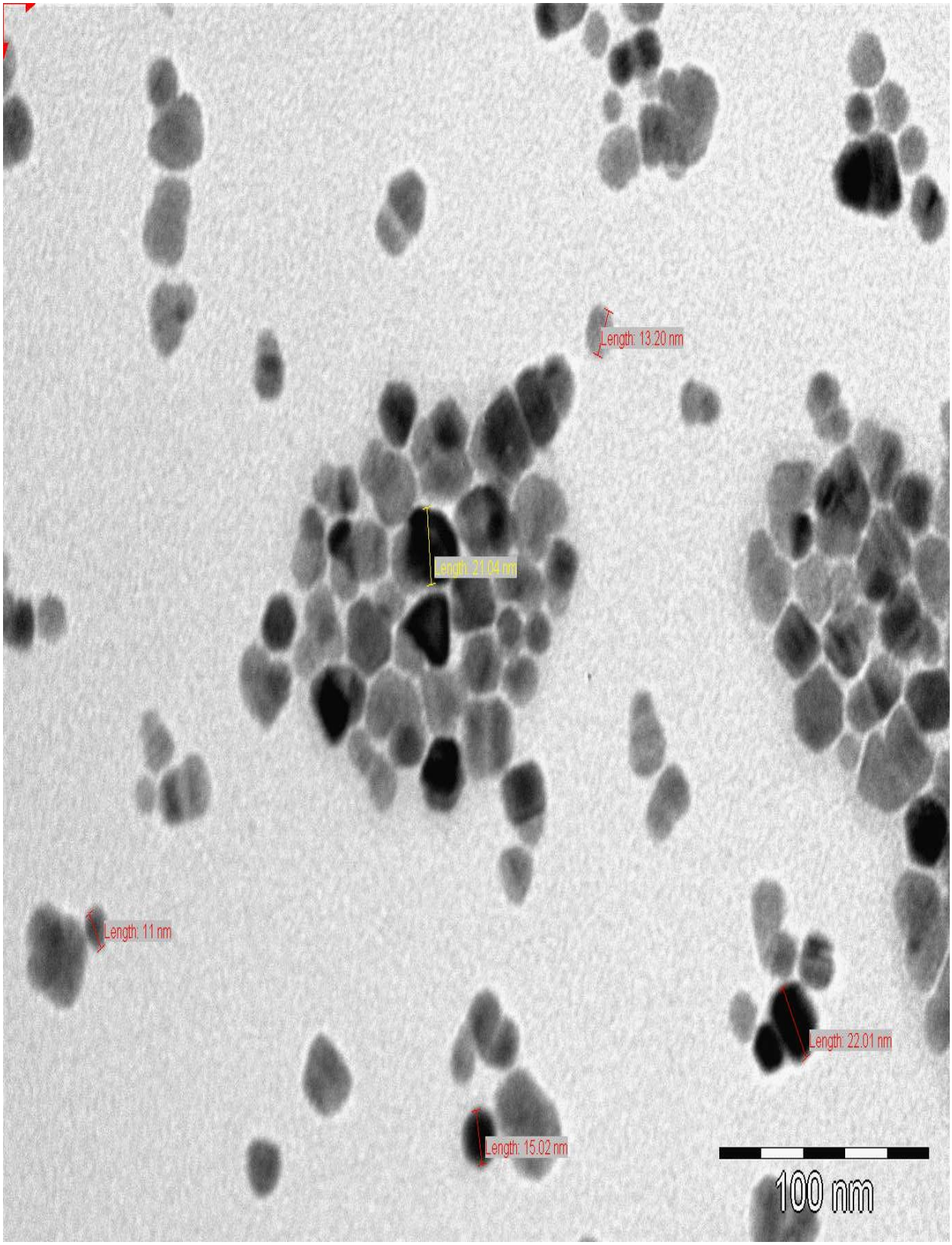

Figure 4.4: TEM image of HDA-capped CdS2 nanoparticles prepared from (N- phenyl-N, N-methyl phenyl dithiocarbamate)Cd(II) complex

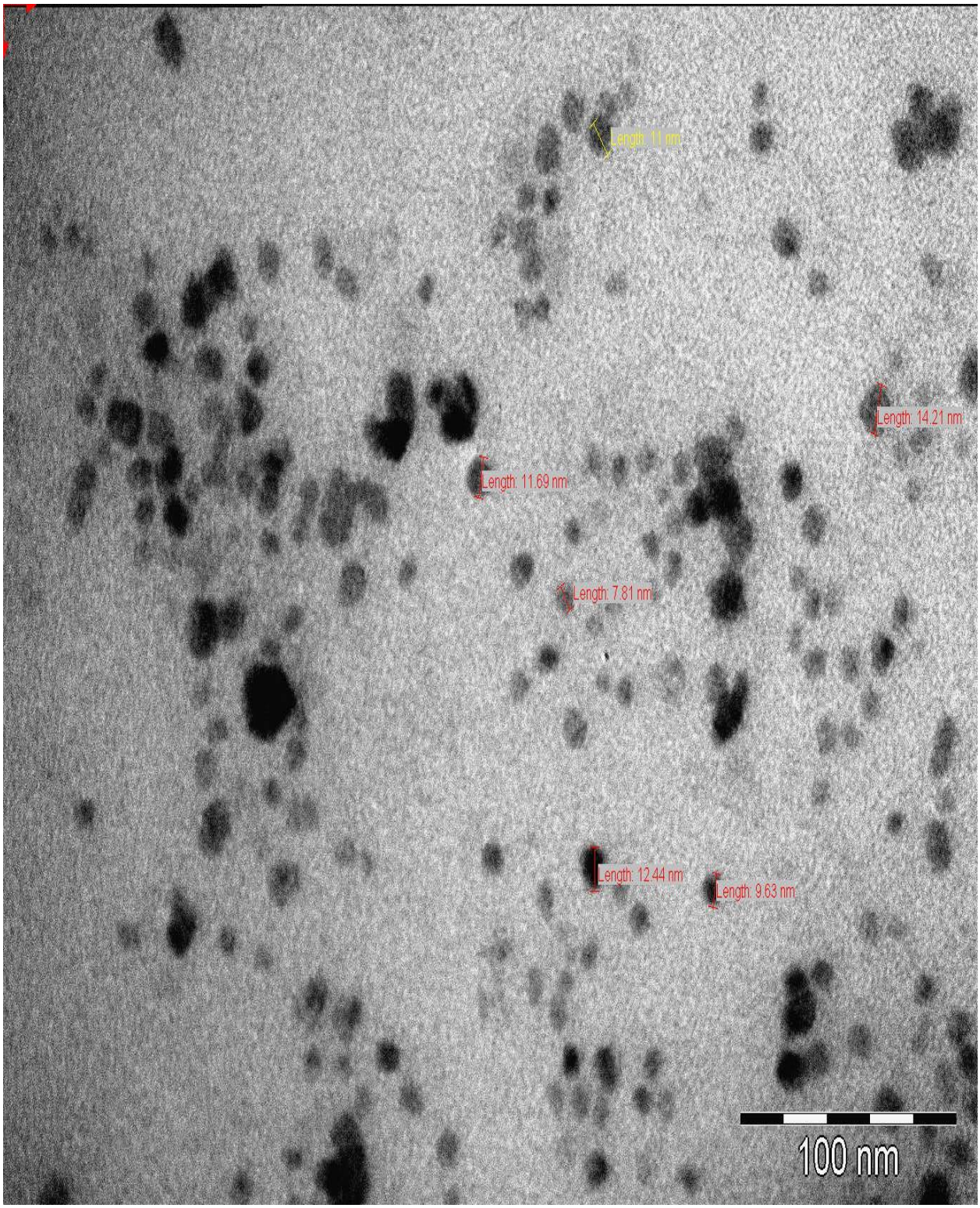

Figure 4.5: TEM image of HDA-capped HgS2 nanoparticles prepared from (N- phenyl-N, N-methyl phenyl dithiocarbamate)Hg(II) complex

TEM image of HDA-capped HgS2 nanoparticles is shown in Figure 4.5. The nanoparticles showed a close-to-spherical morphology with a diameter range of 7-14 nm. HgS nanoparticles, under the same synthetic conditions, produced spherical and oval shapes with a good uniform size distribution throughout the sample. The shape and size of all prepared HDA-capped nanoparticles are comparable more or less the same which could be attributed to the fact that the organic moieties of the precursor complexes are the same and the central metals are in the same group. These results correspond to those reported in literature [52].

4.2.5 SEM and EDX of HDA-capped ZnS2, CdS2 and HgS2 nanoparticles

The microstructures of the HDA-capped nanoparticles were examined by scanning electron microscopy (SEM) and the elemental compositions of the synthesized nanoparticles were confirmed by energy dispersive X-ray (EDX) analysis. The scanning electron microscopy helps in elucidating the surface morphology and size uniformity of nanoparticles [53, 55]. The morphologies of the as-prepared HDA-capped ZnS nanoparticles annealed in nitrogen environment at 180 °C were captured by SEM as shown in Figure 4.6 (A and B). It can be seen that the surface of the particles appears smooth and seen merging with each other. As expected the particle size is much bigger than that of crystallite size measured by TEM analysis. This may be due to the agglomeration of crystallites which is clearly seen from Figure 4.6 [55]. Although the SEM images did not show well HDA-capped ZnS particles, but the ZnS aggregated particles appear to be composed of smaller crystallites. EDX pattern (Figure 4.7(C)) reveals the predominant peaks of Zn and S. The carbon observed in both samples is attributed to the carbon from the capping agent hexadecylamine (HDA) or the carbon grid of the sample holder while the P is due to the trioctyl phosphine (TOP).

The morphologies of the as-prepared HDA-capped CdS nanoparticles are shown in Figure 4.7(A and B). The SEM shows that the particles are porous with uniform particle dimensions. This porosity may be due to the fact that the sample was completely dry and the uniformity of particles are due to the method of synthesis (SSP) used. Both images in low and high magnification indicate that HDA-capped CdS nanoparticles are hindered because there is a lot of surface stabilizer that prevents good resolution of the particles. The porous and rough surface morphology is evident which makes it difficult to estimate the crystallite size due to agglomeration of the particles [56]. EDX is an important tool to analyze the composition of elements quantitatively and solve the chemical identity of any nanomaterials [57]. EDX spectra of HDA-capped CdS nanoparticles are shown in Figure 4.7 (C). The spectra show that the prepared sample is mainly composed of Cd and S, confirming the presence of CdS nanoparticles in hexagonal phase [58]. Other traces of elements like C, O, Al and P are observed. The carbon observed in both samples is attributed to the carbon from the capping agent hexadecylamine (HDA) or the carbon grid of the sample holder, Al is from aluminium-carbon grid used during coating, O may be due to oxidation of S atom to O atom while the P is due to the trioctyl phosphine (TOP).

The surface morphology of HDA-capped HgS nanoparticles synthesized from HgL^1L^2 was investigated by recording SEM images as displayed in Figure 4.8 (A and B). The SEM images (low magnification and high magnification) reveal that the surface of HgS sample is fairly smooth indicating uniformity of particles. The particles tend to aggregate to secondary particles indicating that the alkyl groups play a very important role in controlling the morphology of the as-prepared nanoparticles [59]. Although there were challenges connected with getting clear morphology since nanoparticles tend to aggregate into larger agglomerates, it could be noticed that the examined particles consist of a number of smaller particles of 0.5

μm to few micrometers in size. Figures (4.8 (C) show a typical EDX patterns of HgS particles. As expected, the observed major peaks are due to the presence of mercury and sulfur indicating the presence of HgS particles.

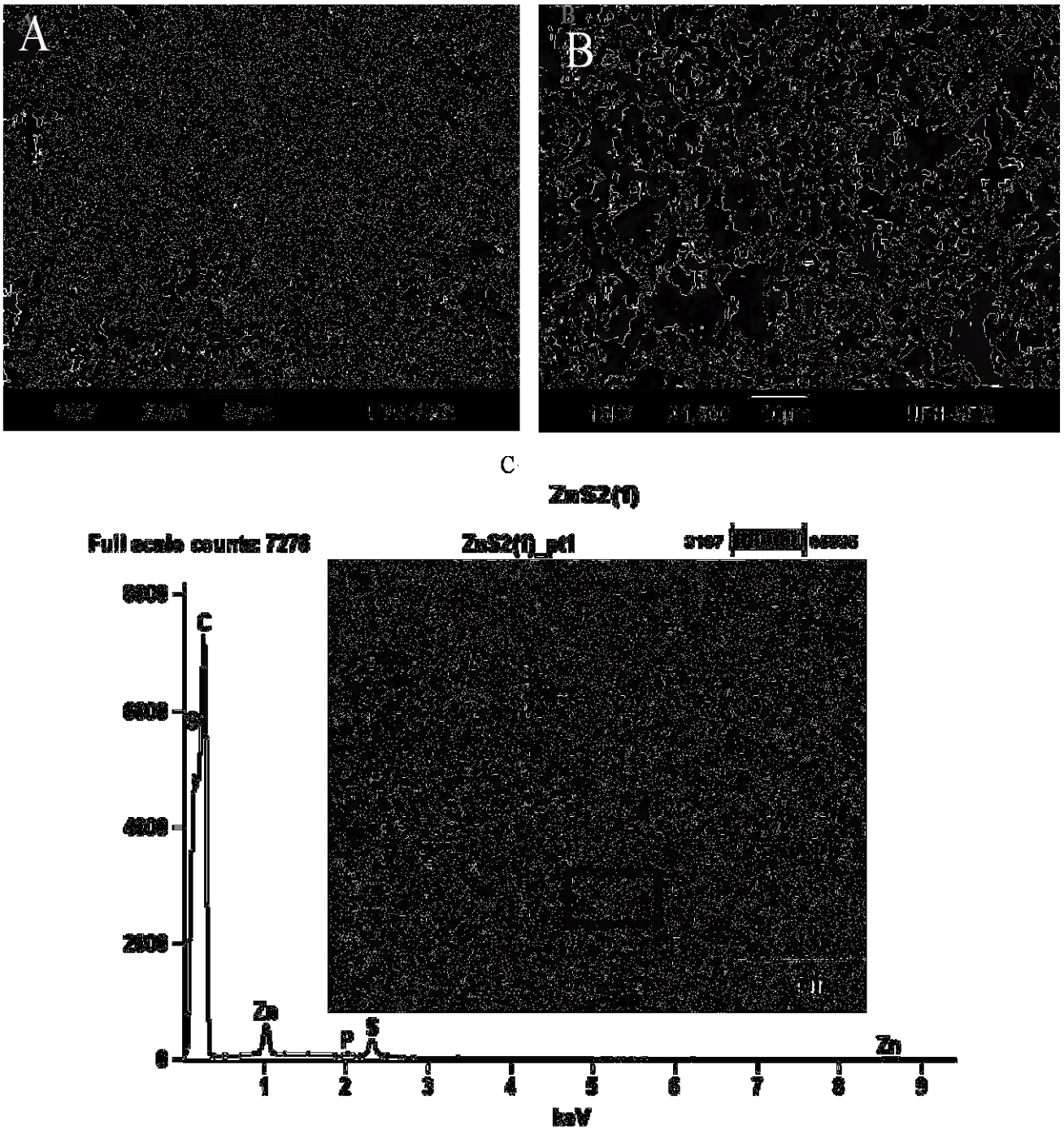

Figure 4.6: SEM micrograph of the ZnS (labeled as ZnS2) from ZnL1L2 complex (A) low magnification, (B) high magnification (C) EDX spectrum of the sample

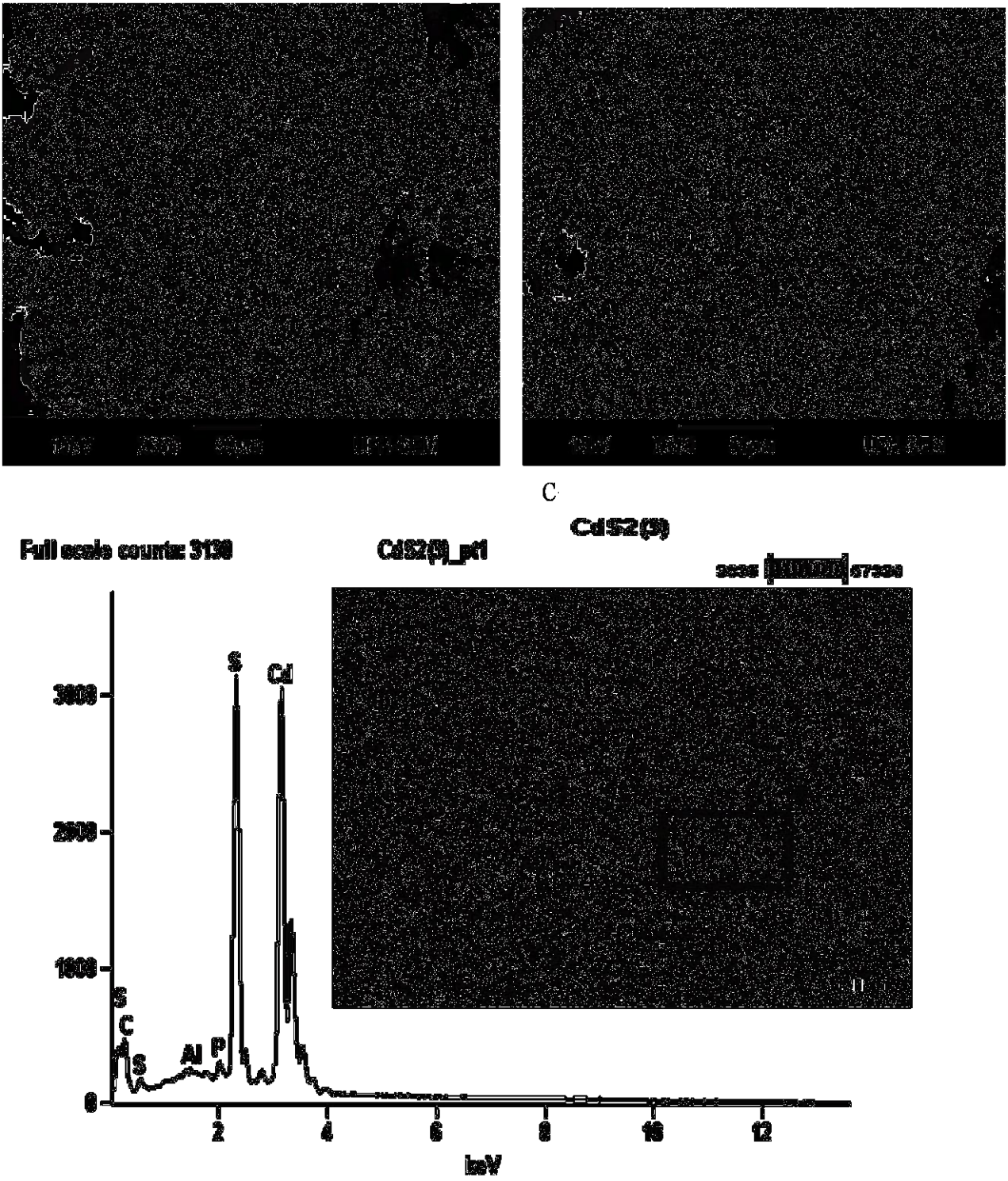

Figure 4.7: SEM micrograph of the CdS (labeled as CdS2) from CdL^1L^2 complex (A) low magnification, (B) high magnification (C) EDX spectrum of the sample

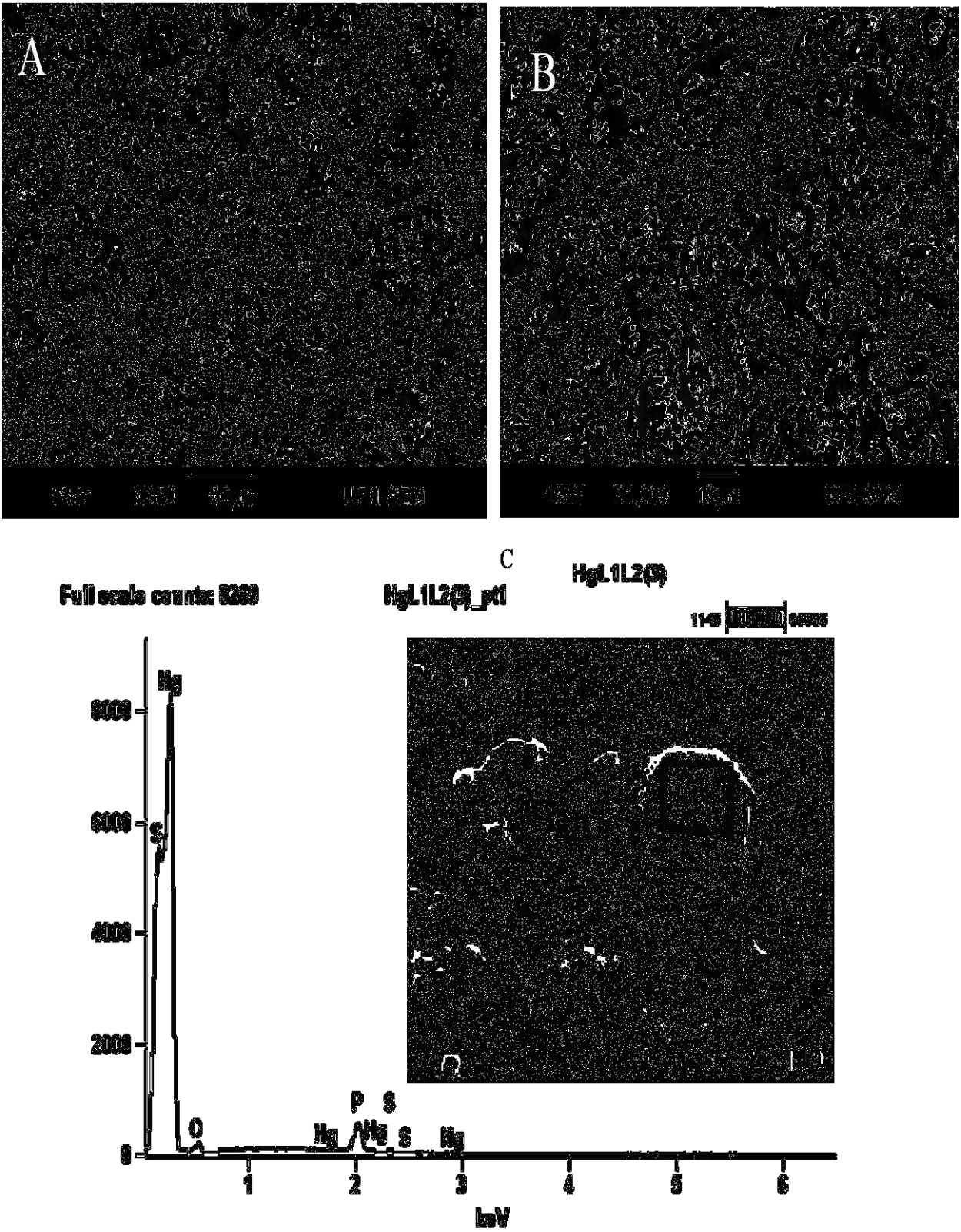

Figure 4.8: SEM micrograph of the HgS (labeled as HgS2) from HgL^1L^2 complex (A) low magnification, (B) high magnification (C) EDX spectrum of the sample

4.3 Characterization of ZnS, CdS and HgS nanoparticles from (N- phenyl-N,N-ethyl phenyl dithiocarbamate)M(II) complexes

4.3.1 Optical properties of HDA-capped ZnS, CdS and HgS nanoparticles

The absorption and emission spectra of HDA-capped ZnS, CdS and HgS nanoparticles (labeled as ZnS3, CdS3 and HgS3) prepared from (N- phenyl-N,N-ethyl phenyl dithiocarbamate)M(II) precursor complexes that were thermolyzed at 180 ^{o}C for 60 min are shown in Figure 4.9. The energy bands and their corresponding parameters are tabulated in Table 4.2. The calculations were done as discussed in section 4.3.1. The UV-Vis spectra exhibited a blue-shift with respect to that of the bulk samples due to quantum confinement [60].

Table 4.2: Energy band gaps of ZnS3, CdS3 and HgS3 nanoparticles

Nanoparticles	***h***	**C**	λ_c	E_g^*	**eV**
ZnS3	6.63E-34	3.00E+08	3.35E-07	5.934E-19	3.71
CdS3	6.63E-34	3.00E+08	3.29E-07	6.042E-19	3.78
HgS3	6.63E-34	3.00E+08	3.16E-07	6.291E-19	3.93

The photoluminescence spectra of HDA-capped ZnS, CdS and HgS nanoparticles was recorded at excitation wavelength of 394 nm at room temperature and the resulting spectra are also shown in Figure 4.9. The photoluminescence spectra showed narrow emission curves with the emission maximum at 385, 393 and 399 nm, for ZnS, CdS and HgS nanoparticles respectively. ZnS emission maximum is blue shifted to the absorption band edges while CdS and HgS gave emission maxima that are red shifted to the absorption band edges [61].

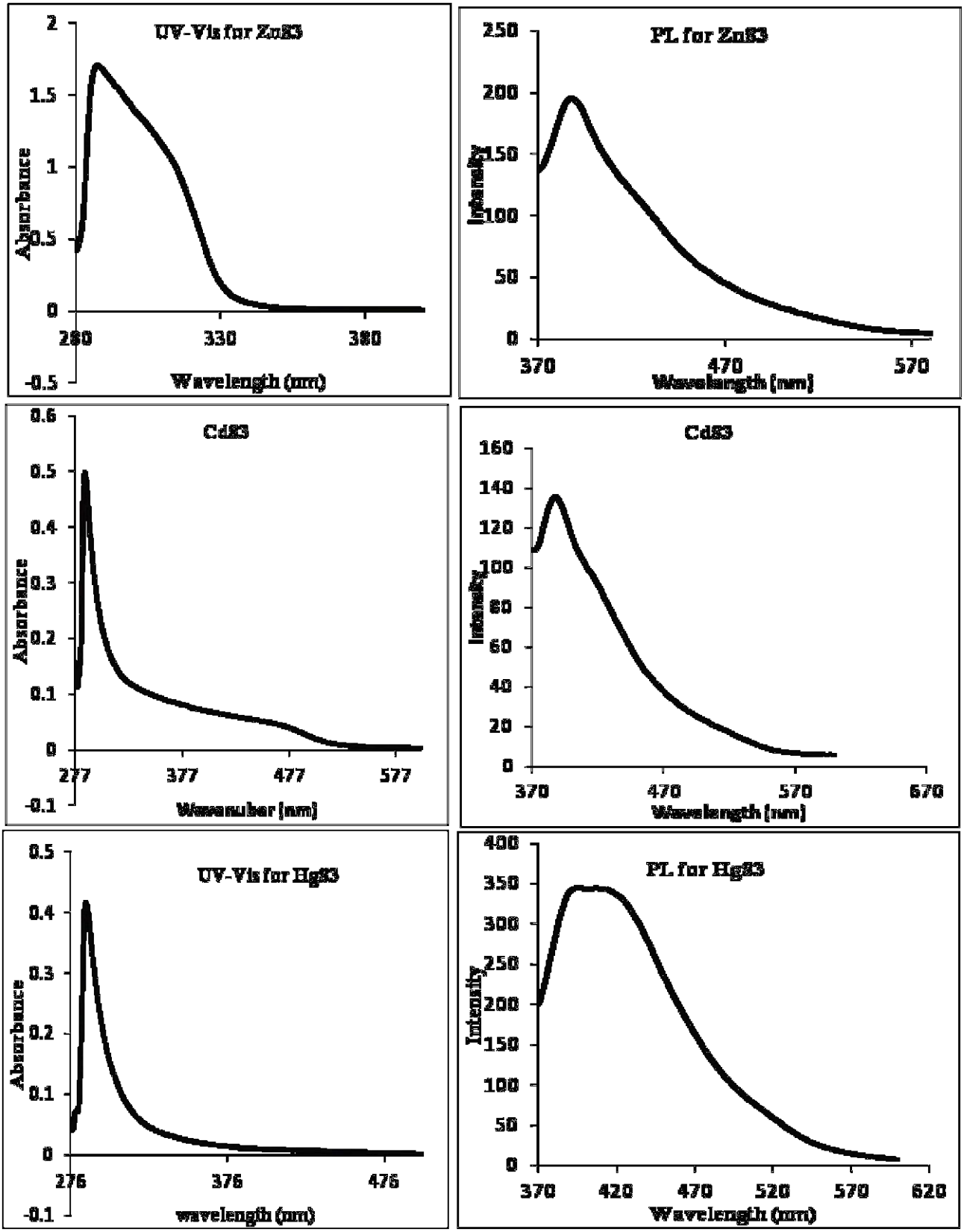

Figure 4.9: Absorption and emission spectra of HDA-capped ZnS, CdS and HgS nanoparticles prepared from (N- phenyl-N,N-ethyl phenyl dithiocarbamate)M(II) complexes

4.3.2 XRD spectra of HDA-capped ZnS3, CdS3 and HgS3 nanoparticles

The XRD pattern of synthesized HDA capped nanoparticles is shown in Figure 4.11. HDA-capped ZnS (A), shows three important peaks corresponding to the (111), (220) and (311) planes, indicates the characteristic peaks of cubic crystal structure of ZnS nanoparticles [62]. The peaks observed in the XRD patterns correspond well with those of the β-ZnS (cubic) reported in the (JCPDS file No.01-0792) [61]. Intensities of the three most important peaks of ZnS, namely (111), (220) and (311) reflections corresponding to 28.5º, 47.6º and 56.4º respectively. The crystallite size was calculated using Scherrer's equation [43]. The calculated average crystallite size from these peaks using Scherer's formula is 5.3 nm. The XRD pattern of CdS is shown in Figure 4.10 (B). It exhibit narrow peaks at 26.79, 29.72, 44.02, 48.58 and 52.20 are assignable to the (111), (220), (311) and (400) Miller indices respectively, suggesting small crystallite sizes of hexagonal phase. The XRD pattern of HgS is shown in Figure 4.10 (C). HgS nanoparticles revealed the major peak centered at 2θ = 25.02, corresponding to (111) plane of the cubic phase on the XRD pattern. The absence of the other important peaks in the HgS spectrum could be ascribed to the presence of the capping agent. All the peaks with the (*) are due to HDA.

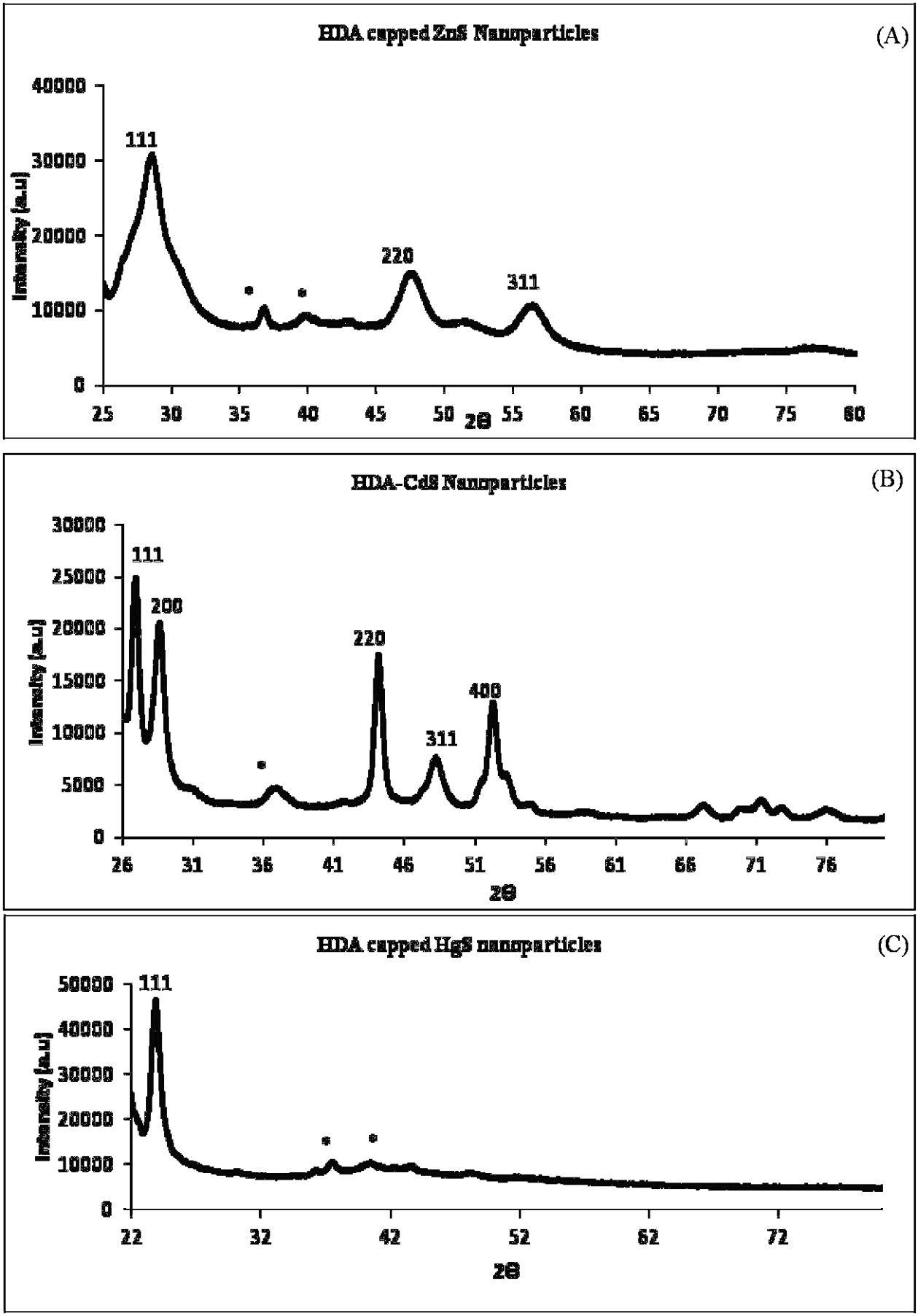

Figure 4.10: XRD studies of HDA-capped ZnS3, CdS3 and HgS3 nanoparticles

4.3.3 TEM image of HDA-capped ZnS3, CdS3 and HgS3 nanoparticles

The transmission electron microscopy (TEM) was used to study the size of nanoparticles and structural morphology of HDA-capped ZnS, CdS and HgS nanoparticles (labeled as ZnS3, CdS3 and HgS3) prepared from (N- phenyl-N,N-ethyl phenyl dithiocarbamate)M(II) precursor complexes. The TEM micrograph of HDA-capped ZnS3 nanoparticles (Figure 4.11) shows well-defined nanoparticles having a diameter of about 9 nm. The particle size is bigger than that of ZnS2 nanoparticles (Figure 4.3) maybe due to increase in the alkyl group when methyl was replaced by ethyl group. Generally the shapes nanoparticles are mainly close-to-spherical and some are elongated with some crystallinity and agglomeration [63]. The TEM image of HDA-capped CdS3 nanoparticles prepared at 180 ^{o}C for 60 min is shown in (Figure 4.12). The method of preparation was similar to that of CdS2 (Figure 4.4) but the precursor used in synthesis of CdS3 was N- phenyl-N, N-ethyl phenyl dithiocarbamate)Cd(II) complex. The TEM image revealed nanoparticles with different shapes ranging from spherical to hexagonal a diameter range of 7 to 14 nm. The particles have some aggregation due to the attachment between the spherical nanoparticles as a result of dipole-dipole interactions between the surfaces of nanoparticles. The reproduction of the shapes obtained could be ascribed to the synthetic method called single-source precursor method (SSP), described in Chapter 3. The SSP offers advantages for the preparation of nanoparticles with increased size control, dramatic decreases in reaction times, improved product crystallinity, reactions exhibiting good reproducibility and high yields [64]. The TEM micrograph of the prepared HDA-capped HgS3 nanoparticles is shown in the (Figure 4.13). The micrograph revealed highly agglomerated nanoparticles crystallites. The nanoparticles are nearly spherical and triangular in shape. The average size of HgS3 nanoparticles ranges from 8 to 22 nm. The determination of exact dimension of HgS3 nanoparticles is a challenge due to the higher degree of agglomeration observed [65].

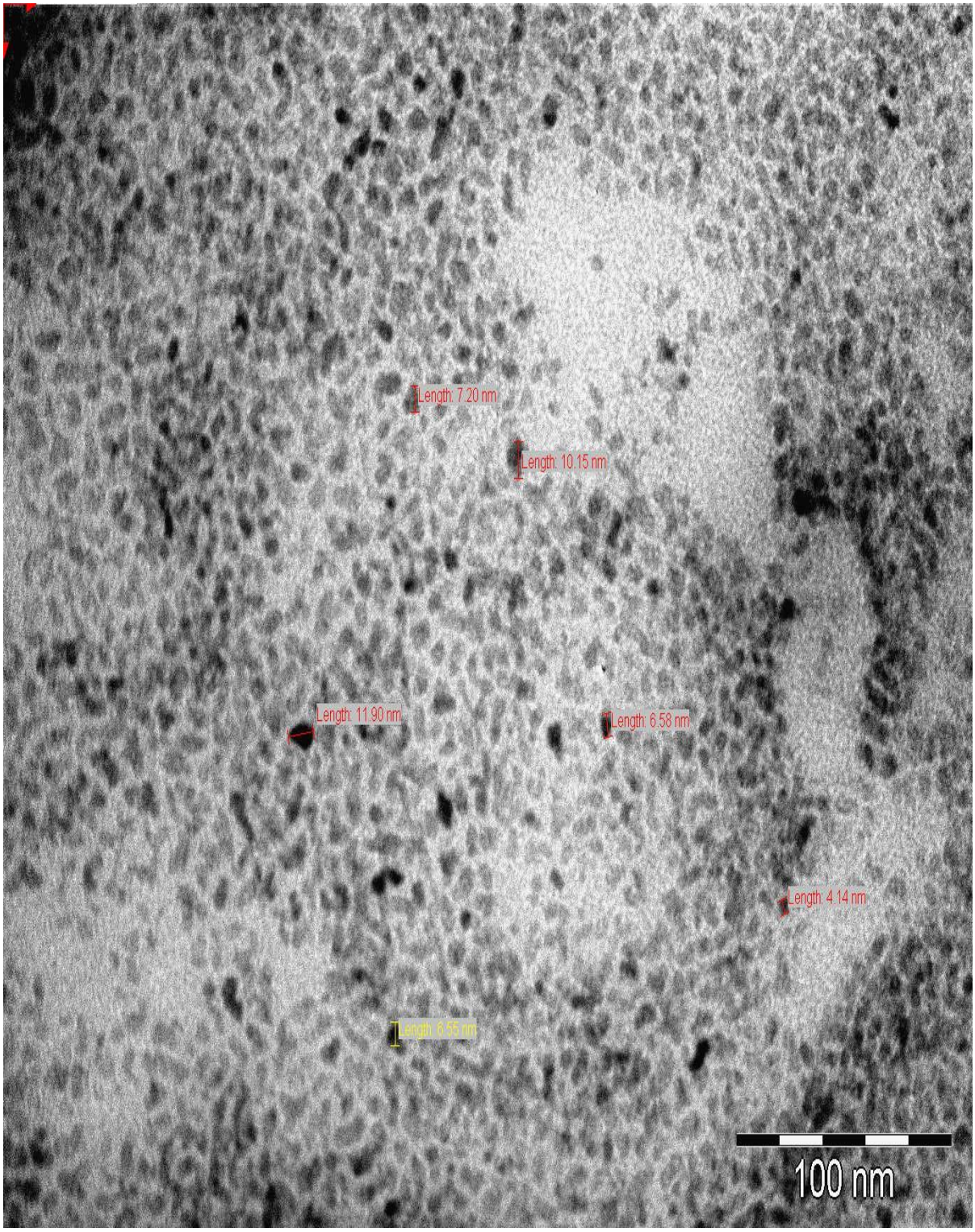

Figure 4.11: TEM image of HDA-capped ZnS3 nanoparticles prepared from (N- phenyl-N,N-ethyl phenyl dithiocarbamate)Zn(II) complex

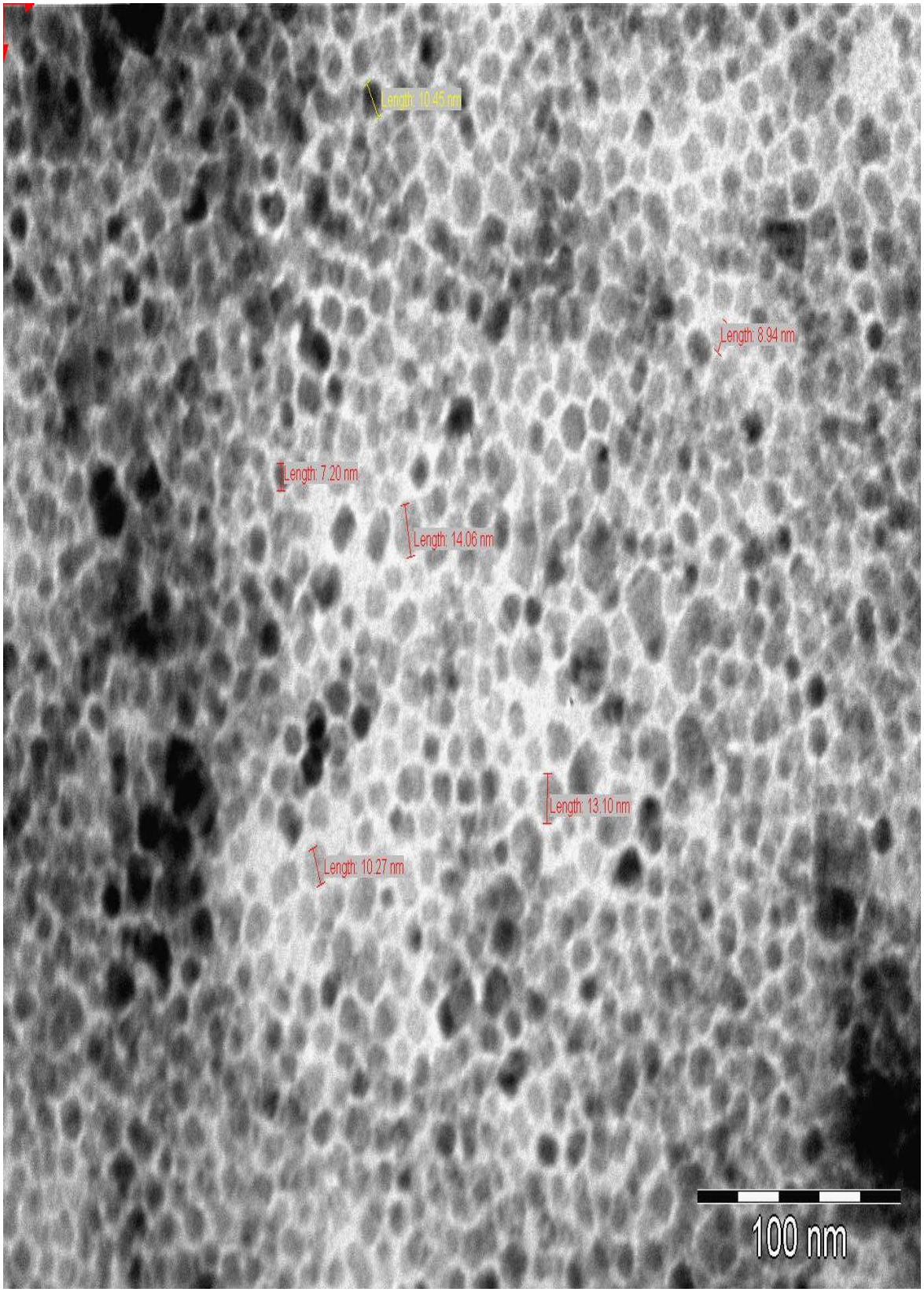

Figure 4.12: TEM image of HDA-capped CdS3 nanoparticles prepared from (N- phenyl-N,N-ethyl phenyl dithiocarbamate)Cd(II) complex

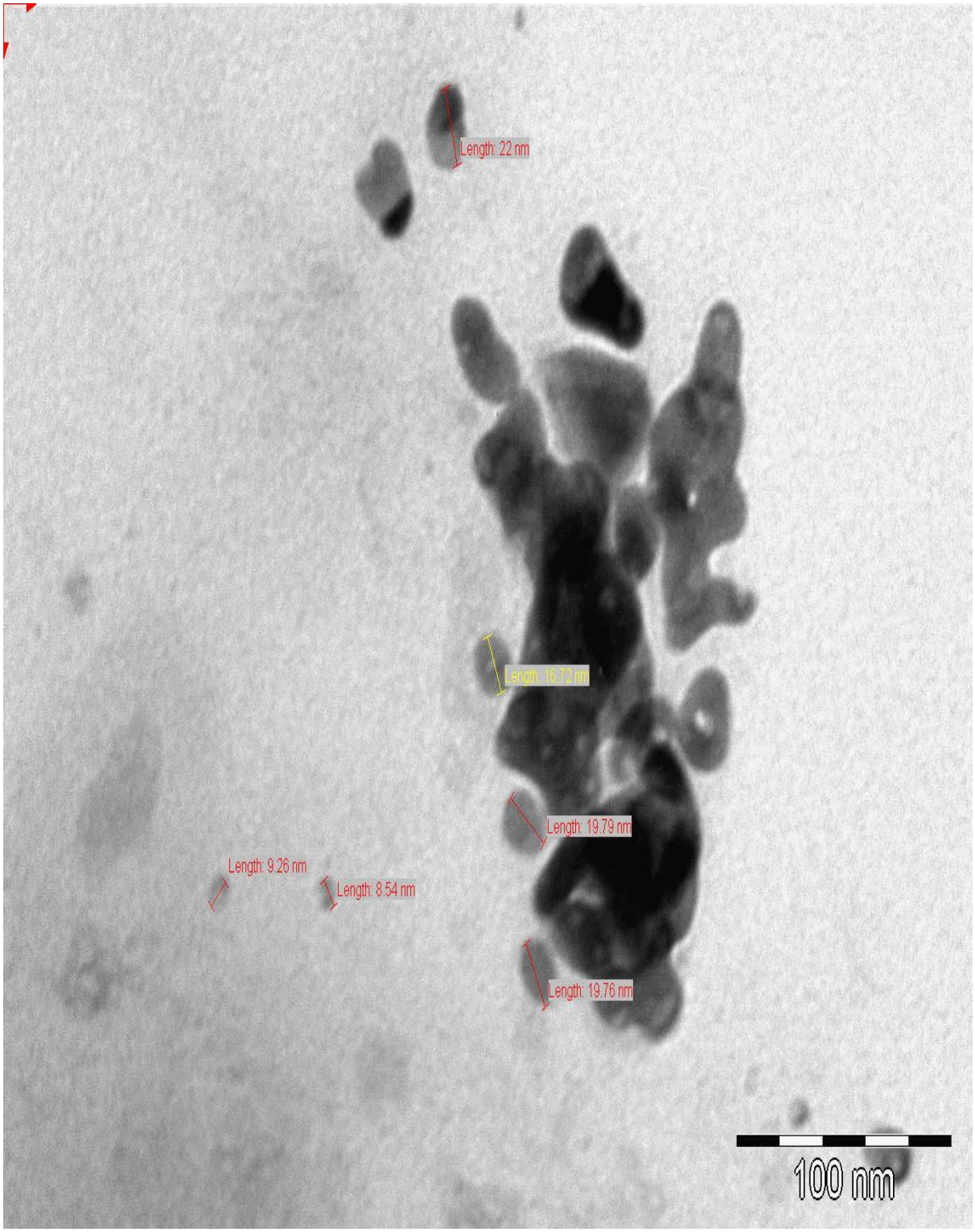

Figure 4.13: TEM image of HDA-capped HgS3 nanoparticles prepared from (N- phenyl-N, N-ethyl phenyl dithiocarbamate)Hg(II) complex

4.3.4 SEM and EDX of HDA-capped ZnS3, CdS3 and HgS3 nanoparticles

The surface of the particles in Figure 4.14 (A and B) exhibit cluster of particles which are nearly spherically agglomerated due to high surface energy of the growth particles in nanoscale [66]. The EDX spectrum of HDA-capped ZnS nanoparticles is shown in Figure 4.14 (C). EDX pattern reveal the predominant peaks of Zn and S.

The morphologies of the as-prepared HDA-capped CdS3 nanoparticles is as presented in Figure 4.15. The SEM images reveal that the particles are porous with uniform particle dimensions. The porous and rough surface morphology is evident which makes it difficult to estimate the crystallite size due to agglomeration of the particles [67]. EDX spectra of HDA-capped CdS nanoparticles are shown in Figure 4.15 (C). Both spectra reveal that the prepared samples are mainly composed of Cd and S, confirming the presence of CdS nanoparticles in hexagonal phase [67]. Other traces of elements like C, O, Al and P are observed were observed in both ZnS3 and CdS3. The carbon observed in both samples is attributed to the carbon from the capping agent hexadecylamine (HDA) or the carbon grid of the sample holder, Al is from aluminium-carbon grid used during coating, O may be due to oxidation of S atom to O atom while the P is due to the trioctyl phosphine (TOP).

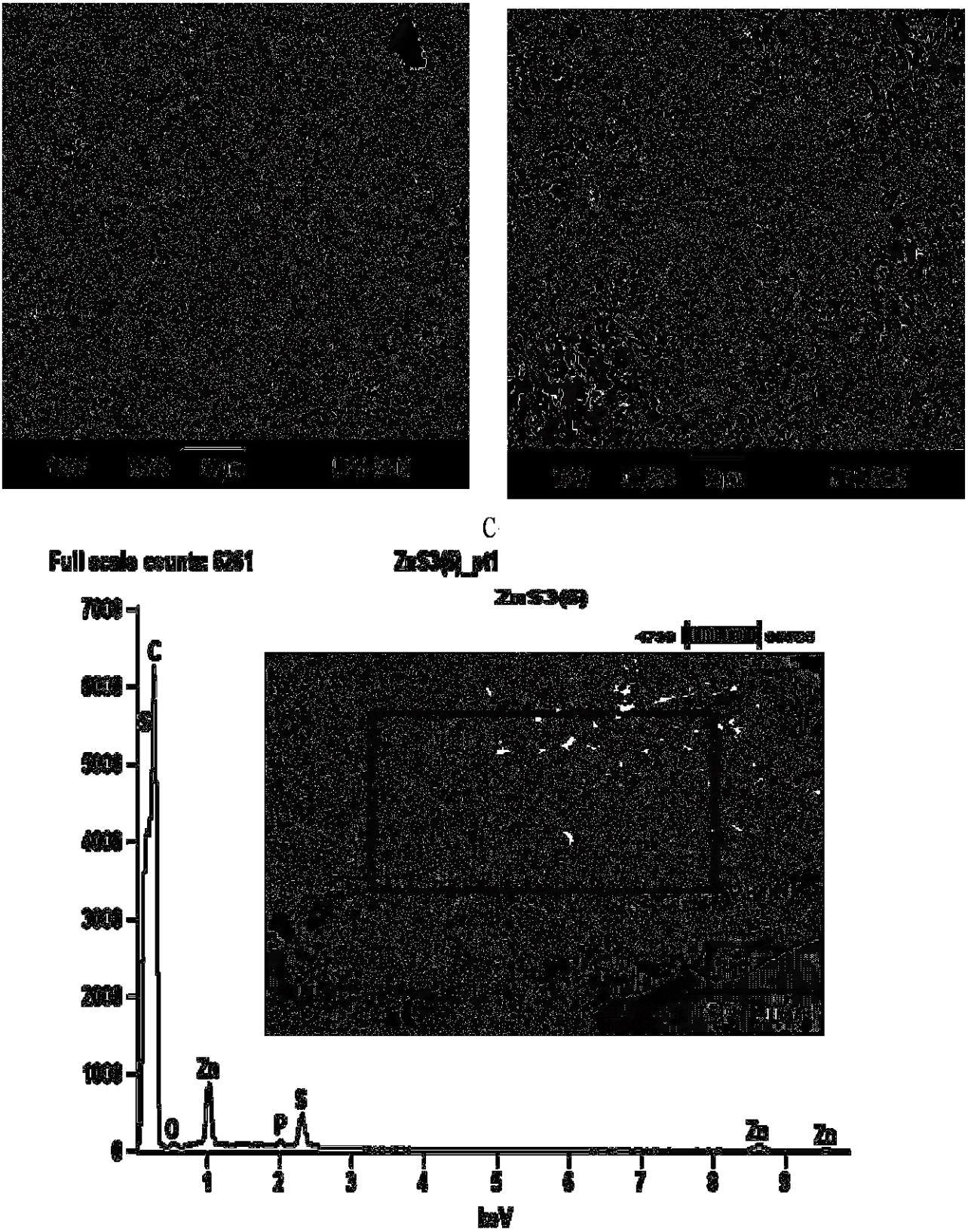

Figure 4.14: SEM micrograph of the ZnS (labeled as ZnS3) from ZnL^1L^3 complex (A) low magnification, (B) high magnification (C) EDX spectrum of the sample

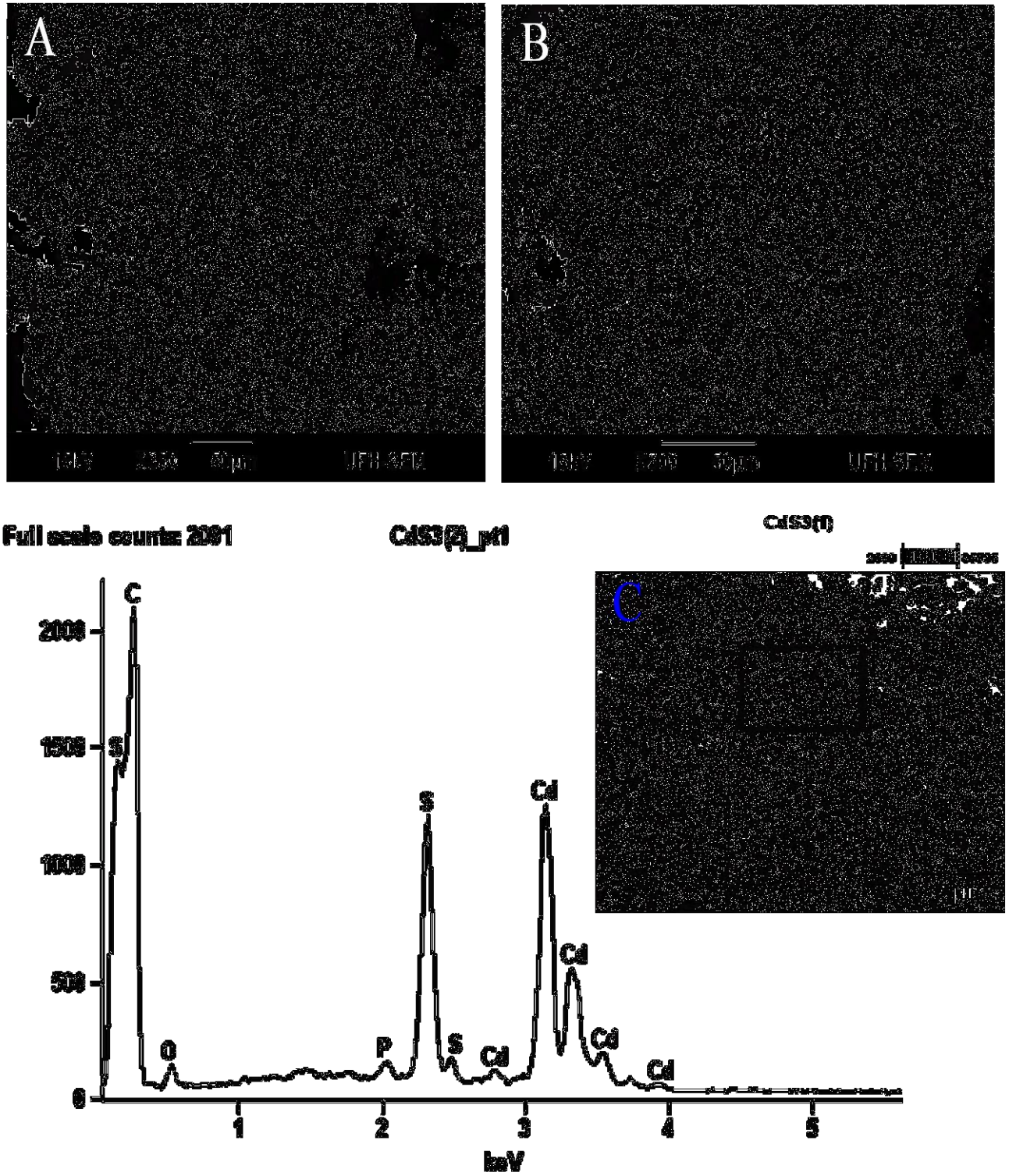

Figure 4.15: SEM micrograph of the CdS (labeled as CdS3) from CdL^1L^3 complex (A) low magnification, (B) high magnification (C) EDX spectrum of the sample

The surface morphology of HDA-capped HgS3 nanoparticles synthesized from HgL^1L^3 were investigated by recording SEM images as displayed in Figure 4.16. The SEM images reveal that the surface of HgS nanoparticles is fairly smooth. Both the particles tend to aggregate to secondary particles indicating that the alkyl groups play a very important role in controlling the morphology of the as-prepared nanoparticles [68]. Although there were challenges connected with getting clear morphology since nanoparticles tend to aggregate into larger conglomerates, it could be noticed that the examined particles consist of a number of smaller particles of 0.5 μm to few micrometers in size. Figures 4.16 (C) show a typical EDX patterns of HgS particles. As expected, the observed major peaks are due to the presence of mercury and sulfur indicating the presence of HgS particles in a sample. There is a negligible amount of oxygen ascribed to the oxidation of S atom to O atom during synthesis. The P is due to the trioctyl phosphine (TOP).

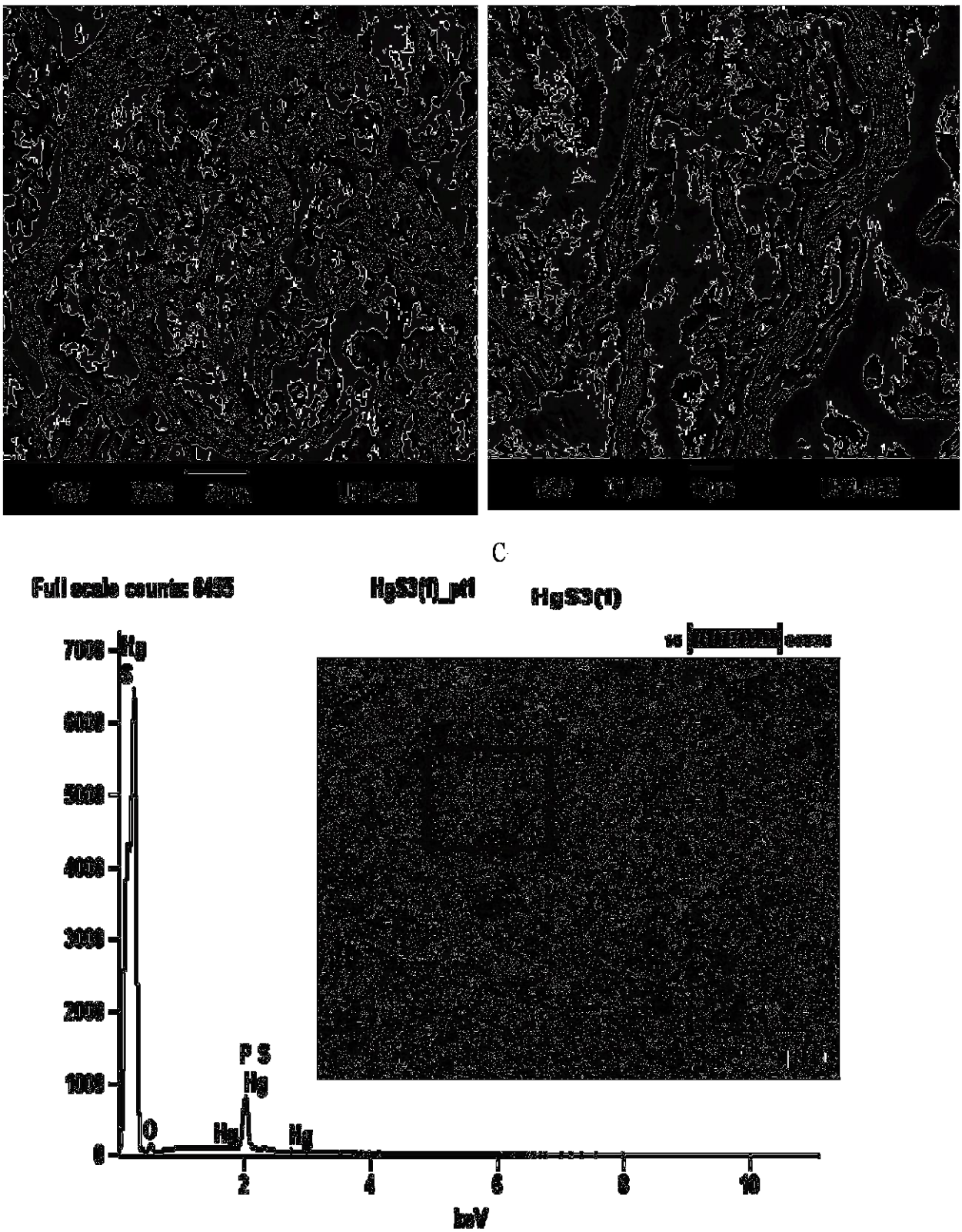

Figure 4.16: SEM micrograph of the HgS (labeled as HgS3) from HgL^1L^3 complex (A) low magnification, (B) high magnification (C) EDX spectrum of the sample

4.4 References

1. Li, Z.; Zhang, J.; Du, J.; Mu, T.; Liu, Z.; Chen, J.; Han, B. Preparation of cadmium sulfide/poly(methyl methacrylate) composites by precipitation with compressed CO_2. *J. Appl. Poly.Sci.* **2004**, *94*, 1643-1648.
2. Ma, R.M.; Wei, X.L.; Dai, L; Huo, H.B.; Qin, G.G. Synthesis of CdS nanowire networks and their optical and electrical properties. *Nanotech.* **2007**, *18*, 1-5.
3. Fasol, G. Nanowires: Small is beautiful. *Sci.* **1998**, *280*, 545-546.
4. Nair, P.S.; Radhakrishnan, T.; Revaprasadu, N.; Kolawole, G.; O'Brien, P. Cadmium ethylxanthate: A novel single-source precursor for the preparation of CdS nanoparticles. *J. Mater. Chem*. **2002**, *12*, 2722-2725.
5. Mahtab, R.; Rogers, J.P.; Murphy, C.J. Protein-sized quantum dot luminescence can distinguish between 'straight", "bent", and "kinked" oligonucleotides. *J. Am. Chem. Soc.* **1995**, *117*, 9099-9100.
6. Hao, Y.F.; Meng, G.W.; Wang, Z.L.; Ye, C.H.; Zhang, L.D. Periodically twinned nanowires and polytypic nanobelts of ZnS: The role of mass diffusion in vapor–liquid–solid growth. *Nano Lett.* 2006, *6*, 1650-1655.
7. Gao, X.D.; Li, X.M.; Yu, W.D. Morphology and optical properties of amorphous ZnS films deposited by ultrasonic-assisted successive ionic layer adsorption and reaction method. *Thin Solid Films* **2004**, *468*, 43-47.
8. Derfus, A.M.; Chan, W.C.W.; Bhatia, S.N. Probing the cytotoxicity of semiconductor quantum dots. *Nano Lett.* **2004**, *4*, 11-18.
9. Xia, B.; Lenggoro, I.W.; Okuyama, K. Synthesis and photoluminescence of spherical $ZnS:Mn^{2+}$ particles. *Chem. Mater.* **2002**, *14*, 4969-4974.

10. Nicolau, Y.F.; Dupuy, M.; Bruuel, M. Solution growth of ZnS, CdS, and Zn1–*x*Cd*x*S thin films deposited by the successive ion layer adsorption and reaction process. *J. Electrochem. Soc.* **1998**, *137*, 2915-2924.

11. Arai, T.; Senda, S.I.; Sato, Y.; Takahashi, H.; Shinoda, K.; Jeyadevan, B.; Tohji, K. Cu-doped ZnS hollow particle with high activity for hydrogen generation from alkaline sulfide solution under visible light. *Chem. Mater.* **2008**, *20*, 1997-2000.

12. Elidrissi, B.; Addou, M.; Regragui, M.; Bougrine, A.; Kachoune, A.; Bernecde, J.C. Structure, composition and optical properties of ZnS thin films prepared by spray pyrolysis. *Mater. Chem. Phys.* **2001**, *68*, 175-179.

13. Gangopadhyay, U.; Kim, K.; Mangalaraj, D.; Yi, J. Low cost CBD ZnS antireflection coating on large area commercial mono-crystalline silicon solar cells. *Appl. Surf. Sci.* **2004**, *230***,** 364-370.

14. Bhargava, R.N.; Gallagher, D.; Hong, X.; Nurmikko, D. Optical properties of manganese doped nanocrystals of zinc sulfide. *Phys. Rev. Lett.* **1994**, *72*, 416-419.

15. Tang. W.; Cameron, D.C. Electroluminescent zinc sulfide devices produced by sol-gel processing. *Thin Solid Films* **1996**, *280***,** 221-226.

16. Quan, Z.W.; Wang, Z.L.; Yang, P.P.; Lin, J.; Fang, J.Y. Synthesis and characterization of high-quality ZnS, ZnS:Mn^{2+}, and ZnS:Mn^{2+}/ZnS (core/shell) luminescent nanocrystals. *Inorg. Chem.* **2007**, *46***,** 1354-1360.

17. Bol, A.A.; Meijerink, A. Long-lived Mn^{2+} emission in nanocrystalline ZnS:Mn^{2+}. *Phys. Rev.* B **1998**, *58***,** R15997-R6000.

18. Tsuji, I.; Kudo, A. H_2 evolution from aqueous sulfite solutions under visible-light irradiation over Pb and halogen-codoped ZnS photocatalysts. *J. Photochem. Photobio. Chem.* **2003**, *156*, 249-252

19. Chinnu, M.K.; Saravanan, L.; Jayavel, R. Synthesis and characterization of hexamethylene tetramine (HMTA) capped CdS nanoparticles by hydrothermal method. *Inter. J. Nanosci.* **2011**, *10*, 441-445.
20. Maity, R.; Chattopadhyay, K.K. Synthesis and optical characterization of CdS nanowires by chemical process. *J. Nanopart. Res.* **2006**, *8*, 125-130.
21. El- Bially A.B.; Seoudi R.; Eisa W.; Shabaka A.A.; Soliman S.I.; Abd El-Hamid R.K.; Ramadan R.A. Preparation, characterization and physical properties of CdS nanoparticles with different sizes. *J. Appl. Sci. Res.* **2012**, *8*, 676-685.
22. Zhang, Y.C.; Wang, G.Y.; Hu, X.Y. Solvothermal synthesis of hexagonal CdS nanostructures from a single-source molecular precursor. *J. Alloys Compd.* **2007**, *437*, 47-52.
23. Rao, B.S.; Kumar, B.R.; Reddy, V.R.; Rao, T.S. Preparation and characterization of CdS nanoparticles by chemical co-precipitation technique. *Chalco. Lett.* **2011**, *8*, 177-185.
24. Singh, V.; Chauhan, P. Synthesis and structural properties of wurtzite type CdS nanoparticles. *Chalco. Lett.* **2009**, *6*, 421-426.
25. Onwudiwe, D.C.; Ajibade, P.A. ZnS, CdS and HgS nanoparticles via alkyl-phenyl dithiocarbamate complexes as single source precursors. *Int. J. Mol. Sci.* **2011**, *12*, 5538-5551.
26. O'Brien, P.; Park, J.H.; Waters, J. A single source approach to deposition of nickel sulfide thin films by LP-MOCVD. *Thin Solid Films* **2003**, *431*, 502-505.
27. Maity, R.; Chattopadhyay, K.K. Synthesis and optical characterization of CdS nanowires by chemical process. *J. Nanopart. Res.* **2006**, *8*, 125-130.
28. Ethayaraja, M.; Ravikumar, C.; Muthukumaran, D.; Dutta, K.; Bandyopadhyaya, R. CdS-ZnS core-shell nanoparticle formation: Experiment, mechanism, and simulation. *J. Phys. Chem. C*, **2007**, *111*, 3246-3252.

29. Soltani, N.; Saion, E.; Erfani, M.; Rezaee, K.; Bahmanrokh, G.; Drummen, G.P.C.; Bahrami, A.; Hussein, M.Z. Influence of the polyvinyl pyrrolidone concentration on particle size and dispersion of ZnS nanoparticles synthesized by microwave irradiation. *Int. J. Mol. Sci.* **2012**, *13*, 12412-12427.

30. Winkelmann, K.; Noviello, T.; Brooks, S. Preparation of CdS nanoparticles by first-year undergraduates. *J. Chem. Educ.* **2007**, *84*, 709-710.

31. Sahiner, N.; Sel, K.; Meral, K.; Onganer, Y.; Butun, S.; Ozay, O.; Silan, C. Hydrogel templated CdS quantum dots synthesis and their characterization. *Col. Surf. A: Physicochem. Eng. Aspects* **2011**, *389*, 6-11.

32. Marimuthu, G.; Ramalingam, K.; Rizzoli, C.; Arivanandhan, M. Solvothermal preparation of nano-*b*-HgS from a precursor, bis(dibenzyldithiocarbamato)mercury(II). *J. Nanopart. Res.* **2012**, *14*, 1-11.

33. Zhu, J.; Liu, S.; Palchik, O.; Koltypin, Y.; Gedanken, A. A novel sonochemical method for the preparation of nanophasic sulfides: Synthesis of HgS and PbS Nanoparticles. *J. Solid State. Chem.* **2000**, *153*, 342-348.

34. Brus, L.E. Electron-electron and electronhole interactions in small semiconductor crystallites: The size dependence of the lowest excited electronic state. *J. Chem. Phys.* **1984**, *80*, 4403-4409.

35. Marandi, M.; Hajisalem, G.; Taghavinia, N.; Houshiar, M. Fast two-step microwave-activated synthesis of Mn doped ZnS nanocrystals: Comparison of the luminescence and doping process with thermochemical approach. *J. Lumin.* **2011**, *131*, 721-726.

36. Tamrakar, R.; Ramrakhiani, M.; Chandra, B.P. Effect of capping agent concentration on photophysical properties of zinc sulfide nanocrystals. *Open Nanosc. J.* **2008**, *2*, 12-16.

37. Lippens, P.E.; Lannoo, M. Optical properties of II-VI semiconductor nanocrystals. *Semicond. Sci. Technol.* **1991**, *6*, A157-A160.

38. Dhanam, M.; Devasia, D.P.; Kavitha, B.; Maheswari, B. Structural and optical analysis of CdS nanocrystals prepared by low temperature thermolysis. *Dig. J. Nanomater. Biostruct.* **2010**, 5, 587-592.

39. Chen, D.; Weng, S. Chemical effects of size quantization of CdS nanoparticles. *Sci. China. B* **1996**, *39*, 646-653.

40. Chakraborty, I.; Mitra, D.; Moulik, S.P. Spectroscopic studies on nanodispersions of CdS, HgS, their core-shells and composites prepared in micellar medium. *J. Nanopart. Res.* **2005**, *7*, 227-236.

41. Wichiansee, W.; Nordin, M.N.; Green, M.; Curry, R.J. Synthesis and optical characterization of infra-red emitting mercury sulfide (HgS) quantum dots. *J. Mater. Chem.* **2011**, *21*, 7331-7336.

42. Revaprasadu, N.; Mlondo, S.N. Use of metal complexes to synthesize semiconductor nanoparticles. *Pure Appl. Chem.* **2006**, *78*, 1691-1702.

43. Yin, Y.; Xu, X.; Ge, X.; Lu, Y; Zhang, Z. Synthesis and characterization of ZnS colloidal particles via γ-Radiation. *Radiat. Phys. Chem.* **1999**, *55*, 353-356.

44. Parmar, P.R.; Mangrola, M.H.; Parmar, B.H.; Joshi, V.G. A software to calculate crystalline size by Debye-Scherrer formula using VB.NET. *Multi Discipl. Edu. Glob. Quest.* **2012**, *1*, 146-154.

45. Ding, T.; Zhu, J.-J. Microwave heating synthesis of HgS and PbS nanocrystals in ethanol solvent. *Mater. Sci. Eng. B* **2003**, 100, 307-313.

46. Sharma, R. Optical studies of CdS:Mn nanoparticles. *Luminesc.* **2012**, *27*, 501-504.

47. Sharma, M.; Kumara, S.; Pandey, O.P. Photo-physical and morphological studies of organically passivated core-shell ZnS nanoparticles. *Dig. J. Nanomater. Biostruct.* **2008**, *3*, 189-197.

48. Liao, X.-H.; Zhu, J.-J.; Chen, H.-Y. Microwave synthesis of nanocrystalline metal sulfides in formaldehyde solution. *Mater. Sci. Eng. B* **2001**, *85*, 85-89.

49. Song, C.; Yang, M.; Wang, D.; Hu, Z. Synthesis and optical properties of ZnS hollow spheres from single source precursor. *Mater. Res. Bull*. **2010**, *45*, 1021-1025.

50. Liu, S.; Zhang, H.; Swihart, M.T. Spray pyrolysis synthesis of ZnS nanoparticles from a single-source precursor. *Nanotech*. **2009**, *20*, 1-8.

51. Moloto, M.J.; Revaprasadu, N.; Kolawole, G.A.; O'Brien, P.; Malik, M.A.; Motevalli, M. Synthesis and X-ray single crystal structures of cadmium(II) complexes: $CdCl_2[CS(NHCH_3)_2]_2$ and $CdCl_2(CS(NH_2)NHC_6H_5)_4$ single source precursors to CdS nanoparticles. *E-J. Chem.* **2010**, *7*, 1148-1155.

52. Onwudiwe, D.C.; Ajibade, P.A. Zn(II), Cd(II) and Hg(II) complexes of N-methyl-N-phenyl dithiocarbamate as single-source precursors for the synthesis of metal sulfide nanoparticles. *Mater. Lett*. **2011**, *65*, 3258-3261.

53. Kumar, S.; N.K. Verma, N.K.; Singla, M.L. Reflective characteristics of Ni doped ZnS nanoparticle-pigment and their coatings. *Chalco. Lett.* **2011**, *8*, 561-569.

54. Tiwari, A.; Khan, S.A.; Kher, R.S. Surface characterization and optical properties of polyphosphate capped ZnS nanoparticles. *Adv. Appl. Sci. Res*. **2011**, *2*, 105-110.

55. Moloto, N.; Revaprasadu, N.; Moloto, M.J.; O'Brien, P.; Raftery, J. N,N'-diisopropylthiourea and N,N'-dicyclohexylthiourea zinc(II) complexes as precursors for the synthesis of ZnS nanoparticles. *South. Africa. J. Sci*. **2009**, *105*, 258-263.

56. Venkatesu, P.; Ravichandran, K. Manganese doped cadmium sulfide (CdS: Mn) quantum particles: Topological, photoluminescence and magnetic studies. *Adv. Mat. Lett.* **2013**, *4*, 202-206.

57. Chinnu, M.K.; Saravanan, L.; Jayavel, R. Synthesis and characterization of hexamethylene tetramine (HMTA) capped CdS nanoparticles by hydrothermal method. *Inter. J. Nanosci*. **2011**, *10*, 441-445.

58. Jothi, N.S.N.; Gunaseelan, R.; Raj, T.M.; Sagayaraj, P. Investigation on mild condition preparation and structural, optical and thermal properties of PVP capped CdS nanoparticles. *Arch. Appl. Sci. Res*. **2012**, *4*, 1723-1730.

59. Ajibade, P.A.; Onwudiwe, D.C. Optical and structural characterization of ZnS, CdS and HgS Nanoparticles synthesized from N-Alkyl-N-Phenyl dithiocarbamate complexes. *Synth. React. Inorg. Metal-Org. Nano-Metal Chem*. **2013**, 43, 10-18.

60. Ramamurthy. N.; Rajesh, K.M.; Murugadoss, G. Synthesis and study of optical properties of CdS nanoparticles using effective surfactants. *Nanosci. Nanotech: An Inter. J*. **2011**, *1*, 12-16.

61. Dhanam, M.; Kavitha, B.; Jose, N.; Devasia, D.P. Analysis of ZnS nanoparticles prepared by surfactant micelle-template inducing reaction. *Chalco. Lett*. **2009**, *6*, 713-722.

62. Soosen, S.M.; Lekshmi, B.; George, K.C. Optical properties of ZnO nanoparticles. *Acad. Rev*. **2009**, *14*, 57-65.

63. Kandasamy, K.; Singh, H.B.; Kulshreshtha, S.K. Synthesis and characterization of CdS and CdSe nanoparticles prepared from novel intramolecularly stabilized single-source precursors. *J. Chem. Sci*. **2009**, *121*, 293-296.

64. Sun, C.; Westover, R.D.; Long, G.; Bajracharya, C.; Harris, J.D.; Punnoose, A.; Rodriguez, R.G.; Pak.J.J. A large-scale synthesis and characterization of quaternary CuIn*x*Ga1−*x*S2 chalcopyrite nanoparticles via microwave batch reactions. *Inter. J. Chem. Eng*. **2011**, 1-8.

65. Wang, H.; Zhu, J.-J. A sonochemical method for the selective synthesis of α-HgS and β-HgS nanoparticles. *Ultrason. Sonochem*. **2004**, *11*, 293-300.

66. Bang, J.H.; Suslick, K.S. Applications of ultrasound to the synthesis of nanostructured materials. *Adv. Mater*. **2010**, *22*, 1039-1059.

67. Ahamad, T.; Alshehri, S.M. Synthesis of CdS nanocrystals using polymer metal complex as a single source precursor and their physicochemical properties. *Nano. Hybr.* **2012**, *1*, 45-56.

68. Mehta, S.K.; Kumar, S.; Chaudhary, S.; Bhasin, K.K. Nucleation and growth of surfactant-passivated CdS and HgS nanoparticles: Time-dependent absorption and luminescence profiles. *Nanoscale* **2010**, *2*, 145-152.

CHAPTER FIVE

5.0 CHARACTERIZATION OF METAL SULFIDE NANOPARTICLES / POLY METHYL METHACRYLATE NANOCOMPOSITES

5.1 Introduction

Over the past few years there have been reports where metal sulfide nanoparticles were incorporated into polymer by chemical methods where the precursors were directly reacted in the presence of a polymer matrix which serves to protect the particle surfaces [1]. Among the broad variety of available polymers, poly(methyl methacrylate) or PMMA is one of the most widely studied due to its outstanding and promising mechanical and chemico-physical properties [2,3]. The chemical structure of PMMA is shown in Figure 5.1 and the characteristic FTIR frequencies are presented in Table 5.1. The choice of the polymer is guided mainly by its properties such as mechanical, thermal, electrical, optical and magnetic behaviours.

Table 5.1: Characteristic frequencies of PMMA in FTIR [7]

Chemical bond	**Wavenumber cm^{-1}**
-OH	3650 ~ 3450
-C=C	1500 ~ 1900
-C=O	1725 ~ 1660
Aromatic ring CH (stretch)	3100 ~ 3000
Monosubstituted aromatic ring CH (bending)	710 ~ 665

However, other properties such as hydrophobic/hydrophilic balance, chemical stability, bio-compatibility, opto-electronic properties and chemical functionalities (*i.e.*, solvation,

wettability, templating effect, *etc.*) have to be considered in the choice of the polymer [4]. The PMMA has a polar ester group $–COOCH_3$ with a dipole moment of 1.6 Debye and dielectric constant of 3.4 [6]. Its wide applications in many technological fields take advantage of the unique combination of excellent optical properties (clarity, transparency from the near UV to the near IR), with chemical inertness, some good mechanical properties, electrical properties, safety, weather resistance, formability, moldability, easy shaping, good abrasion resistance, hardness and stiffness and is widely used in many applications, such as lenses, glazing (particularly in aircraft), light pipes, meter covers, bathroom fittings, skylights and toys [1-9].

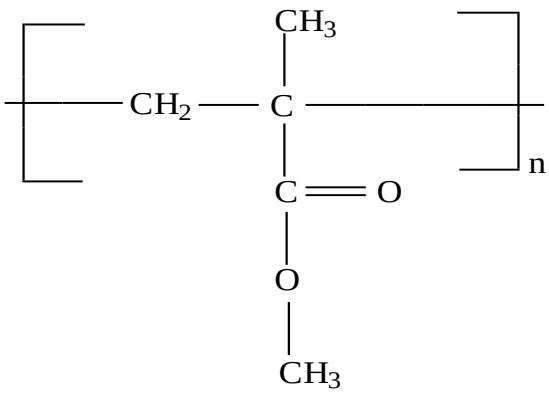

Figure 5.1: Repeating units of poly(methyl methacrylate)

However, PMMA has limitations which have severely restricted its use, such as its thermal instability and not able to filter ultra-violet (UV) light. The drawback may be overcome by incorporation of semiconductor nanoparticles into the polymer matrix to form nanocomposites [10,11]. A nanocomposite is defined as a mixture of two or more materials with different physical and chemical properties and distinguishable interface [12]. Recently, researchers have focused on the synthesis, characterization and optical properties of metal sulfide/polymer nanocomposites such as ZnS/PMMA and CdS/PMMA nanocomposites. For example poly(N-isopropylacrylamide) has been interacted with CdS nanoparticles, resulting

in a thermoresponsive CdS/ poly(N-isopropylacrylamide) nanocomposites [13]. The incorporation of metal sulfide nanocrystals into polymer matrixes has been demonstrated via direct blending [14,15], in situ synthesis of nanoparticles within polymer media [16,17], surface modification of nanoparticles with monomers followed by polymerization from nanoparticle surface and grafting of preformed functionalized polymers to nanoparticles [18]. The major goal for the synthesis of nanocomposites is to obtain combinations of functionalities, such as thermally stable materials with good mechanical properties that are optically clear [19]. However shape control has been much more difficult to achieve, hence exploration of novel method for the preparation of differently shaped nanoparticles in polymer matrix is a challenging area of research [20]. The experimental procedure for the synthesis of metal sulfide nanoparticles / poly (methyl methacrylate) nanocomposites was described in Chapter Two, Section 2.6. the metal sulfide nanoparticles / poly (methyl methacrylate) nanocomposites were synthesized from six metal sulfide nanoparticles in the presence of poly (methyl methacrylate) matrix. The scheme 5.1 shows the reaction stages undertaken in the synthesis metal sulfide nanoparticles / poly (methyl methacrylate) nanocomposites.

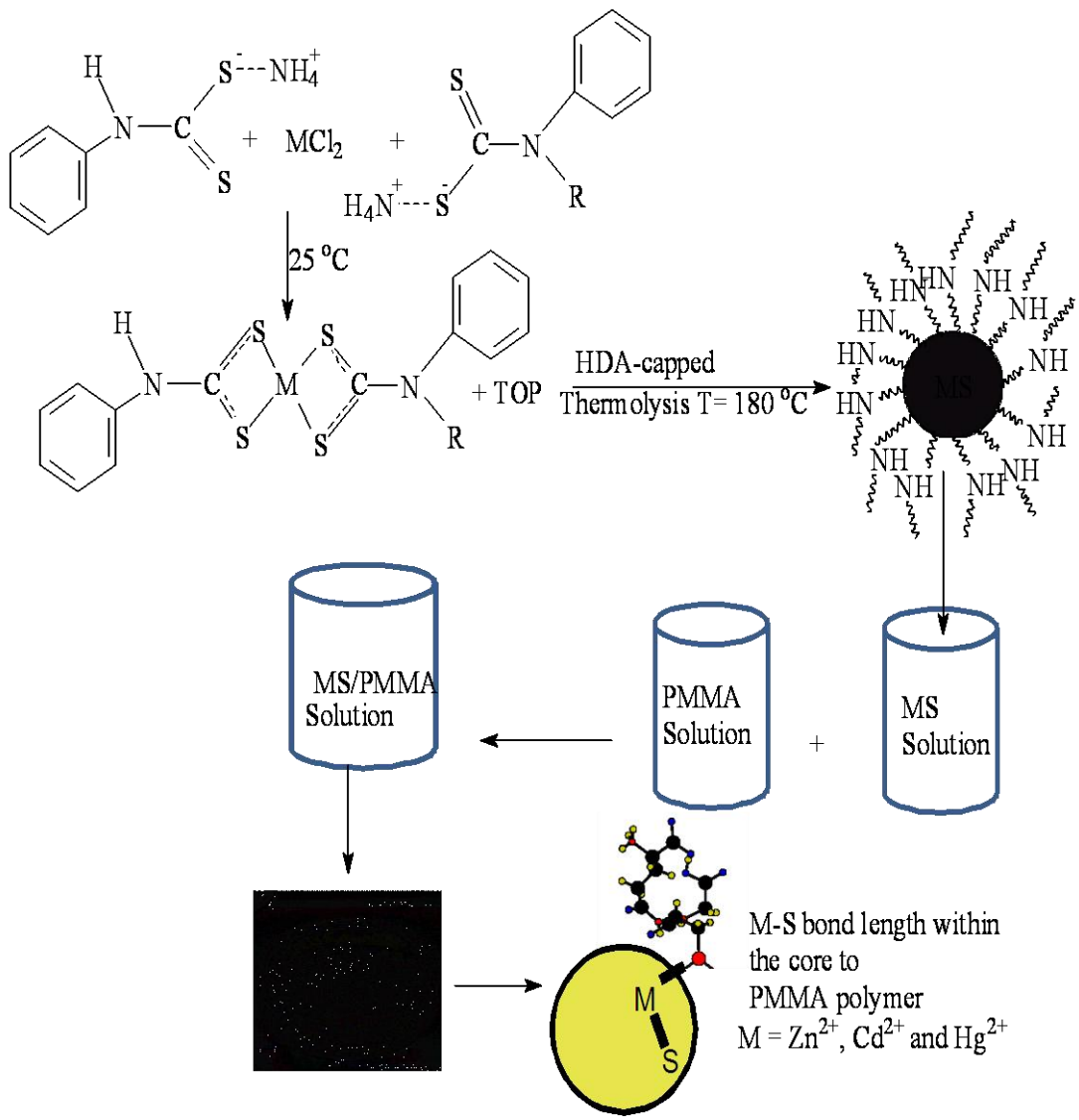

Scheme 5.1: Preparative scheme showing reaction steps from dithiocarbamates ligands, metal complexes, HDA-capped nanoparticles and then MS/PMMA nanocomposites

5.2 Characterization of metal sulfide nanoparticles/ poly (methyl methacrylate) nanocomposites synthesized form ZnS2, CdS2 and HgS2

5.2.1 Infrared spectra of ZnS2/PMMA, CdS2/PMMA and HgS2/PMMA nanocomposites

The PMMA and ZnS2/PMMA, CdS2/PMMA, HgS2/PMMA nanocomposites were characterized with ATR-FTIR (Figure 5.2) to determine if any changes in functionality occurred in the nanocomposites due to any chemical interaction between the PMMA and the metal sulfide nanoparticles.

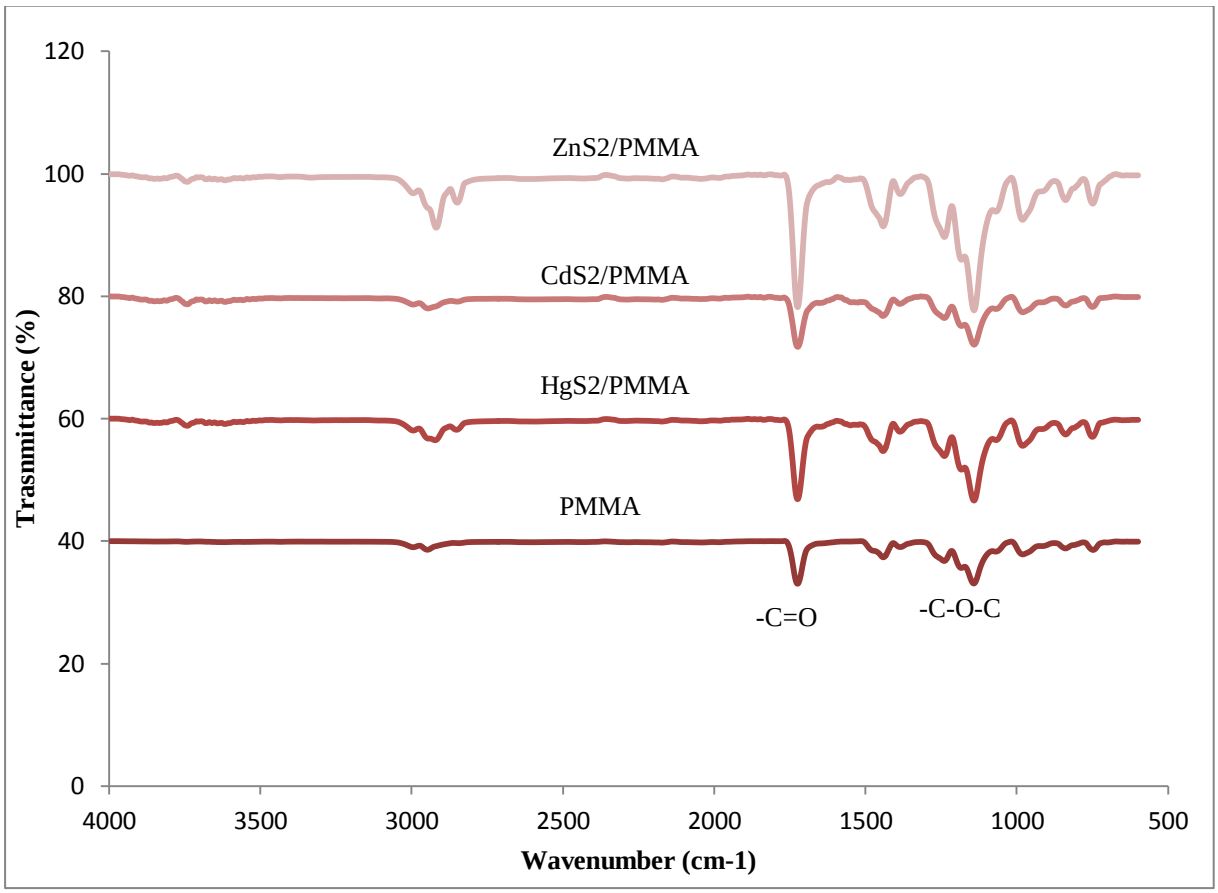

Figure 5.2: The FTIR spectra of PMMA and its MS2/PMMA nanocomposites

For the PMMA, the peak assigned to the C–H stretching vibration was observed at 2977 cm^{-1}. The strong peak at 1730 cm^{-1} is assigned to the carbonyl functionality (C=O). The peaks at

1157, 1199 and 1265 cm^{-1} correspond to stretching and deformation vibrations of C–O–C. The peaks observed at 999 cm^{-1} and 858 cm^{-1} correspond to the bending vibrations of C–H and the peak at 746 cm^{-1} is attributed to the vibrations of the polymer chains [11, 21]. The ATR-FTIR spectra of ZnS2/PMMA, CdS2/PMMA and HgS2/PMMA nanocomposites were compared to free PMMA spectra. The comparison gave almost identical feature, except the absence of peak around 1640 cm^{-1}, which would originate due to the double bond of MMA monomer [22]. This also indicates the homogeneity of nanocomposites solution since only 3% weight of metal sulfide nanoparticles was used. These results confirmed that the dispersion of metal sulfide nanoparticles into PMMA was successful.

5.2.2 X-ray diffraction patterns

The XRD pattern of ZnS2/PMMA, CdS2/PMMA and HgS2/PMMA nanocomposites were carefully studied and compared with that of pure PMMA as shown in Figure 5.3.

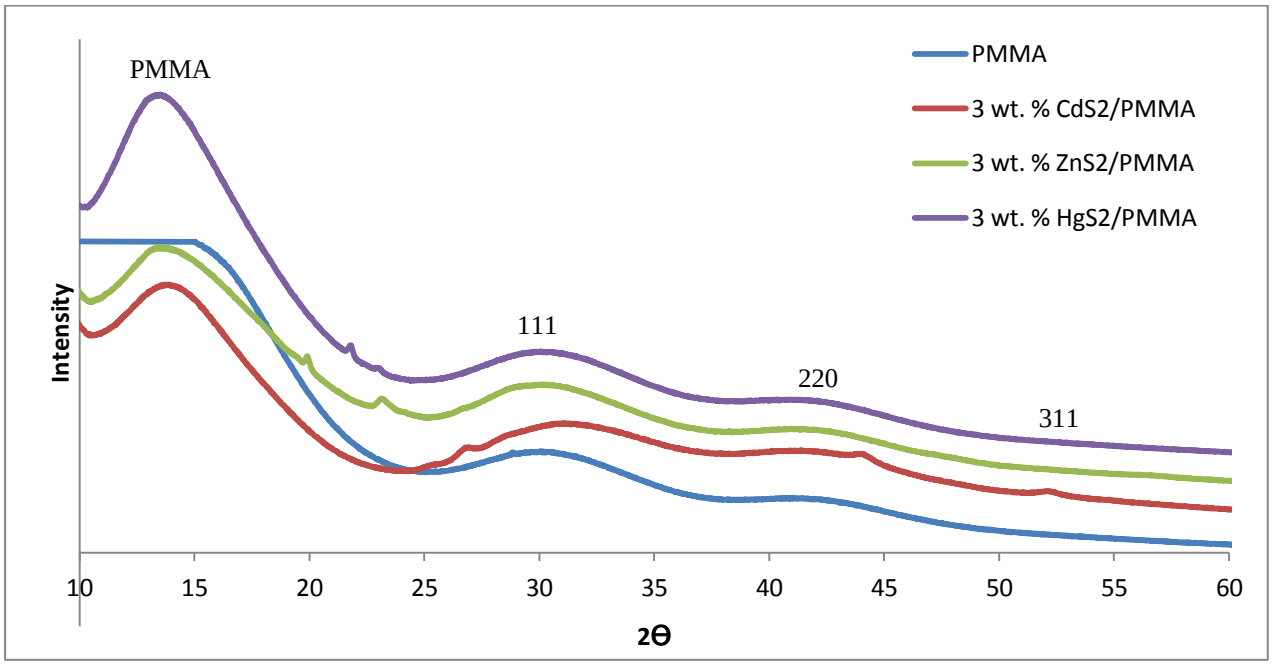

Figure 5.3: XRD patterns of pure PMMA, ZnS2/PMMA, CdS2/PMMA and HgS2/PMMA nanocomposites

The metal sulfides/PMMA nanocomposites were prepared by simply dispersing 3wt. % of metal sulfides nanoparticles into PMMA solution. Very broad peaks were observed for pure PMMA matrix, suggesting the absence of ZnS2 nanoparticles. However, broad diffraction peaks appeared in the case of the ZnS2 embedded in PMMA matrix. The peak broadening in the XRD patterns clearly indicates the formation of ZnS nanoparticles of small size [23, 24]. Three characteristic peaks of ZnS2/PMMA nanocomposites corresponded to the lattice planes of (111), (220) and (311), are very well matched with the cubic ZnS structure (JCPDS No. 05-0566) [25]. It is worth noting that the peak percentage and intensity of inorganic phase in a nanocomposite sample is low but the signal corresponding to the most abundant crystallographic planes of PMMA matrix can be detected at diffraction angle $2\theta = (10\text{-}20^{o})$ [24, 26-28]. The average particle size has been calculated from X-ray diffraction study using Debye Scherrer formula as shown in Equation 4.3 [29]. The calculated size was found to be 1.02 nm, indicating the presence of nano-sized ZnS nanoparticles. The XRD pattern (Figure 5.3) obtained for CdS2/PMMA nanocomposites corresponded to pure cubic CdS when compared with the standard reference (JCPDS 03-065-2887) [30]. Three peaks with 2θ values of 29.4, 43.3 and 52.3 appeared in the spectrum of the sample and may be assigned to the (111), (220) and (311) Miller indices. This confirms the presence of CdS2 nanoparticles incorporated into PMMA matrix because the pure PMMA pattern do not clearly display all the peacks observed in CdS2/PMMA nanocomposites. The very broad XRD peak at a low diffraction angle, around $2\theta = 13.5°$, indicates amorphous PMMA [31]. The average crystallite size calculated using Equation 4.3, was found to be 1.35 nm.

The phase composition of as-synthesized HgS2/PMMA nanocomposites was also compared to PMMA characterized by XRD as shown in Figure 5.3. The pattern show three broad characteristic peaks for HgS2/PMMA nanocomposites ($2\theta = 29.7^{o}$, 41.5^{o} and 52.5^{o}

corresponding to Miller indices (111), (220) and (311) respectively [32-34]. The broadness of the XRD peaks could be due to the homogeneity of the prepared nanocomposites solution. The broadening of the diffraction peaks allows an approximate evaluation of crystallite size by the Scherrer's formula and the distribution of peak intensities may give also an idea of nanoparticle shape [24]. The diffraction peak due to PMMA in the HgS2/PMMA sample is at $2\theta = 13.5^{o}$. The crystallite size as calculated from Scherrer equation 5.1, was found to be 1.07 nm. The increasing order of particle sizes are ZnS2/PMMA< HgS2/PMMA< CdS2/PMMA ranging from 1.02-1.35 nm. These calculated particle sizes are smaller than those particles obtained from electron microscopy, suggesting that estimating the particles using the XRD alone is not enough because of the presence of materials not directly estimated via XRD studies.

5.2.3 Thermogravimetric analyses of MS2/PMMA nanocomposites

In order to study the thermal stability of MS nanoparticles embedded in PMMA host matrix, the TGA decomposition patterns of MS2/PMMA = (ZnS2/PMMA, CdS2/PMMA and HgS2/PMMA) nanocomposites were studied and carefully compared with the decomposition curves of the PMMA polymer and their respective precursor complexes in Figure 5.4.

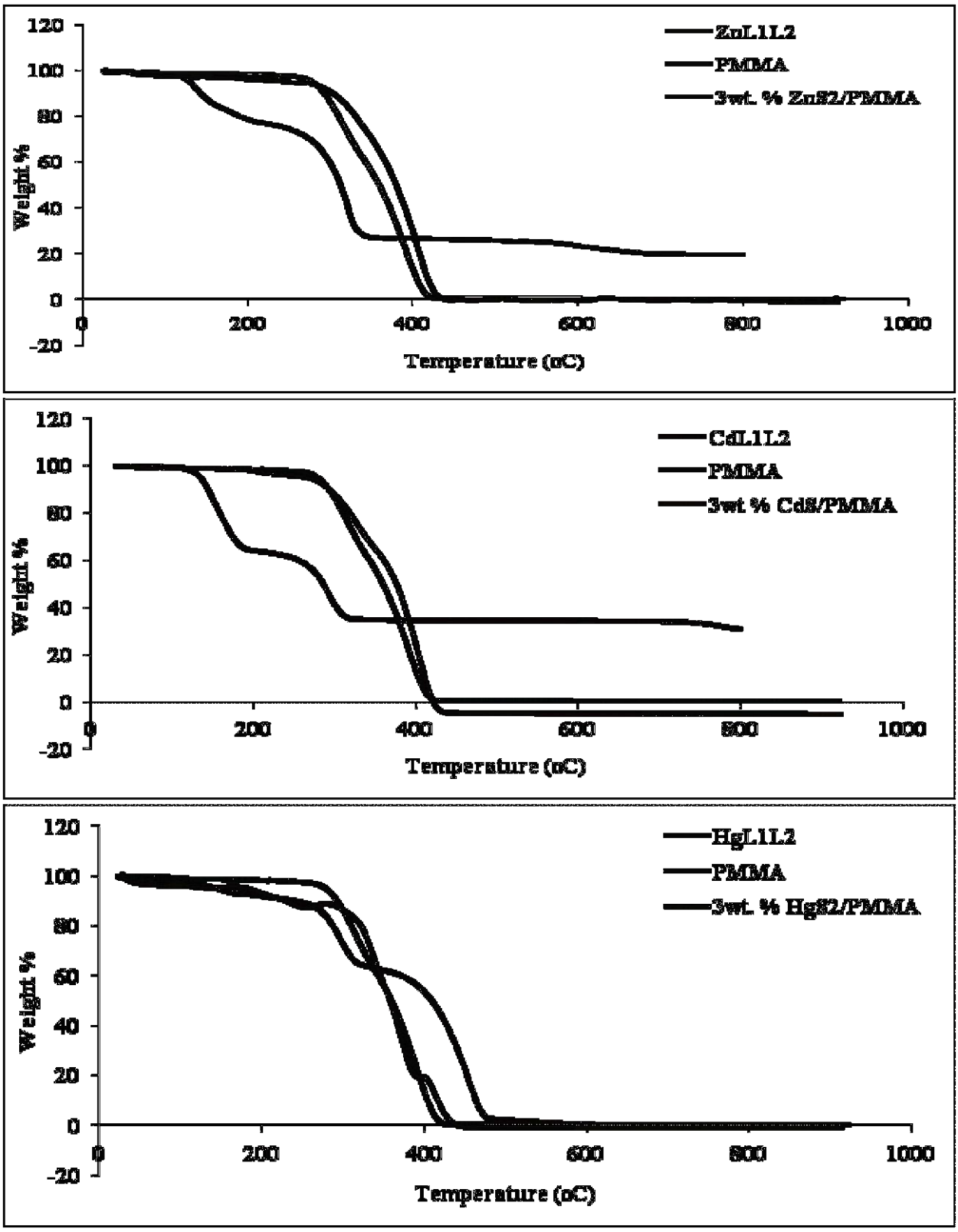

Figure 5.4: TGA curves for ML^1L^2 precursor complex, pure PMMA and their MS2/PMMA nanocomposites. M = Zn, Cd and Hg

The main degradation step of ZnS2/PMMA nanocomposites occurs at 265-425 ^{o}C. The TGA curves for free PMMA show one major decomposition step (260-420 ^{o}C), owing to the decomposition of PMMA matrix [35]. However, the thermal stability of the ZnS2/PMMA nanocomposites is enhanced compared to the pure PMMA, which may be due to partially altered molecular mobility of the polymer chains due to their adsorption on the surface of the nanoparticles because of the amount of ZnS2 nanoparticles embedded into PMMA matrix [36]. The major decomposition step for CdS2/PMMA nanocomposite occurs at about 270-430 ^{o}C. These results depict that the thermal stability of CdS2/PMMA nanocomposites is higher than that of its PMMA matrix showing strong interactions between the CdS nanoparticles and the PMMA polymer matrix. The TGA curve of the nanocomposites also indicates the presence of residue ascribed to the presence of the CdS2 nanoparticles dispersed in PMMA matrix. The TGA decomposition curves for HgS2/PMMA nanocomposites indicates that the thermal stability for HgS2/PMMA nanocomposites is similar to that of the PMMA matrix except that the nanocomposites started to decompose at a temperature below 100 ^{o}C, accompanied with a weight loss of about 10 %.

When ZnS2/PMMA, CdS2/PMMA and HgS2/PMMA nanocomposites are compared to their respective precursor complexes used in the synthesis of the metal sulfide nanoparticles, it could be noted that the nanocomposites are more thermally stable than their precursor complexes at temperatures below 400 ^{o}C. This confirms strong interaction between metal sulfide nanoparticles and the polymer matrix. The precursor complexes seem to be more stable after 400 ^{o}C due to the presence of metal sulfide nanoparticles residue although HgL^1L^2 precursor complex show the process of volatilization of the sample. Salavati-Niasari and Ghanbari [12] discussed different effects that cause a sample to lose, or even gain mass to include evaporation of volatile constituents such as desorption of gases and moisture,

thermal decomposition in an inert atmosphere with the formation of gaseous products and oxidation of constituents.

5.2.4 SEM and EDX of ZnS2/PMMA, CdS2/PMMA and HgS2/PMMA nanocomposites

Scanning electron microscope was employed as a convenient technique to study the microstructure of nanocomposites. Figures 5.5 (A and B) show SEM micrographs of ZnS2/PMMA nanocomposites at different magnifications synthesized from 3wt. % ZnS2 nanoparticles dispersed in PMMA matrix. Figure 5.5 C shows the EDX spectrum of the ZnS2/PMMA nanocomposites. The accelerating voltage of 15 kV was used for all prepared nanocomposites. The SEM pictures showed the regular well spherical morphology of nanocomposites. From these Figures, it was very clear that ZnS2 nanocomposites were hosted within PMMA matrix. EDX spectrum of ZnS2/PMMA nanocomposites reveals that the prepared nanocomposites are mainly composed of zinc and sulfur atoms within the scan area, confirming the presence of ZnS nanoparticles in PMMA matrix. Other traces of elements like carbon and oxygen are observed possibly due to the use of carbon tape and retained solvent after the deposition step [25]. The intense Au peaks are due to gold and palladium coating which was used to overcome charging of samples. Figure 5.6 (A and B) show the CdS2/PMMA composite prepared by 3wt% ratio of CdS in PMMA matrix. An EDX spectrum of both CdS2/PMMA composite is displayed in Figure 5.6 (C). In these images, it could be seen that there is existence of CdS particles which are homogeneously dispersed in the PMMA matrix [37]. EDX spectrum of CdS2/PMMA nanocomposites reveals that the prepared nanocomposites are mainly composed of cadmium and sulfur atoms within the scan area, confirming the presence of CdS nanoparticles in PMMA matrix. Other traces of elements like carbon and oxygen are observed possibly due to the use of carbon tape and

retained solvent after the deposition step. The intense Au peaks are due to gold and palladium coating which was used to overcome charging of samples.

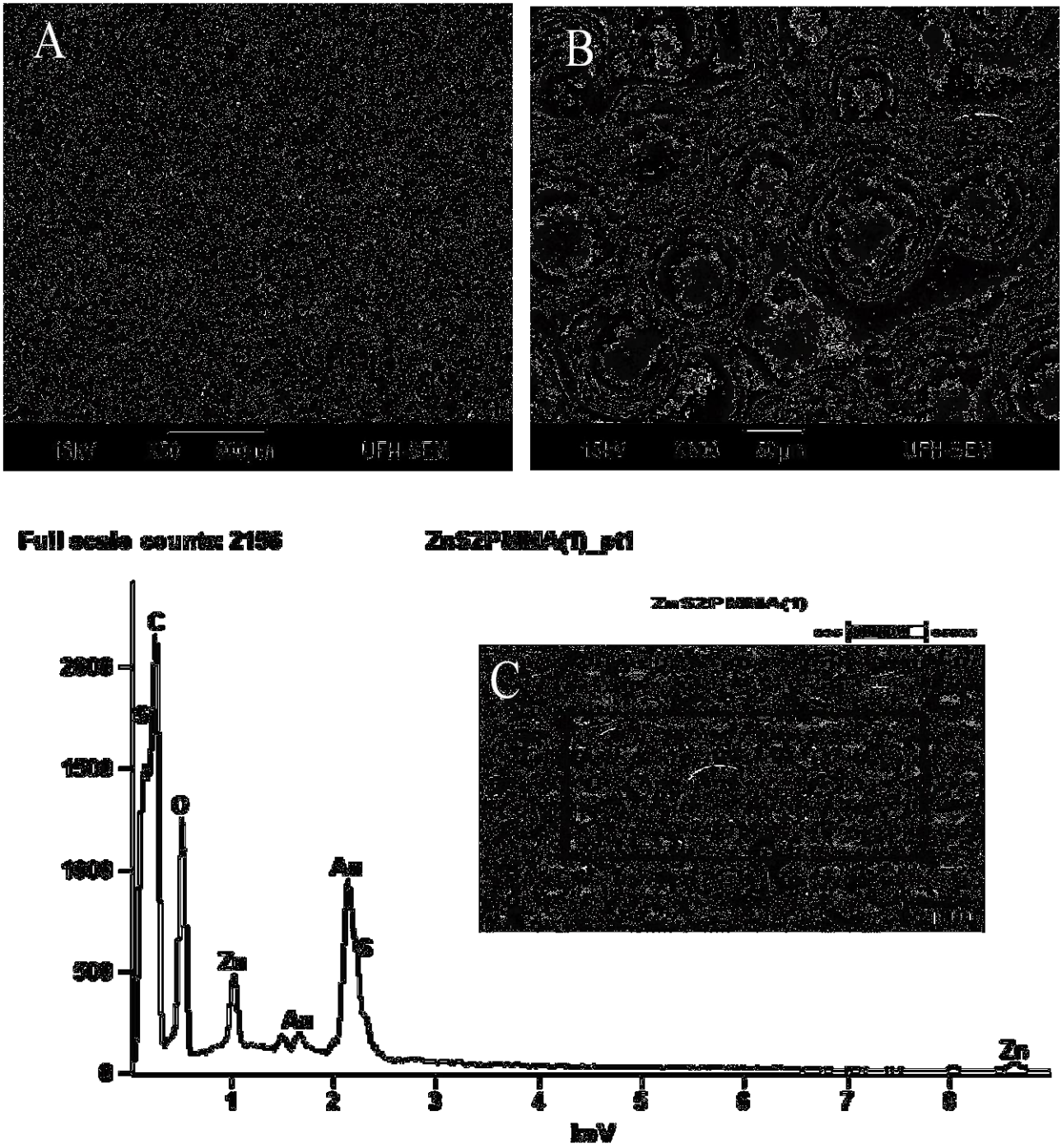

Figure 5.5: (A) and (B) are SEM micrograph of ZnS2/PMMA nanocomposites at different magnification prepared from 3wt. % ZnS2 nanoparticles dispersed in PMMA matrix. (C) EDX spectrum of the sample

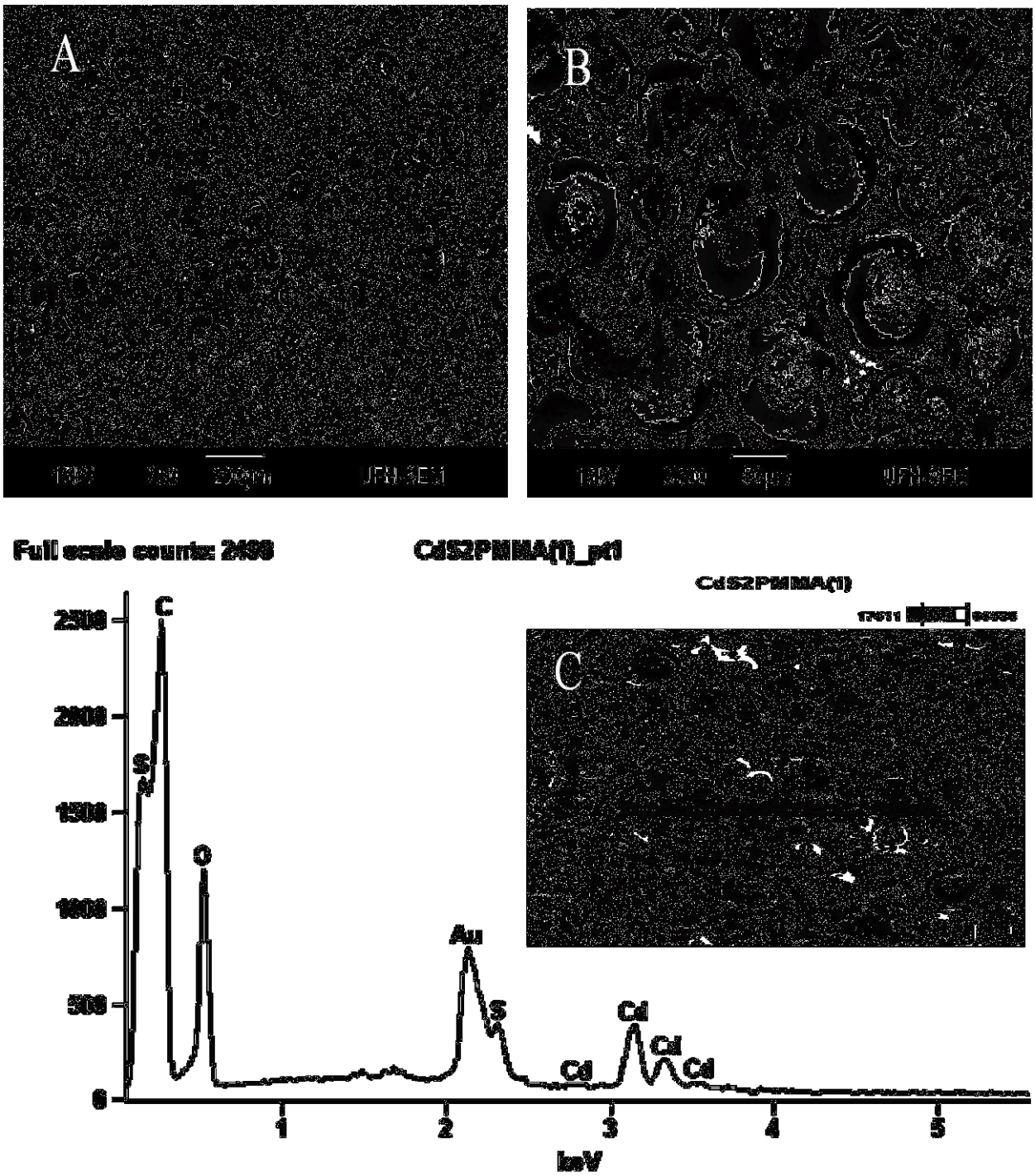

Figure 5.6: (A) and (B) are SEM micrograph of CdS2/PMMA nanocomposites at different magnification prepared from 3wt. % CdS2 nanoparticles dispersed in PMMA matrix. (C) EDX spectrum of the sample

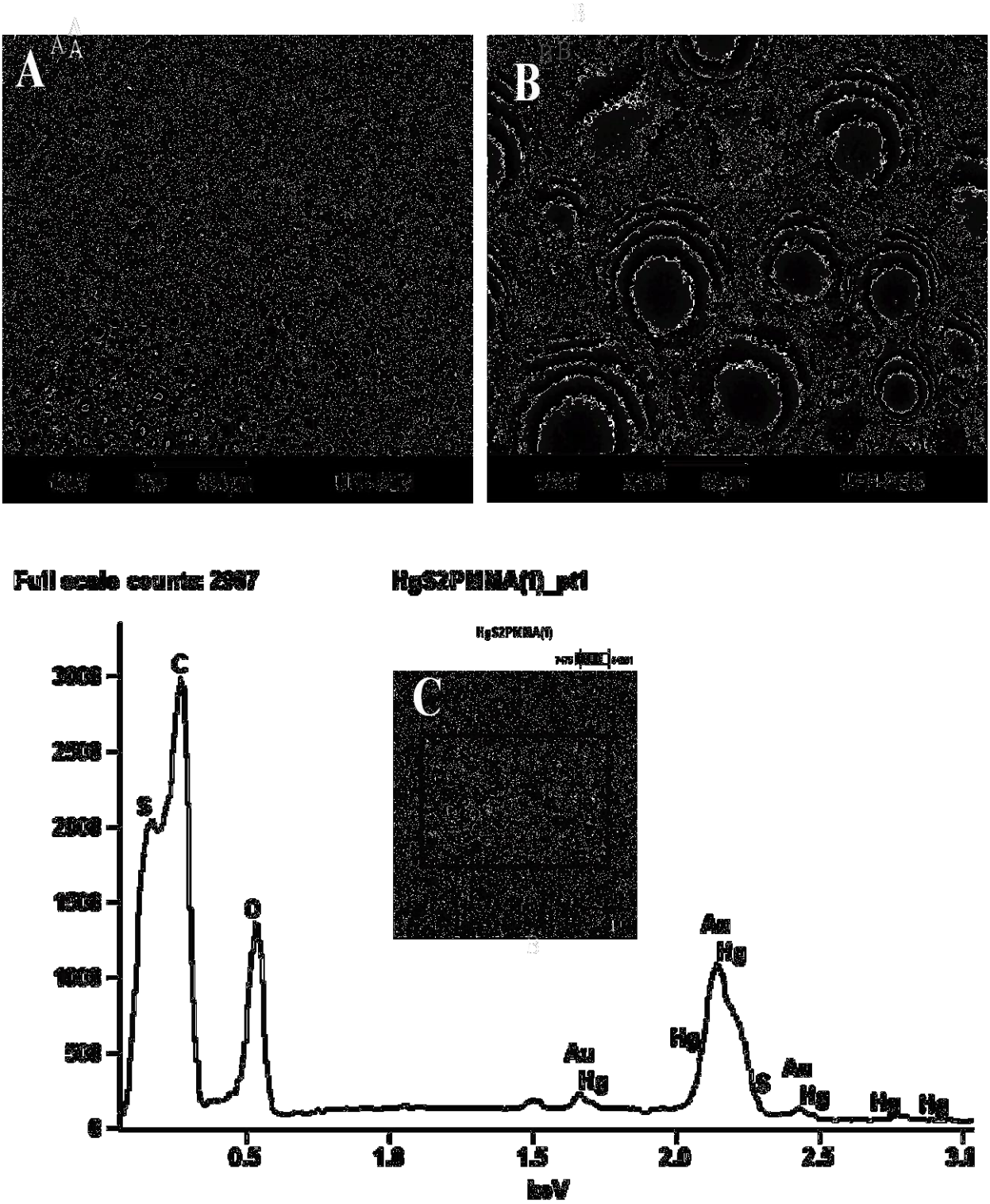

Figure 5.7: (A) and (B) are SEM micrograph of HgS2/PMMA nanocomposites at different magnification prepared from 3wt. % HgS2 nanoparticles dispersed in PMMA matrix. (C) EDX spectrum of the sample

The surface morphology of the HgS2/PMMA nanocomposites is shown in Figure 5.7 (A and B). The pictures show evenly distributed spherical particles with agglomeration [38]. An EDX spectrum of the HgS2/PMMA nanocomposites (Figure 5.7 (C)) reveals that the prepared nanocomposites are mainly composed of Hg and S, confirming the presence of HgS nanoparticles within the host PMMA matrix.

5.2.5 TEM images of ZnS2/PMMA, CdS2/PMMA and HgS2/PMMA nanocomposites

The TEM image of ZnS2/PMMA nanocomposites prepared from ZnS2 nanoparticles within the host PMMA matrix is shown in Figure 5.8. The TEM image showed monodispersed metal sulfide nanoparticles within the host PMMA matrix [39]. All the particles lay within a narrow particle size range of 4.31-7.32 nm and nearly 70% particles exhibit diameter around 4 nm asmall degree of agglomeration of nanocomposites is also evident.

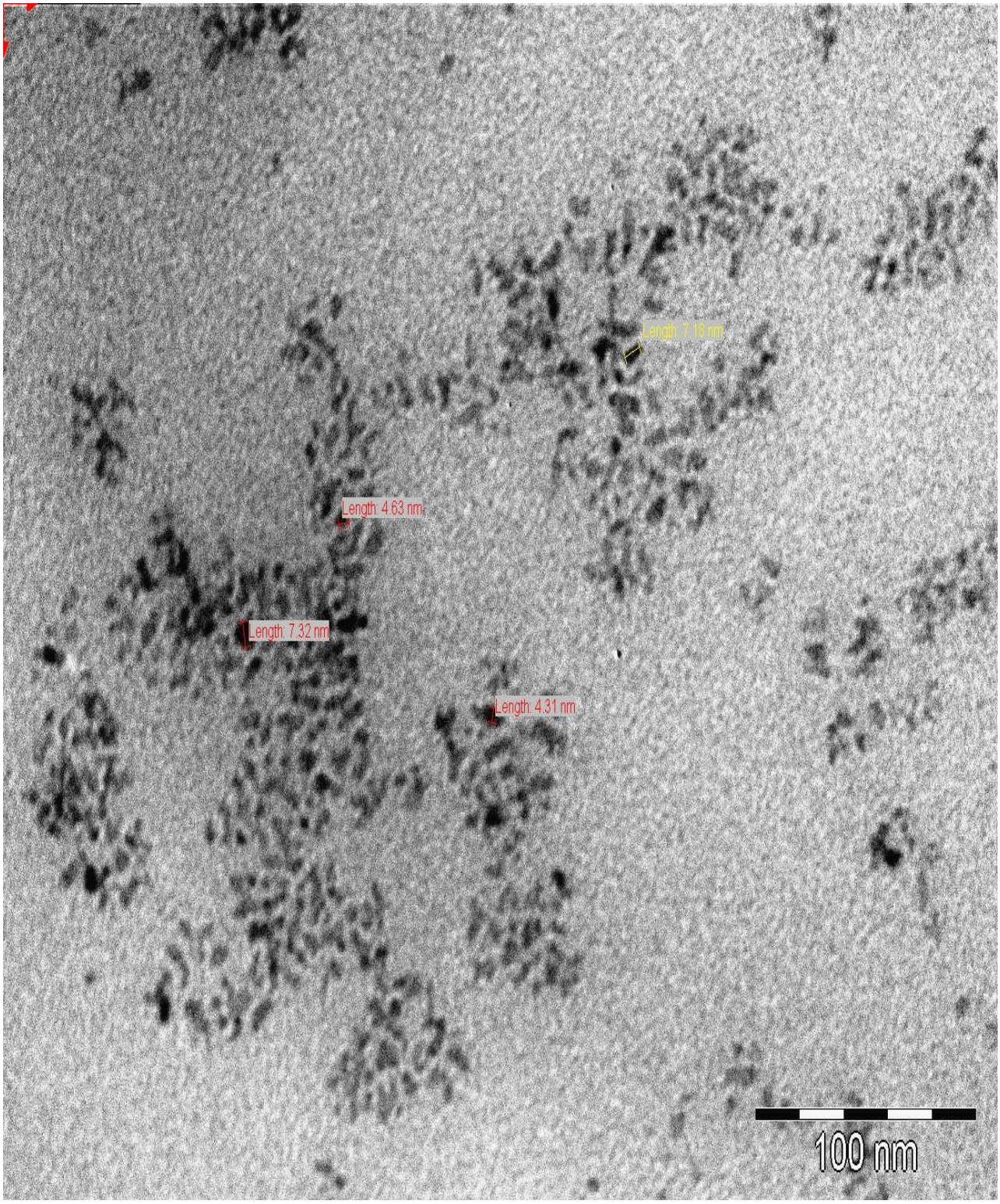

Figure 5.8: TEM image of ZnS2/PMMA nanocomposites prepared from 3wt. % ZnS2 nanoparticles dispersed in PMMA matrix

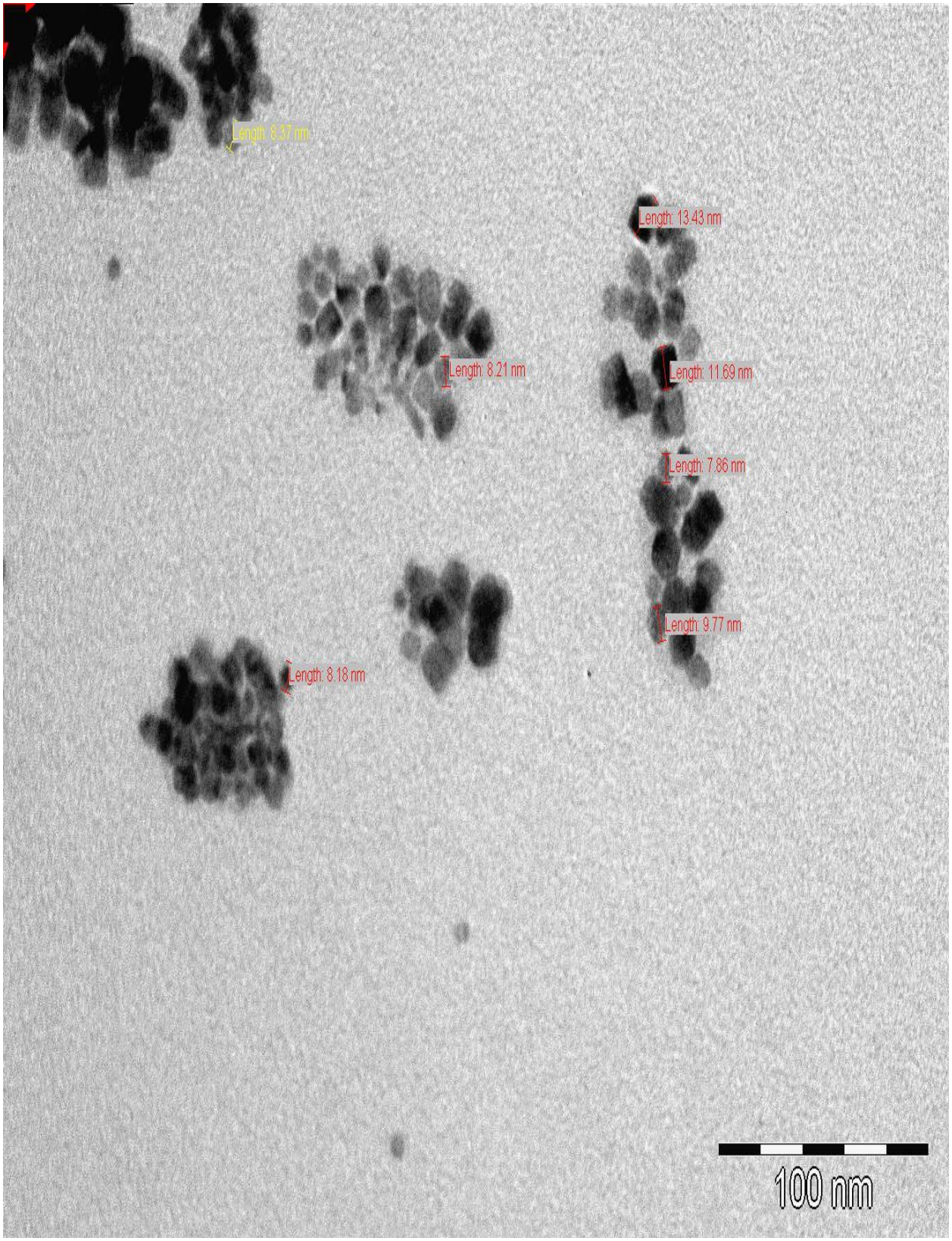

Figure 5.9: TEM image of CdS2/PMMA nanocomposites prepared from 3wt. % CdS2 nanoparticles dispersed in PMMA matrix

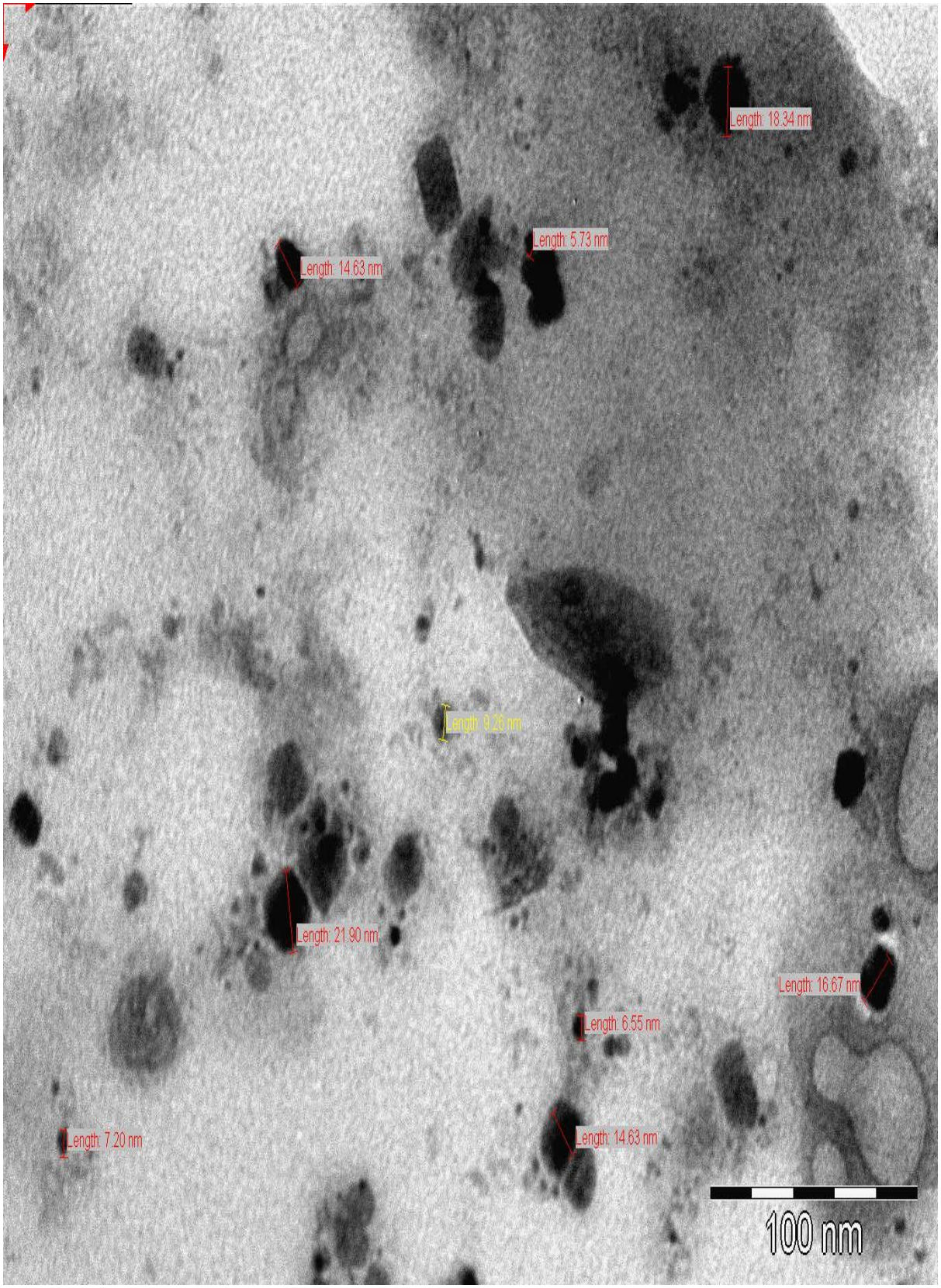

Figure 5.10: TEM image of HgS2/PMMA nanocomposites prepared from 3wt. % HgS2 nanoparticles dispersed in PMMA matrix

The homogeneity of the synthesized CdS2/PMMA nanocomposites was studied using transmission electron microscopy (TEM). Figure 5.9 show the TEM image of CdS2/PMMA nanocomposites. It indicates monodisperse particles with an average nanocomposites size of about 10 nm with a standard deviation of less than 2.0 nm. The nanocomposites are distinguishable from mixture of cubic, hexagonal and close-to-spherical morphology similar to the TEM image of HDA-capped CdS2 nanoparticles. This similarity indicates that the shape of CdS2 nanoparticles is not affected by dispersing into the polymer matrix. The polymer matrix holds the nanoparticles together and let them function as a unit. Lee *et al* [30] reported similar results for CdS nanoparticles in thermotropic liquid crystal monomers.

The TEM micrograph of HgS2/PMMA nanocomposites is shown in Figure 5.10. The particles were agglomerated and in contact with each other. However most of the particles were similar in size having irregular rounded shapes with relatively wide size distributions. The particles are within a range of 6-21 nm which is in agreement to those reported by Nair *et al* [40]. There is a lack of information from the literature where PMMA is used as a host matrix for HgS nanoparticles. Oshal and Mossalayi [41] synthesized HgS/PVP, HgS/PVA and HgS/SiO2 nanocomposites to study the effect of matrices on size and morphology of HgS nanoparticles. It was found that the morphology of HgS/PVP is cubic, HgS/PVA is hexagonal and HgS/SiO_2 has mixtures of nanospheres and hexagonal shapes.

5.3 Characterization of metal sulfide nanoparticles/ poly (methyl methacrylate) nanocomposites synthesized form ZnS3, CdS3 and HgS3

5.3.1 Infrared spectra of ZnS3/PMMA, CdS3/PMMA and HgS3/PMMA nanocomposites

The ATR-FTIR spectra of the nanocomposites are presented in Figure 5.11. In the PMMA, C–H stretching vibration was observed at 2977 cm^{-1}, C=O strong peak around 1730 cm^{-1}, C–O–C stretching and deformation vibrations peaks at 1157, 1199 and 1265 cm^{-1}, the peaks observed at 999 cm^{-1} and 858 cm^{-1} corresponding to the bending vibrations of C–H and the peak at 746 cm^{-1} is attributed to the vibrations of the polymer chains [1,7]. The spectra of pure PMMA and the obtained ZnS3/PMMA, CdS3/PMMA and HgS3/PMMA nanocomposites are identical, which could be attributed to the following:

- the metal sulfides crystallites formed in the pores of PMMA networks without disturbing the continuous three-dimensional network of the matrix and both are independent in their chemical behaviour [42].
- there is a weak interaction (Van der Waals interaction) between PMMA and metal sulfides nanoparticles [43, 44].
- the metal sulfides nanoparticles are very small (less than 5 nm) and separated from each other in each sample, the 3 wt. % of metal sulfides nanoparticles does not affect the transparency of the nanocomposites [45].

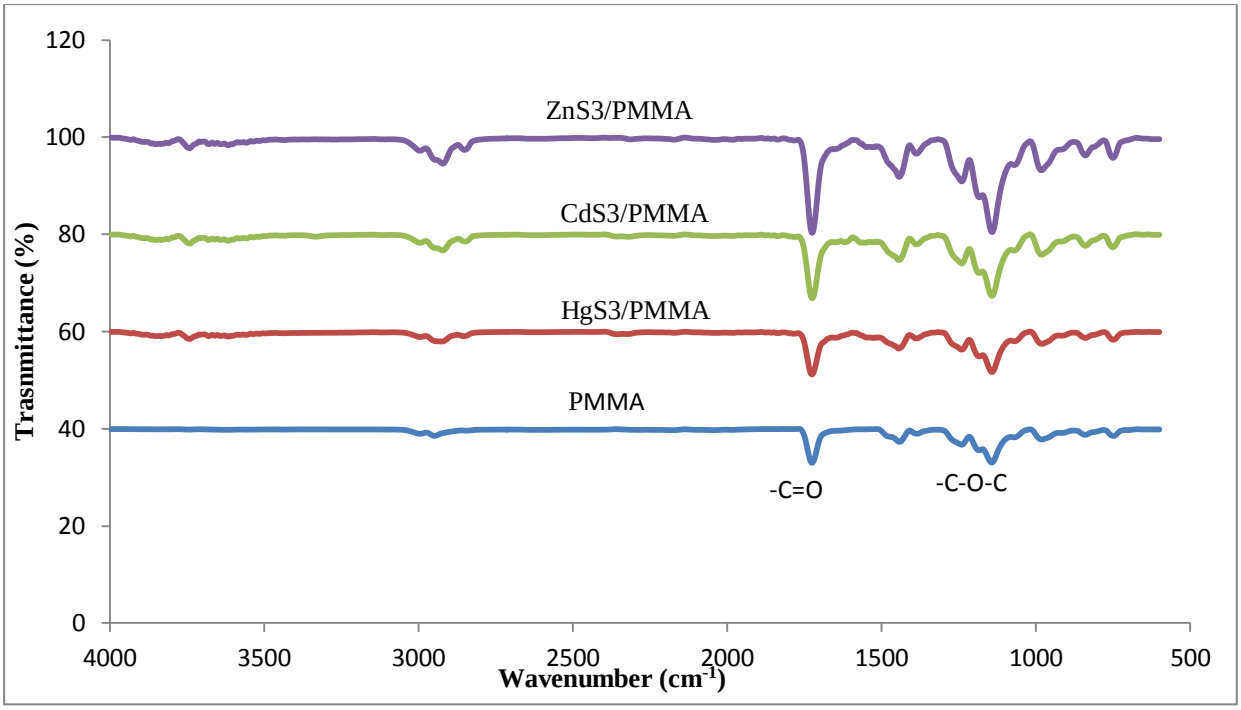

Figure 5.11: The FTIR spectra of PMMA and its MS3/PMMA nanocomposites

These results confirmed that the homogeneity dispersion of metal sulfide nanoparticles into PMMA was a success and also proves that the organic component PMMA is coordinated onto the metal sulfides particle surface. The vibration absorption peak around 405-265 cm^{-1} corresponding to M-S bond could not be observed since it was beyond the extent of our measurement [46]. Since there are no much significant difference between the spectra of free PMMA and its MS/PMMA nanocomposites. The major difference may be observed if the dosages or loading of MS, temperature of synthesis and the molar ratio between MS to PMMA and the polymer matrices are varied.

5.3.2 X-ray diffraction patterns

Figure 5.12 illustrates the powder X-ray diffraction (XRD) patterns of free PMMA, ZnS3/PMMA, CdS3/PMMA and HgS3/PMMA nanocomposites. The broad hump diffraction peak present in both PMMA, ZnS3/PMMA, CdS3/PMMA and HgS3/PMMA nanocomposites at a low diffraction angle, around $2\theta = 15°$, indicates amorphous PMMA

[47]. For ZnS3/PMMA nanocomposites, the other peaks with 2θ values of 29.9, 42.4 and 52.3 ^{o}C corresponded to the ZnS cubic phase assigned to (111), (220) and (311) crystalline planes of ZnS which were consistent with the literature data of JCPDS 5-0566 [48]. All the XRD peaks of ZnS are relatively broad, which confirms the small size of ZnS nanoparticles in the composite.

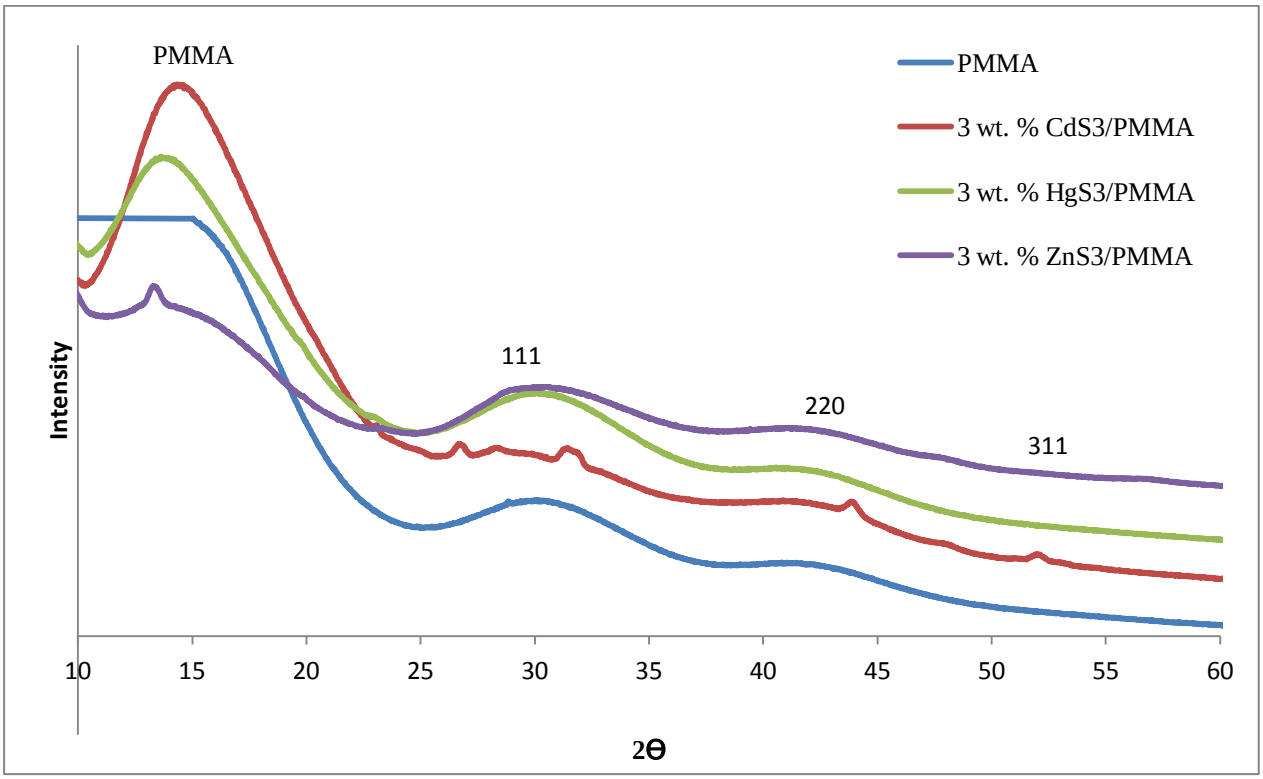

Figure 5.12: XRD patterns PMMA, ZnS3/PMMA, CdS3/PMMA and HgS3/PMMA nanocomposites

The average particle size calculated from X-ray diffraction study using Debye Scherrer formula [29] was found to be 1.08 nm. The XRD pattern of as-prepared CdS3/PMMA nanocomposites and PMMA also indicate the characteristic peaks of cubic crystal structure corresponding to (111), (220) and (311) reflections. The pattern reveals broad XRD peaks which suggest the small size of CdS3 in the nanocomposites. The average particle size of 2.3

nm was obtained from X-ray diffraction study using Debye Scherrer formula. The XRD patterns of HgS3/PMMA nanocomposites shows three characteristic peaks at (2θ = 29.5^o, 42.5^o and 52.5^o) corresponding to Miller indices (111), (220) and (311) [32-34]. The broad XRD peaks could be attributed to small average particle size of the nanocomposites. The very broad XRD peak at a low diffraction angle, around 2θ = 14°, indicates amorphous PMMA [31]. The average particle size of 1.8 nm has been calculated from X-ray diffraction study using Debye Scherrer formula.

5.3.3 TGA of ZnS3/PMMA, CdS3/PMMA and HgS3/PMMA nanocomposites

Figure 5.13 show the TGA decomposition curves for MS3/PMMA nanocomposites, pure PMMA matrix and their respective precursor complexes. As noted earlier the TGA curve for pure PMMA reveal one major decomposition step in the range 260-420 ^{o}C, owing to the decomposition of polymer main chain. The major decomposition of CdS3/PMMA nanocomposites occurs at about 272-435 ^{o}C. These results depict that the thermal stability of CdS3/PMMA nanocomposites is enhanced when compared to its PMMA matrix showing strong interactions between the CdS3 nanoparticles and the PMMA polymer matrix.

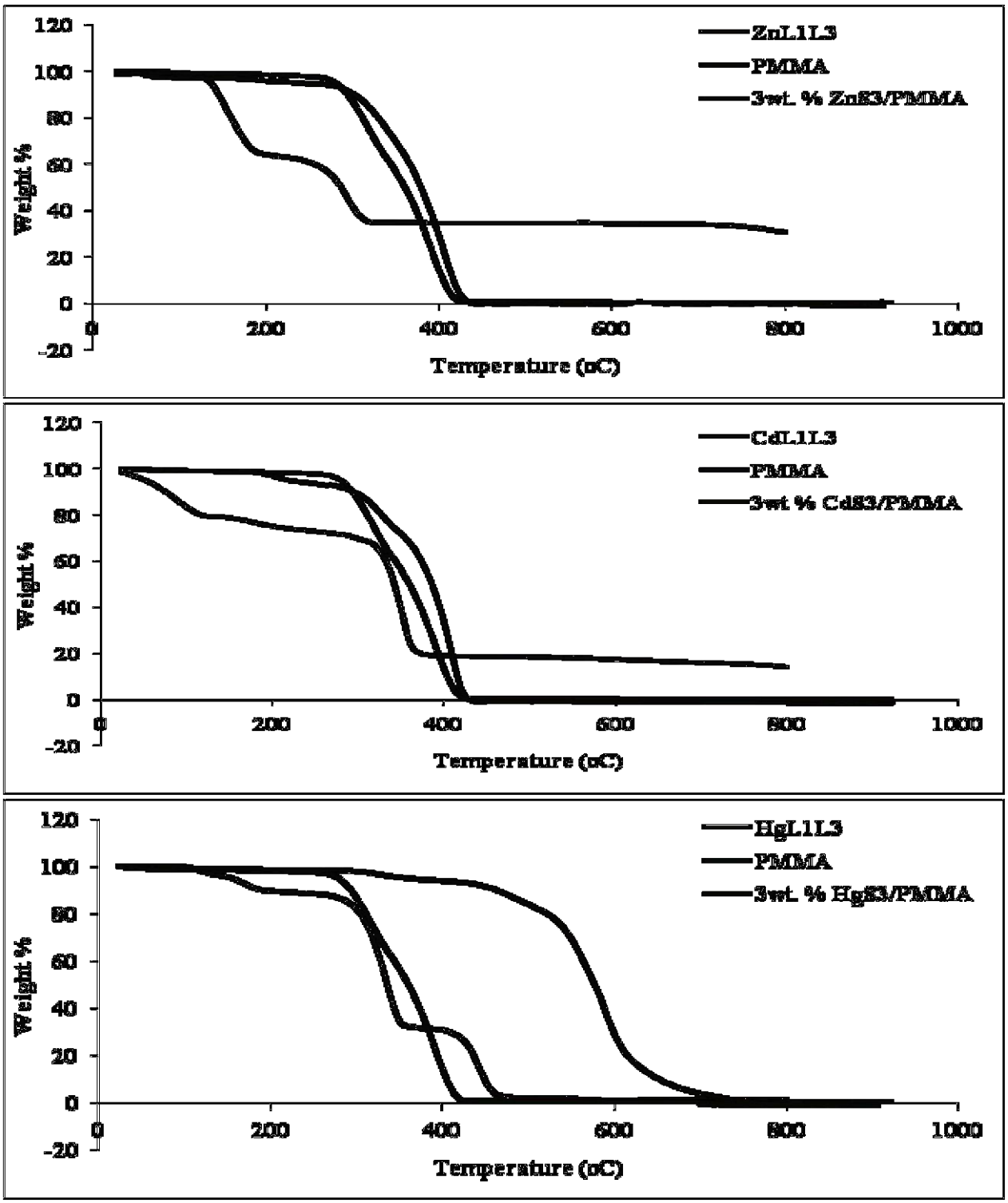

Figure 5.13: TGA curves for ML^1L^3 precursor complexes, pure PMMA and their MS3/PMMA nanocomposites. M = Zn, Cd and Hg

The residue observed could be ascribed to the presence of the CdS3 nanoparticles dispersed in PMMA matrix. The CdS3/PMMA nanocomposite has more thermal stability up to 400 ^{o}C when compared to the precursor CdL^1L^3 complex. It might be related to the combination of CdS nanoparticles in the polymer matrix, which yielded stronger binding force due to the interactions between CdS nanoparticles and polymer backbone [35, 49]. The TGA curve for HgS3/PMMA nanocomposites show outstanding thermal stability compared to the PMMA matrix and precursor complex confirming that the nanoparticle-polymer interaction is strong. The major decomposition occurs at about 300-750 ^{o}C, accompanied with about 90 % weight loss of the nanocomposite. This may be due to volatilization of HgS at high temperature leaving trace amount of HgS3/PMMA nanocomposites residue. Since only 3wt. % of MS nanoparticles is present in the nanocomposites, it could be expected that interaction between PMMA matrix and MS nanoparticles increases with increase in the amount nanoparticle dispersed into the PMMA matrix [50]. The main degradation step of ZnS3/PMMA nanocomposites is around 264-427 ^{o}C and has more thermal stability than pure PMMA, which can be due to the amount of ZnS3 nanoparticles embedded into PMMA matrix. This clearly indicated that the thermal stability for the ZnS3/PMMA nanocomposites has been improved significantly as higher decomposition temperature compared to pure PMMA [51].

5.3.4 SEM and EDX studies of ZnS3/PMMA, CdS3/PMMA and HgS3/PMMA nanocomposites

SEM micrograph and EDX spectrum of ZnS3/PMMA nanocomposites are shown in Figure 5.14. The EDX spectrum of the ZnS^3/PMMA nanocomposites is presented in Figure 5.14 C. Both Figures at high and low magnifications show spherical morphologies indicating that all ZnS3 nanoparticles were covered within PMMA matrix with very small agglomeration. ZnS3/PMMA nanocomposites show spherical particles with smooth surface and narrow

distributed particle size [52, 53]. Unlike what was obtained from ZnS2/PMMA nanocomposites which showed rough surfaces. Energy-dispersive X-ray spectroscopy (EDX) also showed improved Zn:S stoichiometry and reduced oxygen content in the spectra of ZnS3/PMMA nanocomposites, confirming the presence of ZnS nanoparticles in PMMA matrix [54].

Figure 5.15 (A and B) show the CdS3/PMMA composite that confirm the existence of CdS nanoparticles which are homogeneously dispersed in the PMMA matrix [37]. It shows that PMMA played an important role in controlling the size and mono-dispersion of the CdS nanoparticles. The absence of agglomerates is ascribed to the role played by PMMA matrix because it is adsorbed onto the different planes of the incipient CdS nuclei and it prevents the particles from agglomeration [55]. EDX spectra of CdS3/PMMA nanocomposites spectra also reveal that the prepared nanocomposites are mainly composed of Cd and S, confirming the presence of CdS nanoparticles in PMMA matrix [56].

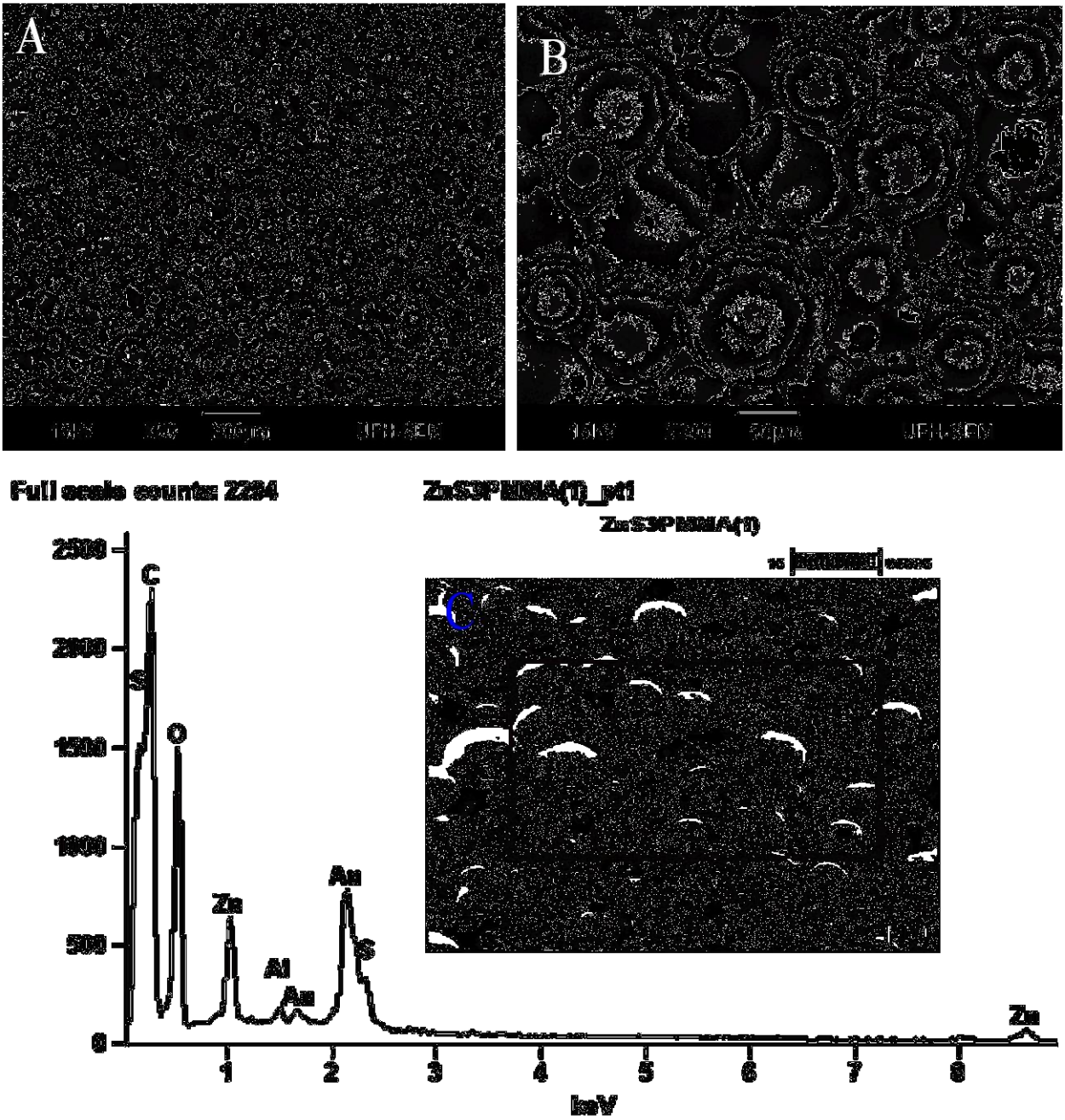

Figure 5.14: (A) and (B) are SEM micrograph of ZnS3/PMMA nanocomposites at low and high magnification prepared from 3wt. % ZnS3 nanoparticles dispersed in PMMA matrix. (C) EDX spectrum of the sample

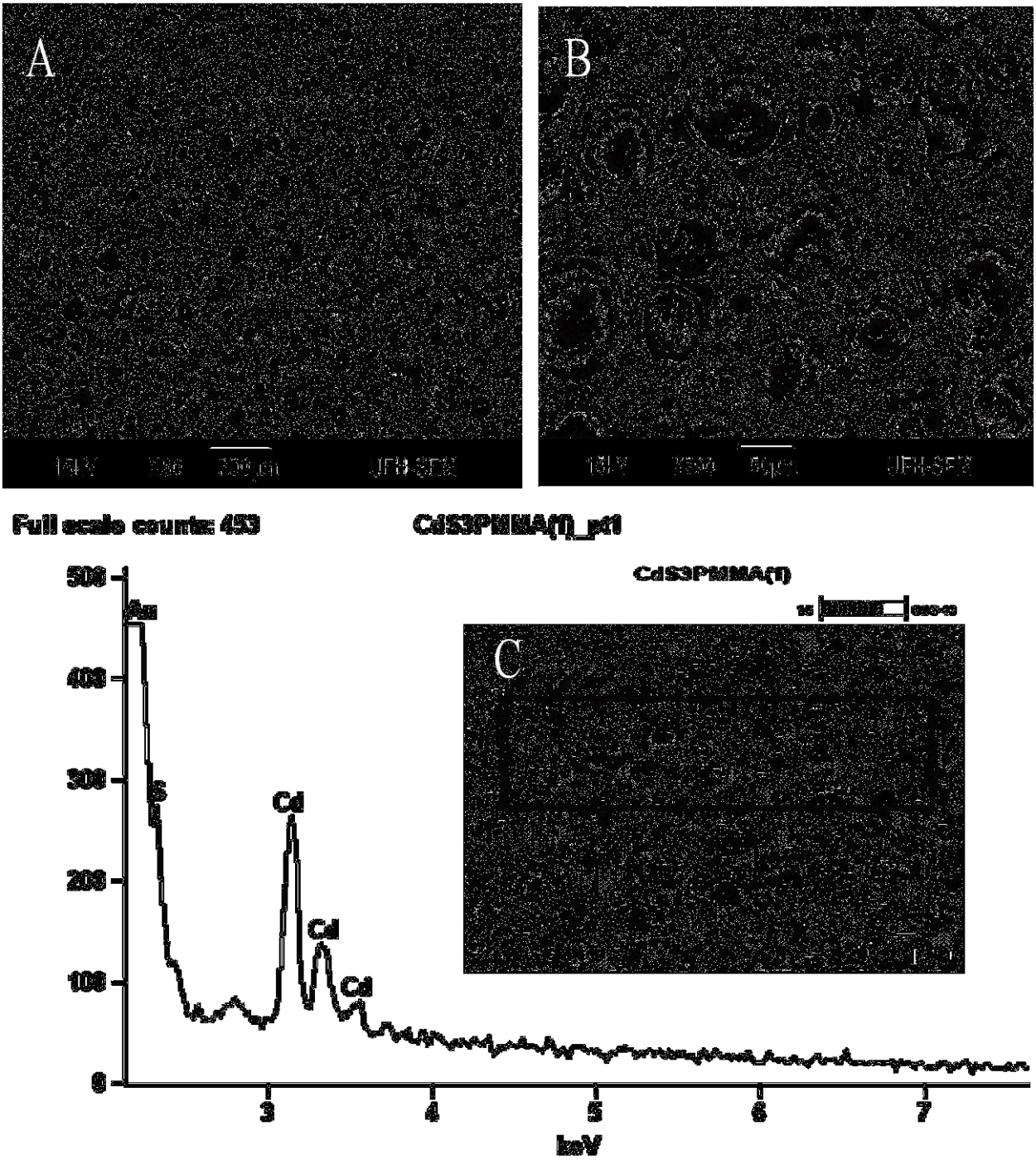

Figure 5.15: (A) and (B) are SEM micrograph of CdS3/PMMA nanocomposites at low and high magnification prepared from 3wt. % CdS3 nanoparticles dispersed in PMMA matrix. (C) EDX spectrum of the sample

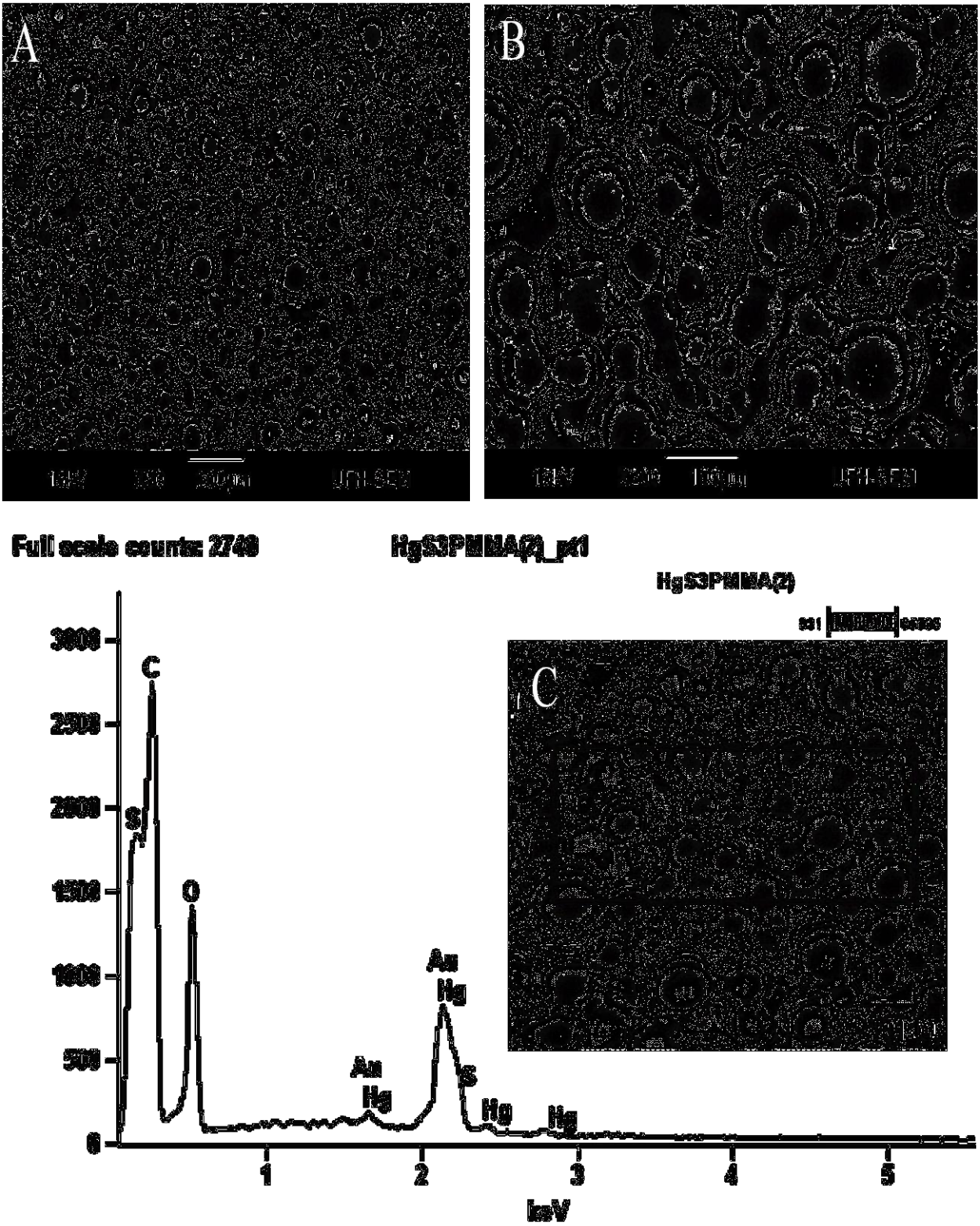

Figure 5.16: ((A) and (B) are SEM micrograph of HgS3/PMMA nanocomposites at low and high magnification prepared from 3wt. % HgS3 nanoparticles dispersed in PMMA matrix. (C) EDX spectrum of the sample

Figure 5.16 (A and B) show the micrograph of HgS3/PMMA nanocomposites. The picture show evenly distributed spherical particles with agglomeration. EDX spectrum of the sample reveal that the prepared nanocomposites are mainly composed of Hg and S, confirming the presence of HgS nanoparticles within the host PMMA matrix. The EDX of all ZnS3/PMMA, CdS3/PMMA and HgS3/PMMA nanocomposites reveal the presence of traces of elements like C, O and Au. Carbon and oxygen are observed possibly due to the use of carbon tape and retained solvent after the deposition step [25]. The intense Au peaks are due to gold and palladium coating which was used to overcome charging of samples.

5.3.5 TEM of ZnS3/PMMA, CdS3/PMMA and HgS3/PMMA nanocomposites

Figure 5.17 show the TEM image of ZnS3/PMMA nanocomposites prepared from 3wt. % ZnS3 nanoparticles dispersed in PMMA matrix. The TEM image indicates that the particles are monodispersed in PMMA although there is small agglomeration. The TEM picture shows nanocomposites having narrow size distribution of particles ranging from 3-5 nm which is in agreement with that estimated from XRD. The image also indicates that the ZnS nanoparticles have their size in the nano regime even after being dispersed to PMMA matrix [15, 57, 58].

TEM image of CdS3/PMMA nanocomposites is shown in Figure 5.18. The image shows that CdS3 particles were homogeneously dispersed in PMMA polymer matrix with a standard deviation of about 2. The particle sizes found in TEM are slightly different from that obtained from the XRD. This slight difference in particle size estimation through the XRD and TEM is due to the intrinsic twining and dislocations present in the lattice of the sample [59]. The CdS particles become agglomerated. TEM image of HgS3/PMMA nanocomposite

prepared from HgS3 nanoparticles is shown in Figure 5.19. Like any other metal sulfide studied in this work, the HgS polymer nanocomposites were deposited in copper carbon grid. The TEM image shows nanoparticles in the 6-12 nm range. This confirmation of nano size and homogeneities of HgS nanoparticles dispersed into PMMA matrix was not clearly shown through the SEM image as shown in Figure 5.16. All the transmission electron microscopy (TEM) images confirm the nanocrystalline nature of the ZnS, CdS and HgS nanocomposites studied.

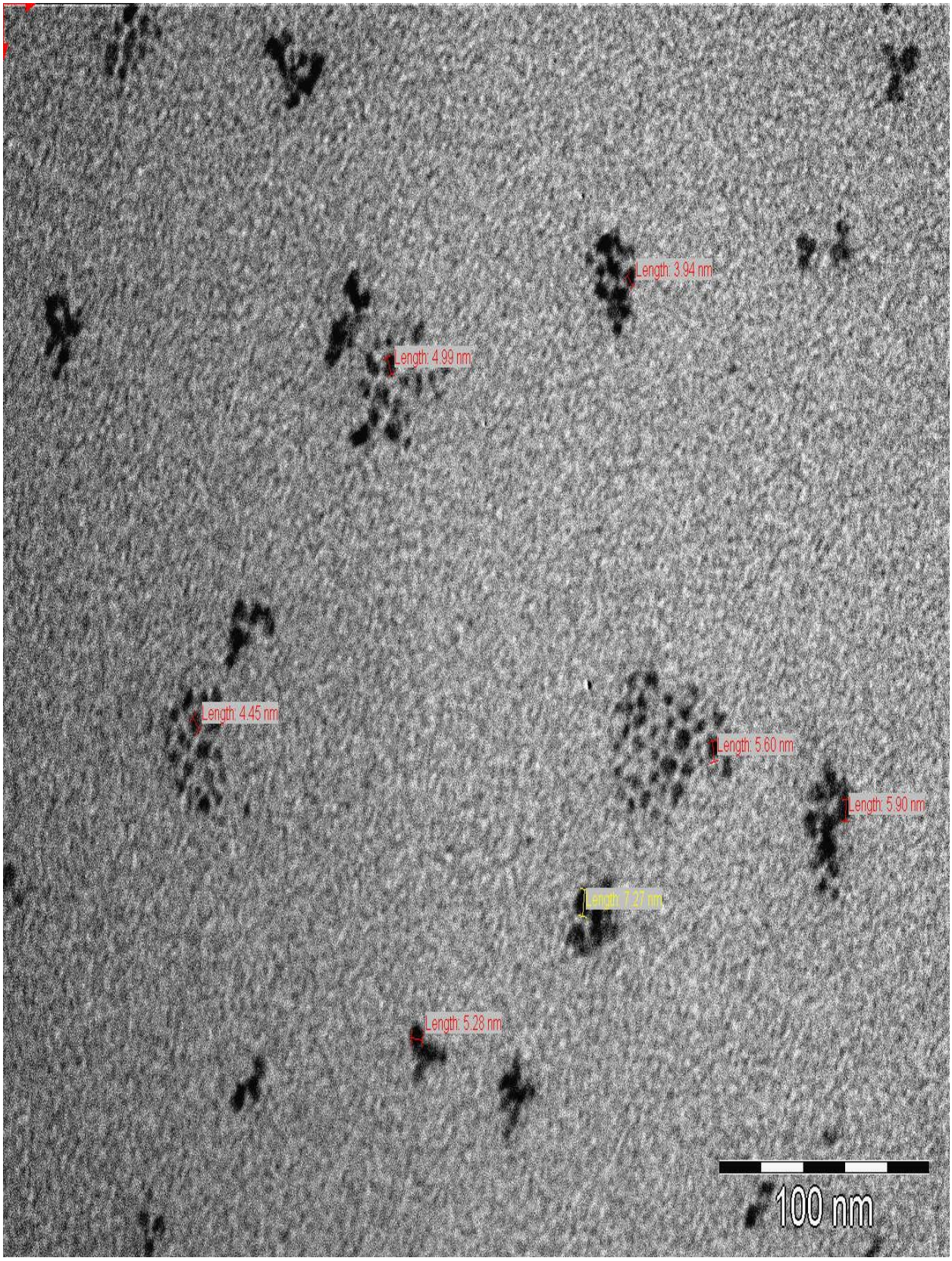

Figure 5.17: TEM image of ZnS3/PMMA nanocomposites prepared from 3wt. % ZnS3 nanoparticles dispersed in PMMA matrix

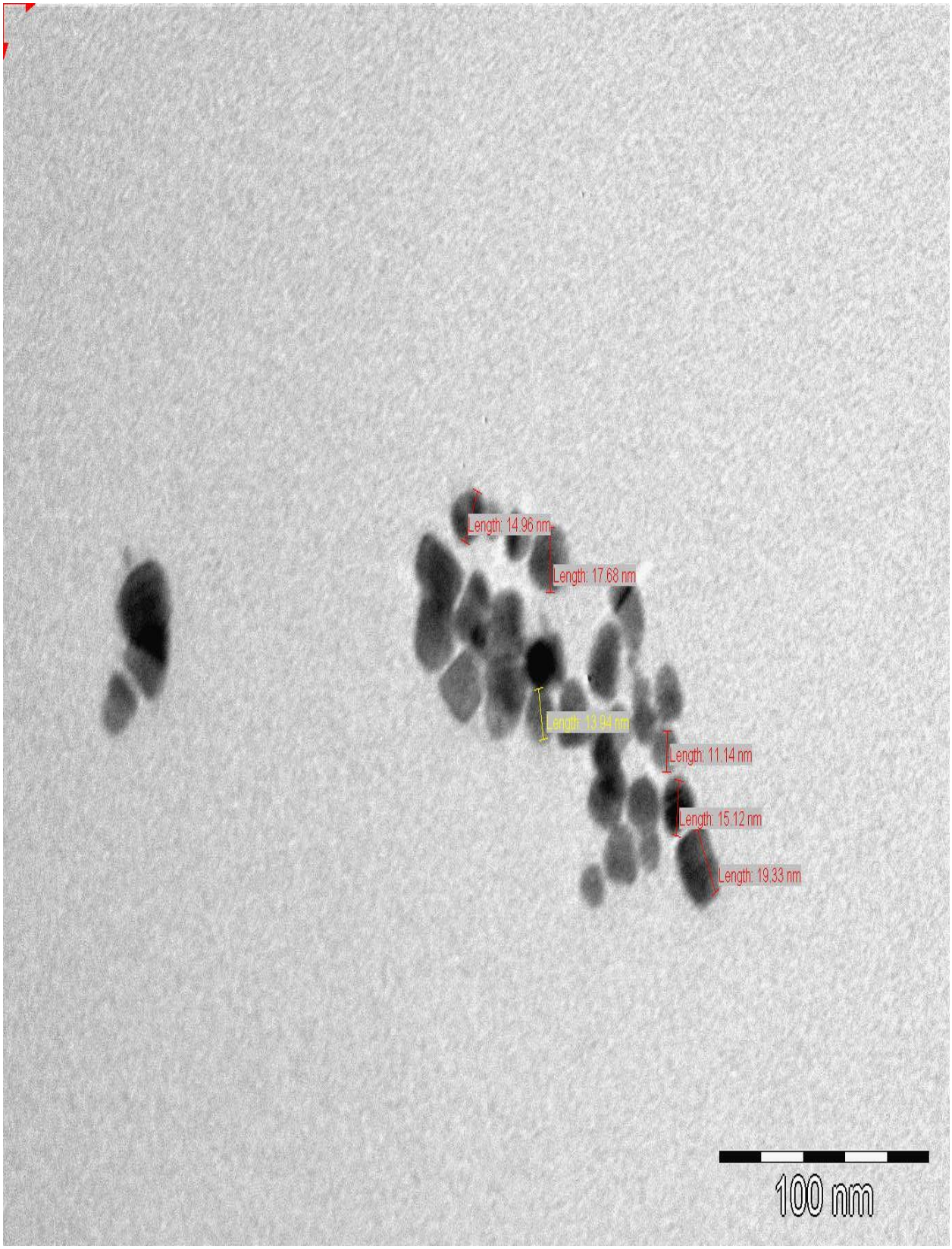

Figure 5.18: TEM image of CdS3/PMMA nanocomposites prepared from 3wt. % CdS3 nanoparticles dispersed in PMMA matrix

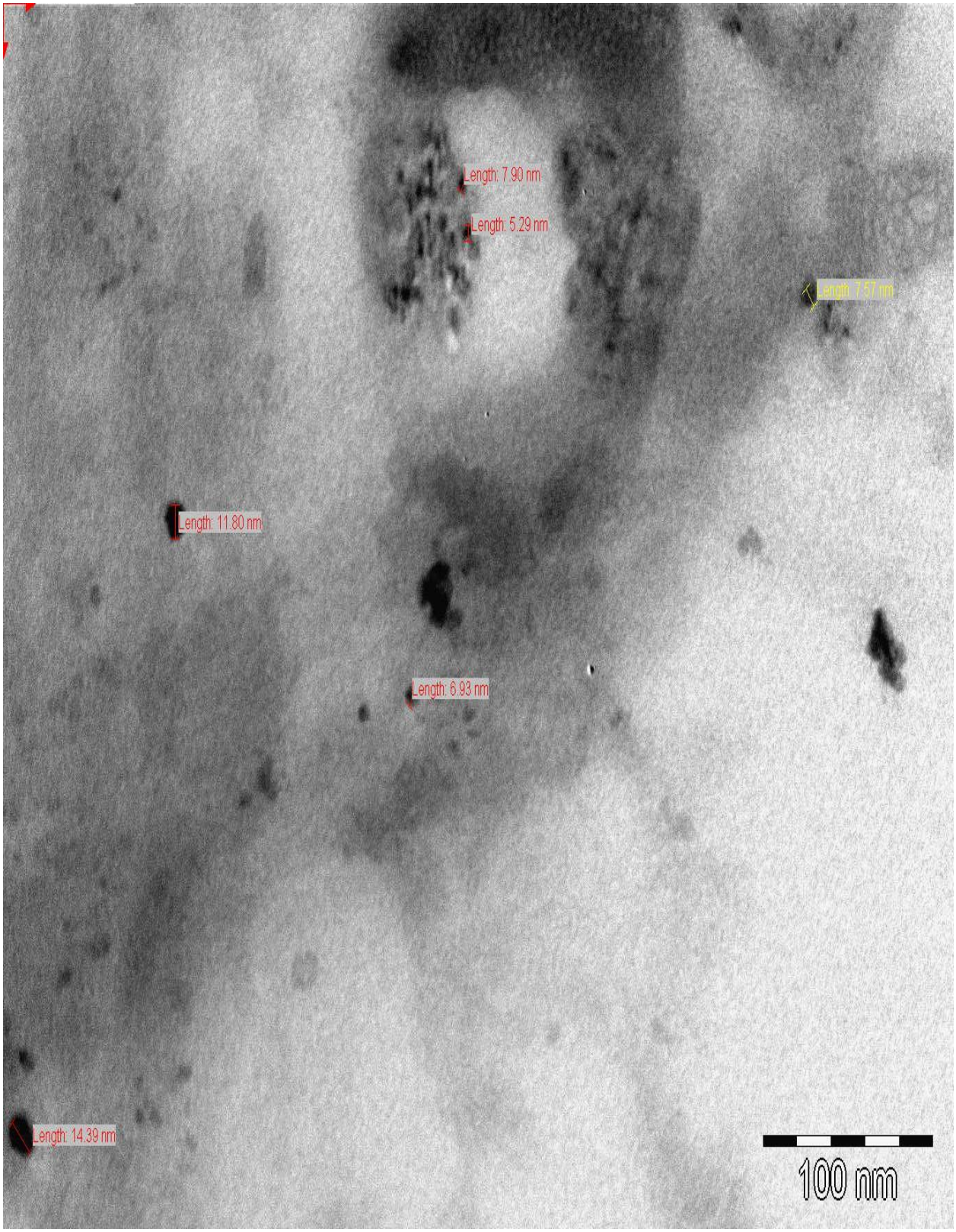

Figure 5.19: TEM image of HgS3/PMMA nanocomposites prepared from 3wt. % HgS3 nanoparticles dispersed in PMMA matrix

5.4 References

1. Mthethwa, T.P.; Moloto, M.J.; De Vries, A.; Matabola, K.P. Properties of electrospun CdS and CdSe filled poly(methyl methacrylate) (PMMA) nanofibres. *Mater. Res. Bull*. **2011**, *46*, 569-575.
2. Dixit, M.; Gupta, S.; Mathur, V.; Rathore, K.S.; Sharma, K.; Saxena, N.S. Study of glass transition temperature of PMMA and CdS-PMMA composite. *Chalco. Lett.* **2009**, *6*,131-136.
3. Gross, S.; Camozzo, D.; Noto, V.D.; Armelao, L.; Tondello, E. PMMA: A key macromolecular component for dielectric low-*k* hybrid inorganic–organic polymer films. *Euro. Poly. J*. **2007**, *43*, 673-696.
4. Jeon, I.-Y.; Baek, J.-B. Nanocomposites derived from polymers and inorganic nanoparticles. *Materials* **2010**, *3*, 3654-3674.
5. Uddin, M.A.; Chan, H.P. Materials and process optimization in the reliable fabrication of polymer photonic devices. *J. Optoelectron. Adv.Mat.* **2008**, 10, 1-17.
6. Chen, R.; Gao, Y.; Zhang, G.; Wu, R.; Xiao, L.; Jia, S. Electric field induced fluorescence modulation of single molecules in PMMA based on electron transfer. *Int. J. Mol. Sci.* **2012**, *13*, 11130-11140.
7. Alexandratos, S.D. Ion-exchange resins: A retrospective from industrial and engineering chemistry research. *Ind. Eng. Chem. Res.* **2009,** *48*, 388-398.
8. Kondawar, S.B.; Acharya, S.A.; Dhakate, S.R. Microwave assisted hydrothermally synthesized nanostructure zinc oxide reinforced polyaniline nanocomposites. *Adv. Mat. Lett*. **2011**, *2*,362-367.
9. Ummartyotin, S.; Bunnak, N.; Juntaro, J.; Sain, M.; Manuspiya, H. Hybrid organic–inorganic of ZnS embedded PVP nanocomposite film for photoluminescent application.

C. R. Physique. **2012**, http://dx.doi.org/10.1016/j.crhy.2012.09.008. Published Online: Sept 27, 2012

10. Zhao, R.; Chen, C.Z.; Li, Q.F.; Luo, W.B. Effects of stress and physical ageing on nonlinear creep behavior of poly(methyl methacrylate), *J. Cent. South Univ. Technol*. **2008**, *15*, 582-588.
11. Zhang, L.; Li, F.; Chen, Y.; Wang, X. Synthesis of transparent ZnO/PMMA nanocomposite films through free-radical copolymerization of asymmetric zinc methacrylate acetate and in-situ thermal decomposition. *J. Luminesc*. **2011**, *131*, 1701-1706.
12. Salavati-Niasari, M.; Ghanbari, D. *Polymeric Nanocomposite Materials, Advances in Diverse Industrial Applications of Nanocomposites*. Reddy, B., Eds.; InTech: Europe, **2011**; pp 501-521. http://www.intechopen.com/books/advances-in-diverse-industrial-applications-ofnanocomposites/polymeric-nanocomposite-materials (accessed Mar 22, 2011).
13. Khan, A. CdS nanoparticles with a thermoresponsive polymer: Synthesis and properties. *J. Nanomater*. **2012**, 1-8.
14. Prabhu1, S.G.; Pattabi, B.M. Incorporation of acetoacetanilide crystals in host PMMA polymer matrix and characterizations of the hybrid composite. *J. Mine. Mater. Charact. Eng*. **2012**, *11*, 519-527.
15. Agrawal, S.; Patidar, D.; Saxena, N.S. Glass transition temperature and thermal stability of ZnS/PMMA nanocomposites. *Phase Trans.* **2011**, *84*, 888-900.
16. Hashmi, L.; Sana, P.; Malik, M.M.; Siddiqui, A.H.; Qureshi, M.S. Novel fork architectures of Ag_2S nanoparticles synthesized through in-situ self-assembly inside chitosan matrix. *Nano Hybrids* **2012**, *1*, 23-43.

17. Thanh, N.T.K.; Green, L.A.W. Functionalisation of nanoparticles for biomedical applications. *Nano Today* **2010**, *5*, 213-230.
18. Ezhov, A.A.; Shandryuk, G.A.; Bondarenko, G.N.; Merekalov, A.S.; Abramchuk, S.S.; Shatalova, A.M.; Manna, P.; Zubarev, E.R.; Talroze, R.V. Liquid-crystalline polymer composites with CdS nanorods: Structure and optical properties. *Langmuir* **2011**, *27*, 13353-13360.
19. Pilla, V.; Alves, L.P.; Munin, E.; Pacheco, M.T.T. Radiative quantum efficiency of CdSe/ZnS quantum dots suspended in different solvents. *Optics Commun*. **2007**, *280*, 225-229.
20. Sabah, A.; Siddiqi, S.A.; Ali, S. Fabrication and characterization of CdS nanoparticles annealed by using different radiations. *World Ac. Sci, Eng. Tech*. **2010**, 82-89.
21. Jang, J.; Kim, S.; Lee, K.J. Fabrication of CdS/PMMA core/shell nanoparticles by dispersion mediated interfacial polymerization. *Chem. Commun*. **2007**, 2689-2691.
22. Wei, S.; Sampathi, J.; Guo, Z.; Anumandla, N.; Rutman, D.; Kucknoor, A.; James, L.; Wang, A. Nanoporous poly(methyl methacrylate)-quantum dots nanocomposite fibers toward biomedical applications. *Polym*. **2011**, *52*, 5817-5829
23. Barman, B.; Sarma, K.C. Luminescence properties of ZnS quantum dots embedded in polymer matrix. *Chalc. Lett*. **2011**, *8*, 171-176.
24. Nicolais, L.F.; Carotenuto, G. Synthesis of polymer-embedded metal, semimetal, or sulfide clusters by thermolysis of mercaptide molecules dissolved in polymers. *Recent Pat. Mater. Sci.* **2008**, *1*, 1-11.
25. Matras, K.; Bredol, M.; Szatkowski, A.; Sakhno, O.; Stumpe, J.; Bogdal, D. Composites from luminescent nanosized zns and optical polymer. *Mol. Cryst. Liq. Cryst*. **2008**, *485*, 776-779.

26. Tomar, A.K.; Mahendia, S.; Kumar, S. Structural characterization of PMMA blended with chemically synthesized PAni. *Adv. Appl. Sci. Res*. **2011**, *2*, 65-71.

27. Qazi, S.J.S.; Rennie, A.R.; Cockcroft, J.K.; Vickers, M. Use of wide-angle X-ray diffraction to measure shape and size of dispersed colloidal particles. *J. Col. Interf. Sci*. **2009**, *338*, 105-110.

28. Chen, Q.; Suo, C.; Zhang, S.; Wang, Y. Effect of PdS on photocatalytic hydrogen evolution of nanostructured CdS under visible light irradiation. *Inter. J. Photoenergy* **2013**, 1-5.

29. Luna-Martinez, J.F.; Hernandez-Uresti, D.B.; Reyes-Melo, M.E.; Guerrero-Salazar, C.A.; Gonzalez-Gonzalez, V.A.; Sepulveda-Guzman, S. Synthesis and optical characterization of ZnS-sodium carboxymethyl cellulose nanocomposite films. *Carbohydr. Polym*. **2011**, *84*, 566-570.

30. Lee, H.L.; Mohammed, I.A.; Belmahi, M.; Assouar, M.B.; Rinnert, H.; Alnot, M. Thermal and optical properties of CdS nanoparticles in thermotropic liquid crystal monomers. *Materials* **2010**, *3*, 2069-2086.

31. Matusinovic, Z.; Shukla, R.; Manias, E.; Hogshead, C.G.; Wilkie, C.A. Polystyrene/molybdenum disulfide and poly (methyl methacrylate)/molybdenum disulfide nanocomposites with enhanced thermal stability. *Polym. Degrad. Stabil*. **2012**, *97*, 2481-2486.

32. Wichiansee, W.; Nordin, M.N. Green, M.; Curry, R.J. Synthesis and optical characterization of infra-red emitting mercury sulfide (HgS) quantum dots. *J. Mater. Chem.* **2011**, *21*, 7331-7336.

33. Mehta, S.K.; Kumar, S.; Chaudhary, S.; Bhasin, K.K. Nucleation and growth of surfactant-passivated CdS and HgS nanoparticles: Time-dependent absorption and luminescence profiles. *Nanoscale* **2010**, *2*, 145-152.

34. Oshal, F.; Mossalayi, H. Effect of matrices on size and morphology of HgS nanoparticles. *Der. Pharma. Chemica.* **2010**, *2*, 33-37.

35. Jang, J.; Kim, S.; Lee. K.J. Fabrication of CdS/PMMA core/shell nanoparticles by dispersion mediated interfacial polymerization. *Chem. Commun*. **2007**, 2689-2691.

36. Kuljanin, J.; Marinovic´-Cincovic´, M.; Stojanovic´, Z.; Krkljesˇ, A.; Abazovic´, N.D.; Comor, M.I. Thermal degradation kinetics of polystyrene/cadmium sulfide composites. *Polym. Degrad. Stab*. **2009**, *94*, 891-897.

37. Sheng, C.K.; Isa, M.I.N.; Loo, L.H. Study of formation and characterization of CdS/PMMA Composite Film. In *UMT 11th International Annual Symposium on Sustainability Science and Management*, Terengganu, Malaysia, 2012, pp 1080-1082.

38. Barman, B.; Sarma, K.C. Luminescence properties of ZnS quantum dots embedded in polymer matrix. *Chalc. Lett*. **2011**, *8*, 171-176.

39. Mutlugun, E.; Hernandez-Martinez, P.L.; Eroglu, C.; Coskun, Y.; Erdem, T.; Sharma, ller, A.; Demir, H.V.

Large-area (over 50 cm × 50 cm) freestanding films of colloidal InP/ZnS quantum dots. *Nano. Lett*. **2012**, *12*, 3986-3993.

40. Nair, P.S.; Radhakrishnan, T.; Revaprasadu, N.; Kolawole, G.A.; O'Brien, P. The synthesis of HgS nanoparticles in polystyrene matrix. *J. Mater. Chem*. **2004**, *14*, 581-584.

41. Oshal, F.; Mossalayi, H. Effect of matrices on size and morphology of HgS nanoparticles. *Der. Pharma. Chemica.* **2010**, *2*, 33-37.

42. Barman, J.; Borah, J.P.; Sarma, K.C. Synthesis and characterization of CdS nanoparticles by chemical growth technique. *Optoelectron. Adv. Mater-Rap. Commun*. **2008**, 2, 770-774.

43. Agarwal, S.; Patidar, D.; Saxena, N.S. Effect of ZnS nanofiller and temperature on mechanical properties of poly (methyl methacrylate). *J. Appl. Polym. Sci*. **2012**, *123*, 2431-2438.

44. Li, Z.; Zhang, J.; Du, J.; Mu, T.; Liu, Z.; Chen, J.; Han, B. Preparation of cadmium sulfide/poly(methyl methacrylate) composites by precipitation with compressed CO_2. *J. Appl. Polym. Sci*. **2004**, *94*, 1643-1648.

45. Guan, C.; Lu¨, C.; Cheng, Y.; Song, S.; Yang, B. A facile one-pot route to transparent polymer nanocomposites with high ZnS nanophase contents via in situ bulk polymerization. *J. Mater. Chem.* **2009**, 19, 617-621.

46. He, R.; Qian, X.-F.; Yin, J.; Bian, L.-J.; Xi, H.-A.; Zhu, Z.-K. In situ synthesis of CdS/PVK nanocomposites and their optical properties. *Mater. Lett*. **2003**, *57*, 1351-1354.

47. Yao, J.; Zhao, G.; Wang, D.; Han, G. Solvothermal synthesis and characterization of CdS nanowires/PVA composite films. *Mater. Lett*. **2005**, 59, 3652-3655.

48. Borah, J.P.; Sarma, K.C. Photo-physical properties of of ZnS/PVA nanocrystals. *Optoelectr. Adv. Mater-Rapid Commun.* **2009**, *3*, 891-898.

49. Bhaiswar, J.B.; Salunkhe, M.Y.; Dongre, S.P. Synthesis, characterization and thermal, electrical study of CdS-polyaniline nanocomposite via oxidation polymerization. *Inter. J. Scient. Res. Public.* **2013**, 3, 1-4.

50. Wang, L.; He, X.; Wilkie, C.A. The utility of nanocomposites in fire retardancy. *Materials* **2010**, *3*, 4580-4606.

51. Lu, C.; Cui, Z.; Wang, Y.; Li, Z.; Guan, C.; Yang, B.; Shen, J. Preparation and characterization of ZnS-polymer nanocomposite films with high refractive index. *J. Mater. Chem.* **2003**, 13, 2189-2195.

52. Lui, Y. Mesoporous silica/polymer nanocomposites. Ph.D. Dissertation, Georgia Institute of Technology, Georgia, **2009**.

53. Wei, S.; Sampathi, J.; Guo, Z.; Anumandla, N.; Rutman, D.; Kucknoor, A.; James, L.; Wang, A. Nanoporous poly(methyl methacrylate)-quantum dots nanocomposite fibers toward biomedical applications. *Polym*. **2011**, *52*, 5817-5829.

54. Liu, S.; Zhang, H.; Swihart, M.T. Spray pyrolysis synthesis of ZnS nanoparticles from a single-source precursor. *Nanotech*. **2009**, *20*, 1-8.

55. Jothi, N.S.N.; Gunaseelan, R.; Raj, T.M.; Sagayaraj, P. Investigation on mild condition preparation and structural, optical and thermal properties of PVP capped CdS nanoparticles. *Arch. Appl. Sci. Res.* **2012**, *4*, 1723-1730.

56. Sharma, R. Optical studies of CdS:Mn nanoparticles. *Luminesc*. **2012**, *27*,501-504.

57. Sharma, M.; Kumara, S.; Pandey, O.P. Photo-physical and morphological studies of organically passivated core-shell ZnS nanoparticles. *Digest J. Nanomater. Biostruct*. **2008**, *3*, 189-197.

58. Amah, A.N.; Echi, I.M.; Kalu, O. influence of polyvinyl alcohol and alpha-methacrylic acid as capping agents on particle size of ZnS nanoparticles. *Appl. Phys. Res*. **2012**, *4*, 26-34.

59. Liu, L.; Zheng, Z.; Wang, X. Preparation and properties of polythiourethane/ZnS nanocomposites with high refractive index. *J. Appl. Polym. Sci*. **2010**, *117*, 1978-1983.

CHAPTER SIX

6.0 CONCLUSIONS AND RECOMMENDATIONS

6.1 Summary of results

Three dithiocarbamate ligands were synthesized and characterized by elemental analyses, UV-Vis, FTIR, ^{1}H- and ^{13}C-NMR spectroscopy. The NMR study confirmed the formation of ammonium N-phenyldithiocarbamate, ammonium N-methyl-N-phenyldithiocarbamate and ammonium N-ethyl-N-phenyldithiocarbamate ligands. Six metal complexes of Zn (II), Cd(II) and Hg(II) were synthesized from the dithiocarbamate ligands and characterized by elemental analyses, FTIR, ^{1}H- and ^{13}C-NMR and TGA. The complexes were obtained in powder form and stable at room temperature with the yield ranging from 85-95 %. The dithiocarbamato metal complexes were bidentately coordinated to the central metal ion through the sulfur atoms, forming a 4-coordinate tetrahedral geometry. The FTIR confirmed bidentate coordination of the ligand moieties through sulfur donor-atom. The NMR peaks were carefully assigned confirming the formation of the complexes. Two complexes of zinc and mercury were characterized by single crystal X-ray crystallography.

Six metal sulfide nanoparticles were synthesized form their respective complexes and characterized by UV-Vis, PL, XRD, SEM and TEM. Particle sizes in the nano rigime were obtained. XRD revealed that zinc nanoparticles were cubic whereas cadnium nanoparticles were hexagonal. SEM and TEM morphologies of the synthesized nanoparticles were in agreement and comparable.

Six metal sulfide nanoparticles/poly (methyl methacrylate) nanocomposites formulated as (ZnS2/PMMA, ZnS3/PMMA, CdS2/PMMA, CdS3/PMMA, HgS2/PMMA and

HgS3/PMMA) were synthesized from their metal sulfide nanoparticles in the presence of poly (methyl methacrylate) matrix.

6.2 Conclusions

Three dithiocarbamate ligands, six metal complexes, six metal sulfides nanoparticles and six nanocomposites were successfully synthesized and characterized. The electronic spectra of dithiocarbamate ligands showed three most intense absorption bands assigned to the chromophore group NCS_2. The FTIR spectra of both ligands and complexes revealed the diagnostic peaks attributed to the *v*(C–N), *v*(C_2–N) and *v*(C-H) frequencies. The NMR confirmed the formation of the ligands and complexes. The thermal decomposition of all complexes of zinc and cadmium showed two stage decomposition patterns leaving the residual weight corresponding to ZnS and CdS respectively. The thermal behaviour for mercury complexes showed stages of decomposition leaving about 2 % residue due to volatilizition. Base of their thermal decomposition profiles show the thermal stability of the complexes increases in this order: Hg < Zn < Cd complexes. The SEM/EDX of (N- phenyl-N, N-methyl phenyl dithiocarbamato)Cd(II) complex after thermal decomposition showed uniform, crystalline and hexagonal particles. The EDX shows the presence of cadmium and sulfur in the decomposed sample confirming the suitability of the complexes as single molecule precursor complexes to prepare metal sulfide nanoparticles. The single crystals X-ray crystallography of Zn complex showed a antrosymmetric dimeric structure while the mercury complex crystallizes with two monomeric mercury complexes and two molecules of toluene solvent in the asymmetric unit.

The single-source molecular precursor method was successfully used to synthesize HDA-capped ZnS, CdS and HgS nanoparticles. All the UV-Vis and photoluminescence

spectroscopy of semiconductor metal sulfide nanoparticles were in quantum size regime and exhibited the phenomenon of quantum confinement with the estimated particle sizes ranging from 2.8-4.3 nm. The TEM images reveal that the particle morphology ranges from cubic, spherical and close-to-spherical shapes. TEM images show the crystallinity of particles confirmed by the lattice planes observed on the XRD. All metal sulfide synthesized revealed that the particles are monodisperse with narrow distribution. The SEM microgram showed spherical shape particles. All the EDX spectra confirmed the presence of metal sulfide nanoparticles. The average particle size of the crystallites was estimated by optical absorption, XRD and TEM measurements and the values obtained are ranging below 6 nm confirming the high quality semiconductor nanoparticles produced.

All the prepared nanocomposites showed reasonably good interaction between metal sulfide nanoparticles and PMMA matrix. The PMMA was demonstrated as a good host matrix since it does not affect the shape and properties of metal sulfide nanoparticles dispersed to it, but provided combinations of functionalities. The 3wt. % MS nanoparticles dispersed within PMMA matrix reveal that the particles have uniform distribution and were having some form of agglomeration. Metal sulfides nanoparticles in PMMA matrix were more thermally stable as compared to pure PMMA but less thermally stable compared to their respective metal dithiocarbamate complexes which were used during metal sulfide nanoparticles syntheses. The CdS2/PMMA and CdS3/PMMA nanocomposites revealed relatively broad XRD peaks which indicate that CdS nanoparticles in the nanocomposite were small in sizes. The characteristic peaks of a cubic crystal structures are corresponding to (111), (220), (311) and (400) reflections. The average particle size ranging below 4nm of the crystallites was estimated by XRD and TEM measurements. The prepared materials were found to have unique sizes and structures and are expected to find various novel applications [1-24].

6.3 Recommendations and suggestions for future studies

Most researchers have used the single-source precursor method for the synthesis of metal sulfides nanoparticles but no report has been made on the best synthetic conditions. It is recommended that an extensive study be carried out on the use of single-source precursor method when varying: time of synthesis, temperature of thermolysis, capping agents and precursor to capping agent ratios. After the comparison has been made, this would shed more light on the best synthetic condition that gives crystalline structures with definable morphologies. This would in turn save lot of chemicals and time of synthesis. It is recommended that adducts of volatile complexes such as HgL^1L^2 and HgL^1L^3 be synthesized to see if decomposition profile is not improved.

Since only 3wt. % of metal sulfide dispersed in PMMA matrix for nanocomposites preparation, it is recommend that there should be an extensive study where the metal sulfide to PMMA ratio be varied from 0, 3, 6 and 9 wt. %. This would provide an insight to which ratio gives nanocomposites with enhanced optical and structural properties. Varying of polymer matrix is also recommended, so as to compare nanocomposites morphologies and crystallinity.

6.4 References

1. Onwudiwe, D.C.; Ajibade, P.A. ZnS, CdS and HgS nanoparticles via alkyl-phenyl dithiocarbamate complexes as single source precursors. *Int. J. Mol. Sci.* **2011**, *12*, 5538-5551.
2. Prabhu1, S.G.; Pattabi, B.M. Incorporation of acetoacetanilide crystals in host PMMA polymer matrix and characterizations of the hybrid composite. *J. Mine. Mater. Charact. Eng*. **2012**, *11*, 519-527.
3. Agrawal, S.; Patidar, D.; Saxena, N.S. Glass transition temperature and thermal stability of ZnS/PMMA nanocomposites. *Phase Trans.* **2011**, *84*, 888-900.
4. Alexandrescu, R.; Morjan, I.; Tomescu, A.; Simion, C.E.; Scarisoreanu, M.; Birjega, R.; Fleaca, C.; Gavrila, L.; Soare, I.; Dumitrache, F.; Prodan, G. direct production of a novel iron-based nanocomposite from the laser pyrolysis of $Fe(CO)_5$/MMA mixtures: Structural and sensing properties. *J. Nanomater.* **2010**, 1-12.
5. Sounderya, N.; Zhang, Y. Use of core/shell structured nanoparticles for biomedical applications. *Rec. Pat. Biomed. Eng.* **2008**, *1*, 34-42.
6. Xu, Z.; Yoon, J.; Spring, D.R. Fluorescent chemosensors for Zn^{2+}. *Chem. Soc. Rev.* **2010**, *39*, 1996-2006.
7. Yu, X.; Zhu, J.; Zhang, Y.; Weng, J.; Hu, L.; Dai, S. $SnSe_2$ quantum dot sensitized solar cells prepared employing molecular metal chalcogenide as precursors. *Chem. Commun.* **2012**, *48*, 3324-3326.
8. Cotton, F. A.; Wilkinson, G; Murillo, C.A.; Bochmann, M. Advanced inorganic chemistry, 6th ed.; Wiley and Sons: New York, **1999**.
9. Alfassi, Z.B. Instrumental multi-element chemical analysis. *Kluwer Acad. Pub.* Netherlands, **1998**.

10. Onwudiwe, D.C.; Ajibade, P.A. Synthesis and characterization of metal complexes of N-alkyl-N-phenyl dithiocarbamates. *Polyhedron* **2010**, *29*, 1431-1436.
11. Onwudiwe, D.C.; Ajibade, P.A. Synthesis and crystal structure of bis(N-alkyl-N-phenyl dithiocarbamato)mercury(II). *J. Chem Crystallogr*. **2011**, *41*, 980-985.
12. Hao, Y.F.; Meng, G.W.; Wang, Z.L.; Ye, C.H.; Zhang, L.D. Periodically twinned nanowires and polytypic nanobelts of ZnS: The role of mass diffusion in vapour-liquid-solid growth *Nano Lett.* **2006**, *6*, 1650-1655.
13. Gao, X.D.; Li, X.M.; Yu, W.D. Morphology and optical properties of amorphous ZnS films deposited by ultrasonic-assisted successive ionic layer adsorption and reaction method. *Thin Solid Films* **2004**, *468*, 43-47.
14. Chinnu, M.K.; Saravanan, L.; Jayavel, R. Synthesis and characterization of hexamethylene tetramine (HMTA) capped CdS nanoparticles by hydrothermal method. *Inter. J. Nanosci.* **2011**, *10*, 441-445.
15. Maity, R.; Chattopadhyay, K.K. Synthesis and optical characterization of CdS nanowires by chemical process. *J. Nanopart. Res.* **2006**, *8*, 125-130.
16. El- Bially A.B.; Seoudi R.; Eisa W.; Shabaka A.A.; Soliman S.I.; Abd El-Hamid R.K.; Ramadan R.A. Preparation, characterization and physical properties of CdS nanoparticles with different sizes. *J. Appl. Sci. Res.* **2012**, *8*, 676-685.
17. Zhang, Y.C.; Wang, G.Y.; Hu, X.Y. Solvothermal synthesis of hexagonal CdS nanostructures from a single-source molecular precursor. *J. Alloys Compd.* **2007**, *437*, 47-52.
18. O'Brien, P.; Park,J.H.; Waters, J.A single source approach to deposition of nickel sulfide thin films by LP-MOCVD. *Thin Solid Films* **2003**, *431*, 502-505.
19. Jeon, I.-Y.; Baek, J.-B. Nanocomposites derived from polymers and inorganic nanoparticles. *Mater*. **2010**, *3*, 3654-3674.

20. Nair, P.S.; Radhakrishnan, T.; Revaprasadu, N.; Kolawole, G.; O'Brien, P. Cadmium ethylxanthate: A novel single-source precursor for the preparation of CdS nanoparticles. *J. Mater. Chem*. **2002**, *12*, 2722 - 2725.
21. Plante, I.J.-L.; Zeid, T.W.; Yang, P.; Mokari, T. Synthesis of metal sulfide nanomaterials via thermal decomposition of single-source precursors. *J. Mater. Chem*. **2010**, *20*, 6612-6617.
22. Agrawal, S.; Patidar, D.; Saxena, N.S. Glass transition temperature and thermal stability of ZnS/PMMA nanocomposites. *Phase Trans.* **2011**, *84*, 888-900.
23. Zhao, R.; Chen, C.Z.; Li, Q.F.; Luo, W.B. Effects of stress and physical ageing on nonlinear creep behavior of poly(methyl methacrylate), *J. Cent. South Univ. Technol*. **2008**, *15*, 582-588.
24. Dixit, M.; Gupta, S.; Mathur, V.; Rathore, K.S.; Sharma, K.; Saxena, N.S. Study of glass transition temperature of PMMA and CdS-PMMA composite. *Chalc. Lett.* **2009**, *6*, 131-136.

6.5 Appendix

FH460 = ^{1}H- and ^{13}C-NMR spectra of ammonium N-phenyldithiocarbamate ligand respectively

FH461 = ^{1}H- and ^{13}C-NMR spectra of ammonium N-methyl-N-phenyldithiocarbamate ligand respectively

FH462 = ^{1}H- and ^{13}C-NMR spectra of ammonium N-ethyl-N-phenyldithiocarbamate ligand respectively

FH463 = ^{1}H- and ^{13}C-NMR spectra of (N-phenyl-N, N-methyl phenyl dithiocarbamato)Zn(II) complex respectively

FH464 = ^{1}H- and ^{13}C-NMR spectra of (N-phenyl-N,N-methyl phenyl dithiocarbamato)Cd(II) complex respectively

FH465 = ^{1}H- and ^{13}C-NMR spectra of (N-phenyl-N,N-methyl phenyl dithiocarbamato)Hg(II) complex respectively

FH466 = ^{1}H- and ^{13}C-NMR spectra of (N-phenyl-N, N-ethyl phenyl dithiocarbamato)Zn(II) complex respectively

FH467 = ^{1}H- and ^{13}C-NMR spectra of (N-phenyl-N,N-ethyl phenyl dithiocarbamato)Cd(II) complex respectively

FH468 = ^{1}H- and ^{13}C-NMR spectra of (N-phenyl-N,N-ethyl phenyl dithiocarbamato)Hg(II) complex respectively

Appendix 6.5.1: ^{1}H- and ^{13}C-NMR spectra of ammonium N-phenyl dithiocarbamate

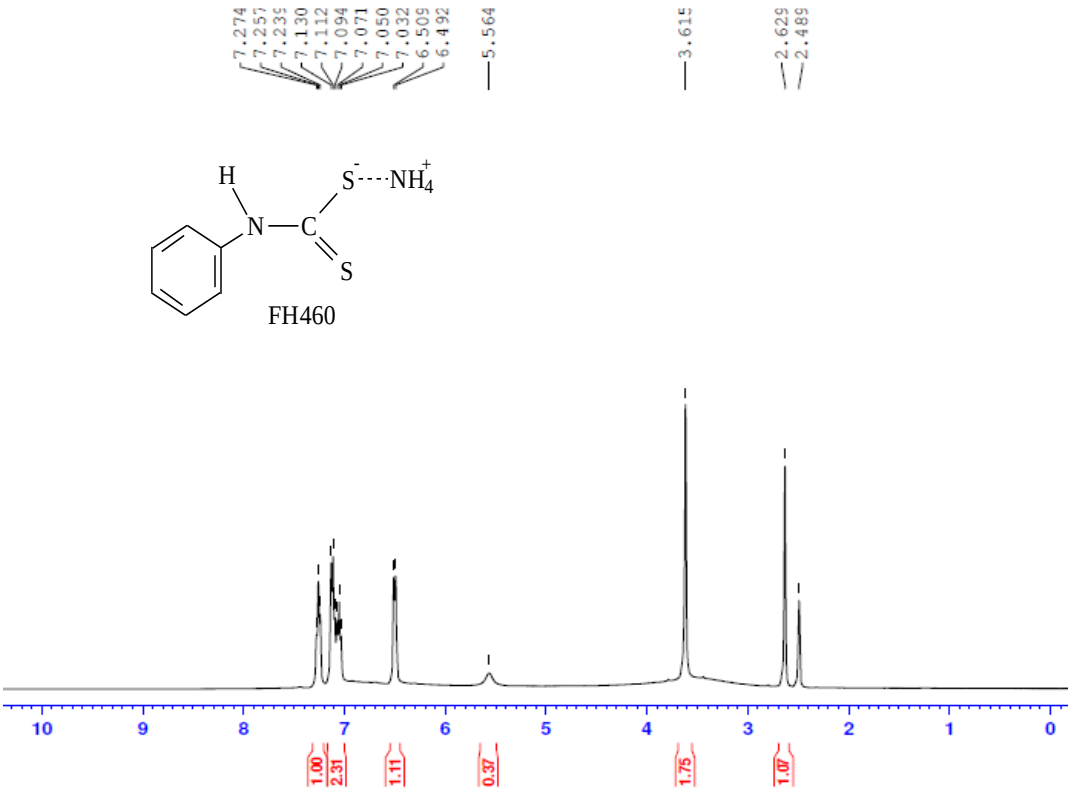

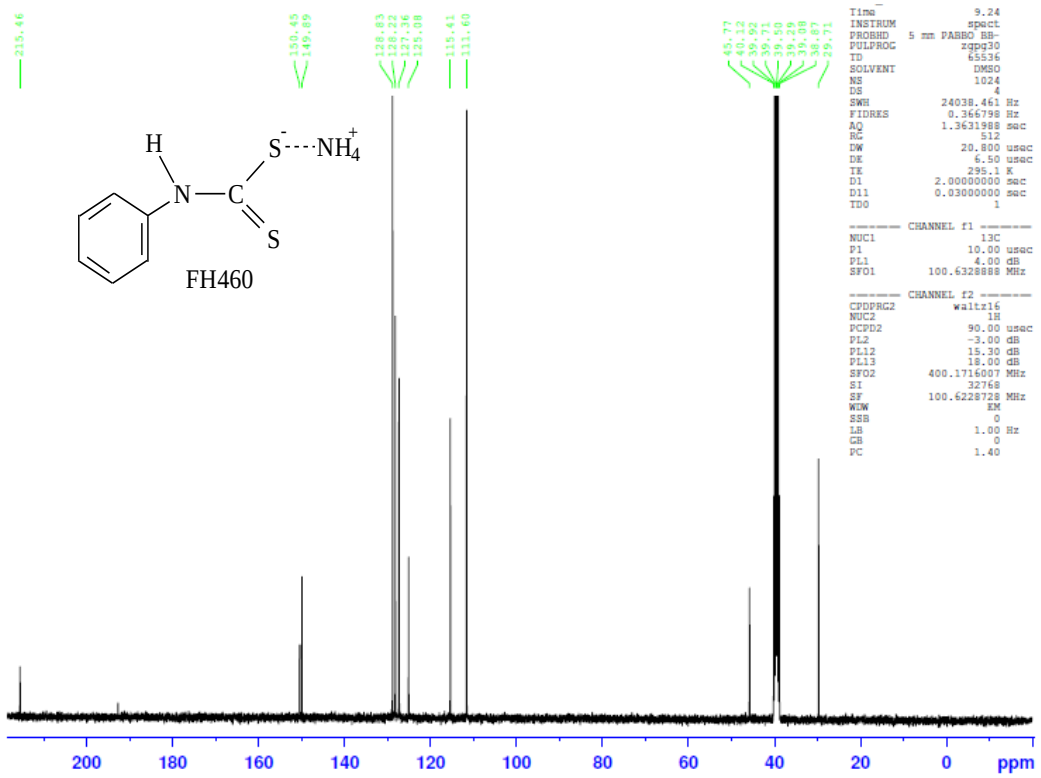

Appendix 6.5.2:

^{1}H- and ^{13}C-NMR spectra of ammonium N-methyl-N-phenyldithiocarbamate

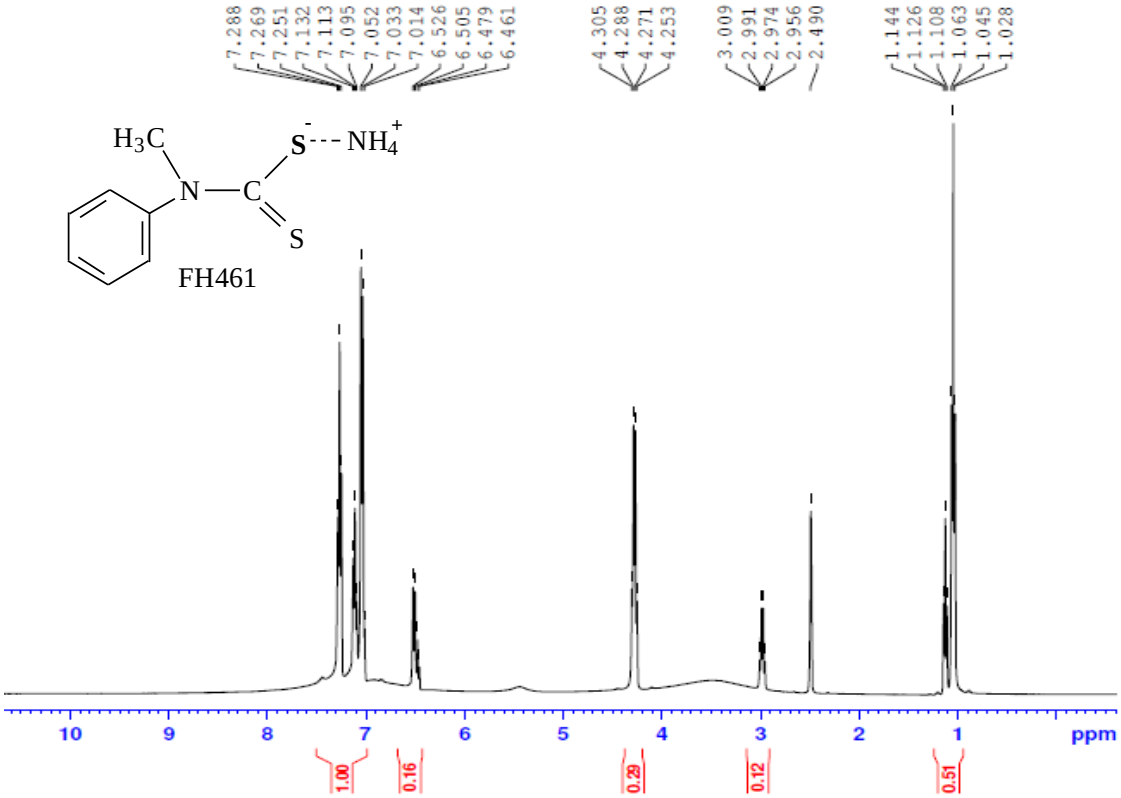

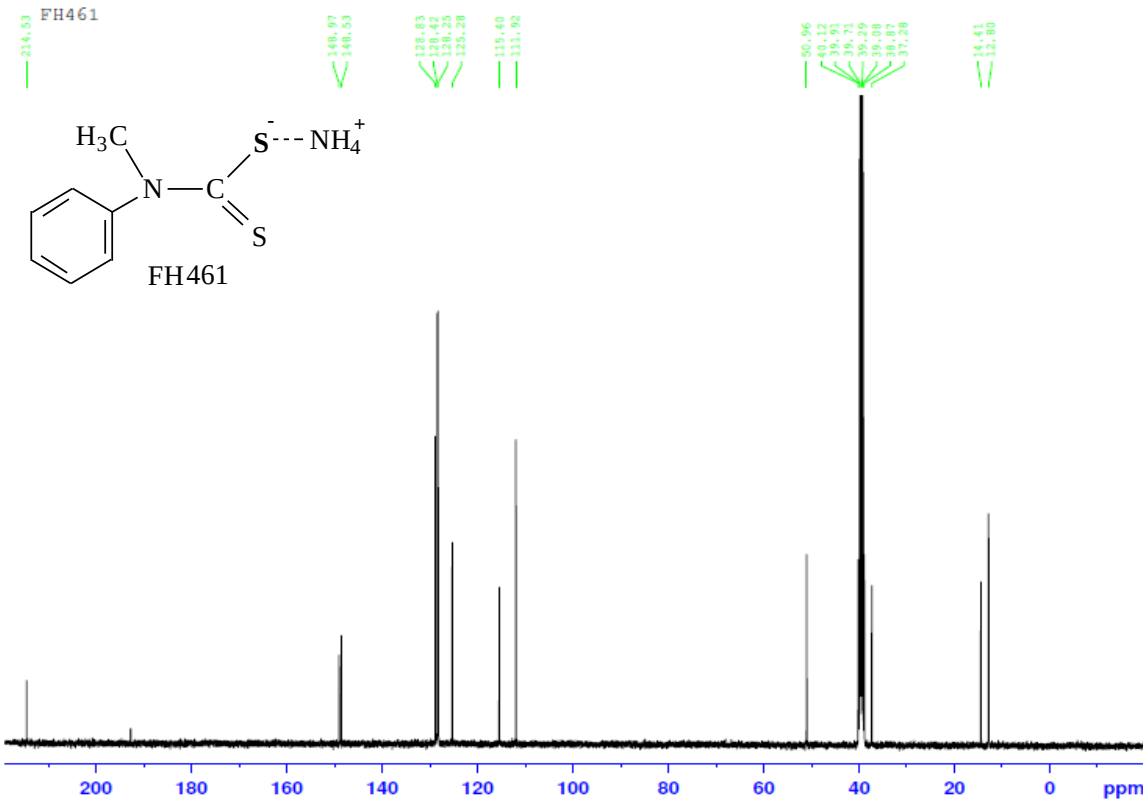

Appendix 6.5.3:

^{1}H- and ^{13}C-NMR spectra of ammonium N-ethyl-N-phenyldithiocarbamate

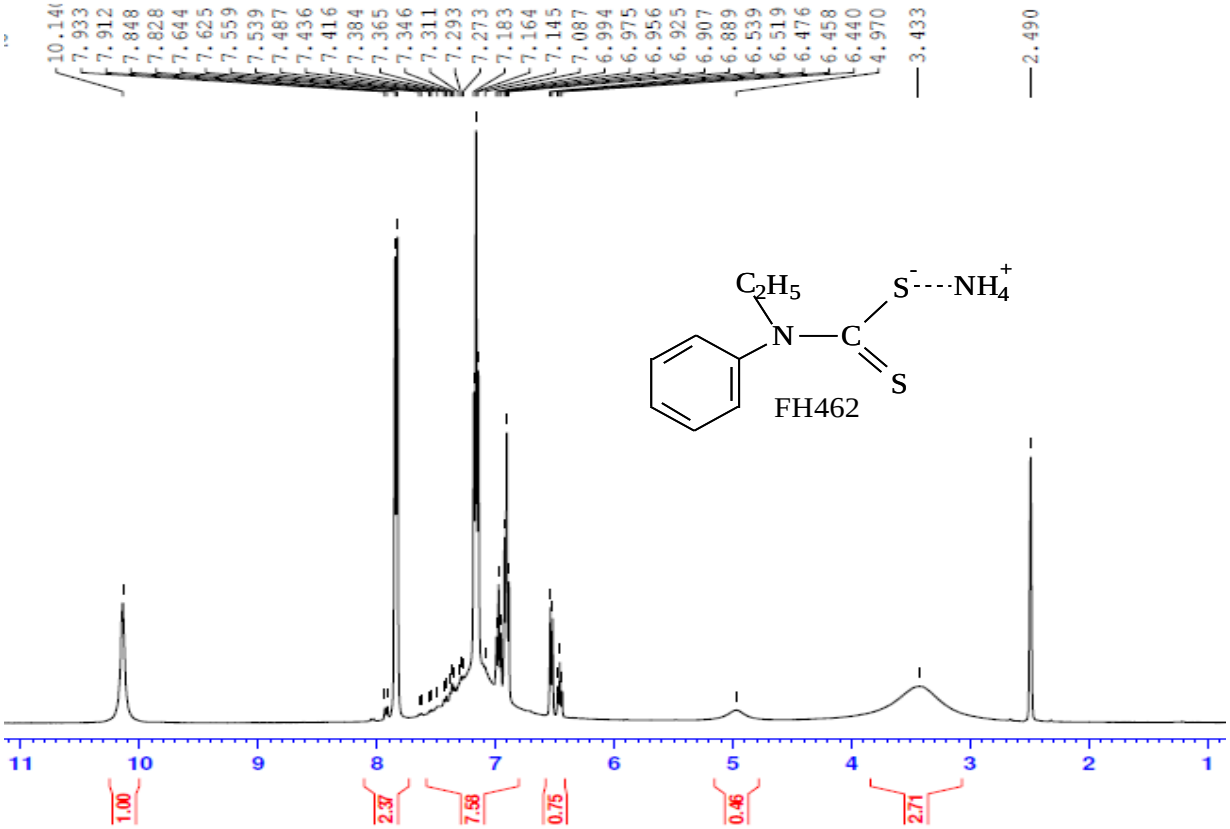

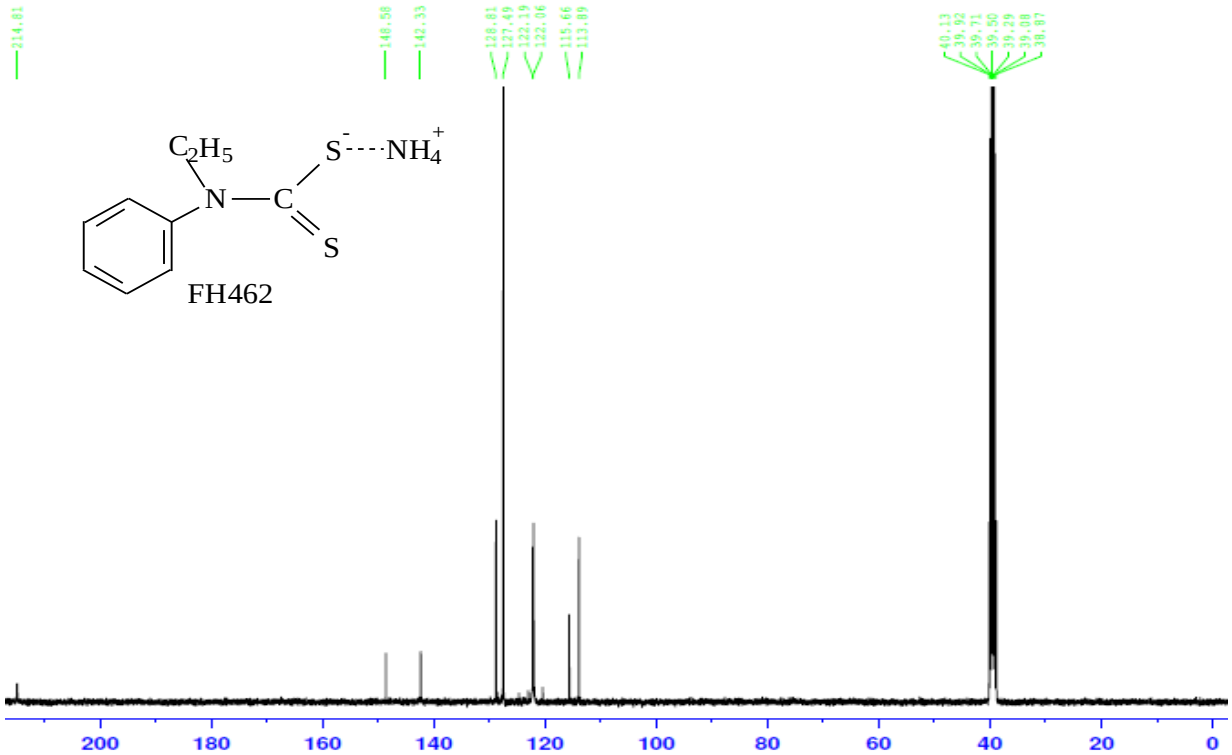

Appendix 6.5.4:

^{1}H- and ^{13}C-NMR spectra of (N-phenyl-N, N-methyl phenyl dithiocarbamato)Zn(II)

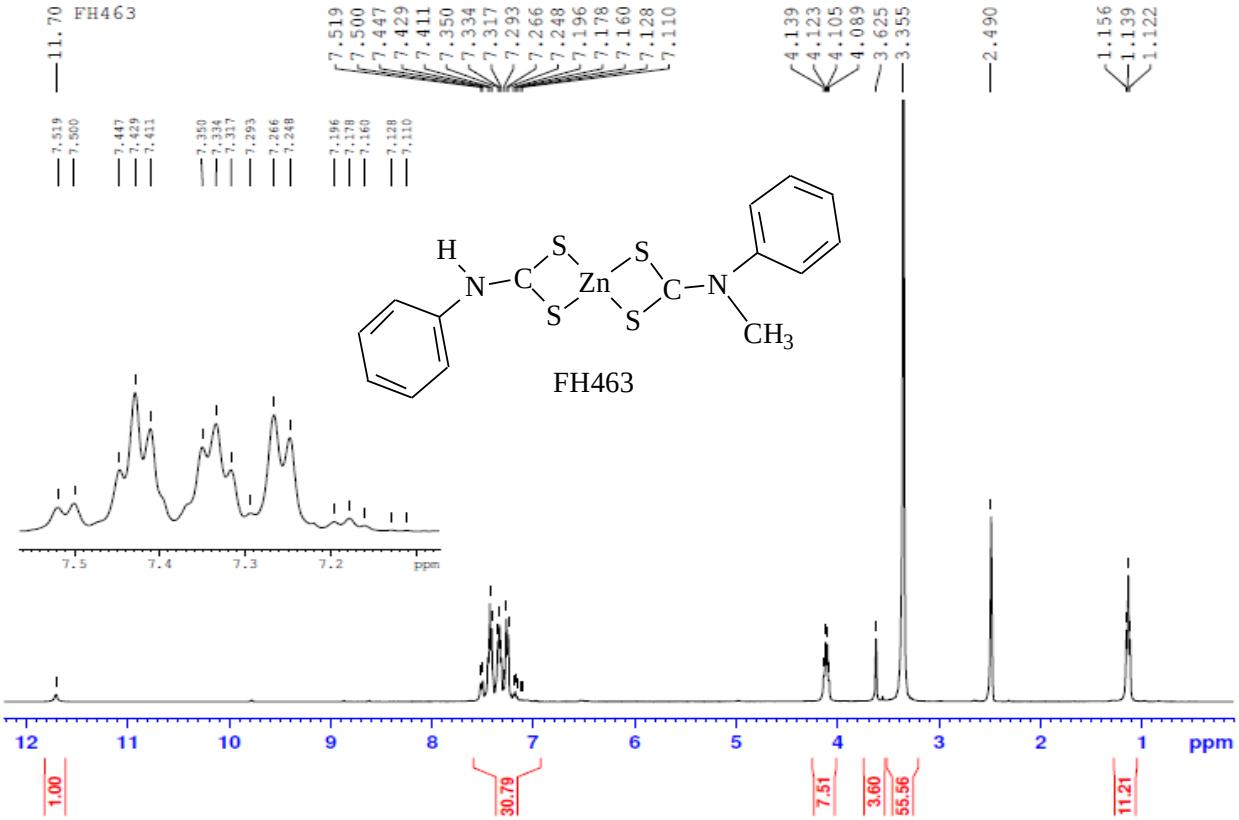

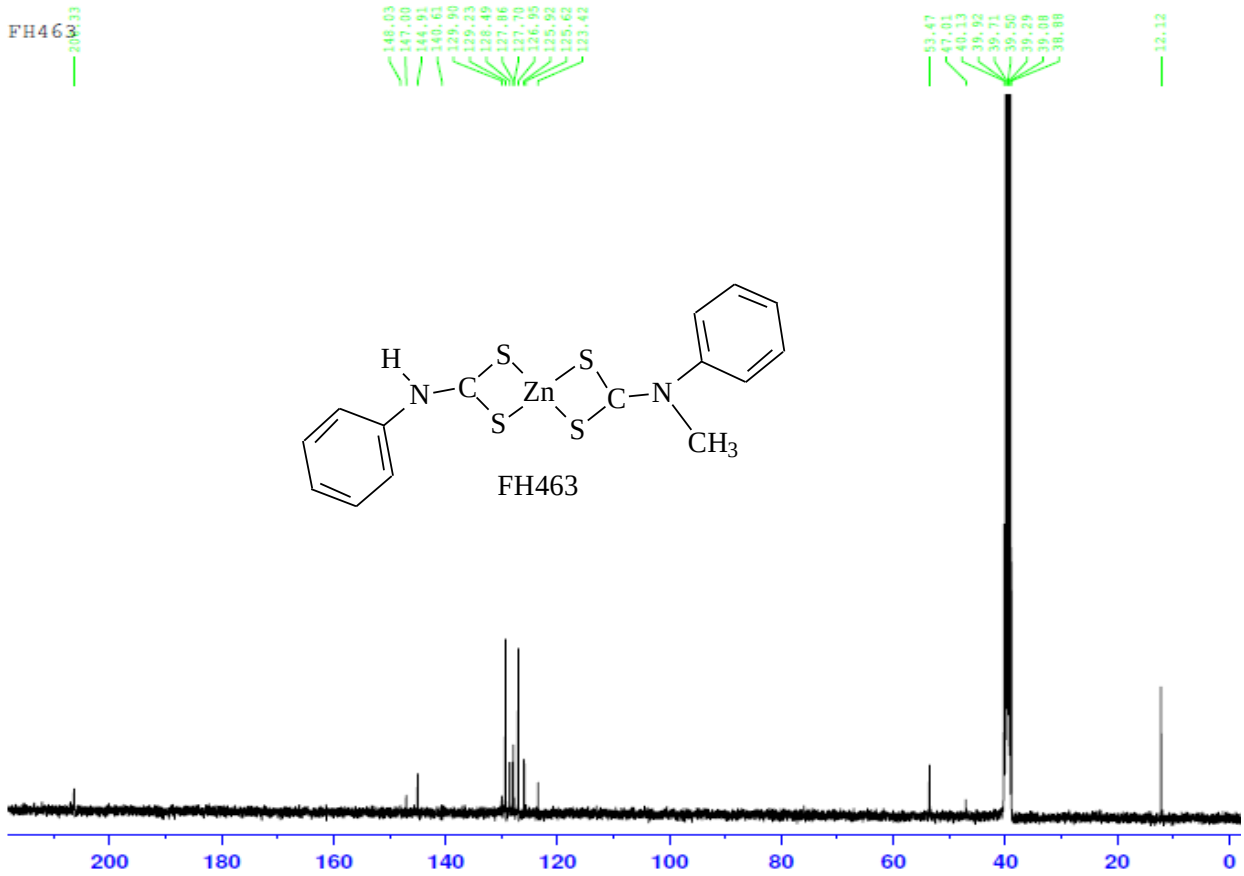

Appendix 6.5.5:

^{1}H- and ^{13}C-NMR spectra of (N-phenyl-N, N-methyl phenyl dithiocarbamato)Cd(II)

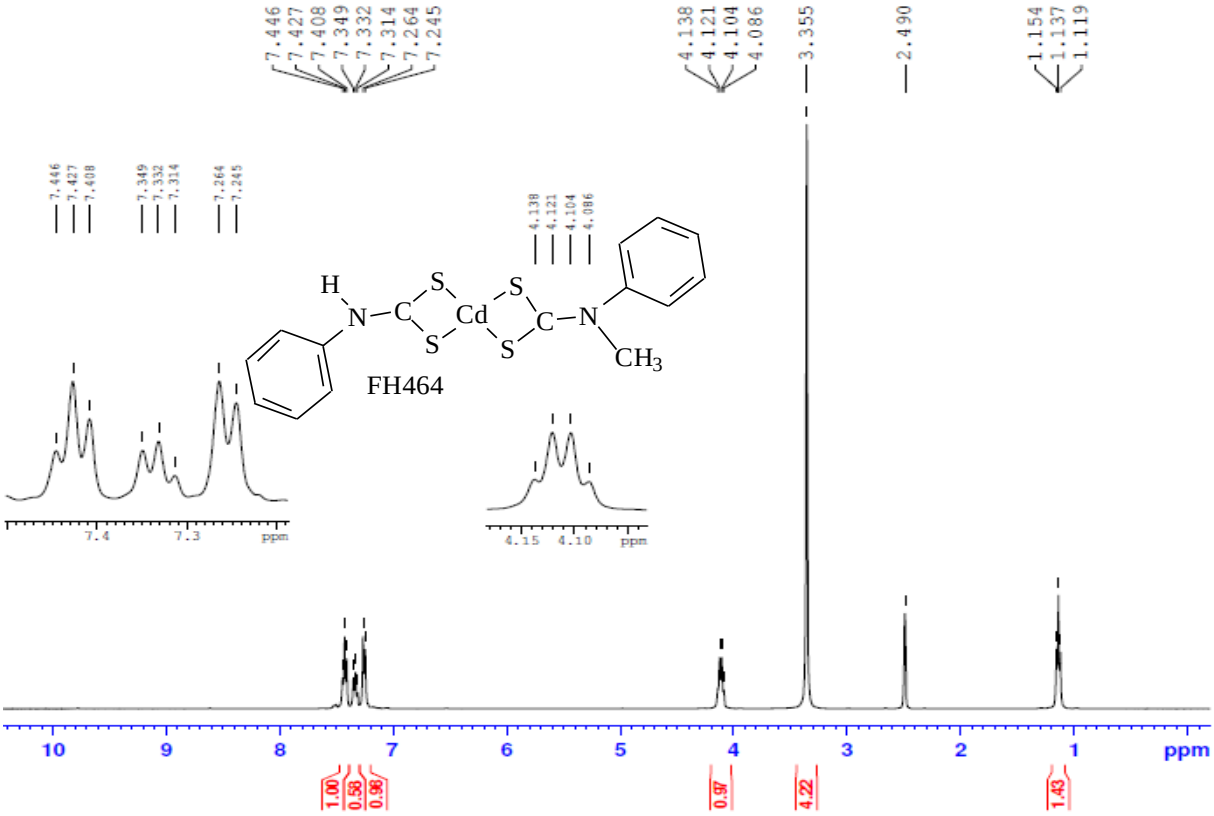

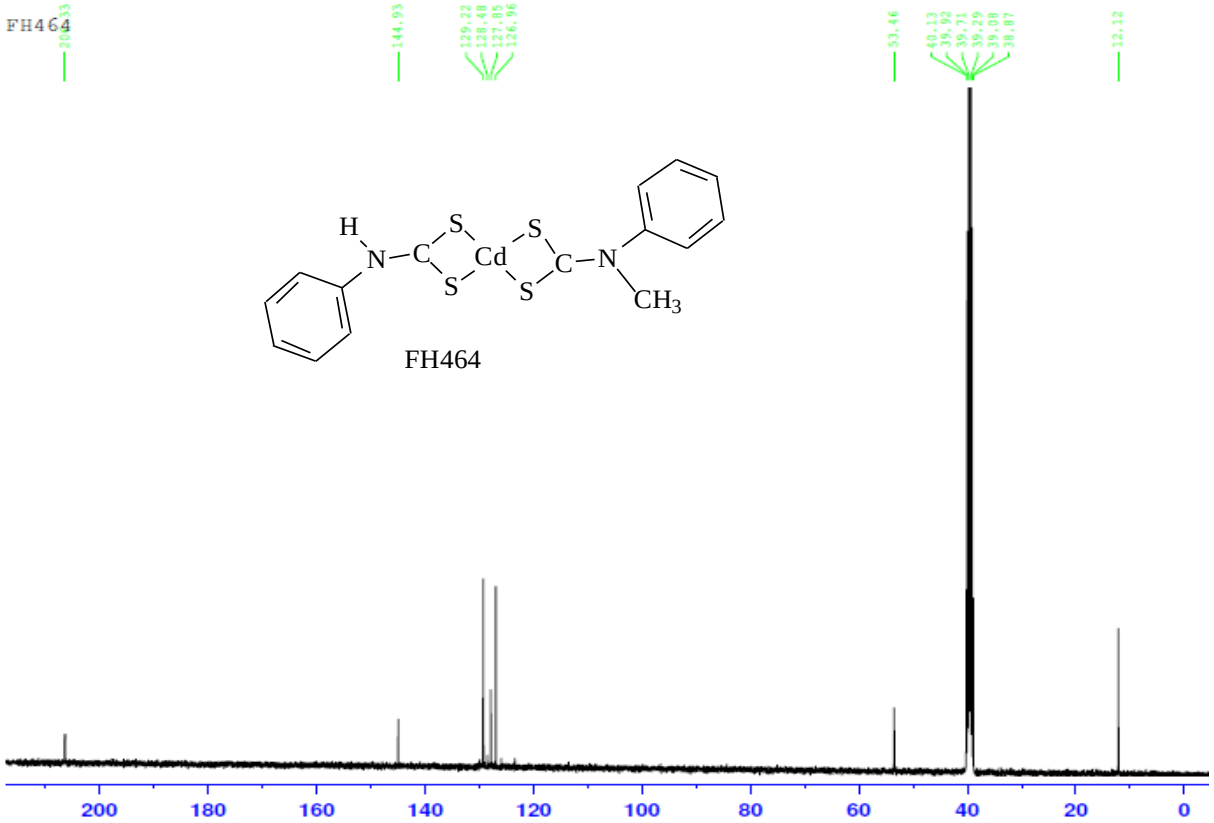

Appendix 6.5.6:

^{1}H- and ^{13}C-NMR spectra of (N-phenyl-N, N-methyl phenyl dithiocarbamato)Hg(II)

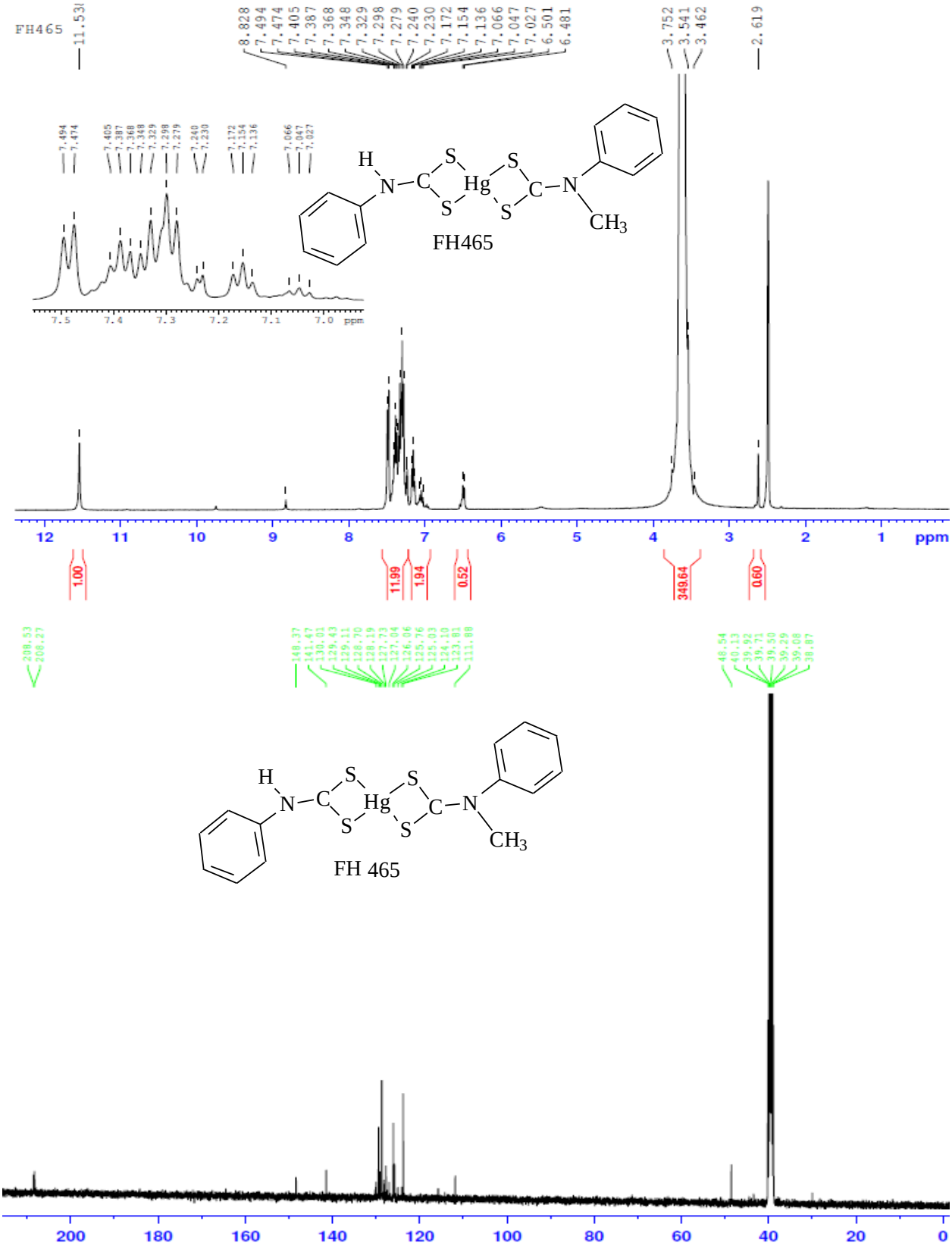

Appendix 6.5.7:

^{1}H- and ^{13}C-NMR spectra of (N-phenyl-N, N-ethyl phenyl dithiocarbamato)Zn(II)

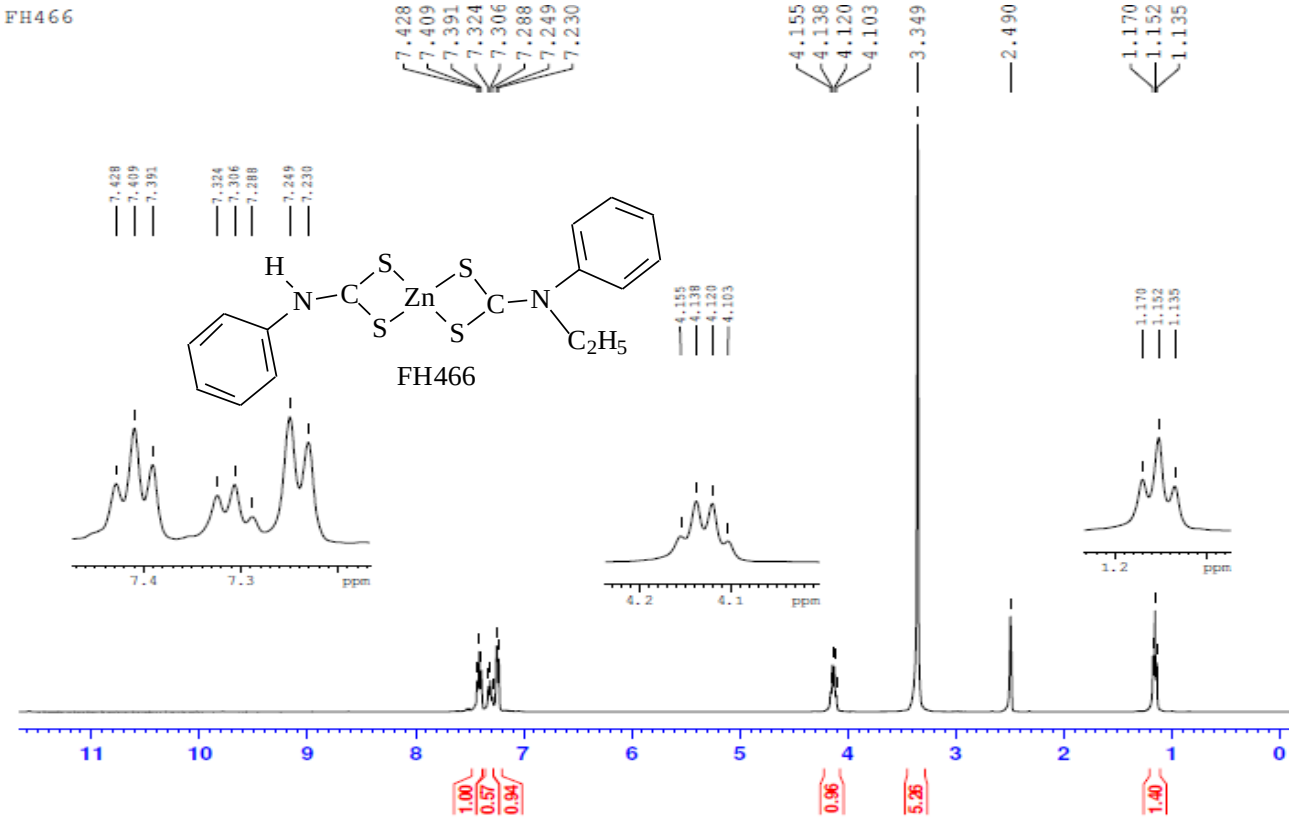

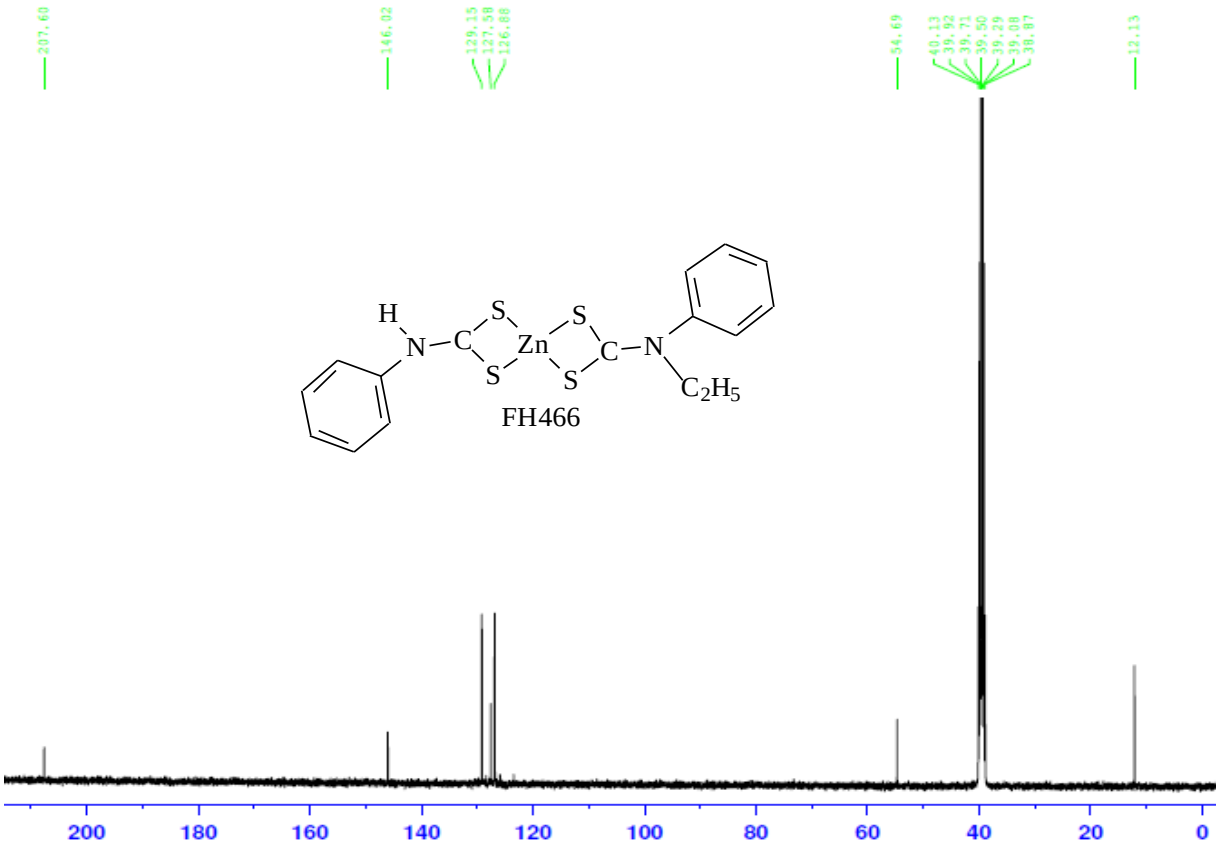

Appendix 6.5.8:

^{1}H- and ^{13}C-NMR spectra of (N-phenyl-N, N-ethyl phenyl dithiocarbamato)Cd(II)

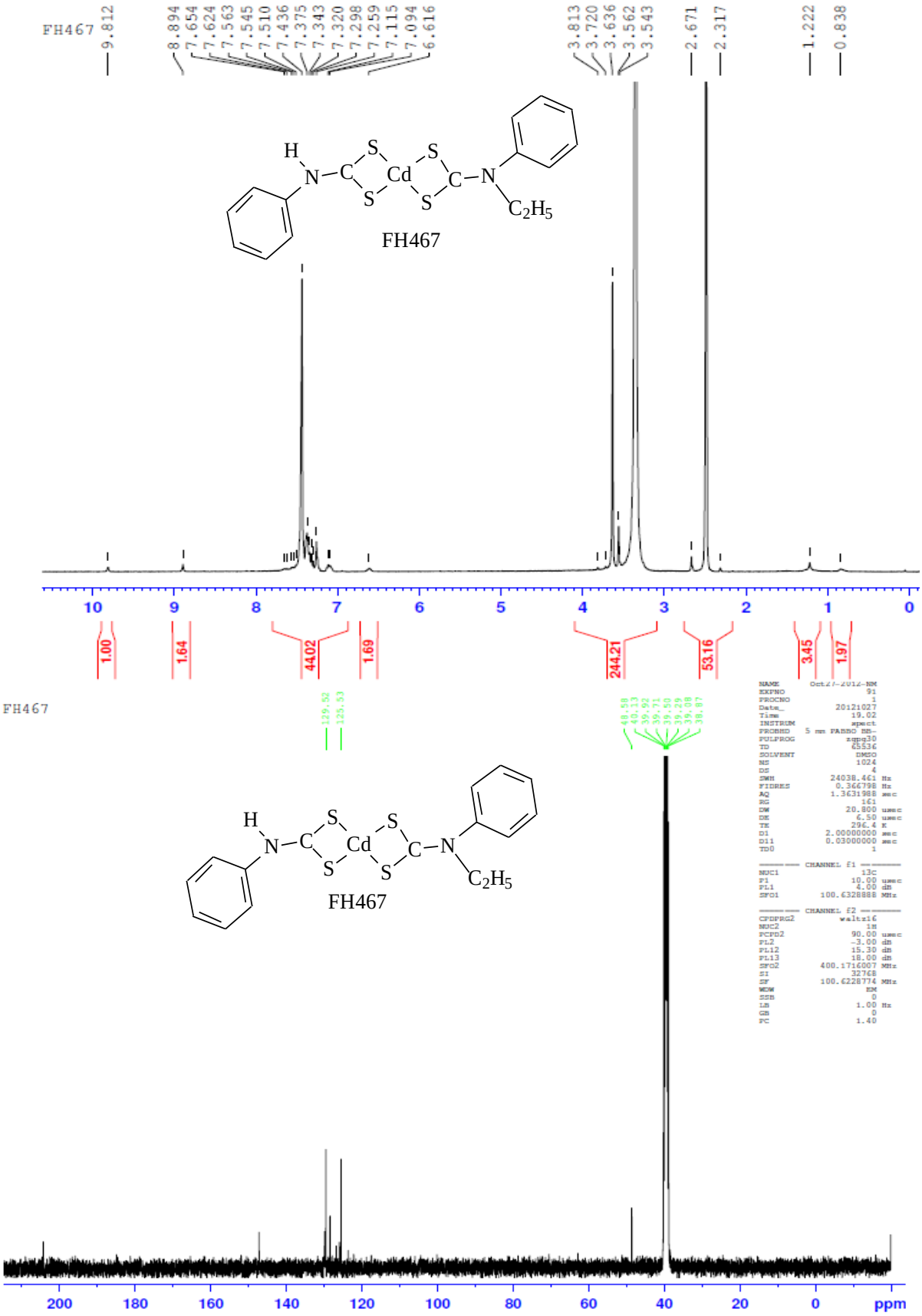

Appendix 6.5.9:

^{1}H- and ^{13}C-NMR spectra of (N-phenyl-N, N-ethyl phenyl dithiocarbamato)Hg(II)

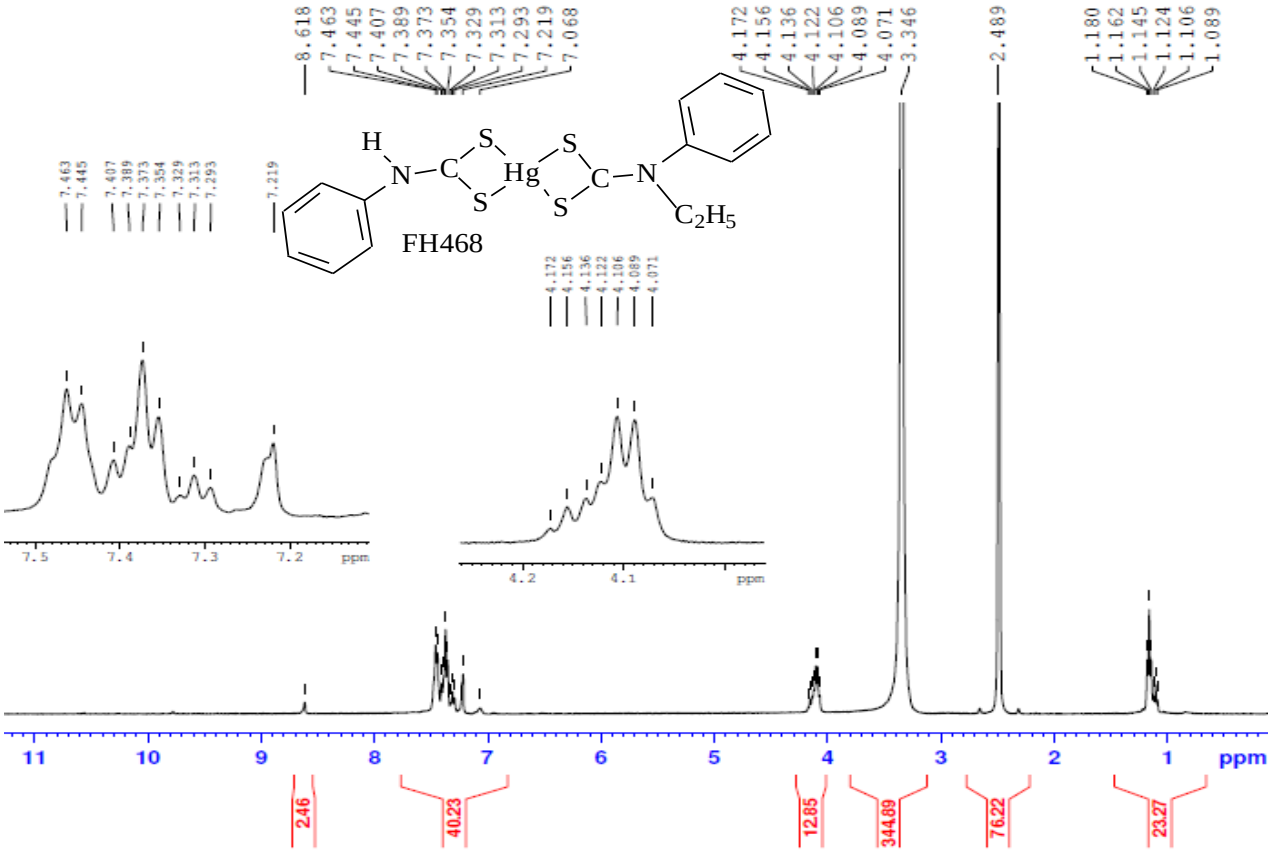

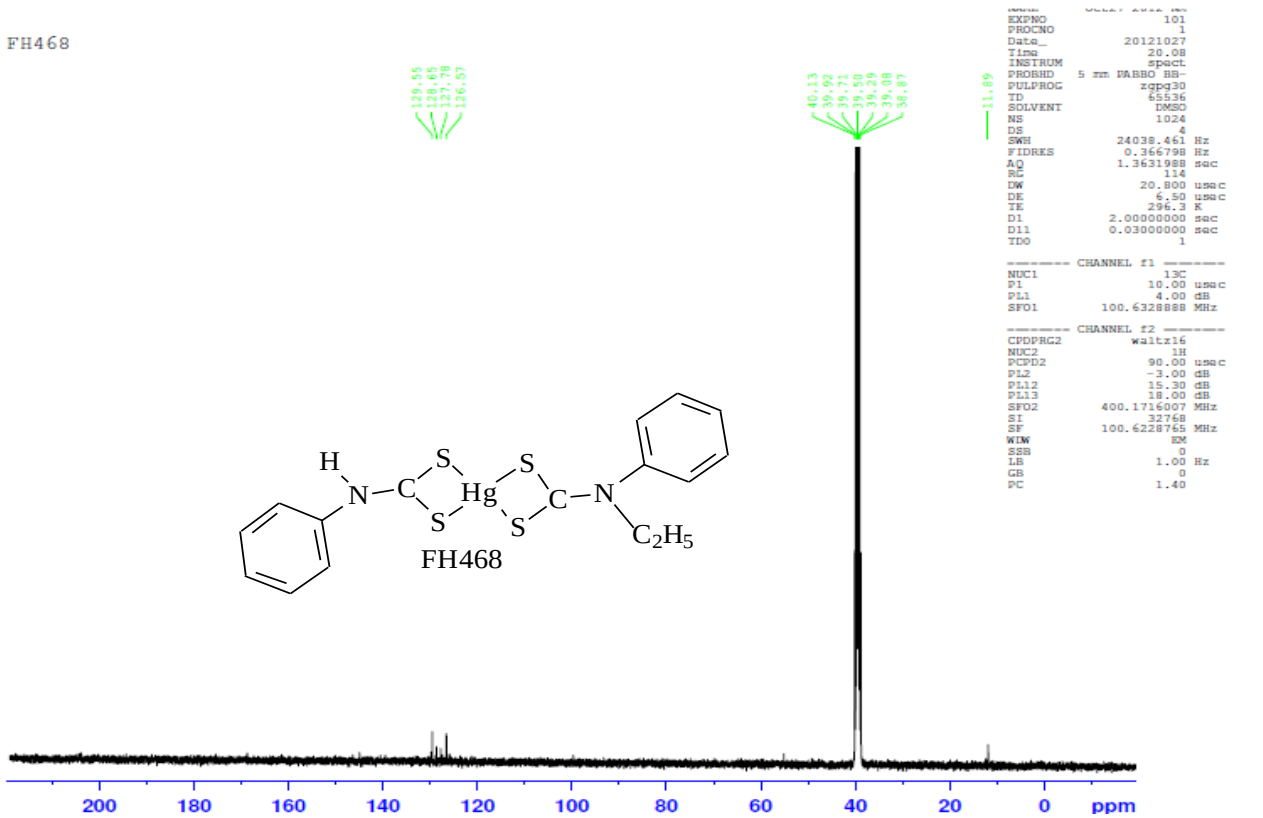

Appendix 6.5.10: Manuscripts resulting from this dissertation

Johannes Z. Mbese and Peter A. Ajibade, **2014**. Synthesis, structural and optical properties of ZnS, CdS and HgS nanoparticles from dithiocarbamato single molecules precursors. *Journal of Sulfur Chemistry*. (ID: 912280 DOI:10.1080/17415993.2014.912280).

Peter Ajibade and Johannes Mbese, **2014**. Synthesis and characterization of metal sulfides nanoparticles/poly(methyl methacrylate) nanocomposites. Under peer-review.

Appendix 6.5.11: Conference contributions from this dissertation

Poster: Johannes Z. Mbese and Peter A. Ajibade. Optical and structural characterization of ZnS and CdS semiconductor nanoparticles. **4th International NanoAfrica Conference on Nanoscience and Nanotechnology**, University of the Free State, Bloemfontein, South Africa from April 1-4th **2012**.

Poster: Johannes Z. Mbese and Peter A. Ajibade. Preparation and characterization of metal sulfides nanoparticles/ PMMA nanocomposites. **16th South Africa Chemical Institute (SACI) inorganic chemistry conference (INORG2013) held at the Southern Sun Elangeni Hotel,** Durban from 30 June to 4 July **2013**.

Oral: Johannes Z. Mbese and Peter A. Ajibade. Synthesis and characterization of metal sulfides nanoparticles/ PMMA nanocomposites. **41st SACI Convention at River Park Conference Center**, East London, South Africa held from December 1-6th **2013**.